UNIVERSITY OF LIVERPOOL

The Distribution and Vertical Transport of Resources in the Upper Ocean

Thesis submitted in accordance with the requirements of the University of Liverpool for the degree of

Doctor in Philosophy

by

Shaun James Rigby

January 2021

in the

Faculty of Science and Engineering

School of Environmental Sciences

Department of Earth, Ocean and Ecological Sciences

Abstract

The Distribution and Vertical Transport of Resources in the Upper Ocean

Shaun J. Rigby

Marine phytoplankton support higher trophic levels and are a key component of the biological carbon pump. The growth of marine phytoplankton is supported by the availability of bio-essential resources and incident light in the upper ocean. Over long periods, the biological carbon pump is sustained by the replenishment of depleted resources. In winter, the deepening of the mixed layer entrains underlying waters, transferring resources between the seasonal thermocline and mixed layer. The transfer of properties by entrainment is augmented by other physical processes, such as diapycnal diffusion and aeolian deposition. This thesis aims to synthesise and exploit new datasets in the Atlantic Ocean and Equatorial Pacific Ocean to quantify mixed-layer resource availability and physical resource transfers into the upper ocean.

The availability of resources in the winter mixed-layer is quantified by combining observational data from the *GEOTRACES* programme with mixed layer estimates from a global data assimilation model. Basin-scale patterns in the availability of nitrate, phosphate, silicic acid, cadmium, zinc, cobalt, iron and manganese throughout the Atlantic Ocean mixed-layer are identified. Relative to phosphate, we show that the subtropical North Atlantic is depleted in nitrate and cadmium, while enriched in silicic acid, zinc, cobalt, iron and manganese, with the reverse true in high latitudes. Intermediate conditions in relative resource availability are located in mid latitudes. Differences in the availability of each resource are linked to the vertical structure, where mixed-layer resource stoichiometry is governed by offsets in nutricline depths between resources. We note a coupling of silicic acid and zinc vertical profiles in the subtropical North Atlantic, in contrast to recent works highlighting the rapid recycling of zinc compared to silicic acid; however, we suggest that reversible scavenging plays a crucial role in setting the zinc vertical profile in the deep water column, causing an alignment with silicic acid. Winter-time entrainment increases the availability of nutrient-type resources, such as nitrate, while surface stocks are eroded for those resources with scavenged-type resources, such as manganese, due to their vertical

distributions, inducing a transfer of these resources from the mixed layer into the seasonal thermocline. In the mixed-layer, singular nitrogen limitation is identified in low latitudes, while singular iron limitation is identified at high latitudes, highlighting the potential for high latitude iron availability to influence low latitude biogeochemistry. Inter-annual variability in the depth of winter mixing causes changes in the winter mixed-layer resource stoichiometry, most notably in the low latitude North Atlantic where the mixed layer becomes richer in silicic acid, zinc, cobalt, iron and manganese relative to phosphate under a shoaled winter mixed-layer scenario. Changes to winter mixed-layer resource stoichiometry has important ecological implications. For example, in the equatorial Atlantic, changes to the distributions of nitrate and iron expand the diazotroph niche and hamper the success of non-diazotrophs.

To further understand the importance of winter-time entrainment, this thesis applied the helium 'flux gauge' approach to estimate physical mixing in the upper ocean during two seasonally different field campaigns. Results demonstrate that active entrainment increases total physical mixing by a factor of ~7 compared to regions where entrainment is relatively weak. Vertical resource fluxes are also controlled by gradients in vertical resource profiles. Vertical gradients in resource profiles are linked to oxygen gradients, as expected from current knowledge of trace element redox chemistry, however, there are differences relationships with oxygen between resource and region. In the subtropical North Atlantic, we demonstrate that variability in resource fluxes is governed by mixing, while in the equatorial Pacific, variability in resource gradients and mixing equally controls resource flux variability. The vertical resource flux stoichiometry is compared to the cellular stoichiometry of *in-situ* biota to show there are mismatches between external resource supply and biological demand.

Finally, an investigation into the effect of seafloor topography on resource transport showed that mixing in the upper 1000 m is a factor ~2 greater over shallow topography (Rainbow hydrothermal vent site, ~2700 m depth) compared to a deeper topographic site (Trans-Atlantic Geotraverse hydrothermal vent site, ~3600 m depth) along the Mid-Atlantic Ridge. Vertical resource fluxes are inferred by combining data from vertical microstructure profilers with resource profiles based on the geographic

position and external forcing by wind and tides. Generally, nutrient-type and scavenged-type resources demonstrated upwards and downwards diapycnal fluxes, respectively. Vertical diffusivity at the shallow topographic site was estimated as a factor ~2 larger when compared to the deep topographic site. The increase in mixing at the shallow topographic site was not matched by the magnitude of resource fluxes, as gradients in vertical resource profiles were weaker at the shallow site, mitigating against the increase in mixing. Differences in the vertical resource profiles are linked to differences in the mixing rates, water mass contributions and regeneration rates between the sites. The contrasting vertical diffusivity observed at the shallow and deep topographical sites may be used to gain insights into a future ocean where vertical diffusivity is reduced, and stratification increased. In such a scenario, vertical resource profiles may adjust to a reduction in mixing and therefore mitigate change to the overall vertical resource flux. Thus, the first-order view that a reduction in diffusivity drives a proportional decrease in the resource flux is challenged when concurrent changes to resource profiles are considered.

Declaration of Authorship

I hereby declare that the content of this thesis titled “The Distribution and Vertical Transport of Resources in the Upper Ocean” is a product of my own work. The work contained within this thesis has not been previously presented, in whole or in part, for the award of any other degree or qualification at any other institution.

Shaun James Rigby

Contents

List of Figures

List of Tables

mmol m^{-2} yr^{-1}, Fe, Mn and Al flux estimates in µmol m^{-2} yr^{-1}. K_z estimated from ARGO float data (Whalen et al. 2012). Resource concentration data from GA13.

Acknowledgements

I would like to thank my supervisors, Alessandro Tagliabue, Ric Williams and Eric Achterberg for their continued support throughout my PhD. First, Al, thank you for your guidance, enthusiasm, encouragement and input over the years. I have gained an awful lot from your supervision. Second, special thanks to Ric for your help, patience and offering another point of view, it certainly strengthened this work. I still remember visiting the University of Liverpool as a BSc applicant and us discussing aspects of the undergraduate course and life in Liverpool. Finally, thanks to Eric, your feedback has been invaluable in improving the quality of my scientific analysis and writing.

I'd like to thank all of the academic staff in the Ocean Sciences department at the University of Liverpool. Throughout my studies, initially as a BSc student, then transferring to the MOSci and later pursuing a PhD, all academic staff have been approachable and supportive. Perhaps I overstayed my welcome, but perhaps not, I like to think the latter.

Of course, I must thank the friends I have made along the way. Lewis, Kieran, Dave W, Jenny, Arthur, Dave B, Kat, Amy, Ty, everyone who has passed through rooms 205 and 206, you have all helped me finish this PhD thesis. I also have to thank an international group of PhD students whom I met at the *GEOTRACES* summer school in the first year of my PhD. Koko, Laramie, Colleen and Susanna, I hope we can continue to meet up at more conferences and other places around the world. Thanks go to the scientists and crew of the *RRS James Cook* during JC156 for making the expedition such a memorable experience.

I honestly do not believe I would be in the position I am now without the University of Liverpool Golf Team. Thanks to everyone who has joined and contributed to the club in my too many years involved. Cooper, Animal, Parky, Bryony, Osbourne, Fosker, Vardz, Dec, Louis, Johno, Alf, Dhiz, Hurrell, Cal, Spencer, WW, Danial, JT, Nathan, Amos, McQueen, Hosty, Ethan, Ryan and finally Stu (obviously). Wednesday afternoons plus the odd extra game at Royal Liverpool GC really helped me detach from work and offered a chance to reset. Plus, the competition against other

universities was a welcome distraction. My time at university would not be the same without it. See you all at alumni.

Finally, and most importantly, I cannot thank my family enough. You have always provided support, whether it be talking about my current studies or help with moving between the numerous university houses. Thank you for providing the safety net where I always knew I'd have a place to go, no matter what.

Chapter 1

Introduction

The ocean is a key component of the Earth system, responsible for around 50% of net global primary production and acting as a major carbon sink (Field et al., 1998, Gruber et al., 2002, Landschützer et al., 2015). Oceanic primary production is the generation of organic biomass by marine phytoplankton. Net primary production is a product of growth rate and biomass, where the growth rate is shaped by the availability of resources and light (bottom up control), and predation controls phytoplankton biomass (top down control) (Martin and Fitzwater, 1988, Landry et al., 1997, Falkowski et al., 1998, Mills et al., 2004, Moore et al., 2013, Browning et al., 2017a). Over long periods, export removes resources from the upper ocean which must be replenished to maintain productivity. Numerous external inputs, including those from continental margins (Noble et al., 2012, van Hulten et al., 2017), aeolian deposition (Jickells et al., 2005, Baker et al., 2013, Shelley et al., 2017), rivers (Tréguer et al., 1995, Sharples et al., 2017) and hydrothermal vents (Tagliabue et al., 2010), act in tandem to supply resources to the ocean. Resources are redistributed in the ocean interior by physical processes, including winter-time entrainment (Tagliabue et al., 2014, Achterberg et al., 2018), nutrient streams (Pelegrí et al., 1996, Williams et al., 2006), eddy pumping (Falkowski et al., 1991, Siegel et al., 1999, McGillicuddy, 2016), Ekman redistribution (Williams and Follows, 1998) and diapycnal mixing (Painter et al., 2014, Tuerena et al., 2019). However, vertical fluxes of key resources, particularly trace elements, remain poorly quantified on a basin-scale. Examining contemporary resource distributions and understanding how resource fluxes shape global productivity are imperative to predicting the oceanic response to future climate change.

In this Chapter, the biogeochemical cycling and physical resupply pathways of key resources are introduced.

1.1 Biological Resource Demands

The Redfield Ratio of carbon, nitrogen (N) and phosphorus (P) of 106:16:1 respectively is a cornerstone of marine biogeochemistry and reflects the cellular composition of plankton in seawater (Redfield, 1958). Recently, the Redfield Ratio has been extended to include trace elements and variability between taxa groups (Ho et al., 2003). The productivity of marine phytoplankton is limited where resource stocks become insufficient to sustain growth, light levels are reduced (due to self-shading or a deep mixing event), or grazing rates become greater than primary production (de Baar, 1994) .

The role of micronutrients as potentially limiting productivity in the ocean was suggested during the *Discovery* cruise series in the early 20th century (Hart, 1942). However, accurate measurements of trace metal concentrations in seawater were not possible until advances in trace metal clean sampling approaches and analytical techniques were made. Field observations of dissolved iron (Fe) consistent with modern observations were first published in 1982, demonstrating nanomolar (10^{-9} mol kg^{-1}) Fe concentrations (Gordon et al., 1982). Iron-addition bioassay experiments during the VERTEX programme in the late 1980s revealed that low Fe availability in the upper ocean prevented the complete drawdown of major nutrients, highlighting Fe as a potential growth limiting resource (Martin and Fitzwater, 1988, Martin et al., 1991). These Fe focused studies catalysed trace element oceanography and would form the origins of the iron hypothesis, suggesting changing Fe supply plays an important role in controlling glacial changes in the global carbon cycle (Martin, 1990).

Alongside Fe, marine phytoplankton require a suite of other resources for metabolic processes (Sunda, 1989, Twining and Baines, 2013), including macronutrients nitrate (NO_3), phosphate (PO_4) and silicic acid (Si), as well as micronutrient trace elements zinc (Zn), manganese (Mn), cadmium (Cd) and cobalt (Co). NO_3 and PO_4 are fundamental to life and are required for the production of DNA, proteins and enzymes. Si is primarily used in diatom frustules (Tréguer et al., 1995). Among other uses, Fe is an electron transporter in photosynthesis (Raven et al., 1999) and the metalloenzyme nitrogenase increases the Fe demand of di-nitrogen-fixing organisms (Raven, 1988a,

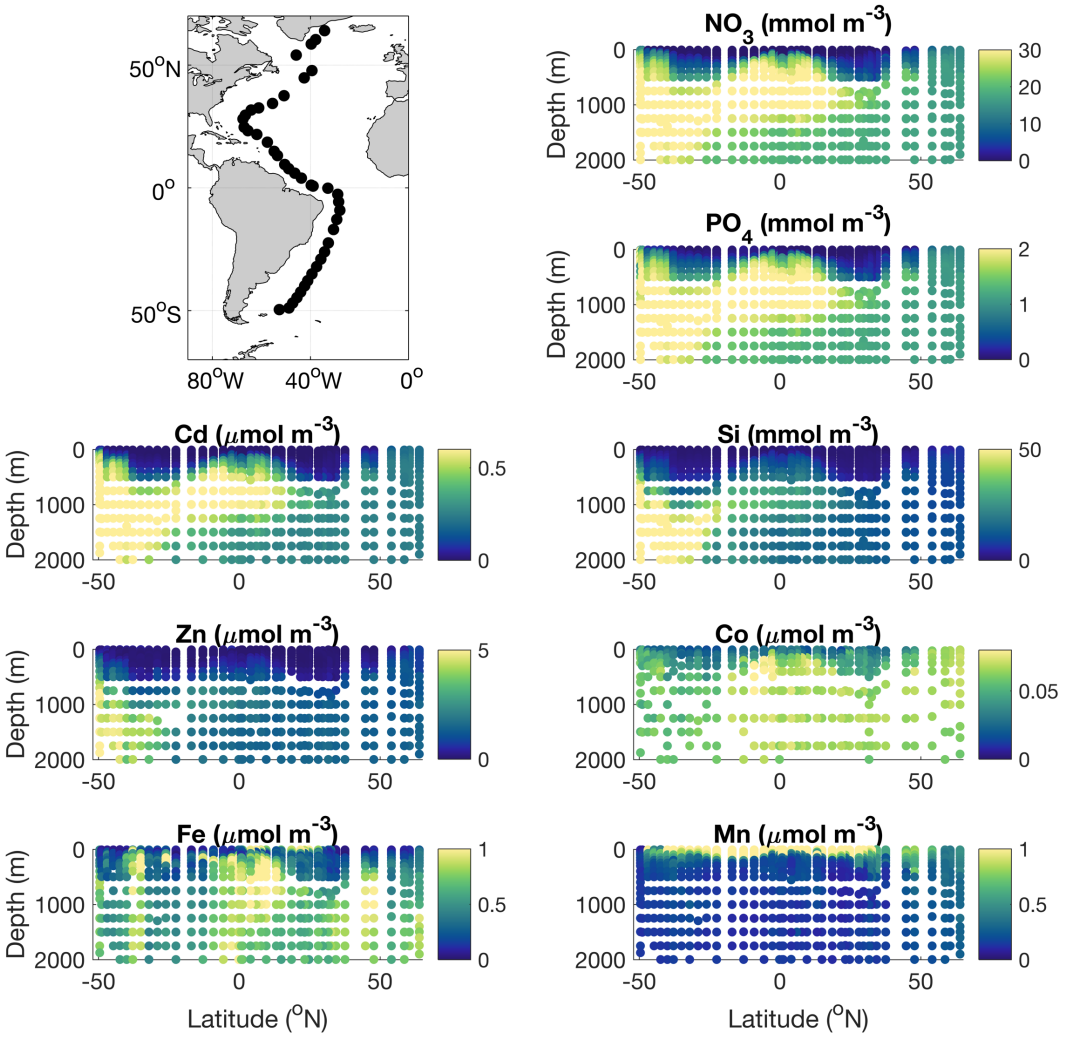

Figure 1.1. Distributions of nitrate (NO_3), phosphate (PO_4), cadmium (Cd), silicic acid (Si), zinc (Zn), cobalt (Co), iron (Fe) and manganese (Mn) in the upper 2000m. Data from the *GEOTRACES* GA02 transect (upper left panel) available in the 2017 *GEOTRACES* Intermediate Data Product (Schlitzer et al., 2018).

Kustka et al., 2003). Zn is used in alkaline phosphatase, a metalloenzyme used by biota to access dissolved organic phosphate as a source of PO_4 (Coleman, 1992), in carbonic anhydrase, a carbon concentrating agent for the acquisition of dissolved inorganic carbon (Sunda, 1989), as well as DNA and RNA. Mn is required in photosystem II and in the breakdown of harmful superoxide radicles by superoxide dismutase (Sunda, 1989). Cd has been shown to substitute for Zn in some marine diatoms (Prince and Morel, 1990). Finally, Co is required by vitamin B12 (Ludwig and Matthews, 1997, Rodionov et al., 2003).

There are differences in the large-scale distributions of NO_3, PO_4, Si, Cd, Zn, Co, Fe and Mn (Figure 1.1). Generally, the greatest quantities of macronutrients and Cd are found in the Southern Ocean, where concentrations of NO_3, PO_4 and Cd of ~30 mmol m^{-3}, ~2 mmol m^{-3}, and ~0.8 μmol m^{-3} respectively, are typical in the upper 1000 m (Schlitzer et al., 2018). The distributions of NO_3, PO_4 and Cd show signals of Antarctic Intermediate Water in full Atlantic meridional sections (Rijkenberg et al., 2014, Schlitzer et al., 2018). In the upper ocean, NO_3, PO_4 and Cd contours deepen in the subtropics and shoal around the equator, akin to isotherms and linked to anticyclonic gyre rotation in the subtropics (Williams and Follows, 2013). Generally, NO_3, PO_4 and Cd follow a nutrient-type structure in the vertical as these resources are consumed at the surface and regenerated at depth (Tagliabue, 2019).

Si and Zn show similar broad-scale distributions to PO_4 and Cd (Figure 1.1). In the Southern Ocean, Si is used by diatoms to build their frustules. Diatoms then perish and sink through the water column, gradually releasing resources though remineralization. The long remineralization length scale of Si causes the release of Si to occur in deeper water than that of PO_4 and Cd (Twining et al., 2014). Unlike Si, Zn is released rapidly into the water column at a similar rate to PO_4 (Twining et al., 2014, Boyd et al., 2017). However, Zn is reactive and scavenged onto sinking particles at intermediate depths before release in deeper waters, known as reversible scavenging (Weber et al., 2018). The transfer of Zn from intermediate depths to deep waters couples the vertical profiles of Si and Zn (Bruland, 1980). Further, the release of Si and Zn into deep waters reduces their transport out of Southern Ocean, meaning water mass signals in low latitudes are reduced compared to PO_4 and Cd.

The large-scale patterns of Co, Fe and Mn are unique to each resource in the Atlantic Ocean (Figure 1.1). There are subsurface maxima in the distribution of Co throughout the Atlantic Ocean, linked to oxygen minimum zones around major upwelling sites in the east or the influence of Co-rich Labrador Sea Water in the western and central North Atlantic (Noble et al., 2017). The distribution of Fe is complex, exhibiting surface depletion in high latitudes and surface maxima in the subtropical North Atlantic due to proximity to the Sahara Desert (Martin and Fitzwater, 1988, Hatta et al., 2015, Achterberg et al., 2018). The subsurface Fe distribution shows signals from multiple sources, such as hydrothermal vents along the Mid-Atlantic Ridge and

sediment inputs at ocean margins (Tagliabue et al., 2010, Hatta et al., 2015). Fe is considered a hybrid-type element as Fe exhibits nutrient-type behavior in the upper water column and scavenged-type behavior at depth (Tagliabue, 2019). Finally, Mn, typical of a scavenged-type resource, exhibits surface maxima throughout the Atlantic Ocean due to dust inputs and the photoreduction of Mn-oxides (Sunda and Huntsman, 1994). The concentration of Mn decreases to around ~0.2 μmol m^{-3} consistently in the ocean interior. Overall, the relative availability of resources is highly varied throughout the global ocean.

In vast regions of the global ocean, phytoplankton growth is limited by the availability of resources (Moore et al., 2013). Resource limitation occurs in three categories: (1) singular limitation, (2) serial-limitation and (3) co-limitation (Saito et al., 2008, Browning et al., 2017a). Under singular limiting conditions, the addition of the limiting resource stimulates phytoplankton growth. Serial, or secondary limitation, occurs where an additional resource becomes limiting following the addition of the primary limiting resource. Co-limitation occurs where two resources independently limit growth, or the addition of a limiting resource relieves growth limitation of multiple resources. For example, in the subtropical North Atlantic, the ability of biota to access growth-limiting P is dependent upon the supply of Zn for use in alkaline phosphatase (Mahaffey et al., 2014).

There is a distinction between resource limitation and resource deficiency (Moore, 2016). Limitation occurs where resource stocks are exhausted and phytoplankton growth is prevented, while deficiency occurs where the relative availability of a resource falls below that of biological demand, however phytoplankton growth can occur. For example, compared to the Redfield Ratio of 16:1, waters with N:P values of 10:1 are considered N deficient and waters with N:P values of 20:1 are considered deficient in P; uptake at the Redfield ratio leads to depletion of N in the low N:P case and the depletion of P in the high N:P case. Deficiency indicates a potential for limitation following removal processes at a fixed stoichiometric ratio.

The stochiometric demand of marine phytoplankton varies between each taxa group, leading to competitive advantages for biota able to exploit environmental conditions (Ho et al., 2003, Twining and Baines, 2013). For example, where oceanic sources of

N, such as NO_3 or ammonia (NH_3), are depleted, nitrogen-fixing cyanobacteria are able to use atmospheric di-nitrogen gas (N_2) as a source of N, meaning they possess a competitive advantage over non-nitrogen fixers (Ward et al., 2013). Trichodesmium, a genus of cyanobacteria, are found in the temperate subtropical North Atlantic due N deplete and Fe replete waters. Here, the high Fe requirements of nitrogenase (the enzyme responsible for the conversion of N_2 to NH_3) are satisfied and energetic demands are met by high light intensity penetrating deep into the water column (Capone et al., 2005, Luo et al., 2012, Ward et al., 2013). Ultimately, Trichodesmium flourishes in the subtropical North Atlantic as the growth rates of non-nitrogen fixers are limited by N availability. Large-scale areas of resource deficiency are established by imbalances in the external inputs of bio-essential resources and the uptake of resources during phytoplankton growth followed by the sinking of detrital material. These resources are replenished by external processes which deliver resources to the upper ocean and hence maintain productivity over long periods.

1.2 Physical Controls on Productivity

1.2.1 The Surface Mixed Layer

The mixed layer is a turbulent region of the upper water column and considered vertically homogeneous by definition. The mixed layer extends from the surface to a depth generally defined by enhanced turbulent kinetic energy or by temperature or density at a reference depth of 10 m plus a given criteria ($T_{z=10m}$ + 0.2ºC or $\rho_{z=10m}$ + 0.03 kg m^{-3} (de Boyer Montegut et al., 2004)). The mixed-layer depth is controlled by multiple processes which drive turbulent mixing and stratification (Chen et al., 1994, Williams and Follows, 2013). Surface inputs of heat and freshwater act to reduce the density of upper waters relative to that in underlying waters, enhancing stratification and reducing the mixed-layer depth. Conversely, water in the mixed layer becomes denser by surface heat losses and mixing with underlying waters, reducing stratification and increasing the mixed-layer depth. Underlying waters are entrained into the mixed layer due to inputs of mechanical energy causing turbulence at the base of the mixed-layer, such as wind stress, the breaking of internal waves or tides passing over rough topography (Munk and Wunsch, 1998, Whalen et al., 2012, Waterhouse et

al., 2014, Tuerena et al., 2019). The myriad of physical processes influencing the mixed-layer depth causes a seasonal cycle which is crucial in the supply of resources to biota in the mixed layer via entrainment (Tagliabue et al., 2014, Achterberg et al., 2018).

The seasonal cycle of the mixed layer is a fundamental feature of oceanography and key in supporting primary production (Williams and Follows, 2013). From the spring equinox to summer solstice, high inputs of heat and the relaxation of winds at the surface increase stratification and trap phytoplankton in the surface layer. Primary production by biota in the thin summer mixed layer consumes resources, which are partially recycled and partially exported to underlying waters (Eppley and Peterson, 1979, Boyd and Ellwood, 2010). Export gradually reduces mixed layer resource stocks until resource availability becomes the growth limiting factor, preventing further phytoplankton development. From the summer solstice to autumn equinox, heat inputs to the mixed layer are reduced while mechanical forcing acts to overcome stratification, the competing effects cause a slow and gradual deepening of the mixed layer. From the autumn equinox to spring equinox, heat loss and mechanical mixing from the winds act in tandem to breakdown stratification and entrain waters from below, rapidly deepening the mixed-layer depth. Underlying thermocline waters are rich in resources which were previously exported from the mixed layer in earlier months and subsequently recycled in the underlying thermocline. This process replenishes resources throughout the homogeneous mixed layer in winter months. The annual maximum mixed-layer depth is achieved at the spring equinox where the net heat input transitions from negative to positive, leading to warming as the periodic annual mixed layer cycle restarts.

The depth of the maximum monthly mixed-layer depth varies dramatically around the globe. In low latitude upwelling regions, the maximum mixed-layer depth rarely exceeds 50 m depth (de Boyer Montegut et al., 2004). In comparison, mixed-layer depths exceed 400 m in turbulent regions such as the Gulf Stream, exceed 600 m in the Pacific and Indian sectors of the Southern Ocean and exceed 1600 m in the Labrador Sea (Holte et al., 2017). In summer, mixed-layer depths are generally less than 50 m depth throughout the global ocean, meaning the amplitude of the mixed layer cycle varies dramatically between the tropical and sub-polar regions (de Boyer

Montegut et al., 2004, Williams and Follows, 2013, Holte et al., 2017). Differences in the depth attained by the winter mixed-layer cause substantial differences in the importance of winter-time entrainment. For example, in the tropics, the amplitude of the mixed-layer cycle is low (~20 m), meaning little underlying water is entrained into the mixed-layer, resulting in a low entrainment flux of depleted resources. In contrast, in mid-latitudes, the mixed-layer depth is around 20 m depth in summer then deepens to 150m in winter (de Boyer Montegut et al., 2004), entraining deep nutrient stocks into the mixed layer. Changes in physical controls, such as the prevalence of storms (de Boyer Montegut et al., 2007) and large-scale climate modes (Sallee et al., 2010), induce interannual variability in the winter mixed-layer depth and inherent volume of water entrained into the mixed layer. This has subsequent effects on the supply of resources to the mixed layer and alters the winter mixed-layer resource availability and stoichiometry (Rigby et al., 2020).

1.2.2 Entrainment

An ocean can be considered with four layers in the vertical, at the surface is the mixed layer, beneath sits the seasonal thermocline (sometimes referred to as the seasonal boundary layer), then the main thermocline and finally the deep ocean. Entrainment is the process whereby the surface mixed layer deepens and properties in the seasonal thermocline are transferred into the mixed layer. At the occurrence of the maximum annual mixed-layer depth, the mixed layer extends to the main thermocline, encompassing the full thickness of the seasonal thermocline. The distinction between the main thermocline, seasonal thermocline and mixed layer is important when considering the roles of upwelling and lateral advection in supplying resources to the mixed layer.

In addition to seasonal overturning, wind induced upwelling transports deep waters, typically rich in regenerated resources, vertically towards the surface. Major upwelling sites include the subpolar North Atlantic, Benguela Upwelling zone and Mauritanian Upwelling Zone (Jenkins et al., 2015, McGillicuddy, 2016). Upwelled waters are transported through the main thermocline and seasonal thermocline, then are transferred into the mixed layer by entrainment as the mixed layer deepens.

Therefore, in Chapter 3, estimates of entrainment fluxes into the mixed layer include the influence of upwelling.

An additional pathway of resources to the mixed layer is through induction. Induction is combination of lateral and vertical advection which causes the transfer of resources into the winter mixed-layer (Williams et al., 2006). Subsurface nutrient streams are characterized by fast-moving boundary currents couple with resource stocks at depth, creating a region of elevated nutrient flux moving laterally. In the North Atlantic, the Gulf Stream operates at the western boundary of the subtropical gyre and acts as a nutrient stream within the thermocline (Pelegrí et al., 1996, Williams et al., 2006). Nitrate carried by the Gulf Stream originates from particle export and remineralization in the subtropical and tropical upwelling areas, and the Southern Ocean. Resources are transferred from the Gulf Stream into the seasonal thermocline as the winter mixed layer deepens and becomes denser in the sub-polar North Atlantic. Nitrate rich waters in the seasonal thermocline are then transferred into the mixed layer by entrainment. Hence, estimates of entrainment provided in Chapter 3 include a signal of the induction process, particularly in high latitudes which experience deep winter mixed layers.

1.2.3 Diapycnal Mixing

Diapycnal mixing is a resource supply mechanism driven by tracer gradients and turbulent processes. Mixing 'smoothes' gradients in a tracer profile, transferring properties from a region of high concentration to a region of low concentration. In the case of the mixed layer, biological activity in the mixed layer and regeneration below form gradients in the vertical profiles of key resources, such as NO_3. This drives an upwards vertical transfer of resources as diapycnal mixing erodes the vertical tracer gradients. Diapycnal diffusivity (K_z) reflects the rate at which gradients in tracer are eroded. In the quiescent deep ocean, K_z ranges from 10^{-6} to 10^{-5} m^2 s^{-1} (Martin et al., 2010, Painter et al., 2014, Tuerena et al., 2019). However, in turbulent regions, such as around ocean ridges, seamounts and the upper water column, K_z typically approaches 10^{-4} m^2 s^{-1} (Whalen et al., 2012, Tuerena et al., 2019). The principle forcing mechanisms which control K_z are the inputs of turbulent kinetic energy from the

mechanical work done by the winds and tides (Munk and Wunsch, 1998). Wind stress at the surface generates near-inertial gravity waves (NIWs) which propagate along isopycnals in the stratified upper ocean (Alford et al., 2016). NIWs are generated as the convergence and divergence of surface wind stress push down and lift up isopycnals respectively, pumping energy into the mixed layer. This energy gradually dissipates and radiates downwards into the ocean interior, ultimately leading to turbulent mixing. K_z operates throughout the year and therefore offers a continuous source of major nutrients such as NO_3 to a resource depleted mixed layer.

There are numerous methods available to estimate K_z (Jenkins, 1988, Forryan et al., 2012, Whalen et al., 2012, Painter et al., 2014, Stanley et al., 2015, Cronin et al., 2015, Tuerena et al., 2019). In this thesis, K_z is calculated using observations of helium captured during *GEOTRACES* field campaigns and by the use of vertical microstructure profilers (VMPs).

Helium is chemically and biologically inert noble gas and therefore an ideal physical tracer. In the helium flux gauge approach, excess mixed layer helium is attributed to air-injection processes (partially and completely dissolved bubbles at the air-sea interface), the *in-situ* decay of tritium (the radioactive parent isotope of ^{3}Helium) and vertical transport of deep helium stocks (Jenkins, 1988, Jenkins and Doney, 2003). After accounting for air-injection and *in situ* tritium decay, residual helium supersaturation in the mixed layer must exist due to the physical upward transport of deep helium. Equipped with knowledge of the upwards helium flux and the vertical gradient of helium, an estimate of K_z due to physical processes may be estimated.

Freefalling VMPs are deployed from vessels and capture estimates of temperature, salinity and turbulent horizontal velocity fluctuations. The vertical shear of horizontal currents is used alongside viscosity to infer the turbulent kinetic energy dissipation rate. K_z is then calculated from the turbulent kinetic energy dissipation rate, buoyancy frequency squared and mixing ratio (Osborn, 1980). The buoyancy frequency squared is related to the vertical density shear and is a measure of water column stability (Simpson and Sharples, 2012). The mixing ratio refers to the change in potential energy compared to the energy lost (Gregg et al., 2018). Physical resource fluxes are

then calculated from K_z estimates alongside concurrent resource observations (Forryan et al., 2012, Tuerena et al., 2019).

1.2.4 Additional Resource Supply Pathways

The supply of resources to the mixed layer by winter-time entrainment and diapycnal mixing is augmented by a number of external processes.

Aeolian deposition (dust) is an important source of trace metals, particularly Fe and Mn, to the subtropical North Atlantic (Jickells et al., 2005, Rijkenberg et al., 2012, Ussher et al., 2013, Jickells et al., 2016). Of trace elements included in this thesis, dust is most abundant in Fe (5.0%), followed by Mn (0.1%), Zn (0.0067%), Co (0.0017%) and Cd (0.000009%) (Rudnick and Gao, 2003). However, the solubility of these trace elements is also highly varied, where Zn is most soluble (31.7% ± 26.3%), followed by Cd (31.6% ± 19.8%), Mn (30.0% ± 14.2%), Co (12.0% ± 11.1%) and Fe (3.7% ± 5.0%) in the subtropical North Atlantic (Shelley et al., 2018). The phenomena of high dust deposition rates, which deposit lithogenic particles originating from the northwest region of Africa, has been acknowledged since 1846 (Darwin, 1846). Dust particles are mobilized during high wind speeds and transported over vast distances, then deposited during a relaxation of wind speeds or precipitation events, known as dry and wet deposition respectively (Baker et al., 2013, Shelley et al., 2017). Dust events are highly episodic, meaning pulses of key resources are delivered to the mixed layer at the air sea interface at irregular intervals. The fraction of deposited minerals which are soluble in seawater is complex and influenced by multiple processes, include source minerology, atmospheric processing and particle size (Baker and Croot, 2010). Nevertheless, the Atlantic Ocean receives around 26% of the total global mineral deposition, making dust a key source of resources to the region (Duce et al., 1991).

The eddy transfer of properties into the upper ocean is driven by numerous processes. Cyclonic (rotating clockwise in the northern hemisphere) eddies cause upwelling as the eddy rotation coupled with the rotation of Earth causes the divergence of water which must be replaced by water from below, known as eddy pumping and forming cold-core eddies (Williams and Follows, 2003b, McGillicuddy, 2016). Cold-core

eddies reduce the winter mixed-layer depth as upwelling transfers cooler dense water upwards and causes the doming of isopycnals (Williams, 1988, Falkowski et al., 1991). Further, primary production is influenced the eddy-driven upwelling of nutrient rich deep waters (Falkowski et al., 1991). Eddies 'trap' properties and are advected causing lateral transfer. In the North Atlantic, eddies break away from the turbulent Gulf Stream, forming Gulf Stream Rings which transfer Fe rich waters from the continental slope to the gyre interior (Conway et al., 2018). Finally, the coupling of slanting of isopycnals and eddy stirring in the thermocline induces a vertical transport to transfer properties into the seasonal boundary layer (Lee and Williams, 2000, Spingys et al., *in prep*). In summary, there are various eddy-driven dynamical processes which transport water into the upper ocean which may ultimately be transferred into the mixed layer by winter-time entrainment or diapycnal exchange throughout the year.

1.3 Key Questions

The importance of bio-essential resource availability, stoichiometry and supply to the upper ocean is clear in current literature. However, there are numerous outstanding questions which are addressed in this thesis:

1. What is the distribution of key resources in the surface mixed layer and how does it vary between resource in the Atlantic Ocean?

2. How does winter-time entrainment affect the availability of trace metal resources in the mixed-layer in the Atlantic Ocean?

3. What are the major processes which influence the vertical flux of resources and how do they vary regionally, temporally and between resource?

4. How do trace-metal resource fluxes vary around mid-ocean topographic features and what controls their magnitude?

1.4 Thesis Structure

To address the key questions posed in this thesis, multiple observational datasets and model output were used in analysis. In Chapter 2, they are introduced and validated. Chapter 2 also provides an overview of the methodology used throughout this thesis and examines two independent formulations of the winter-time entrainment resource supply to the mixed layer.

In Chapter 3, *GEOTRACES* Atlantic Ocean observational data are synthesized and combined with monthly mixed-layer depth model output to estimate winter mixed-layer resource stoichiometry and entrainment. Results are linked to vertical gradients in resource profiles and consequences of temporal variability in the winter mixed-layer depth are explored.

In Chapter 4, *GEOTRACES* observations of helium are exploited to estimate vertical exchanges between the thermocline and mixed layer in the subtropical North Atlantic (GA03) and equatorial Pacific (GP16). The upwards helium flux is used to infer mixing rates and subsequently estimate key resource fluxes, linking to vertical gradients in resource profiles and environmental conditions.

In Chapter 5, data from vertical microstructure profilers are used to provide an instantaneous snapshot of vertical mixing at two sites situated on the subtropical Mid-Atlantic Ridge. Contrasts in vertical resource fluxes between a shallow and deep topographical site are then examined.

Conclusions drawn from this thesis are synthesized in Chapter 6, recommendations for future work are also provided.

Chapter 2

Toolbox

The aim of this chapter is to provide an overview of the observational and modelled datasets used throughout this thesis. Numerous physical and biogeochemical datasets, both from modelling and observational studies, are used in subsequent science chapters. Here, they are introduced, and examples of their results and application are provided. Model output is validated using observational data. Methodology are introduced and explored before use in later chapters.

2.1 Datasets

2.1.1 *FRidge,* GA13

The FRidge field campaign was conducted on the *RRS James Cook* and departed Southampton, UK on 20th December 2017. Briefly, the ship sailed through the English Channel and Bay of Biscay, performing test stations prior to arrival at the Azores. Thereafter, the expedition followed the Mid-Atlantic Ridge, traversing multiple hydrothermal venting sites, such as Rainbow (36^{o}N 34^{o}W), the Trans-Atlantic Geotraverse (TAG, 26^{o}N 45^{o}W) and Lost City (30^{o}N 42^{o}W). The ship docked in Pointe-à-Pitre, Guadeloupe on 1st February 2018.

The onboard responsibilities of the author of this thesis during FRidge were to collect samples for helium analysis from the stainless-steel rosette as well as offering support to other scientific procedures. Additional duties included leading the outreach and engagement programme for the expedition. This involved maintaining daily video log, capturing day-to-day life onboard and scientific procedures in various forms of media, regularly updating a dedicated social media page (twitter: @FRidge_GA13) and answering questions from primary and high school students.

FRidge was a *GEOTRACES* section cruise, GA13, led by Alessandro Tagliabue (Principle Scientific Officer, University of Liverpool) and Maeve Lohan (co-Principle

Investigator, University of Southampton). The sampling strategy offered a unique opportunity to study both large-scale distributions of multiple traces alongside small scale process around hydrothermal sites. A stainless-steel rosette was used to capture samples for the measurement of helium (among others) and a titanium rosette took samples for trace metal analysis. Macronutrients, Mn and Al were measured from both rosettes. Both rosette systems featured a mounted CTD (conductivity, temperature, depth) sensor which delivered a live feed of salinity, temperature, oxygen, fluorescence, light scatter and an Eh sensor (used to measure reducing potential and identify hydrothermal signals). Two vertical microstructure profilers (VMPs) were available for use during the expedition, however staffing and instrumental error restricted the use of the VMP, which ultimately delivered five vertical profiles of turbulent dissipation to a depth greater than 500m. In Chapter 5, hydrographic, trace element, and VMP data are used to quantify vertical resource fluxes in the upper 1000m at the Rainbow and TAG hydrothermal sites.

The vertical profiles of NO_3, PO_4, Si, Fe, Mn and Al at Rainbow and TAG (Figure 2.1), are introduced and examined prior to use in Chapter 5. At both sites, NO_3 and PO_4 are depleted at the surface, typical of a nutrient-type resource in the centre of the subtropical North Atlantic Gyre. The depletion of both NO_3 and PO_4 persists to ~60m at Rainbow and ~150m at TAG, supporting the role of NO_3 and PO_4 as growth limiting resources in the region (Moore et al., 2013). Below these depths, the increase in NO_3 and PO_4 with depth is greater at TAG than at Rainbow, suggesting enhanced regeneration at TAG. The subsurface maxima in NO_3 and PO_4 occurs deeper in the water column at TAG and is of greater concentrations than at Rainbow. The vertical structure of the Si distribution at both sites is broadly similar to NO_3 and PO_4, however Si surface depletion is incomplete. Fe, a hybrid-type resource, exhibits a stronger surface maximum at TAG than Rainbow, suggesting greater delivery of Fe to the surface at the more southern site. The scavenged-type nature of the upper Fe profile is clearer at TAG than Rainbow, where subsurface minima occur at 500m depth and 250m depth respectively. Fe accumulates below the subsurface minima due to remineralization, where greater Fe concentrations are located at the Rainbow site. There is a stronger Mn surface maximum at TAG than at Rainbow, concentrations then decrease rapidly to typical background levels (~0.2 $\mu mol\ m^{-3}$) below 250m depth at both sites. In the Rainbow Mn profile, there are subsurface increases, indicative of

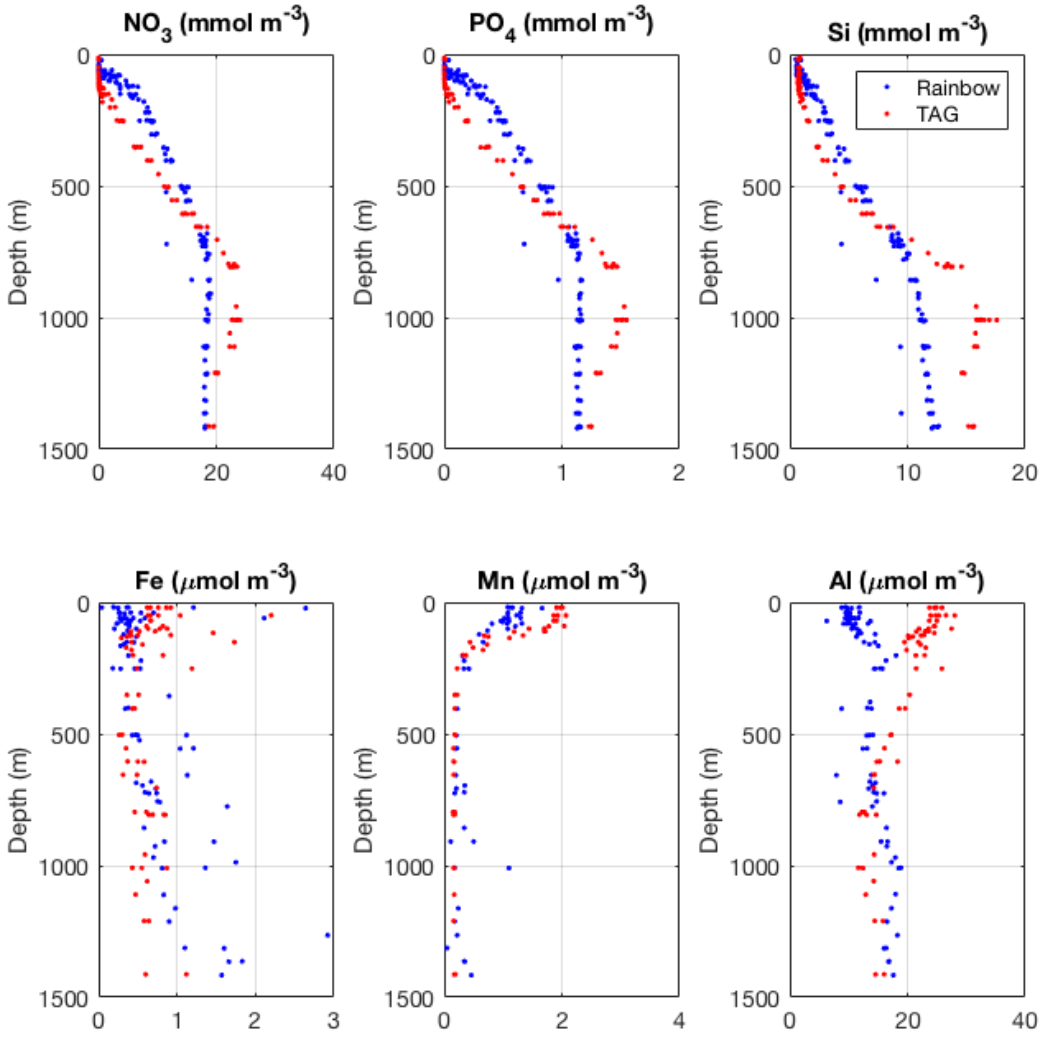

Figure 2.1. Vertical distributions of key resources in the upper 1500m collected during the FRidge GA13 *GEOTRACES* field campaign at the Rainbow (blue) and TAG (red) hydrothermal vent sites.

lateral transport from hydrothermal or sedimentary sources. Al is typically used as an inert tracer of aeolian dust inputs. Higher surface concentrations at TAG than Rainbow suggest a greater input of Saharan dust at TAG. At both sites, there are subsurface increases in Al, suggesting the remote influence of water masses such as Al rich Mediterranean Overflow Water at depth (Menzel Barraqueta et al., 2018) or local inputs from sediments or hydrothermal vents.

2.1.2 RidgeMix

The primary objective of the RidgeMix study was to understand the biogeochemical consequences of enhanced mixing over the Mid-Atlantic Ridge in the subtropical North Atlantic. Interactions between the internal tide and rough topography are recognised to cause an increase in vertical diffusivity, however contemporaneous direct measures of mixing and nutrients and subsequent flux calculations remained unavailable. The *RRS James Clark Ross* departed the Port of Spain, Trinidad and Tobago on 25th May 2016, docking in Immingham, UK, on 10th July 2016. RidgeMix was led by Jonathan Sharples (National Oceanography Centre, Liverpool) and sampled hydrography using a CTD system providing the same parameters as FRidge (excluding the Eh sensor), including oxygen and macronutrient measurements. Current profiles were estimated using acoustic doppler current profilers and microstructure profiles were collected using VMPs. Measurements made during RidgeMix were used to show that:

(1) Nitrate flux to the deep chlorophyll maximum is an order of magnitude larger over the mid-Atlantic Ridge than in the quiescent deep ocean (Tuerena et al., 2019).

(2) Mixing and the associated nutrient flux are eight times greater during spring tides when compared to neap tides (Tuerena et al., 2019).

(3) By incorporating a global tidal model into the study, the project demonstrated that enhanced mixing may be ubiquitous over ridges and seamounts in the global ocean (Tuerena et al., 2019).

A full description of sampling, cruise narrative and data is available in the RidgeMix cruise report and from the British Oceanographic Data Centre (https://www.bodc.ac.uk/resources/inventories/cruise_inventory/report/16043/). In Chapter 5, VMP data from RidgeMix are used to augment VMP data from FRidge.

2.1.3 The *GEOTRACES* Programme

GEOTRACES is an international, multi-lab effort to sample key trace elements and isotopes in the global ocean (Anderson, 2020). The project stems from the earlier Geochemical Ocean Sections Study (GEOSECS) during the 1970s which delivered a global survey of hydrographical parameters alongside major nutrients carbon, nitrate, phosphate and silicate (Craig and Turekian, 1980). However, during GEOSECS, analytical techniques could not determine trace element concentrations as samples were often fraught with contamination (Brewer et al., 1972, Bruland et al., 1978). At present, there are 392 vertical Fe profiles in the *GEOTRACES* Intermediate Data Product (Schlitzer et al., 2018).

Data collected on *GEOTRACES* cruises must comply with the methodology in the *GEOTRACES* protocol (Cutter and Bruland, 2012), meet intercalibration standards and measure a list of key parameters, including trace elements iron, zinc, manganese and cadmium. Accuracy and precision are reported in *GEOTRACES*. Accuracy reflects the ability of a method to measure samples to the true value. Precision is a measure of variability in measurements. The accuracy of individual methods used in *GEOTRACES* is maintained by using SAFe or *GEOTRACES* Consensus Samples as reference material. Precision is measured in two parts: field and analytical, where field precision represents variability owing to sampling techniques and analytical represents variability derived from the analytical procedure applied. Field precision is estimated by measuring two different samples from the same bottle, while analytical precision is estimated by repeated analysis of a single sample. After quality control procedures, data are then made available at the release of the proceeding *GEOTRACES* IDP and can be downloaded from the online portal hosted at the Alfred Wegener Institute (https://geotraces.webodv.awi.de/login). Data is available to downloaded in multiple formats. The NetCDF file format is most suitable for use in Matlab and was therefore preferred for *GEOTRACES* data downloads throughout this thesis. Quality controls must be performed on *GEOTRACES* data before use. Each variable in the NetCDF has an associated ‘flag’ array, comprising of numbers 0 to 9, referring to the quality of the observation, only data with ‘good value’ flags (value = 1) were used. In this thesis, all

trace element abbreviations refer to the dissolved phase and are operational defined by 0.2µm filtered samples.

2.1.4 World Ocean Atlas

The World Ocean Atlas (WOA) is a climatological database of *in-situ* measurements throughout the global ocean (https://www.nodc.noaa.gov/OC5/woa18/). Data are binned into a 1° × 1° longitude-latitude grid and binned in the vertical, with higher resolution towards the surface. Interpolated fields are available, providing complete coverage of the global ocean. In the 2018 World Ocean Atlas, data available are temperature, salinity, dissolved oxygen, percent oxygen saturation, apparent oxygen utilisation, nitrate, silicate, and phosphate (Garcia et al., 2018, Locarnini et al., 2018, Zweng et al., 2018).

2.1.5 Aeolian Deposition Model and Aerosol Solubility

Aeolian deposition (dust) is a major supply pathway of resources to the ocean, particularly in the subtropical North Atlantic. Dust deposition rates, composition and solubility are used to gauge the importance of dust on setting mixed-layer stoichiometry (Chapter 3), as well as understanding the relative roles of entrainment (Chapter 3) and physical transport (Chapter 4) compared to dust inputs. The dust model of Mahowald et al. (2005) is used to estimate the rate of lithogenic particles deposited at the air-sea interface. The elemental composition of these dust particles follows crustal ratios defined in Rudnick and Gao (2003) . Solubility is defined as a percentage of elemental composition of aerosol dissolving in seawater by shipboard measurements made along the *GEOTRACES* GA03 transect in the subtropical North Atlantic (Shelley et al., 2018). In Chapter 3, nitrogen deposition uses the atmospheric particle field of Duce et al., (2008) and assumes complete dissolution upon settling at the air-sea interface. The Duce et al., (2008) model contains anthropogenic sources of nitrogen as they are a major contributor to atmospheric nitrogen.

There are a number of caveats in the choice of dust model and solubilities applied. For instance, dust deposition is recognised as a highly episodic event. During the

GEOTRACES GA03 cruise, scientists reported the ship and equipment were coated in a layer lithogenic dust originating from the Sahara (Boyle et al., 2015b). The sporadic nature of dust storms restricts the use of annual dust models in accurately estimating daily or monthly deposition rates. Following particle deposition at the air-sea interface, solubility defines the fraction of lithogenic aerosol which enters the dissolved phase. The source region affects the solubility of each element. For example, in fine mode particles (< 1μm) supplied to the Atlantic Ocean, the fractional solubility of Fe varies from 38% in aerosol sourced from continental Europe to 54% in aerosols originating in the Sahara (Baker and Jickells, 2017). Solubility is further complicated by additional sources such as biomass burning which reduces fractional Fe solubility by 16% in fine particles sourced from Southern Africa (Baker and Jickells, 2017). Solubility is sensitive to processes during atmospheric transport, for instance, the pH of water vapour in clouds is variable and alters acid processing of lithogenic particles (Baker et al., 2006).

2.1.6 ARGO Diffusivity

At present, the ARGO programme has delivered a wealth of oceanographic data and is expanding to include deep ARGO profiles (below 2000 m depth) and BioARGO to include biological data products. Current ARGO floats undulate in the upper 2000 m, measuring properties such as temperature and salinity at near global coverage. When ARGO floats surface, data is transmitted to receiving stations via satellites. Hydrographic ARGO profiles have been used to produce global maps of the turbulent dissipation rate, used to infer mixing rates (Whalen et al., 2012, Whalen et al., 2015, Whalen et al., 2018). In Chapter 5, ARGO diffusivity, provided by Caitlin Whalen (University of Washington), is used alongside vertical microstructure profilers to calculate upper ocean resource fluxes based on multiple selection criteria.

2.1.7 ECCO Model

The Estimating the Circulation and Climate of the Ocean (ECCO) model is an ocean state estimate which uses the eddy-resolving MITgcm and multiple observational datasets to produce a physically consistent global model (Forget et al., 2015, Fukumori

Acronym	Full Name	Potential Temperature (°C)	Salinity	O_2 (μmol kg^{-1})	Si (μmol kg^{-1})	NO_3 (μmol kg^{-1})	PO_4 (μmol kg^{-1})	Reference	Pstar (μmol kg^{-1})	Nstar (μmol kg^{-1})
MOW	Mediterranean Overflow Water	12.65	36.629	198.4	7.46	11.17	0.67	WOCE A03 1993 Station 6	-0.11	2.96
ISW	Irminger Sea Water	7.11	35.118	272.4	6.70	14.30	0.94	Tanhua et al. (2005)	2.54	1.88
AAIW	Antarctic Intermediate Water	1.37	34.399	188.8	30.99	30.60	2.12	WOCE A07 1993 Station 89	1.28	-0.32
ULSW	Upper Labrador Sea Water	3.50	34.800	296.0	8.35	15.05	1.02	AR7W Line (18HU199990 627 St 68)	0.81	1.46

Table 2.1. Water mass end-member properties, adapted from Jenkins et al. (2015).

et al., 2017). The project uses inverse methods to optimise the ocean state estimate, which filters noise in observational data to study underlying processes, then interpolates or extrapolates to regions where observational data is unavailable. The adjoint method applied in ECCO is a reanalysis least-squares fitting approach used to improve the state estimate compared to observations. Observational datasets used in the ECCO reanalysis include sea level data from satellites, temperature and salinity from ARGO floats and climatology from the World Ocean Atlas. Model output and code are available to download through the ECCO drive subject to account creation (https://ecco.jpl.nasa.gov/drive/files). Throughout this thesis, the latest version of ECCO at the time of writing was used, version 4 release 3 (v4r3). ECCOv4r3 covers the period 1992 – 2015 (extended from version 4 release 2, 1992 – 2011) and contains improved sea-ice dynamics, various new observational data, modified controls and an adjusted grid compared with the previous model release.

2.2 Methods

2.2.1 Working Practice

The primary computational language used for analysis was Matlab (version 9.1, 2016b onwards). Generally, data were downloaded in NetCDF format from online repositories and imported directly into Matlab for analyses. NetCDF files were first interrogated using the *ncdisp* function, which displays all attributes and variables held within the .nc file to the command window. From the command window, information

regarding variable structure, missing values and flags were viewed and processed. The data is then imported using *ncread*. Test figures were produced to ensure imported data were around expected values. For each chapter of this thesis, a central command script and toolbox of bespoke functions were written. A central script which calls functions is recommended as best practice and has several benefits. This prevents a single script from becoming very long which is difficult for the user (and others) to follow the methodology applied. It is more time efficient for the author as similar code does not need to be rewritten for multiple applications (for example, when computing fluxes for multiple resources), this also reduces the risk of errors in code as less code is written. It is computationally more efficient to use functions as arrays generated within functions are not 'passed back' to the central script, meaning the Matlab memory usage is reduced. Functions created may be modified for other uses. Both central scripts and functions should be properly sectioned (using %%) and commented (using %) so that the user can fully understand the purpose of each section and each command. It is important to produce figures of key variables at each stage of analysis, particularly when analyses require multiple steps. This aids the 'debugging' process and ensures code is performing the expected equations or manipulations.

2.2.2 *FRidge* Water Mass Analysis

Initial water mass analyses during the FRidge field campaign were completed by Carl P. Spingys (University of Southampton) and Alessandro Tagliabue (University of Liverpool) using a Modified Optimum Multiparameter Analysis (MOMPA) following the methodology described in Jenkins et al., 2015. Sensitivity tests were later performed by the author of this thesis. The MOMPA approach uses five conservative properties: potential temperature, salinity, silicate, P* (equation 2.1) and N* (equation 2.2) to identify water masses contributing to a water column in a given location. P* is derived from Broecker et al., (1991) in combination with Anderson and Sarmiento, (1994) , who provided an updated Redfield Ratio, where

$$P^* = PO_4 + \frac{O_2}{170} - 1.95 \qquad [2.1]$$

The traditional Redfield Ratio, where C_{org} : N : P : = 106 : 16 : 1, is derived from plankton decomposition studies and assumes the release of nutrients from organic

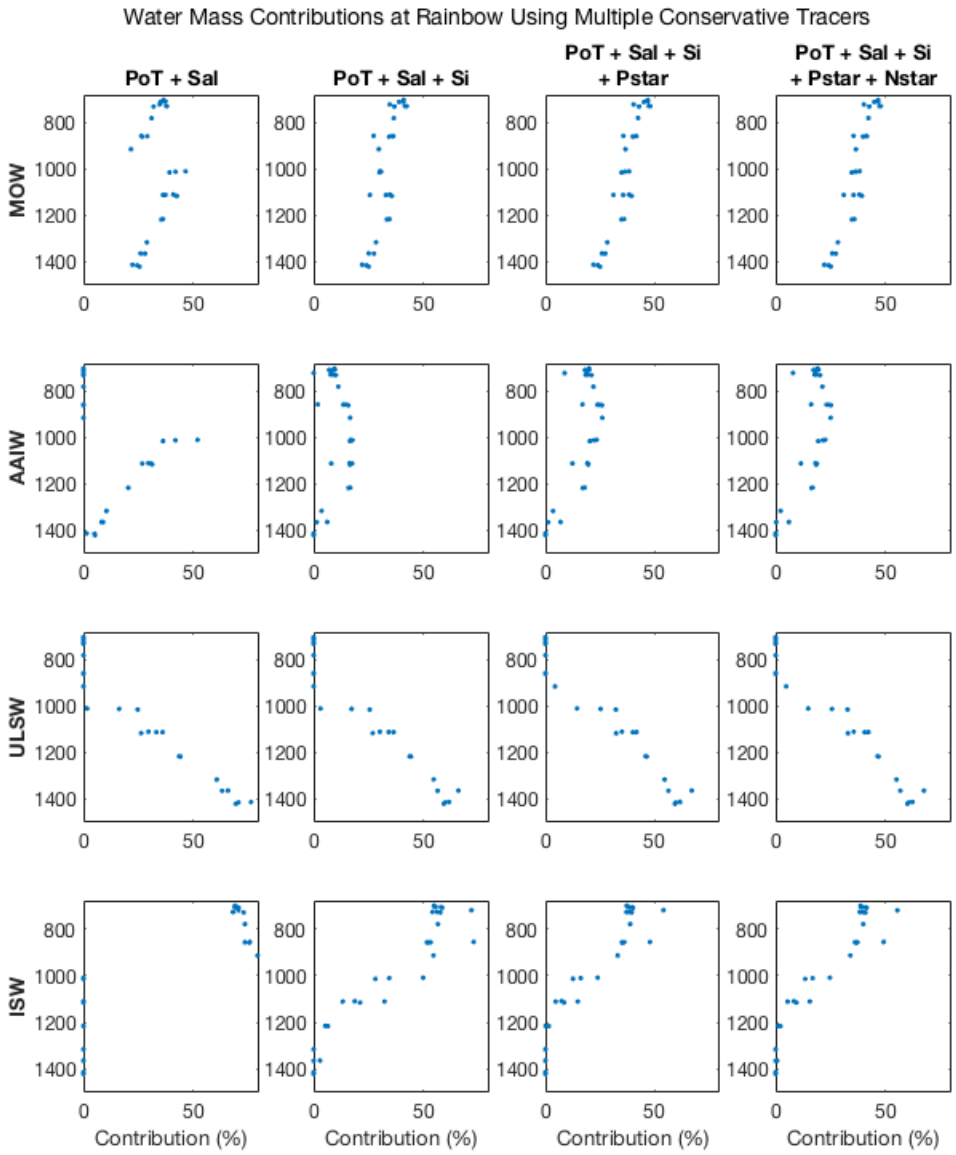

Figure 2.2. Implications of including additional conservative tracers in the MOMPA. Left to right, using potential temperature and salinity, then including silicate, then including P* (equation 2.1), then including N* (equation 2.2). Top to bottom, Mediterranean Overflow Water (MOW), Antarctic Intermediate Water (AAIW), Upper Labrador Seawater (ULSW) and Irminger Sea Water (ISW). Data collected during the FRidge GA13 GEOTRACES Field Campaign. Water mass end-member properties from Jenkins et al. (2015), see Table 2.1.

material during remineralisation is uniform throughout the water column (Redfield, 1958). The preferential remineralisation of some elements over others reduces the adequacy of traditional Redfield Ratio at depth, this is particularly problematic in water mass studies. Hence, Anderson and Sarmiento (1994) developed an updated

Redfield Ratio, where C_{org} : N : P : $-O_2$ = 117 ± 14 : 16 ± 1 : 1 : 170 ± 10, using GEOSECS nutrient data to infer the new Redfield Ratio directly from observations at multiple depth surfaces, which must include remineralised material. The N* conservative tracer is defined following Gruber and Sarmiento (1997), where

$$N^* = 0.87(NO_3 - 16NO_3 + 2.95) \quad [2.2]$$

The N* term is ignored in the main thermocline as the remineralization of N produced by nitrogen-fixers reduces the conservative behaviour of N* at depth and is therefore only used in waters below the thermocline.

The five conservative tracers are used to identify water masses based on an optimised least-square fitting approach using observed tracer concentrations and water-mass end-member compositions (Table 2.1). Weightings are applied to each of the properties used in the MOMPA. In this case, weights of 160, 155, 50, 20, 10 and 150 are used for potential temperature, salinity, silicate, P*, N* and the fractional contribution respectively (Jenkins et al., 2015). The purpose of adding weights to the parameters in MOMPA equation is to reduce dependency on terms associated with high errors and uncertainty in samples and end-member compositions. For instance, the observed variability in N* is similar to the difference between N* in Upper Labrador Sea Water (ULSW) and Irminger Sea Water (ISW) end-members, whereas the variability associated with observed potential temperature and salinity is less than differences in end-member compositions, hence greater weightings are applied to potential temperature and salinity. In the following two paragraphs, the sensitivity of the MOMPA to conservative tracers included and weightings applied is tested.

The sensitivity of the MOMPA is first tested by gradually increasing the number of conservative tracers included in the analysis. In the first experiment, water masses are identified based on their potential temperature and salinity properties only (Figure 2.2). General water mass structures are apparent in the initial experiment, MOW decreases with depth, the AAIW maxima occurs at 1000m depth, ULSW increases below 1000m depth and the ISW contribution decreases from 700m to 1000m depth. However, some unexpected features arise, such as the rapid increase in MOW from 930m to 1000m and decrease in ISW from ~80% at 920m to ~0% at 1000m. The

addition of Si to the MOMPA smooths vertical water mass structures, most notably in MOW between 800m and 1000m depth, throughout the AAIW profile and from 920m to 1300m depth in the ISW profile. The strong influence of Si in setting the AAIW contribution is linked to Si in the end-member composition of AAIW, which is largest of all water masses included in the MOMPA (Table 2.1). The addition of P* and N* to the MOMPA causes differences in the absolute contributions of each water mass,

however general vertical structures remain consistent with MOMPA performed using potential temperature, salinity and Si. Overall, our results demonstrate that ULSW contributions may be calculated from potential temperature and salinity alone, however the calculation of MOW, AAIW and ISW contributions require the inclusion of biogeochemical conservative tracers in the MOMPA.

Next, the sensitivity of the MOMPA to the choice of weighting is tested by recalculating the MOMPA where weightings for each conservative tracer are independently increased and decreased by 25% (Figure 2.3). Generally, changes to the weighting of conservative tracers causes differences in the detail of contribution profiles but does not alter the overall structure. In MOW contributions, sensitivity to changes in potential temperature, salinity, Si and P* is larger in the upper region of the profile, meaning distinguishing MOW above 1000m is more complex than below 1000m depth. AAIW is most sensitive to changes in Si and P*, likely as Si and P* are distinguishing conservative tracers of AAIW. There is little change in ULSW when altering the weightings applied. ULSW is well identified by potential temperature and salinity alone, which themselves are well defined, meaning variability associated with biogeochemical tracers is minimal. ISW contributions are most sensitive to changes in the weighting P* above ~1100m depth. High sensitivity to the weightings applied in the MOMPA occurs where single conservative tracer is used to distinguish between water masses. For instance, if the end-member composition of two water masses is the same for four conservative tracers, the remaining tracer is used to distinguish two water masses. Therefore, changes to the weighting of that distinguishing tracer will cause large shifts in the MOMPA calculation.

In Chapter 5, changes in mixing and resource fluxes around the TAG and Rainbow hydrothermal venting sites are studied. Here, hydrographic differences between the

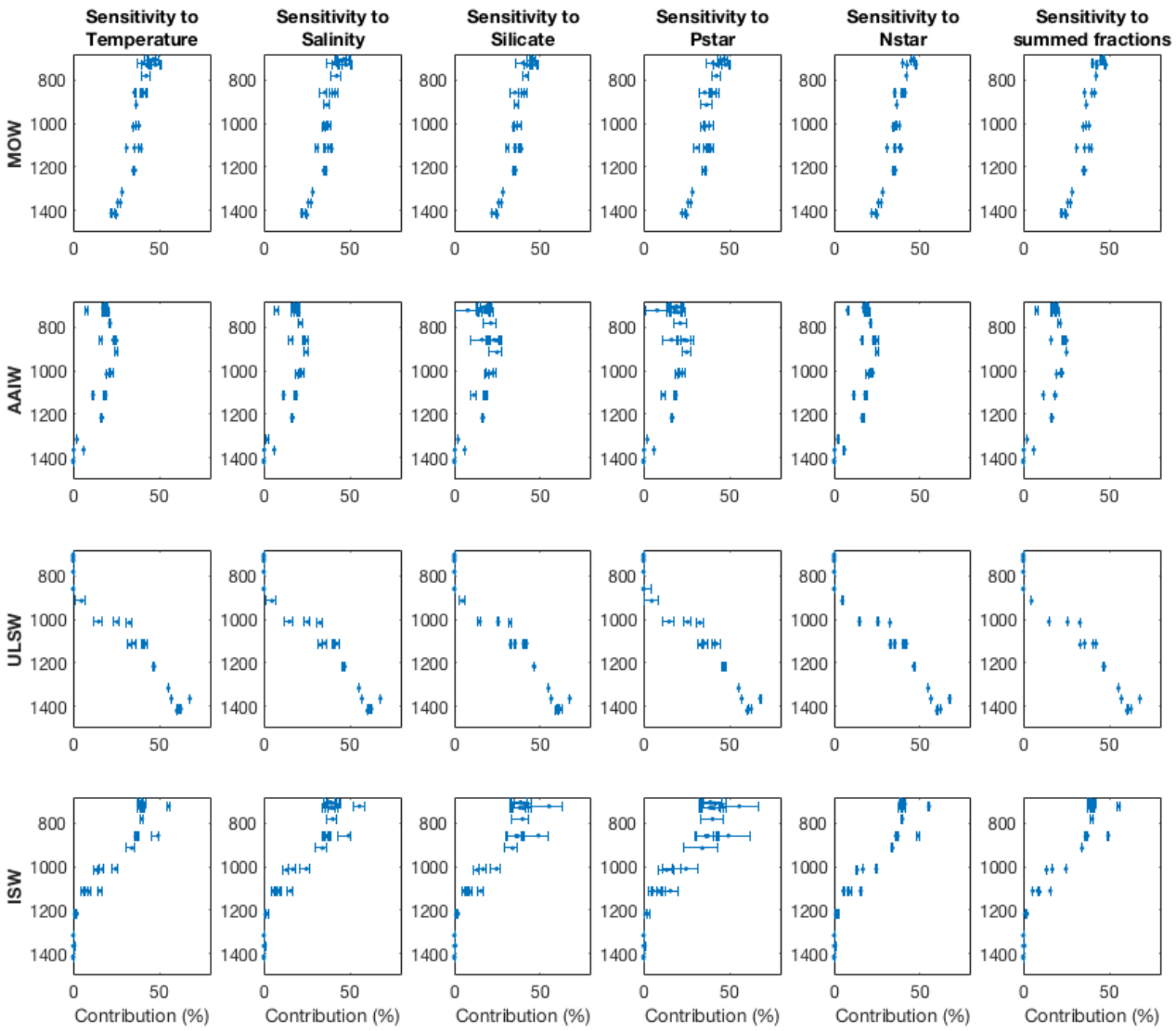

Figure 2.3. Sensitivity of the MOMPA to the choice of weightings applied to conservative tracers. In each case, the weighting of a given tracer was increased and decreased by 25% while other weightings remained constant. Top to bottom, Mediterranean Overflow Water (MOW), Antarctic Intermediate Water (AAIW), Upper Labrador Seawater (ULSW) and Irminger Sea Water (ISW). Data collected during the FRidge GA13 GEOTRACES Field Campaign. Water mass end-member properties from Jenkins et al. (2015), see Table 2.1.

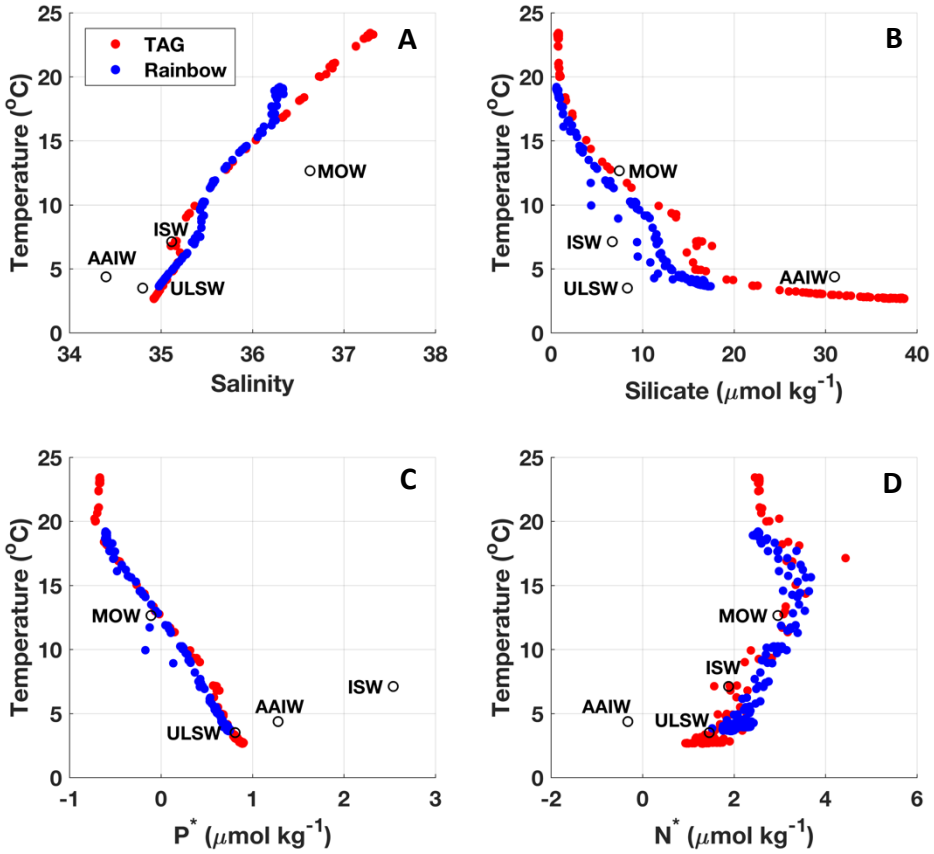

Figure 2.4. Conservative tracer properties at the TAG (red) and Rainbow (blue) hydrothermal vent sites. Data collected during the FRidge GA13 *GEOTRACES* Field Campaign. Water mass end-member properties from Jenkins et al. (2015), see Table 2.1.

two sites are discussed using conservative tracers with reference to end-member water mass properties (Figure 2.4). In the subtropical North Atlantic, major contributors to the upper water column are MOW, AAIW, ULSW and ISW. Within the depth bounds of interest in Chapter 5, 500m to 1500m depth, potential temperature ranges from 5.4°C to 13.0°C at TAG and from 5.6°C to 10.2°C at Rainbow. Offsets between the TAG and Rainbow potential temperature-salinity distributions highlights the differing contributions of water masses at the two sites (Figure 2.4a). Between 5°C and 10°C, seawater has a higher salt content at the Rainbow site, meaning there is a stronger influence of more saline MOW (Figure 2.4a). Si concentrations are greater at the TAG site for the full potential temperature range; however, the largest silicate difference is located between depth and potential temperature bounds of interest (Figure 2.4b). The

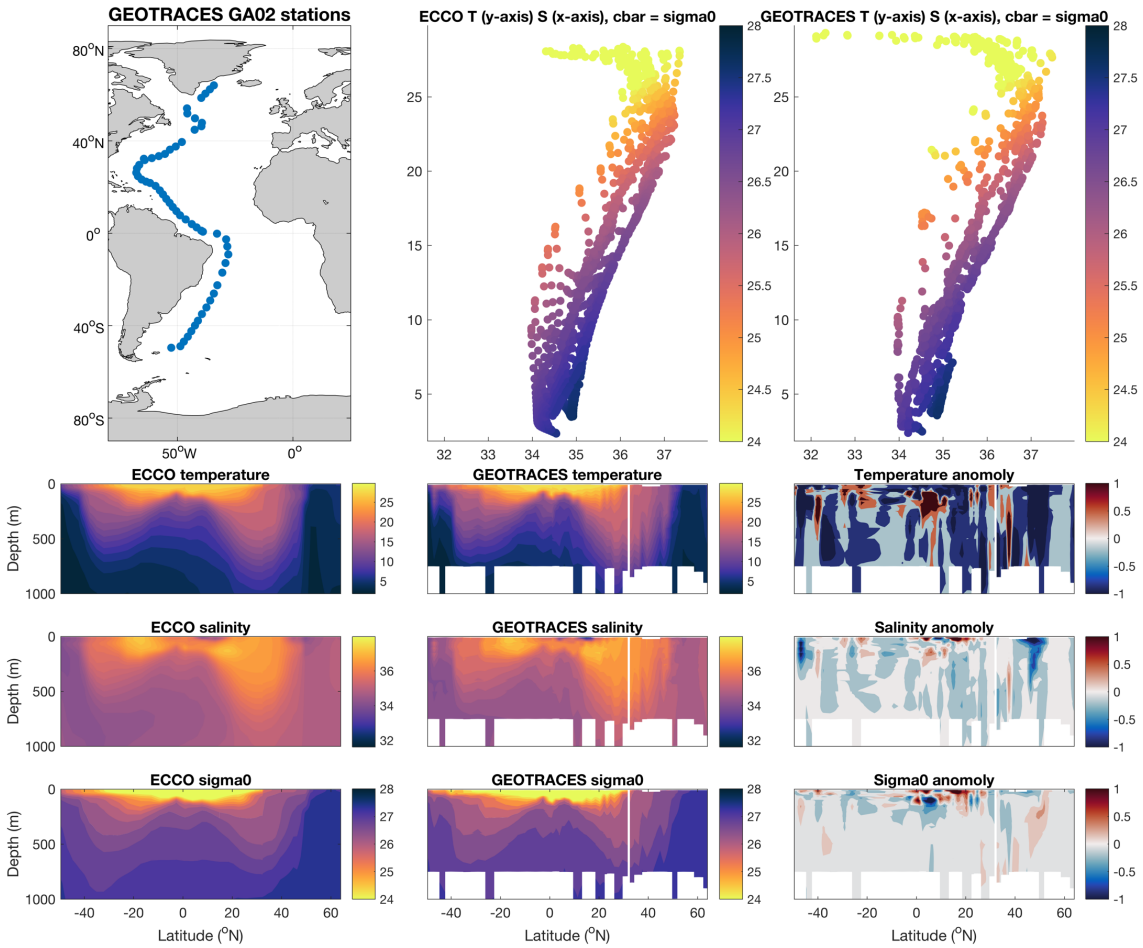

Figure 2.5. Hydrography along *GEOTRACES* section GA02 sourced from direct observations in the *GEOTRACES* 2017 Intermediate Data Product (Schlitzer et al., 2018) and modelled estimates from ECCO version 4 release 3 (Forget et al., 2015, Fukumori et al., 2017).

increase in silicate is indicative of AAIW which is recognised to influence productivity in the low-latitude ocean (Sarmiento et al., 2004). In general, the distribution of P* between the two sites is similar with a slight elevation in P* at TAG from 5°C to 10°C water, suggesting a larger influence of AAIW or ISW which contains a high preformed phosphate signal in end-member properties (Figure 2.4c, Table 2.1). Large estimates of N* observed at TAG and Rainbow are indicative of diazotrophy in the upper ocean and cause the tracer to exhibit non-conservative behaviour, hence N* given minimal

weighting in calculations. Between 5°C and 10°C, N* is lower at TAG, suggesting nitrogen-fixation plays a lesser role at TAG in the surface waters, as in underlying waters the N-remineralization signal is stronger at Rainbow (Figure 2.4d). In

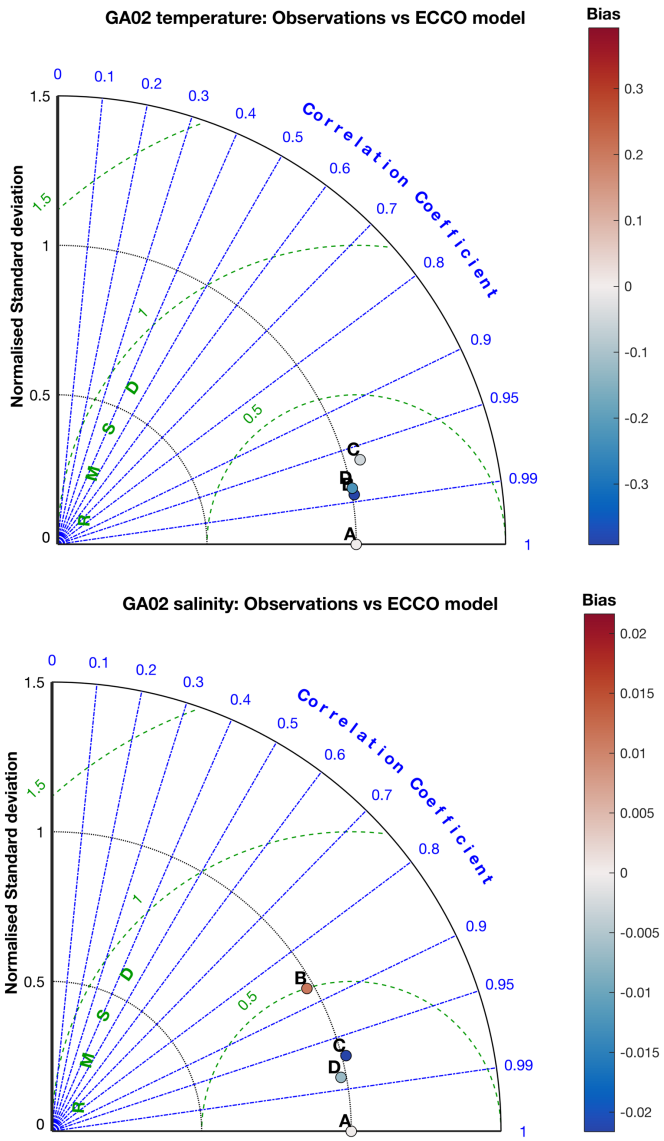

Figure 2.6. Statistical comparisons of temperature and salinity for *GEOTRACES* section GA02 sourced from direct observations in the *GEOTRACES* 2017 Intermediate Data Product (Schlitzer et al., 2018) and modelled estimates from ECCO version 4 release 3 (Forget et al., 2015, Fukumori et al., 2017). Point A marks the example location of identical datasets, B compares data from 0 to 100m, C from 100m to 250m and D from 250m to 1000m. Bias shows offset in ECCO compared to *GEOTRACES*, for example a temperature bias of -0.2 shows ECCO is 0.2ºC cooler than *GEOTRACES* for the given depth bin.

summary, conservative tracers are used to identify differing water mass contributions between the TAG and Rainbow hydrothermal sites. Vertical profiles of fractional water mass contributions at both sites are presented in Chapter 5.

2.2.3 Comparison between *GEOTRACES* and *ECCO* hydrography

As modelled mixed-layer depth estimated by ECCOv4r3 is used throughout this thesis, hydrographical outputs are validated against contemporaneous *GEOTRACES* observations (Figures 2.5, 2.6, 2.7, 2.8). ECCO hydrography is compared to *GEOTRACES* hydrography along the GA02 meridional section and GA03 zonal section as these sections are highlighted in Chapter 3 and Chapter 4 respectively. Temperature and salinity were extracted from monthly ECCO model output at the spatial and temporal location of each *GEOTRACES* station (Forget et al., 2015, Fukumori et al., 2017, Schlitzer et al., 2018).

Along GA02, the distribution of temperature and salinity are well represented by the ECCO model (Figure 2.5). Temperature-salinity plots show ECCO accurately depicts water masses throughout the transect. However, there is a group of low-density waters with salinity below 34 psu in *GEOTRACES* that are not replicated in ECCO. This may be due to processes operating on time scales which are less than the monthly resolution provided by ECCO, such as sampling during heavy rainfall. At depth, there are temperature differences between ECCO and *GEOTRACES* of up to ~1 degree and temperature in ECCO is generally cooler than that in GA02. ECCO salinity is generally slightly lower compared GA02. Therefore, cooler waters are compensated for by reduced salinity when calculating density. The temperature correlation coefficient between ECCO and GA02 is greater than 0.95 in the 0 – 100m, 100m – 250m and 250m – 1000m depth bins where ECCO is cooler by an average of 0.39^{o}C, 0.05^{o}C and 0.22^{o}C in each bin respectively (Figure 2.6). The salinity correlation coefficient in the 0 - 100m depth bin, 0.87, is lower than the 100m – 250m and 250m – 1000m bin, likely due to the low density and low salinity waters (salinity < 34 psu) which are not captured by ECCO (Figure 2.6).

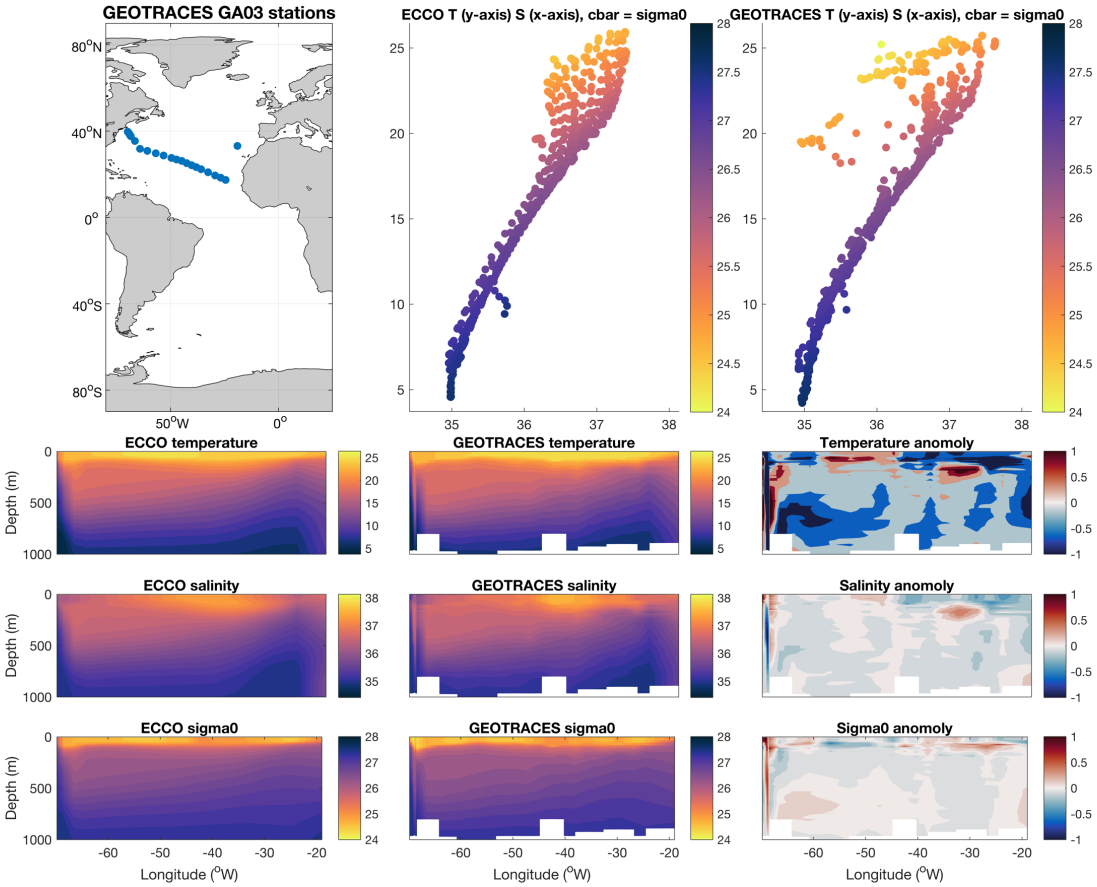

Figure 2.7. Hydrography along *GEOTRACES* section GA03 sourced from direct observations in the *GEOTRACES* 2017 Intermediate Data Product (Schlitzer et al., 2018) and modelled estimates from ECCO version 4 release 3 (Forget et al., 2015, Fukumori et al., 2017).

Generally, ECCO captures hydrographic distributions along GA03 (Figure 2.7). The west to east rising of isotherms, isohalines and isopycnals observed in GA03 are replicated in ECCO. However, the temperature-salinity plots show a region (temperature > 17°C, salinity < 36 psu) which is not well represented by ECCO, located in the upper water column towards the west of the transect. Data in the most western stations of GA03 are around the turbulent Gulf Stream, which drives variability on time-scales shorter than the monthly climatology provided by ECCO, resulting in differences between sampled observation and modelled output. As with GA02, the temperature in the 0 – 100m, 100m – 250m and 250m - 1000m depth bins

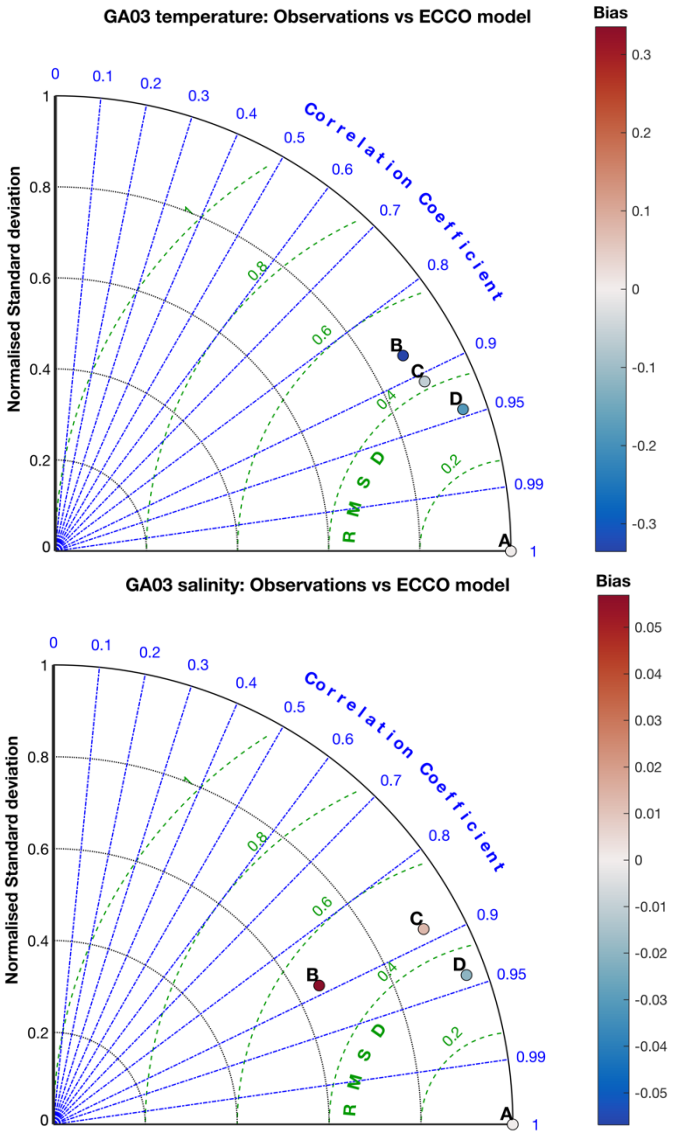

Figure 2.8. Statistical comparisons of temperature and salinity for *GEOTRACES* section GA03 sourced from direct observations in the *GEOTRACES* 2017 Intermediate Data Product (Schlitzer et al., 2018) and modelled estimates from ECCO version 4 release 3 (Forget et al., 2015, Fukumori et al., 2017). Point A marks the example location of identical datasets, B compares data from 0 to 100m, C from 100m to 250m and D from 250m to 1000m. Bias shows offset in ECCO compared to *GEOTRACES*, for example a temperature bias of -0.2 shows ECCO is 0.2ºC cooler than *GEOTRACES* for the given depth bin.

are cooler in ECCO than observed in the GA03 section by 0.34ºC, 0.06ºC and 0.18ºC respectively (Figure 2.8). The temperature correlation coefficient between ECCO and GA03 is greater than 0.87 in each case. In the 0m – 100m and 100m – 250m depth

bins, salinity is higher in ECCO than *GEOTRACES*, with the reverse true for 250m – 1000m (Figure 2.8). However, the correlation coefficient between ECCO and *GEOTRACES* salinity is greater than 0.88 in each vertical bin. In summary, hydrographic correlation coefficients between ECCO and *GEOTRACES* sections are greater than 0.87, meaning ECCO adequately captures the variability in observational data. However, there is a bias where water temperatures estimated by ECCO are generally cooler than those observed in *GEOTRACES*.

2.2.4 Methods to Estimate Vertical Transport

2.2.4.1 Helium Flux Gauge

The helium flux gauge approach provides an estimate of the total physical transport, that is the sum of multiple process including winter-time entrainment, diapycnal diffusion, upwelling and mixing due to the breaking of internal waves over rough topography. Helium is a chemically and biologically inert noble gas and therefore ideal tracer to estimate physical fluxes (Jenkins, 1988). In the mixed layer, the helium budget consists of three source terms, (1) air injection by bubble processes, (2) the *in-situ* decay of tritium and (3) vertical exchange with underlying waters (Jenkins and Doney, 2003). Source terms are equal to outgassing at the air-sea interface. Bubble processes include the full dissolution and partial dissolution of bubbles; both components are proportional to wind speed and temperature and inject atmospheric gases into the mixed layer (Emerson and Bushinsky, 2016, Liang et al., 2013). In the mixed layer, tritium (hydrogen-3) undergoes radioactive beta decay to produce helium-3 and a free electron with a half-life of 12.3 years. The air-sea exchange of helium is calculated as a product of wind speed and supersaturation above an equilibrium value based on temperature and salinity. There is a peak in helium-3 at around 700 m depth in the subtropical Atlantic Ocean due to mid-20th century bomb testing which increased atmospheric tritium abundance and subsequently equilibrated with the surface ocean (Jenkins, 1988, Jenkins et al., 2019). The subduction of upper waters in the high latitude North Atlantic and equatorward propagation combined with the radioactive half-life of tritium have resulted in a helium-3 signature at depth in the modern subtropical Atlantic (Jenkins et al., 2015). After accounting for air-injection

and *in situ* tritium decay, residual helium supersaturation in the mixed layer is due to the physical upward transport of deep helium. The helium flux gauge approach provides an estimate of mixing on weekly time scales.

2.2.4.2 Vertical Microstructure Profilers

Vertical Microstructure Profilers (VMPs) are freefalling apparatus which measure the dissipation rate of turbulent kinetic energy at meter resolution alongside temperature and salinity. Diapycnal mixing is estimated from VMPs by calculation of the buoyancy frequency, mixing ratio and the turbulent kinetic energy dissipation rate. The buoyancy frequency is calculated from vertical density sheer and describes a density anomaly which is released from rest and oscillates around the appropriate isopycnal. The mixing ratio is used to define the proportion of turbulent energy that does work against gravity (ie. mechanical mixing) compared to energy lost to frictional forces as turbulent eddies dissipate, typically 0.2 (Gregg et al., 2018). Importantly, VMPs capture an instantaneous snapshot of water column mixing rather than an estimate averaged over weekly time scales as provided by the helium flux gauge approach.

2.2.4.3 Entrainment

Entrainment is the process whereby one body of water is transported across a boundary by turbulent mixing. In the context of the upper ocean mixed-layer, entrainment is the seasonal deepening of the mixed layer in winter, which causes underlying thermocline waters to augment mixed layer water. Differences in the shape of a tracer profile at the time of entrainment cause contrasting responses in mixed-layer resource stock (Rigby et al., 2020). In the case of a nutrient-type resource profile, which is depleted at the surface and increases in concentration with depth, resources in the mixed layer are replenished by winter-time entrainment (Figure 2.9). Conversely, surface maxima are eroded from scavenged-type resources in winter due to entrainment, reducing mixed-layer resource concentrations (Figure 2.9).

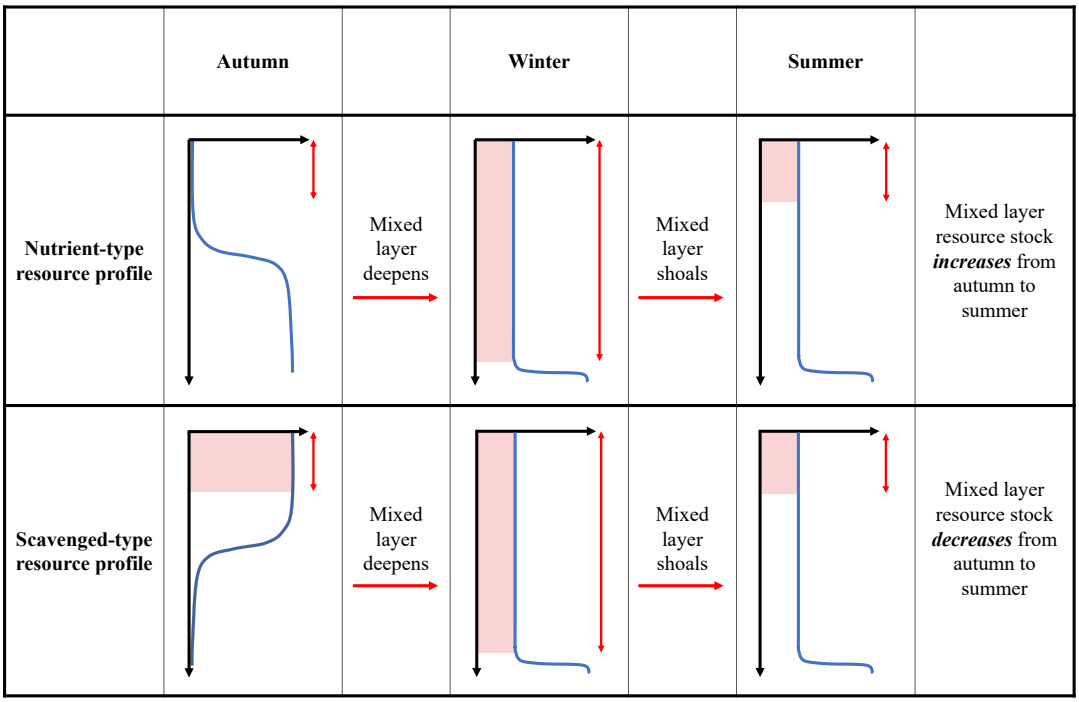

Figure 2.9. Schematic presenting the seasonal evolution of a nutrient-type and a scavenged-type resource profile (blue line) in response to changes in the mixed-layer depth (red arrow). Mixed-layer resource stock is represented by the red shaded area.

Tagliabue et al. (2014) formulation

The formulation to calculate entrainment used in Tagliabue et al. (2014), hereafter T14, is applied to Fe profiles in the Southern Ocean to show that deep winter mixing is a key source of iron to the upper ocean in the region. The approach integrates the vertical nutrient profile to the winter-time mixed-layer depth, then scales the integrated nutrient stock by the ratio of the summer MLD and winter MLD (equation 2.1),

$$Entrainment\ (mol\ m^{-2}\ yr^{-1}) = \int_{Z=-H}^{Z=0} [R]dz\ *\ \frac{MLDmin}{MLDmax} \qquad [2.1]$$

where z is depth, H is the winter mixed-layer depth, [R] is the concentration of a given resource, and MLDmin and MLDmax are the annual minimum and maximum depths of the mixed layer respectively. Conceptually, this approach fully mixes the water column from the surface to the winter MLD, then traps a proportion of the nutrient

stock in the summer mixed layer. In the Southern Ocean, Fe exhibits a nutrient type profile, deplete in upper waters and increases with depth. A simple 1-dimensional model shows that the approximation of T14 is adequate when applied to nutrient type profiles; however, the approximation breaks down where vertical profiles exhibit a scavenged type profile. If a nutrient follows a scavenged type profile, the entrainment of thermocline waters into the mixed layer results in a reduction in mixed layer nutrient availability. This process is analogous to temperature, where a deepening of the MLD entrains underlying, cooler waters into the mixed layer, reducing the surface temperature. In the case of nutrient availability, entrainment applied to a scavenged type profile is effectively a negative flux. However, by definition, the approximation of T14 cannot estimate a negative flux. The approach assumes the summer mixed layer is depleted in nutrient stock, which is not the case for scavenged type profiles. Therefore, in regions such as the subtropical North Atlantic, the approach is not well suited for dust-derived elements such as Mn and Fe which exhibit a scavenged type profile.

Williams et al. (2000) formulation

The entrainment formulation applied in Williams et al. (2000), hereafter W00, uses concentration gradients and mixed layer depth changes to derive short temporal scale contributions to an annual entrainment flux, equation [2.2].

$$Entrainment\ (mol\ m^{-2}\ s^{-1}) = \frac{1}{T}\int_{0}^{year} \Lambda\left([R(t)]_{th} - [R(t)]_{ml}\right)\frac{dH}{dt}\,dt \qquad [2.2]$$

where T represents one year (months), $[R(t)]_{th}$ is the thermocline mean concentration of a resource R (mol m^{-3}) in month t, $[R(t)]_{ml}$ is the mixed layer mean concentration of resource N (mol m^{-3}) in month t, H is the mixed layer thickness (m), t is the month and Λ is the Heaviside function as defined by Kraus and Turner (1967), where

$$\Lambda \equiv \Lambda\left(\frac{dH}{dt}\right) = \begin{matrix}1\\0\end{matrix}\ for\ \frac{dH}{dt} \gtrless 0 \qquad [2.3]$$

The formulation in equation [2.2] applies when the mixed layer is deepening by use of the Heaviside function, equation [2.3] (Kraus and Turner, 1967). Monthly entrainment estimates (mol m^{-2} s^{-1}) are summed and divided by 12 to give an annual entrainment estimate. Use of the concentration gradient approach allows the entrainment flux to become negative, reflecting a dilution of mixed layer resource, meaning the formulation is valid for both nutrient and scavenged type resources. Due to the temporal component of this approach, monthly estimates of mixed-layer depth and vertical resources profiles are required. In this thesis, ECCOv4r3 is used to estimate the annual cycle of the mixed layer in a given location. However, monthly resolved trace element data remain unavailable from observational studies on an ocean basin scale. Ocean transects studies such as *GEOTRACES* provide great detail about large scale spatial distributions of key resources, yet do not provide repeat monthly measurements. To overcome this limitation, monthly resource profiles are reconstructed following density structure and assuming there is zero export to below the winter mixed layer. Monthly density structure is also sourced from ECCOv4r3 for consistency.

1-Dimensional Evolution of the Mixed Layer

A simple 1-dimensional model was developed to assess the differences between formulations of T14 and W00. In the model, a vertical tracer profile is homogenised from the surface to the mixed-layer depth. The tracer profile is initialised as a nutrient-type (Figure 2.10) or a scavenged-type (Figure 2.11) resource. The mixed-layer deepens from month 1 to month 7, causing the entrainment of waters below into the mixed-layer. From months 8 to 12, the mixed-layer shoals and detrainment causes the transfer of some tracer from the mixed-layer to underlying waters. Sources and sinks of resources, such as biological uptake, export and regeneration, are not included in the idealized scenario.

The evolution of the nutrient-type tracer over one year follows an expected cycle. In month 1, the mixed-layer tracer stock is depleted (Figure 2.10). As the mixed-layer deepens, tracer rich waters are entrained into the mixed-layer, gradually increasing mixed-layer tracer stock and concentrations. In month 7 when the mixed layer is deepest, tracer stock has increased to 120.5 mol m^{-2} and concentration increased to

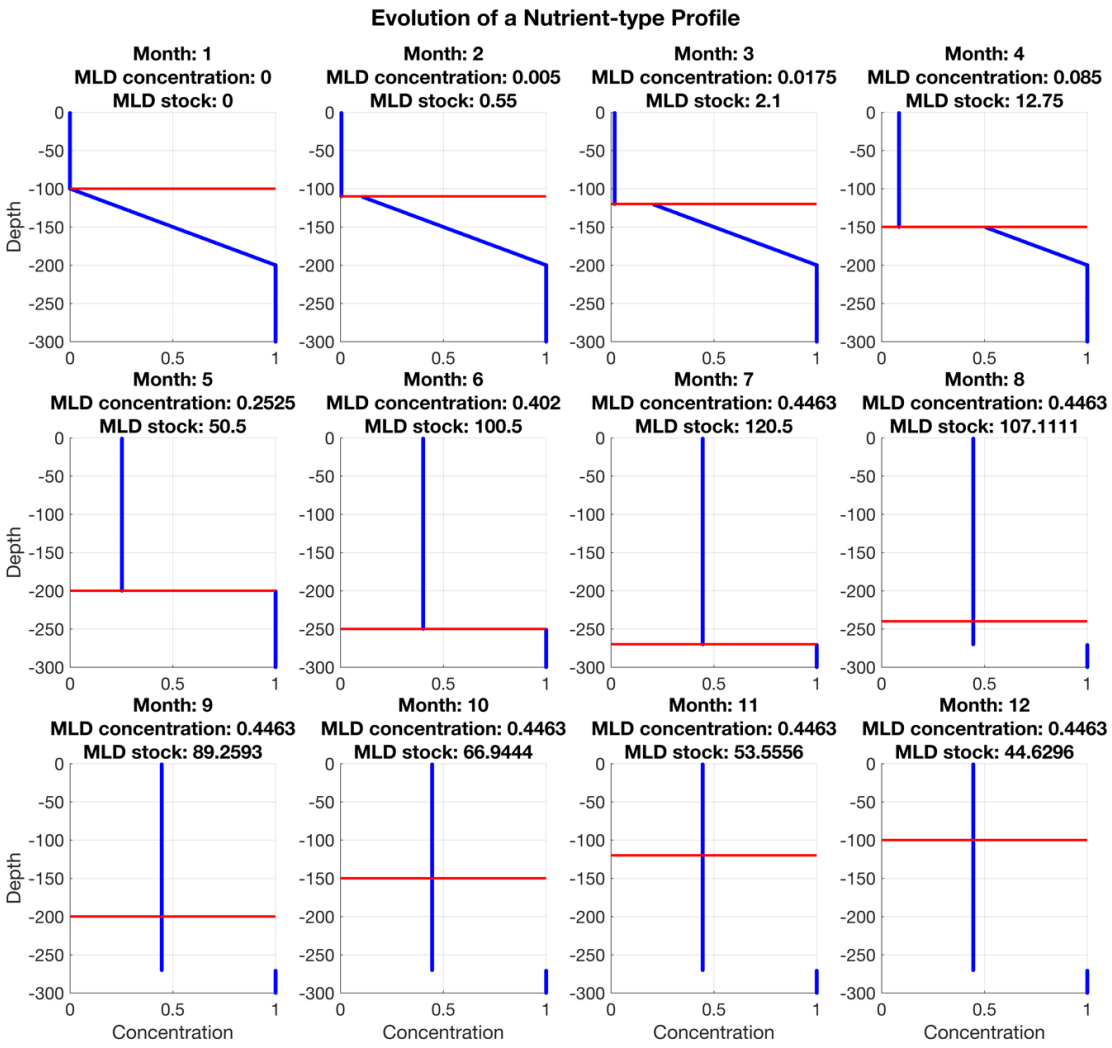

Figure 2.10. Evolution of a one-dimensional tracer (mol m^{-3}) initialized as a nutrient-type resource profile (blue). Tracer is homogenized above the mixed-layer depth (MLD, red), causing entrainment when the mixed-layer deepens from months 1 to 7 and detrainment from months 8 to 12. Biological and chemical effects are not included in this idealized model. MLD concentration (mol m^{-3}) is the average tracer concentration in the mixed layer, while MLD stock is the integrated tracer stock (mol m^{-2}).

0.4463 mol m^{-3}. As the mixed layer shoals to month 12, the tracer concentration remains constant as the tracer profile is homogenised, however the tracer stock is reduced to 44.6296 mol m^{-2} due to detrainment. In summary, the annual cycle of the mixed layer has increased mixed layer tracer concentration by 0.4463 mol m^{-3} and mixed layer tracer stock by 44.6296 mol m^{-2}. The implications of this process may be

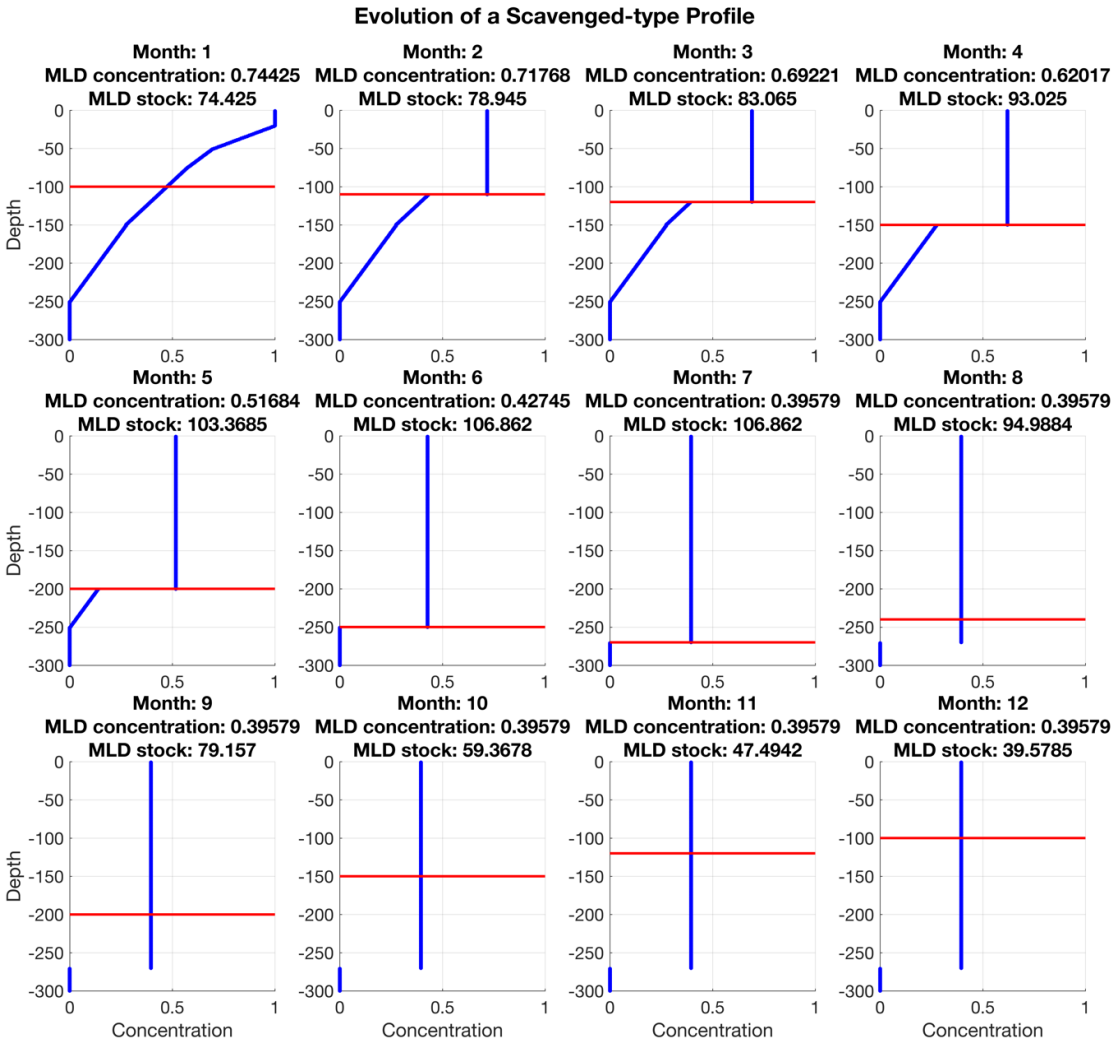

Figure 2.11. Evolution of a one-dimensional tracer (mol m^{-3}) initialized as a scavenged-type resource profile (blue). Tracer is homogenized above the mixed-layer depth (MLD, red), causing entrainment when the mixed-layer deepens from months 1 to 7 and detrainment from months 8 to 12. Biological and chemical effects are not included in this idealized model. MLD concentration (mol m^{-3}) is the average tracer concentration in the mixed layer, while MLD stock is the integrated tracer stock (mol m^{-2}).

applied to the oceanographic setting by considering the example profile as typical nutrient-type resources such as NO_3, PO_4 or Cd.

Entrainment calculated by W00 and T14 using the nutrient-type model (Figure 2.10) results in flux estimates of 96.3 mol m^{-2} yr^{-1} and 44.4 mol m^{-2} yr^{-1} respectively. Differences between the results is due to the inclusion of detrainment in the

calculations. T14 includes detrainment by scaling the winter mixed-layer stock by the ratio of summer and winter mixed-layers, however, W00 does not include detrainment. Excluding the detrainment term allows entrainment to be calculated as a simple integration of a resource profile from the surface to the winter mixed-layer depth, which is calculated during month 7 in Figure 2.10 as 120.5 mol m^{-2}. The entrainment flux calculated by W00 does not equal the winter-time stock as this formulation includes monthly increases in mixed-layer resource stock and calculates the flux using the resource gradient between the mixed layer and entrained waters.

The evolution of the scavenged-type tracer is in contrast to the nutrient-type tracer (Figure 2.11). Initially, the mixed-layer tracer concentration is homogenised to 0.74 mol m^{-3} with an integrated stock of 74.4 mol m^{-2}. Throughout this experiment, tracer concentration in the mixed layer is always greater than in the underlying waters. Therefore, as underlying waters are entrained into the mixed layer from month 1 to month 7, mixed layer tracer concentration decreases. Mixed layer tracer stock decreases while tracer concentration remains constant during detrainment from month 8 to month 12. In this scavenged-type tracer case, the mixed-layer cycle has reduced mixed layer tracer concentration by 0.35 mol m^{-3} and tracer stock by 34.8 mol m^{-2}. The implications of this process are akin to scavenged-type resources Mn or Fe in the subtropical North Atlantic, meaning the annual mixed-layer cycle removes resources from the mixed layer, reducing resource availability.

Entrainment fluxes calculated by formulations of W00 and T14 are in stark contrast when applied to a scavenged-type resource profile, -69.3 mol m^{-2} yr^{-1} and 39.4 mol m^{-2} yr^{-1} respectively. Importantly, the parameterization in W00 allows for a negative flux as mixed-layer concentrations are diluted by the entrainment of underlying waters. A negative entrainment flux causes a reduction in resource availability and is analogous to a reduction in mixed-layer temperature as thermocline waters are entrained in winter. Conversely, T14 does not permit a negative flux as the approximation is an integration of a resource profile from the surface to the winter mixed-layer depth, relying on the standing stock in winter (which must be greater than or equal to zero) to calculate entrainment. In summary, T14 is not suitable to calculate the entrainment flux of scavenged-type resources.

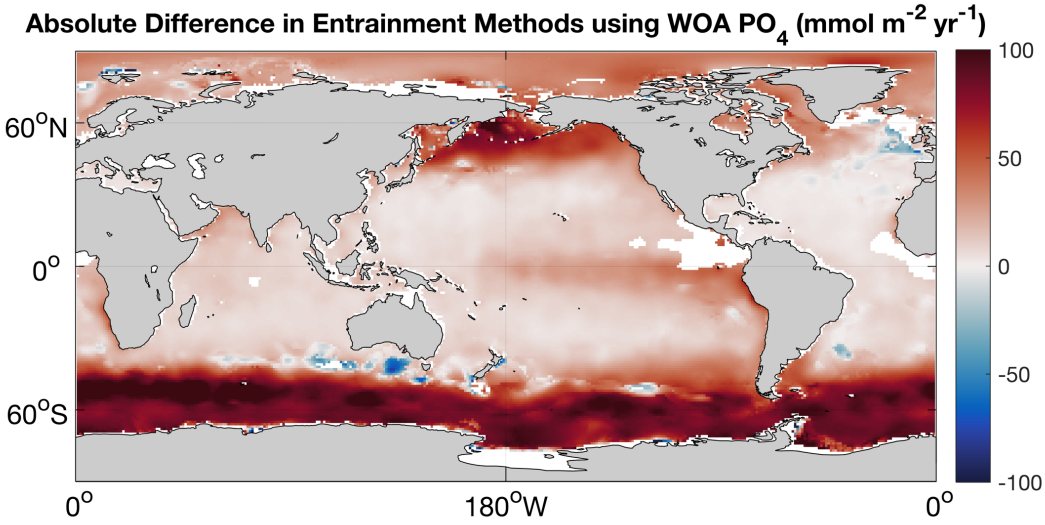

Figure 2.12. The absolute difference in entrainment calculated from the formulation in Tagliabue et al., (2014) and Williams et al., (2000). Mixed-layer depth calculated from density using the de Boyer Montégut et al., (2004) criterion, where density is calculated from World Ocean Atlas (WOA) 2018 temperature (Locarini et al., 2018) and salinity (Zweng et al., 2018). Phosphate (PO_4) is sourced from WOA 2018 (Garcia et al., 2018).

Formulations applied to World Ocean Atlas Phosphate

Applying both entrainment formulations to WOA PO_4 is advantageous over the simple 1-D model used in section 2.3.1.3 as monthly evolving PO_4 profiles contain biogeochemical cycling and the subsequent monthly redistribution of PO_4. Both formulations of entrainment, equations [2.1] and [2.2], are applied to the WOA PO_4 climatology (Figure 2.12). Density is calculated from contemporaneous WOA temperature and salinity using the Gibbs Seawater toolbox (TOES-10). The mixed-layer depth is defined using the de Boyer Montégut et al., (2004) criteria, where a threshold value of the seawater density at 10m depth plus 0.03 kg m^{-3} is used to identify the mixed-layer depth. The entrainment formations applied here are comparable in the major oligotrophic gyre systems. In these regions, PO_4 is depleted in the upper ocean and increases with depth due to regeneration, following a typical nutrient-type resource profile. In the Southern Ocean, there is high standing stock of PO_4 in the mixed layer as upwelled waters are rich in regenerated macronutrients, meaning biota here are considered to be limited by trace elements such as Fe, Mn and

Co. In this case, equation [2.1] performs poorly due to the high initial standing stock which is not compensated for in calculating entrainment. In some regions, such as south of Australia, the equation [2.2] outweighs equation [2.1], indicated by blue colours in Figure 2.8. This is indicative of strong vertical gradients in the vertical profile of PO_4, resulting in a large entrainment flux derived from equation [2.2] which relies on vertical gradients to calculate the entrainment flux. In summary, the formulation applied in equation [2.1] to calculate resource supply to the upper ocean via entrainment is representative in the specific case where a vertical resource profile is nutrient-type and mixed-layer stocks are depleted only. Therefore, in Chapter 3, equation [2.2] is used to estimate the entrainment of both nutrient-type and scavenged-type resources into the mixed layer.

Summary

In Section 2.2.3.3, the approaches of T14 and W00 to estimate the entrainment of resources into the mixed layer are compared. Both formulations are applied to a simple one-dimensional model, for a nutrient-type resource profile and a scavenged-type profile, as well as monthly phosphate profiles available in WOA 2018. Results show that W00, equation [2.2], outperforms T14, equation [2.1], particularly when calculating the entrainment flux of a scavenged-type resource. Therefore, the W00 formulation is used throughout this thesis and recommended as best practice for future calculations of entrainment.

Chapter 3

Resource Availability and Entrainment Are Driven by Offsets Between Nutriclines and Winter Mixed-Layer Depth

Shaun. J. Rigby[1], Richard. G. Williams[1], Eric P. Achterberg[2] and Alessandro Tagliabue[1]

[1] Department of Earth, Ocean and Ecological Sciences, School of Environmental Science, University of Liverpool, UK.

[2] GEOMAR Helmholtz Centre for Ocean Research Kiel, Kiel, Germany.

3.0 Preamble

Study Motivation

The fundamental role of trace elements in controlling marine productivity has been studied and accepted over the past few decades (eg. Sunda, 1989; Ho et al., 2003; Twining and Baines, 2013). However, the relative availability of key resources on a basin-scale had yet to be established. The first goal of this work was to synthesise Atlantic *GEOTRACES* observations of macro- and micro- nutrients to produce the first basin-scale geography of resource availability in the mixed layer, which included trace metal resources. We then investigated the role of winter-time entrainment in constructing large-scale patterns in resource availability. As the depth of the winter mixed layer was shown to play pivotal role in defining mixed-layer resource stoichiometry, we then explored differences in relative resource availability driven by altering the winter mixed-layer depth.

Key points

- There are large scale regimes present in mixed-layer nutrient availability throughout the Atlantic Ocean.
- Entrainment decreases the mixed layer availability of resources where the concentration decreases with depth.
- Variations in nutrient availability and entrainment are linked to gradients in resource profiles combined with the depth of mixing.

Publication and Author Contribution

This work has been published in *AGU: Global Biogeochemical Cycles* with authors Shaun J Rigby, Richard G Williams, Eric P Achterberg and Alessandro Tagliabue. Shaun J Rigby, Alessandro Tagliabue and Richard G Williams designed the research, while Shaun J Rigby undertook the analysis with input from all co-authors. Shaun J Rigby wrote the manuscript with the contribution of all co-authors.

Citation

Rigby, S. J., Williams, R. G., Achterberg, E. P., & Tagliabue, A. (2020). Resource availability and entrainment are driven by offsets between nutriclines and winter mixed-layer depth. *Global Biogeochemical Cycles*, *34*, e2019GB006497. https://doi.org/10.1029/2019GB006497

3.1 Abstract

While phytoplankton play a key role in ocean biogeochemical cycles, the availability and supply pathways of resources that support their growth remain poorly constrained. Here, we show that the availability of various resources varies over several orders of magnitude throughout the Atlantic Ocean, causing regional contrasts in resource deficiency. Regional variations in the relative availability of nitrogen, phosphorus, silicon, iron, zinc, manganese, cobalt, and cadmium are important and result from the contrasts between winter mixing depths and differences in vertical profiles of the different resources. The winter-time thickening of the mixed layer may replenish or deplete resources via entrainment, depending on the vertical nutrient profile. For nutrients like nitrate, phosphate, and cadmium, entrainment is a consistent source term. While for others, such as manganese and iron, entrainment can reduce ocean resource availability, particularly in subtropical regions. We apply a nitrogen-iron relationship to winter mixed-layer resource stocks and infer singular nitrogen limitation in low latitudes, co- and secondary-limitation in mid latitudes and singular iron limitation in high latitudes. The role of iron limitation in high latitudes suggests that high latitude iron availability may exert a remote influence over low latitude biogeochemistry, particularly if concurrent results are found at deep water formation sites such as the Labrador Sea during future studies. Finally, we show that any future change to the depth of winter-time mixing will cause region-specific changes in relative availability of different resources that may have important ecological consequences.

3.2 Introduction

The growth and biomass accumulation of marine phytoplankton are key determinants of ocean biogeochemical cycles and the operation of the ocean carbon cycle. One key factor affecting the large scale distribution of marine phytoplankton in the sunlit upper ocean is the difference between the availability of nutrient and trace metal resources and biological demands (Martin and Fitzwater, 1988, Moore et al., 2013, Moore, 2016). Primary production and other cellular functions require a range of resources, including the macronutrients nitrogen (N), phosphorus (P), and silicon (Si, for diatoms

and some dinoflagellates), as well as micronutrient trace metals such as iron (Fe), zinc (Zn), manganese (Mn), cadmium (Cd), and cobalt (Co) (Sunda, 1989, Price and Morel, 1990, Ludwig and Matthews, 1997, Falkowski et al., 1998, Morel and Price, 2003, Rodionov et al., 2003, Twining and Baines, 2013). The upper mixed layer is the key growth environment for marine phytoplankton and where biota thrive given sufficient resource availability. Changes in the resource supply are often invoked as a driver of variability in phytoplankton growth and primary production (Marra et al., 1990, Okin et al., 2011, Lampe et al., 2019).

The vertical profiles of different resources are known to vary both spatially and between resources (Tagliabue, 2019), driving large-scale patterns in availability of various resources (Moore, 2016). The shape of resource profiles is influenced by biogeochemical and physical processes. Biological consumption removes resources from the upper water column, organic particles then sink and resources are released back into the water column at depth through resupply processes such as remineralization (Twining et al., 2014). The combination of removal in surface waters and resupply at depths forms gradients in the vertical profiles of key resources, with the strongest vertical gradient known as the nutricline (Tagliabue et al., 2014, Omand and Mahadevan, 2015). The reservoir of resources below the nutricline is accessed by the seasonal deepening of the mixed layer. Thus, the relative positioning of multiple nutriclines determines the availability of different resources to phytoplankton. For instance, where the mixed layer extends below the N-nutricline (nitracline) but fails to access below the P-nutricline (phosphocline), the upper mixed layer will be enriched in N relative to P. We do not understand how spatial variations in upper ocean mixing depths and vertical resource profiles shape the availability of different resources on an ocean basin scale.

The availability of different resources is a crucial determinant of phytoplankton growth. Biological communities become deficient in a given resource if its availability is lower than the biological demand. In the Atlantic Ocean, high latitudes are considered as Fe deficient, low to mid-latitudes are N deficient, and the North Atlantic sub-tropical gyre as P deficient (Mills et al., 2004, Nielsdottir et al., 2009, Moore, 2016, Browning et al., 2017a). Deficiency leads to limitation following biological consumption and is intensified if the resource supply to the growth environment is low

in the deficient resource (Moore, 2016). For instance, using shipboard bioassay experiments in the South Atlantic, Browning et al. (2017a) found that evidence of singular limitation (where one resource only limits), serial limitation (or secondary limitation, where a second resource becomes limiting after the supply of the first), or colimitation by Fe and N could be explained by the relative availability of N and Fe. Resource limitation is alleviated by the supply of the exhausted resource, irrespective of other resources; however, resource deficiency is reduced when the supply is abundant in the deficient resource relative to other resources. If the future ocean becomes more stratified (Sen Gupta et al., 2009, Bopp et al., 2001) with reduced upper ocean mixing depths, or mixed layers vary interannually (Holte et al., 2017), then any subsequent impact on the relative availability of resources may affect resource deficiency and biological communities.

Resources are delivered to the upper ocean via atmospheric processes and physical ocean processes. Lithogenic (Jickells et al., 2005) and anthropogenic (Conway et al., 2019) particles can be transported across the ocean by winds, then deposited at the air-sea interface via dry and wet deposition processes. A range of physical ocean processes transport dissolved resources to the upper ocean (Williams and Follows, 2003a), such as upwelling (Oschlies, 2002), lateral advection (Williams et al., 2006), vertical turbulence (Martin et al., 2010), diapycnal mixing (Tuerena et al., 2019), diapycnal diffusion (Rijkenberg et al., 2012, Painter et al., 2014), and eddies (Conway et al., 2018). Here, we focus on the role of deep winter mixing since the entrainment of underlying waters has been shown to be fundamental in the delivery of resources to mixed-layer phytoplankton (Williams et al., 2000, Tagliabue et al., 2014, Achterberg et al., 2018).

Resource availability is altered by entrainment redistributing thermocline waters throughout the seasonal mixed layer. Underlying thermocline waters can be rich in a given resource due to resupply processes; how- ever, these waters can also be deplete in a given resource due to interior ocean removal processes such as particle scavenging. The magnitude of the entrainment input to the mixed layer is determined by the volume of water entrained and the contrast in resource concentration from the mixed layer to underlying waters (Williams et al., 2000). Therefore, variability in the

entrainment flux will likely occur in response to spatial variation in resource profiles and the depth of seasonal mixing.

Here, we use observations of multiple resources and their vertical profiles to explore basin scale patterns of resource availability in the mixed layer. Differences in resource availability are attributed to offsets in vertical profiles between each resource, most important is the depth of the nutricline. The *GEOTRACES* program has delivered a wealth of observations which reveal the array of vertical resource profiles present in the Atlantic Ocean, permitting a large scale analysis of entrainment for multiple resources (Schlitzer et al., 2018). We analyse the role of entrainment in either delivering or diluting resources in the seasonal mixed layer and the subsequent effect on resource availability. Finally, we speculate on changes to mixed-layer resource availability in a warmer climate and the future role of entrainment in biogeochemical cycling.

3.3 Methods

3.3.1 Datasets

Observational data of nitrate (NO_3), phosphate (PO_4), Si, Fe, Zn, Mn, Cd, and Co were extracted from the 2017 *GEOTRACES* Intermediate Data Product (Schlitzer et al., 2018). Only *GEOTRACES* datapoints with "good" data quality flags were included (Figure 3.1). Monthly mean temperature, salinity, and mixed-layer depths were extracted from the 1° × 1° resolution *ECCO* circulation model (version 4, release 3), full period 1992–2015 (Figure 3.1 and Figure 3.2) (Forget et al., 2015, Fukumori et al., 2017).

Vertical profiles are presented in Longhurst Provinces (Longhurst, 2007), where 21 provinces were aggregated into five provinces throughout the Atlantic based on underlying biogeochemistry (Figure 3.3). The North Atlantic subpolar gyre (capped at 65°N due to data limitations) is composed of the Atlantic Arctic, Atlantic Subarctic, Northwest Atlantic Shelves (North of 45°N), and North Atlantic Drift provinces. The North Atlantic subtropical gyre is composed of North Atlantic Subtropical Gyral, Gulf

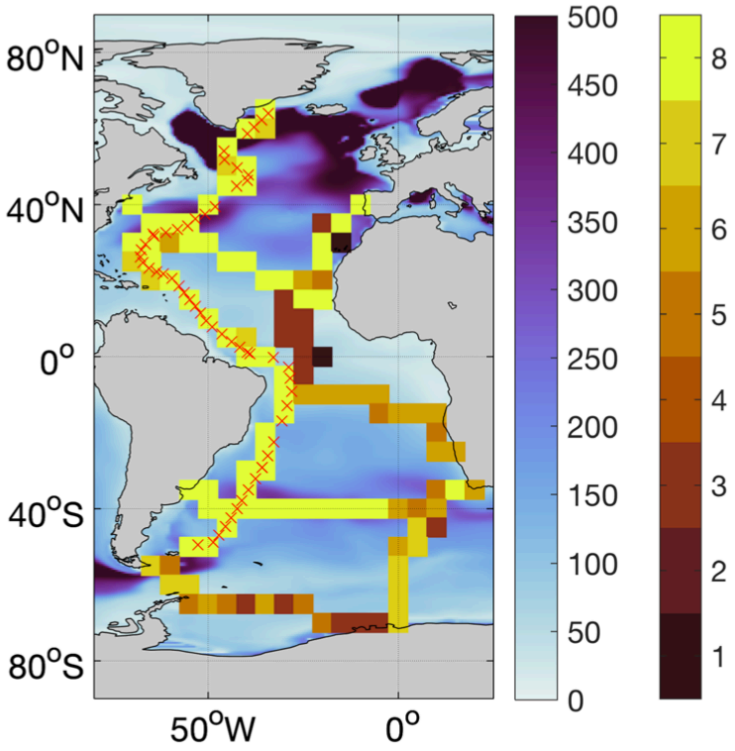

Figure 3.1. Monthly mean maximum mixed-layer depth (white–purple, in m) for the period 1992–2015 as reported in Estimating the Climate and Circulation of the Ocean version 4 release 3 (Forget et al., 2015; Fukumori et al., 2017). Overlaid, maximum number of observations (brown–yellow) available at a single station in 5 × 5 degree grid cells (from nitrate, phosphate, silica, iron, zinc, manganese, cadmium, and cobalt), biogeochemical data from the 2017 *GEOTRACES* Intermediate Data Product (Schlitzer et al., 2018). Stations associated with the *GEOTRACES GA02* cruise are indicated with red crosses.

Stream, and Northwest Atlantic (South of 45°N) provinces. The equatorial Atlantic is composed of the Caribbean, North Atlantic Tropical Gyral, Eastern (Canary) Coastal, Western Tropical Atlantic Eastern Topical Atlantic, Guinea Current Coastal, and Guianas Coastal provinces. The South Atlantic subtropical gyre province is composed of the Brazil Current Coastal, South Atlantic Gyral, and Benguela Current Coastal provinces. The Southern Ocean province is composed of the Southwest Atlantic Shelves, South Subtropical Convergence, Subantarctic Water Ring, Antarctic, and Austral Polar provinces. This aggregated province approach better suits the limited spatial distribution of shipboard measurements available from *GEOTRACES*. The nutricline for each resource is defined as the depth in the upper 500 m where the

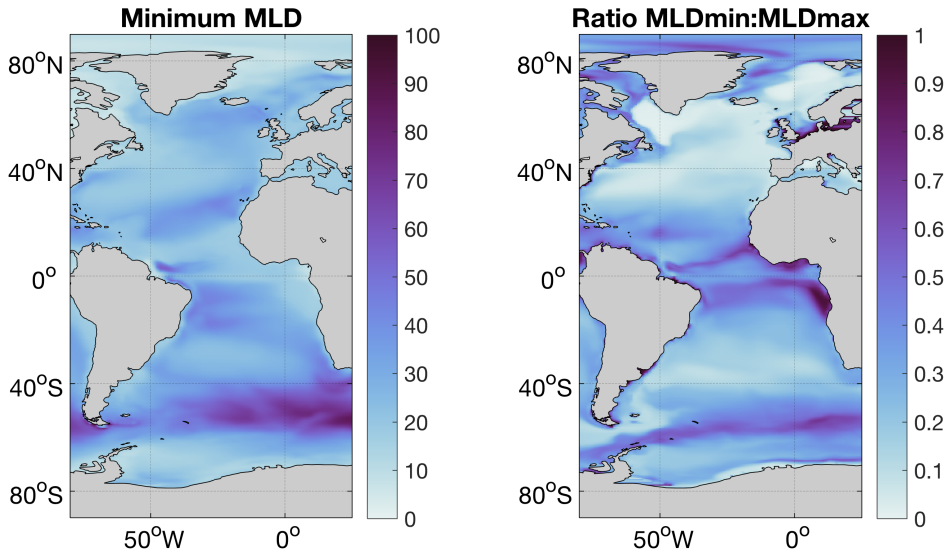

Figure 3.2. (a) minimum (m), and (b) ratio of minimum to maximum, annual mixed layer depths for the period 1992 – 2015 as reported in Estimating the Climate and Circulation of the Ocean version 4 release 3 (Forget et al., 2015, Fukumori et al., 2017).

gradient of a given resource is maximum ($d[R]/dz_{max}$, where [R] is a resource concentration and z is depth).

3.3.2 Winter Mixed-Layer Resource Availability

Due to the spatial and temporal limitations of the observational *GEOTRACES* data set, monthly profiles of each resource were constructed using temperature and salinity derived density profiles from *ECCO*. Density is calculated at each location in the *GEOTRACES* data set from shipboard temperature and salinity observations. On a profile-by-profile basis, the observational relationship between density and each resource was applied to monthly density structures at the corresponding latitude and longitude. This approach assumes resource concentrations are conserved on isopycnals, meaning biogeochemical processes are invariable from the time of observation through to winter.

The winter mixed-layer resource availability is calculated by integrating reconstructed winter resource pro- files from the surface to the maximum annual mixed-layer depth reported in the *ECCO* model, equation (1).

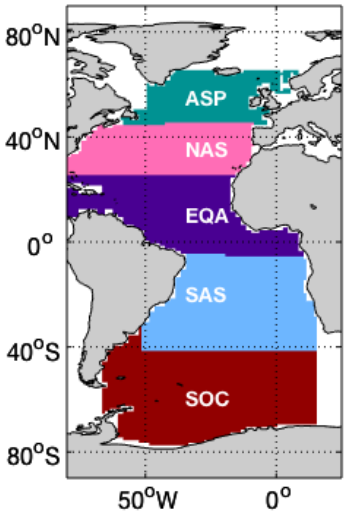

Figure 3.3. Biogeochemical provinces used throughout this study, ASP (North Atlantic sub-polar gyre), NAS (North Atlantic sub-tropical gyre), EQA (Equatorial Atlantic), SAS (South Atlantic sub-tropical) and SOC (Southern Ocean). Aggregated from Longhurst Provinces (Longhurst, 2007), see *Methods*.

$$Resource\ Stock\ (mol\ m^{-2}) = \int_{z=H}^{z=0} [R(z)]\ dz \qquad (1)$$

where z is depth, H is mixed-layer thickness, and R is a given resource concentration. Vertical profiles were required to contain a minimum of two observations in the mixed layer. Profiles were linearly interpolated to meter resolution. The mean value of measurements was taken where multiple observations were available within 1 m. From the surface to the shallowest observation, resource concentrations were set to equal the shallowest observation. Resource concentrations were set to zero where concentrations were below zero as a feature of interpolation.

3.3.3 Entrainment Calculation

The entrainment flux is diagnosed from equation (2) using the mixed-layer thickening and nutrient profiles on a monthly timescale (Williams et al., 2000).

$$Entrainment\ (mol\ m^{-2}\ s^{-1}) = \frac{1}{T}\int_{0}^{year} \Lambda\ ([R(t)]_{th} - [R(t)]_{ml})\frac{dH}{dt}dt \qquad (2)$$

where T represents 1 year (months), $[R(t)]_{th}$ is the thermocline mean concentration of a resource R (mol m^{-3}) in month t, $[R(t)]_{ml}$ is the mixed layer mean concentration of

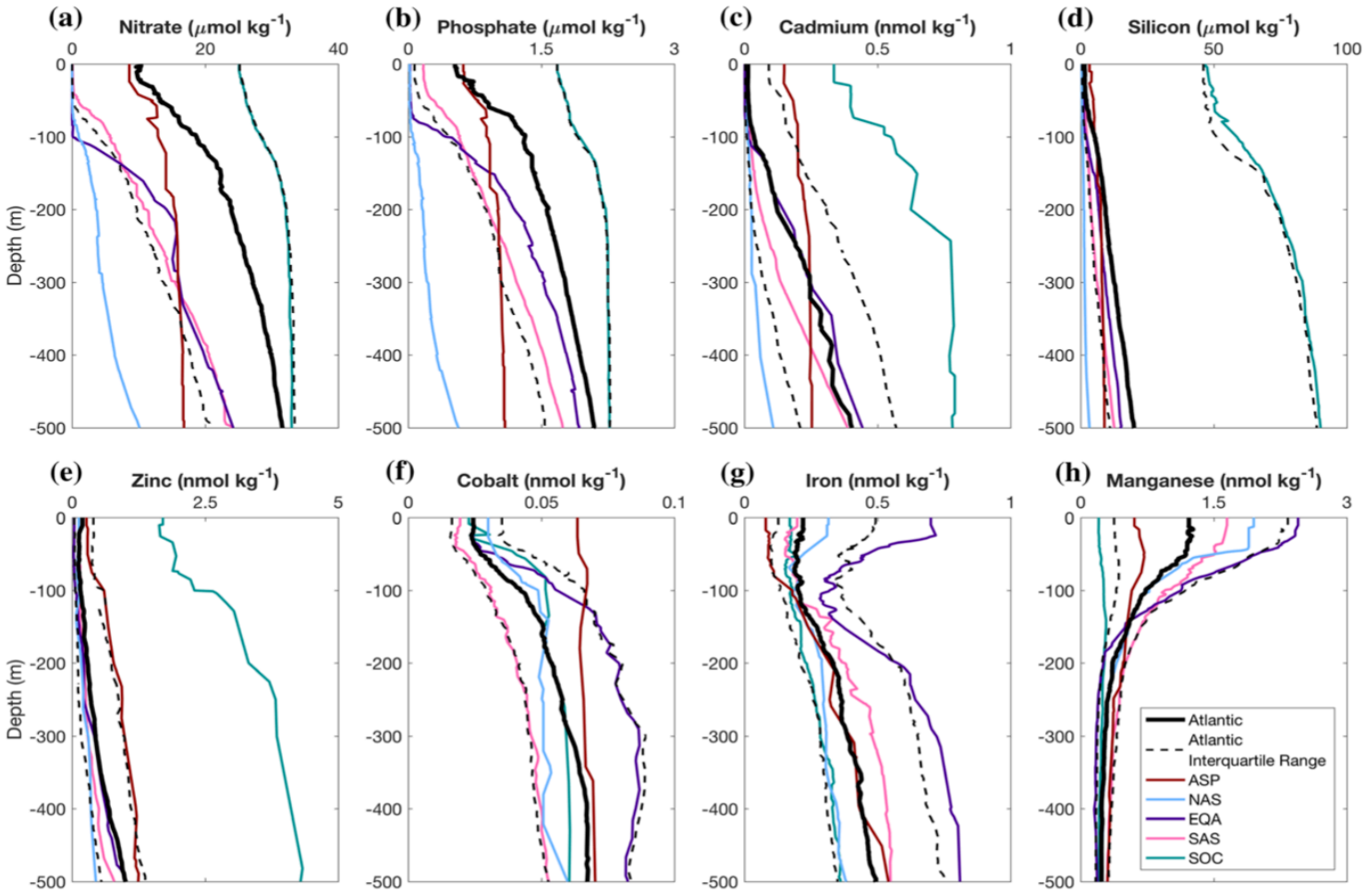

Figure 3.4. Vertical profiles of multiple elements in the Atlantic Ocean, median (black) and lower quartile and upper quartile (dashed black). Separated into biogeochemical provinces: Atlantic sub-polar gyre (ASP), North Atlantic subtropical gyre (NAS), equatorial Atlantic (EQA), South Atlantic subtropical gyre (SAS), and the Southern Ocean (SOC). Interquartile range for each nutrient in each province is provided in Figure 3.5. Data from the 2017 GEOTRACES Intermediate Data Product (Schlitzer et al., 2018).

resource N (mol m^{-3}) in month t and Λ is the Heaviside function as defined by Kraus and Turner (1967), where

$$\Lambda \equiv \Lambda\left(\frac{dH}{dt}\right) = \begin{matrix} 1 \\ 0 \end{matrix} for \ \frac{dH}{dt} \gtrless 0 \tag{3}$$

Entrainment occurs when the mixed layer deepens, such as in winter or due to enhanced convection in other seasons (e.g., storms in summer).

3.4 Results

3.4.1 Upper Ocean Resource Profiles

The vertical profile of a given resource reflects the resource availability throughout the water column (Figures 3.4 and 3.5). Any differences between the vertical profiles of individual resources may be caused by differences in their associated biogeochemical cycles. Further, there is a spatial variability in the vertical pro- files of a single resource due to regional variations in the underlying processes.

3.4.1.1 Nutrient Type Profiles

Nutrient-type resources, such as NO_3, PO_4, Si, Cd, and Zn display a consistent depletion at the surface due to biological uptake, which is accompanied by increasing concentrations with depth due to either the resupply from the remineralization of sinking particles (Tagliabue, 2019) or the transport of nutrient-rich deep water which has received particles upstream (Middag et al., 2018, Middag et al., 2019).

NO_3 and PO_4 display a nutrient-type profile throughout the Atlantic as concentrations increase with depth in all provinces (Figures 3.4a and 3.4b) (Rijkenberg et al., 2014, Tuerena et al., 2015). The Atlantic Ocean median surface NO_3 and PO_4 concentrations are 12 and 0.6 μmol kg^{-1}, increasing to 28 and 2 μmol kg^{-1}, respectively, at a depth of 500 m (Figure 3.4a). There is complete surface depletion in the North Atlantic subtropical gyre, equatorial Atlantic, and South Atlantic gyre, where NO_3 concentrations are below detection limits. However, in the Atlantic subpolar gyre and Southern Ocean, surface NO_3 stocks are not fully exhausted. The Atlantic lower quartile is near zero at the surface, meaning at least 25% of the Atlantic surface

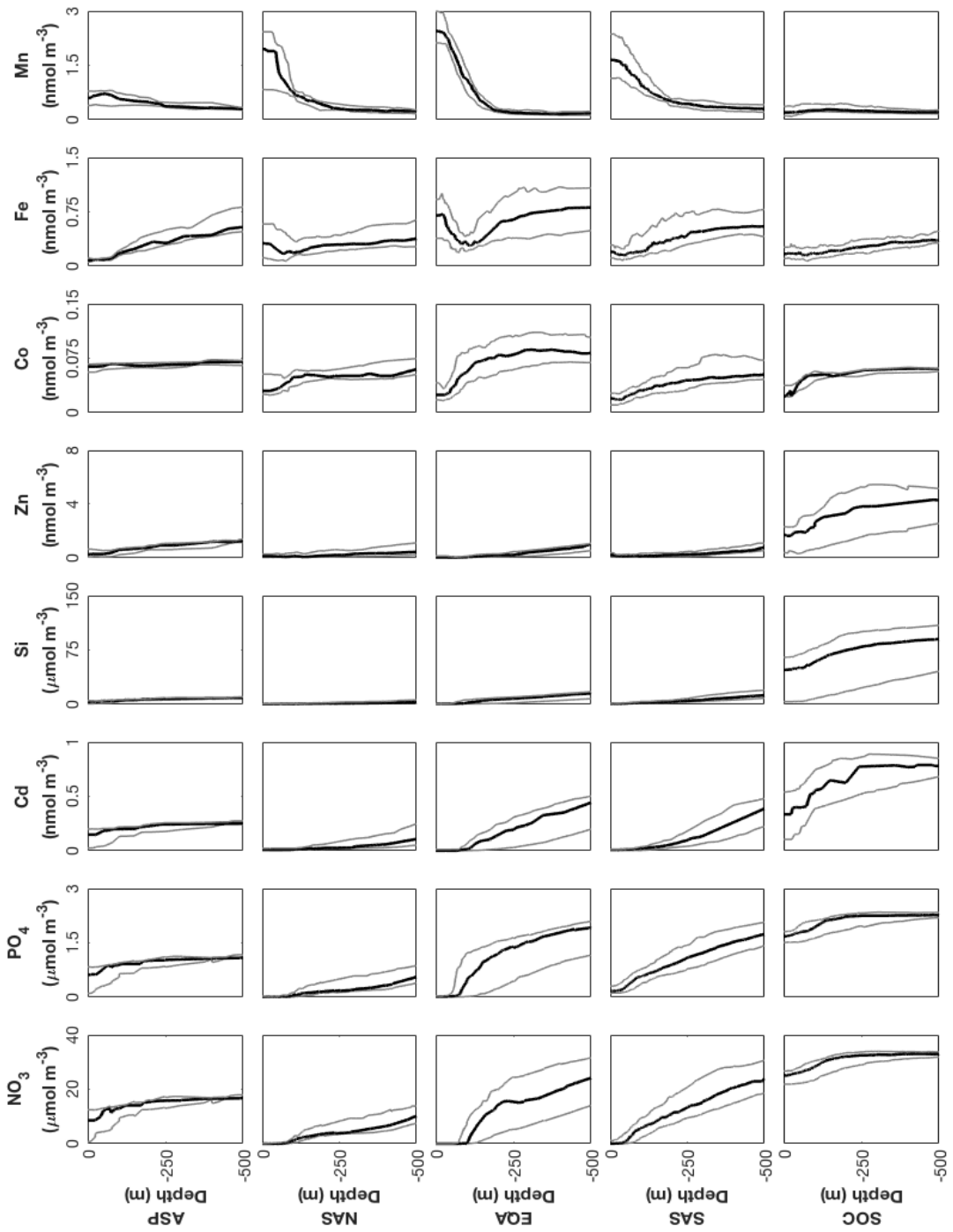

Figure 3.5. Vertical profiles of multiple elements in the Atlantic Ocean, median (black) and lower quartile and upper quartile (grey). Separated into biogeochemical provinces: Atlantic sub-polar gyre (ASP), North Atlantic subtropical gyre (NAS), equatorial Atlantic (EQA), South Atlantic subtropical gyre (SAS) and the Southern Ocean (SOC). Data from the 2017 GEOTRACES Intermediate Data Product (Schlitzer et al., 2018).

observations are deplete in NO_3. The depth at which NO_3 concentrations increase ranges from around 40 m in the North Atlantic subtropical gyre to around 100 m in the equatorial Atlantic. Although many of these features are similar for PO_4, there are some key differences in their distributions (Figure 3.4b). For instance, the Atlantic lower-quartile PO_4 concentration remains greater than zero throughout the water column, meaning less than 25% of observations are deplete in PO_4. Further, in the equatorial Atlantic, the depth at which concentrations increase is around 25 m shallower for PO_4 than NO_3.

The distribution of Cd is similar to that of macronutrients NO_3 and PO_4 (Figure 3.4c) (Boye et al., 2012, Conway and John, 2015, Middag et al., 2019). Cd increases from near zero values in the surface to appreciable concentrations at 500 m, typical of a nutrient-type profile. In the low latitude provinces, Cd concentrations are depleted from the surface to ~100 m depth. Similar to NO_3 and PO_4, the median surface ocean concentration of Cd is only greater than zero in the high latitude provinces, where surface stocks are not fully exhausted. The accumulation of Cd in low latitudes tends to occur deeper in the water column than that of NO_3 and PO_4. The increase in Cd concentration at depth is largest in the equatorial Atlantic and weakest in the North Atlantic subtropical gyre. The greatest Cd concentrations are located in the Southern Ocean, which are approximately one order of magnitude larger than those in the North Atlantic subtropical gyre where the lowest Cd concentrations are found. In high latitudes, the vertical structure of Cd shows little variation between 250 and 500 m compared to the mid-low latitude provinces. Trace element resources exhibiting nutrient-type profiles have long residence times compared to hybrid and scavenged type resources (Bruland and Lohan, 2003). Cd has the longest residence time, ~500,000 years, of trace elements included in this study (Hem, 1985).

The vertical profile of Si also follows a nutrient-type profile (Figure 3.4d) (Conway and John, 2014, Middag et al., 2019). The Atlantic median Si profile increases from near zero in the surface to 18 μmol kg^{-1} at 500 m depth. Si concentrations are below detection limits in the South Atlantic subtropical gyre and equatorial Atlantic. Surface depletion of Si occurs in all provinces as surface concentrations are lower than those at depth. The lowest water column Si concentrations are located at the surface in the North Atlantic subtropical gyre, where Si concentrations show the weakest vertical

increase. The largest increase in Si from the surface to 500 m occurs in the equatorial Atlantic, due to the influence of Si-rich waters laterally transported from the Southern Ocean (Sarmiento et al., 2004). Si concentrations are an order of magnitude higher in the Southern Ocean than any other province. Si accumulates deeper in the water column than NO_3 and PO_4 due to the noted longer regeneration length scale of Si (Holzer et al., 2014) and has a residence time of 8,000 years (Hem, 1985).

The broad distribution of Zn is known to be similar to Si, with both exhibiting a nutrient-type profile (Figure 3.4e) (Conway and John, 2014, Croot et al., 2011, Wyatt et al., 2014). In general, Zn stocks are depleted in the upper waters relative to those at depth and then increase to 500 m depth, with the largest Zn concentrations at each depth level found in the Southern Ocean. There is little increase in either Si or Zn concentrations vertically due to the large remineralization length scale of Si which releases Si into deep waters and reversible scavenging of Zn which transfers remineralized Zn from intermediate depths to deep waters (Bruland, 1980, Weber et al., 2018). There are some differences in the vertical profiles of Si and Zn, with subsurface minima in Zn profiles (e.g., in the tropics) and a smaller increase in Zn with depth than Si in the Atlantic subpolar gyre. The residence time of Zn, ~180,000 years (Hem, 1985) is less than that of Cd, meaning the recycling of Zn is faster than Cd.

3.4.1.2 Hybrid and Scavenged Profiles

Hybrid resources, such as Fe and Co, display a combination of both nutrient-type and scavenged-type characteristics (Tagliabue, 2019). Hybrid profiles are typically depleted at the surface due to biological uptake and concentrations increase with depth due to remineralization before decreasing again as scavenging becomes dominant. Scavenged-type resources, such as Mn, exhibit a surface maxima, usually due to resource inputs, followed by an exponential decline with depth due to scavenging onto sinking particles.

Co displays a hybrid profile throughout the Atlantic, exhibiting a nutrient-type profile above ~500 m and scavenged-type profile deeper in the water column (Noble et al., 2012, Dulaquais et al., 2014). The Atlantic median Co profile shows concentrations are low in the upper 20 m and increase with depth over the upper 500 m, indicative of

a nutrient-type profile (Figure 3.4f). Incomplete surface depletion of Co (relative to 100 – 500 m) occurs in each province, excluding the Atlantic subpolar gyre. In the Atlantic subpolar gyre, Co shows little variation with depth compared to other provinces. The highest Co concentrations are located in the equatorial Atlantic at a subsurface maxima (0.08 nmol kg^{-1}) at 300 m. The vertical profile of Co in the South Atlantic gyre displays a decrease in Co concentration to a subsurface minima at 40 m. The cycling of Co in the ocean is quicker than that of Cd and Zn, typical Co residence times are ~18,000 years (Hem, 1985). Overall, there is little large-scale spatial variability in the vertical distribution of Co as median Co concentrations reported for each individual province fall between the full Atlantic interquartile range (excluding the upper 100 m in the Atlantic subpolar gyre).

Fe shows a mix of both scavenged-type and nutrient-type behaviour in different regions (Figure 3.4g) (Klunder et al., 2011, Rijkenberg et al., 2014, Hatta et al., 2015). There is a surface depletion of Fe in the Atlantic subpolar gyre and Southern Ocean, likely due to biological consumption and the lack of dust input at the air-sea interface. Conversely, in the North Atlantic subtropical gyre, equatorial Atlantic and South Atlantic gyre, the surface ocean is moderately enriched in Fe. Surface maxima due to dust inputs (Shelley et al., 2018) and subsurface minima in response to consumption at the subsurface chlorophyll maximum (Twining et al., 2015) are present in the North Atlantic subtropical gyre and equatorial Atlantic, indicative of a scavenged-type resource. However, below 100 m, Fe expresses consistent nutrient-type behaviour in all provinces as concentrations increase due to the remineralization of sinking particles. The residence time of Fe, ~140 years (Hem, 1985), is the shortest of trace elements included in this study, highlighting the rapid cycling of Fe within the ocean interior.

Mn shows a generally scavenged profile (Figure 3.4h), with a clear surface enrichment in all provinces, excluding the Southern Ocean (Middag et al., 2011, Boye et al., 2012, Noble et al., 2012). The median vertical profile of Mn decreases from surface maxima to a consistent lower level of around 0.2 nmol kg^{-1} at 500 m. Elevated surface stocks are most apparent in the equatorial Atlantic. Across the low latitude regions, dust inputs and the photochemical reduction of manganese oxides to soluble dissolved Mn (II) causes elevated surface concentrations which then decrease vertically (Jickells et

al., 2005, van Hulten et al., 2017, Shelley et al., 2018). The lowest Mn concentrations are located in the Southern Ocean, where the Mn concentration remains relatively uniform over the upper 500 m. Finally, Mn residence times in the ocean interior are ~1,400 years (Hem, 1985), demonstrating that the cycling of Mn is slower than that of Fe, however is notably faster than that of nutrient-type trace elements Cd and Zn.

3.4.2 Vertical Position of Nutriclines

In the following, we focus on the western Atlantic *GEOTRACES* section (GA02, Figure 3.1) to examine how nutricline depths vary as a function of latitude across different resources (Figure 3.6). Detailed maps of nutricline depths and offsets between the nutricline depth and winter mixed-layer depth are referred to below and available in Figures 3.7, 3.8, and 3.9.

There is a clear latitudinal structure in the depth of the nitracline, phosphocline, and Cd-nutricline along the GA02 meridional section (Figure 3.6a). For each resource, the nutricline undulates systematically between the poles and the equator, being deepest in the subtropical gyres and shallowest in the Southern Ocean, North Atlantic and Equatorial Atlantic. The deepening of nutriclines in the subtropical gyres is particularly pronounced for Cd, which can be twice as deep as NO_3 and PO_4, while the phosphocline is deeper than the nitracline only in the low PO_4 North Atlantic subtropical gyre. It is only south of 40°S and north of 40°N that the winter mixed-layer depth is deeper than all three nutriclines, indicating high mixed-layer stocks and a large potential for entrainment inputs.

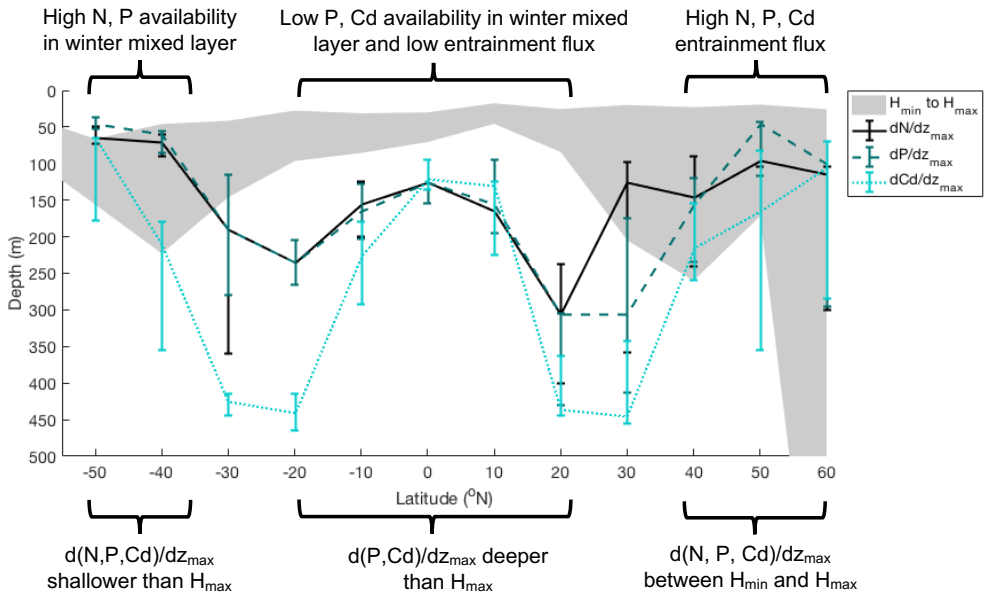
High N, P availability in winter mixed layer
Low P, Cd availability in winter mixed layer and low entrainment flux
High N, P, Cd entrainment flux
Depth (m)
Latitude (°N)
H_min to H_max
dN/dz_max
dP/dz_max
dCd/dz_max
d(N,P,Cd)/dz_max shallower than H_max
d(P,Cd)/dz_max deeper than H_max
d(N, P, Cd)/dz_max between H_min and H_max

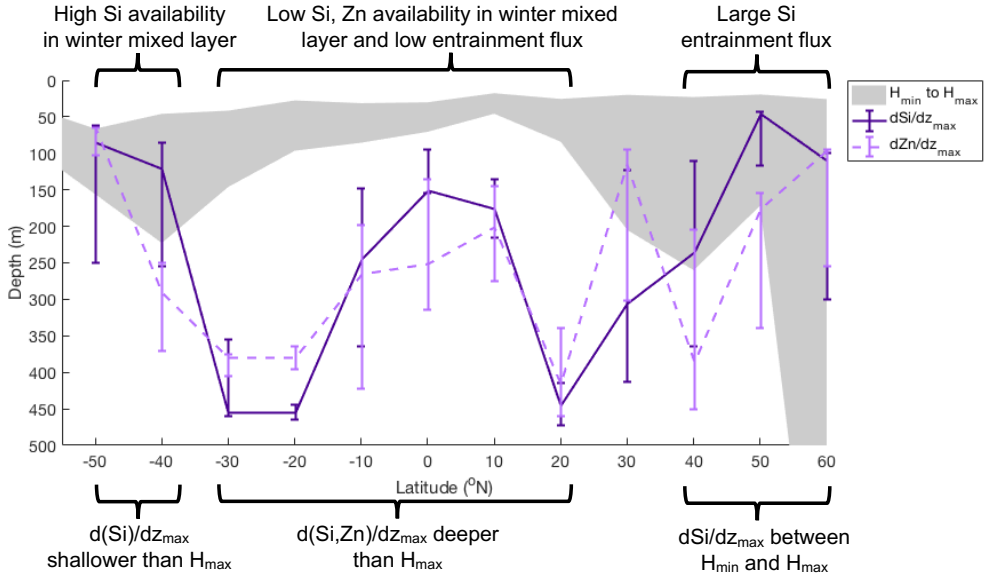
High Si availability in winter mixed layer
Low Si, Zn availability in winter mixed layer and low entrainment flux
Large Si entrainment flux
Depth (m)
Latitude (°N)
H_min to H_max
dSi/dz_max
dZn/dz_max
d(Si)/dz_max shallower than H_max
d(Si,Zn)/dz_max deeper than H_max
dSi/dz_max between H_min and H_max

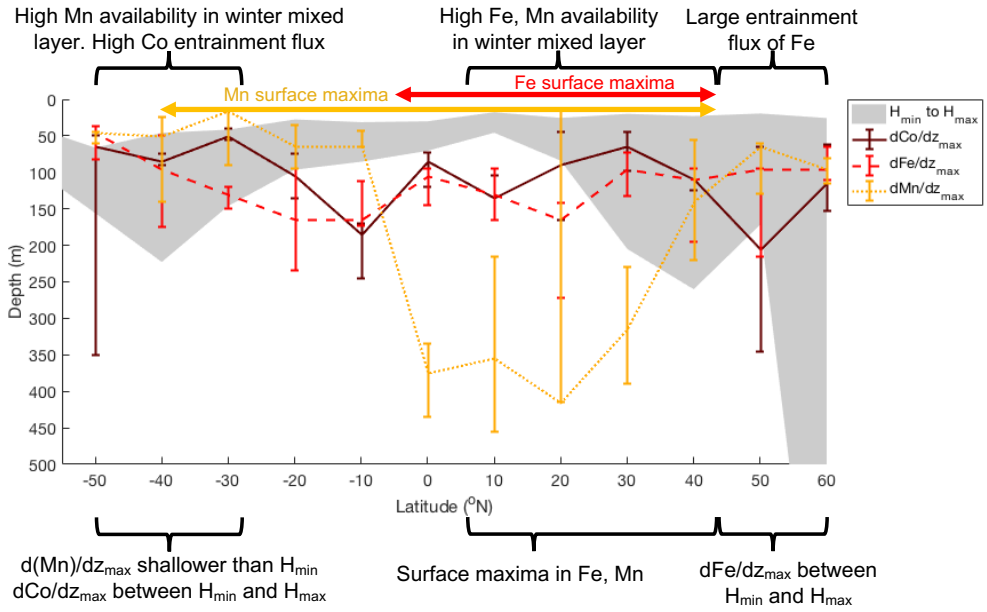
High Mn availability in winter mixed layer. High Co entrainment flux
High Fe, Mn availability in winter mixed layer
Large entrainment flux of Fe
Mn surface maxima
Fe surface maxima
Depth (m)
Latitude (°N)
H_min to H_max
dCo/dz_max
dFe/dz_max
dMn/dz_max
d(Mn)/dz_max shallower than H_min
dCo/dz_max between H_min and H_max
Surface maxima in Fe, Mn
dFe/dz_max between H_min and H_max

Figure 3.6. Depths of the (a) nitracline (dN/dz_{max}, black solid line), phosphocline (dP/dz_{max}, dark green dashed line), Cd-nutricline (dCd/dz_{max}, turquoise dotted line); (b) Si-nutricline (dSi/dz_{max}, purple solid line), Zn-nutricline (dZn/dz_{max}, pink dashed line) and (c) Co-nutricline (dCo/dz_{max}, maroon solid line), ferricline (dFe/dz_{max}, dashed red line) and Mn-nutricline (dMn/dz_{max}, yellow dotted line). Shaded region is the depth over which water is entrained into the mixed layer from the minimum mixed-layer thickness, H_{min}, to the maximum mixed-layer thickness in winter, H_{max}. Nutricline depths, H_{min} and H_{max} are 10° zonal median values from Atlantic Ocean observations. Physical model data from ECCOv4r3 (Forget et al., 2015; Fukumori et al., 2017). Errorbars represent upper and lower quartile nutricline depths in each 10° zonal limit. Biogeochemical data from the western Atlantic (GA02) GEOTRACES cruise, (indicated in Figure 1) available in the 2017 GEOTRACES Intermediate Data Product (Schlitzer et al., 2018).

The Si- and Zn-nutriclines show a similar large-scale pattern to the nitracline and phosphocline along GA02 (Figure 3.6b). However, the latitudinal undulations in the Si and Zn nutriclines are around two-fold more pronounced, likely due to the noted longer remineralization length scale of Si and transfer of remineralized Zn to deep waters by reversible scavenging (Holzer et al., 2014; Weber et al., 2018). The Si- and Zn-nutriclines are deeper than the winter mixed-layer depth from 30°S to 30°N, indicating low mixed-layer stocks and small entrainment inputs in this latitude band, while the Zn-nutricline is only shallower than the winter mixed-layer depth in high latitudes and at 30°N. As a consequence, the winter-mixed layer is replete in both Si and Zn at high latitudes only.

The latitudinal structures of the Co-nutricline, ferricline, and Mn-nutricline are notably different to those of nutrient-type resources (Figure 3.6c). Their large-scale patterns show little variation in the depths of the Co nutricline and ferricline, which do not extend below 200 m. The Mn nutricline does not extend below 200 m in the South Atlantic; however, in the subtropical North Atlantic, the Mn nutricline extends to ~400 m before shoaling towards the subpolar gyre. From 50°S to 30°S and north of

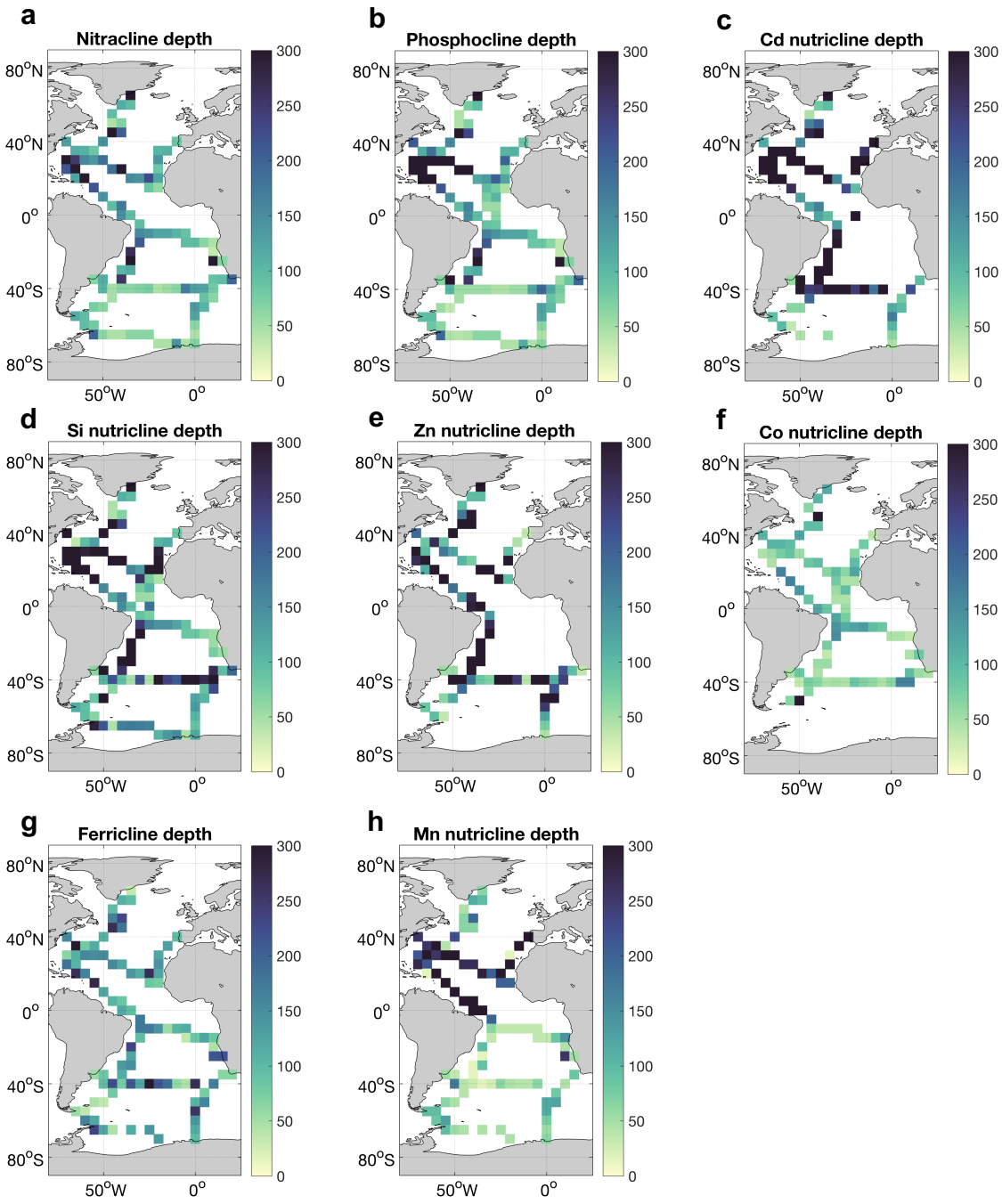

Figure 3.7: Depths (m) of the nutricline ($d[N]/dz_{max}$, where [N] is the concentration of a given resource) for multiple elements. Biogeochemical data from the 2017 GEOTRACES Intermediate data product (Schlitzer et al., 2018).

40°N, each nutricline resides above the winter mixed-layer depth, meaning mixed-layer resource stocks are replenished in winter months. At low latitudes, the nutricline of each resource is deeper than the depth attained by winter mixing, driving low mixed-layer resource stocks of Co, Fe, and Mn. However, surface maxima are present

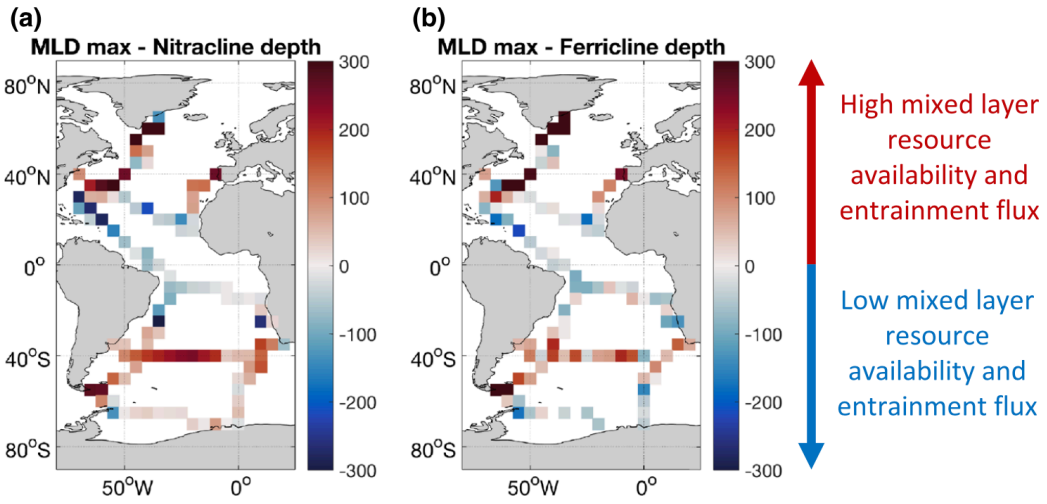

Figure 3.8. Difference (m) between the maximum mixed-layer depth (MLD max) and the nutricline depth (d[N]/dzmax, where [N] is the concentration of a given resource) for (a) nitrate and (b) iron. Biogeochemical data from the 2017 *GEOTRACES* Intermediate data product (Schlitzer et al., 2018), Mixed-layer depth defined by ECCOv4b (Forget et al., 2015; Fukumori et al., 2017).

in the vertical profiles of Fe and Mn causing high mixed-layer Fe and Mn stocks (Figures 3.4g and 3.4h).

The offset between the winter-mixed layer and nutricline depth varies strongly with latitude, evidenced by the meridional *GEOTRACES* transect *GA02* along the western margin (Figures 3.1 and 3.6). However, there are also notable longitudinal variations (Figures 3.7, 3.8 and 3.9). For example, from west to east in the tropical South Atlantic, observations move into the Benguela upwelling zone, which causes the NO_3-, PO_4-, and Si-nutricline to shallow by ~100 m (Figures 3.9a, 3.9b, and 3.9d). Unlike the western side of the basin, the winter mixed-layer nears the NO_3-, PO_4-, and Si- nutriclines within the Benguela upwelling region (Figures 3.8a, 3.9a, and 3.9c). This transition across the tropical South Atlantic is reversed when considering Mn, which has a deeper nutricline within the Benguela upwelling (Figure 3.9f). We find a further transition along 40°S, where the mixed layer penetrates ~250 m deeper than the NO_3-, PO_4-, Co-, and Mn-nutriclines in the open ocean. However, the offset is reduced to ~50 m towards coastal regions (Figures 3.8a, 3.9a, 3.9e, and 3.9f).

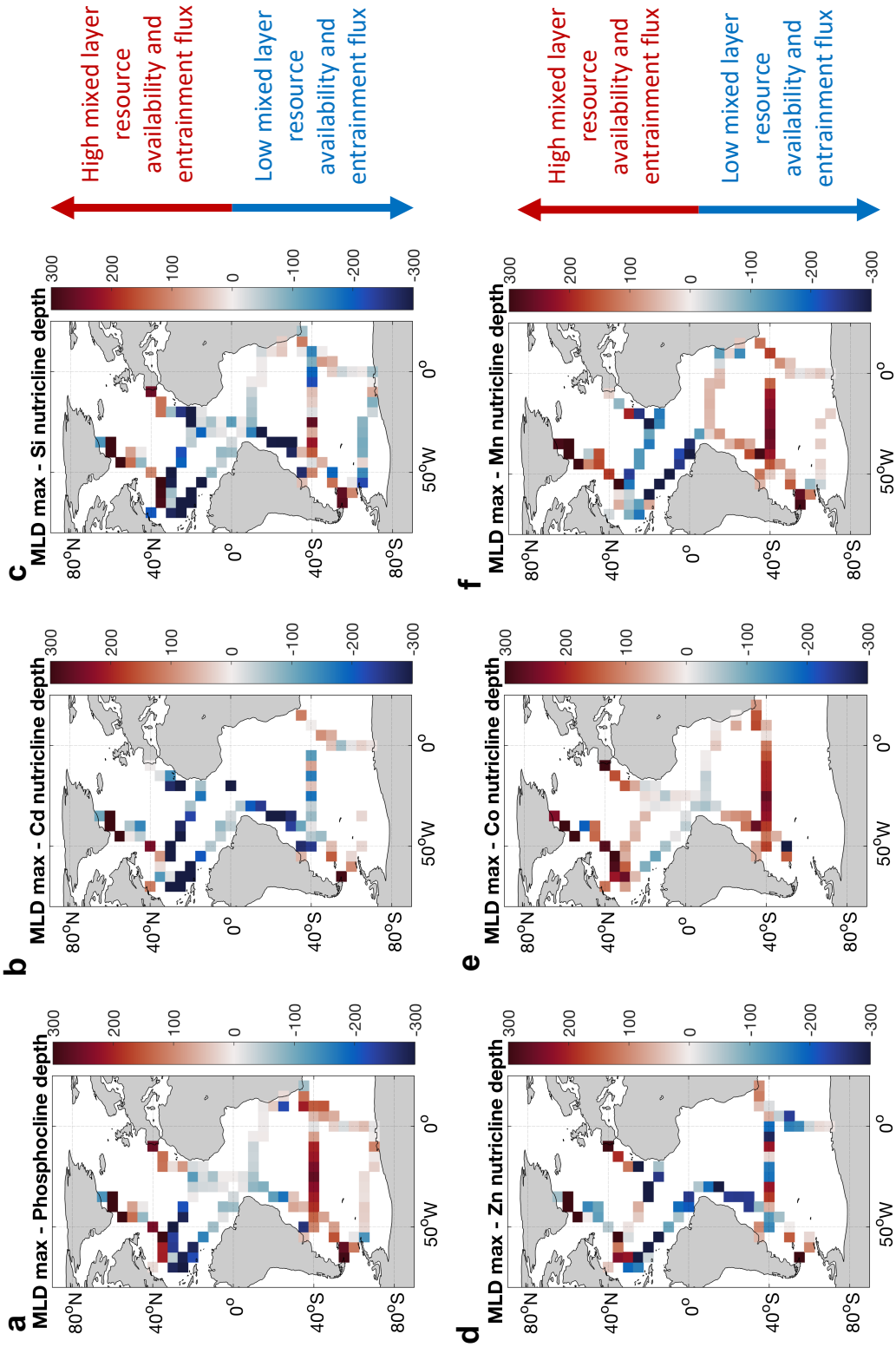

Figure 3.9: Difference (m) between the maximum mixed-layer depth (MLD max) and the nutricline depth ($d[N]/dz_{max}$, where [N] is the concentration of a given resource) for multiple elements. Biogeochemical data from the 2017 *GEOTRACES* Intermediate data product (Schlitzer et al., 2018), Mixed-layer depth defined by ECCOv4b (Forget et al., 2015, Fukumori et al., 2017).

In contrast, longitudinal changes in the nutricline depth and offsets with the mixed-layer depth are less apparent in the subtropical North Atlantic. In the Southern Ocean, south of 50°S, the ferricline resides below the winter mixed-layer depth, meaning that there is low Fe in the mixed layer and little Fe input from winter-time mixing (Figure 3.8b). The general pattern in the ferricline depth shows relatively little spatial structure in absolute depth (Figure 3.7g), but is known to be well structured in an isopycnal context (Tagliabue et al., 2014).

3.4.3 Mixed-Layer Resource Availability

The winter mixed-layer depth varies throughout the Atlantic Ocean, from up to ~1,000 m at high latitudes to ~30 m in the subtropical South Atlantic (Figure 3.1). The winter mixed-layer depth coupled with the vertical distributions of each resource governs the basin-scale patterns in resource availability (Figure 3.10). Due to the challenges presented by ocean sampling during winter, particularly in the harsh Southern Ocean, observations of resource concentrations contemporaneous with the winter mixed-layer depth are not often available. Observed resource profiles are projected to the time of the deepest mixed layer by assuming there is no loss to below the winter mixed layer. Biological uptake and subsequent remineralization effectively redistribute resources within the winter mixed layer; however, the integrated stock of a given resource in the winter mixed layer remains unchanged. The patterns we describe here are robust when resource stoichiometry is recalculated relative to NO_3 instead of PO_4 (Figure 3.11).

3.4.3.1 NO_3/PO_4 and Cd/PO_4

Generally, the availability of NO_3, relative to PO_4, is high in subpolar regions and lowest in the tropics, with enhanced NO_3 levels relative to PO_4 in upwelling regions (Figure 3.10a). The principle driver in the latitudinal structure observed is the relationship between the nitracline, phosphocline, and the winter mixed-layer depth (Figures 3.6a, 3.8a, and 3.9a). For instance, in the North Atlantic subpolar gyre, the deep mixed layers are able to access large subsurface NO_3 and PO_4 stocks resulting in substantial reserves of the two macronutrients in the mixed layer. In the Southern Ocean and North Atlantic, high standing stocks of NO_3 and PO_4 cause a near Redfield NO_3/PO_4 value (Redfield, 1934), irrespective of the mixed-layer depth. Spatial transitions in NO_3/PO_4 occur as the respective nutriclines shift position in the water

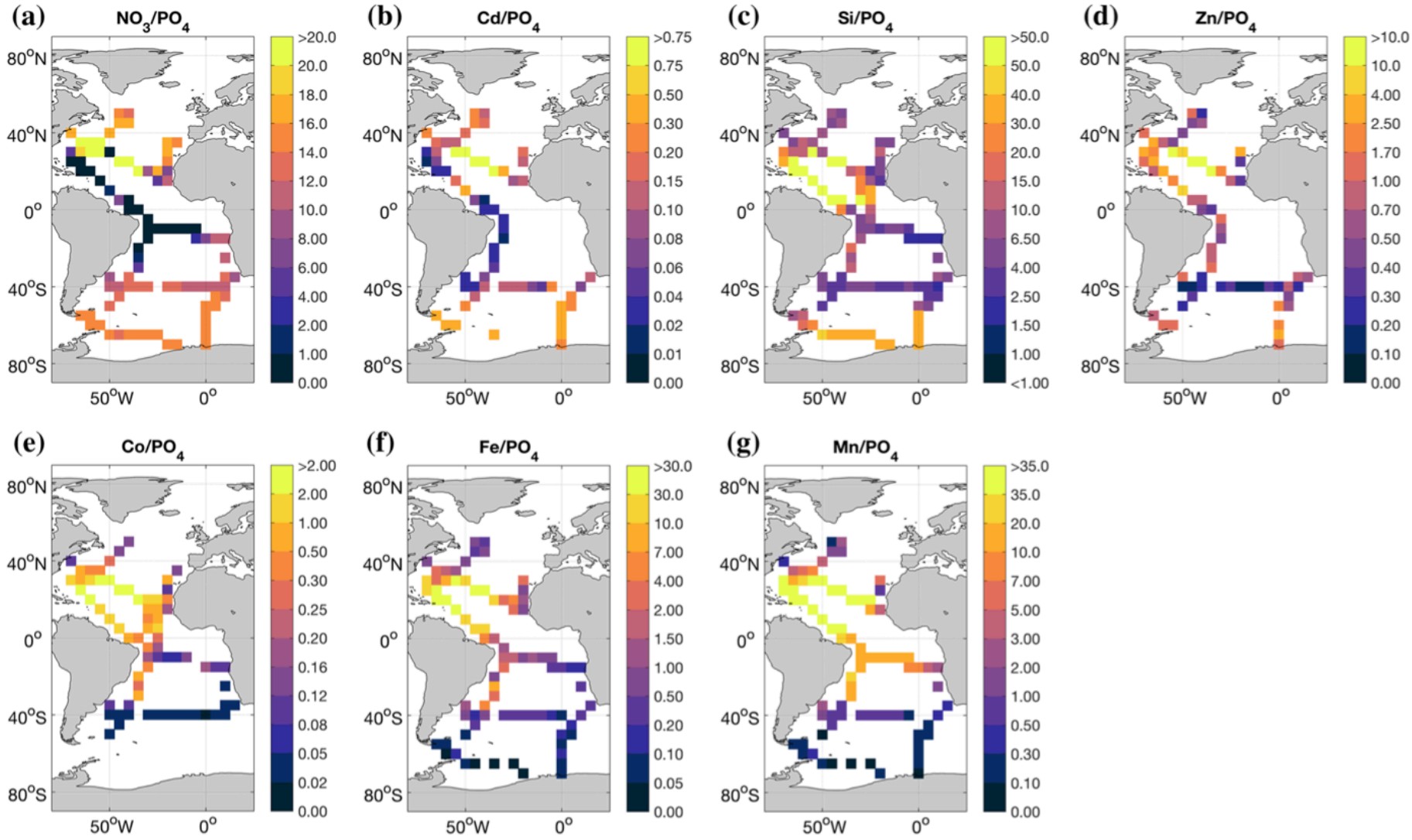
(a)
NO3/PO4
>20.0
20.0
18.0
16.0
14.0
12.0
10.0
8.00
6.00
4.00
2.00
1.00
0.00
(b)
Cd/PO4
>0.75
0.75
0.50
0.30
0.20
0.15
0.10
0.08
0.06
0.04
0.02
0.01
0.00
(c)
Si/PO4
>50.0
50.0
40.0
30.0
20.0
15.0
10.0
6.50
4.00
2.50
1.50
1.00
<1.00
(d)
Zn/PO4
>10.0
10.0
4.00
2.50
1.70
1.00
0.70
0.50
0.40
0.30
0.20
0.10
0.00
(e)
Co/PO4
>2.00
2.00
1.00
0.50
0.30
0.25
0.20
0.16
0.12
0.08
0.05
0.02
0.00
(f)
Fe/PO4
>30.0
30.0
10.0
7.00
4.00
2.00
1.50
1.00
0.50
0.20
0.10
0.05
0.00
(g)
Mn/PO4
>35.0
35.0
20.0
10.0
7.00
5.00
3.00
2.00
1.00
0.50
0.30
0.10
0.00
80°N
40°N
0°
40°S
80°S
50°W
0°

Figure 3.10. Resource ratios of depth integrated profiles obtained from the *GEOTRACES* 2017 IDP (Schlitzer et al., 2018). Ordered by nutrient type to scavenged-type resource (see text). Profiles integrated to the maximum depth reached by the mixed layer over 1 year, as defined by ECCOv4r3 (Forget et al., 2015; Fukumori et al., 2017). (a, c) mol mol^{-1}, (b, e–g) mmol mol^{-1}. Calculations were completed on a profile by profile basis, displayed in 5 × 5 degree bins and median reported.

column relative to the mixed-layer depth, exemplified in the tropical latitudes south of the equator where NO_3/PO_4 is higher in the east (10.9) and lower in the west (0.3; Figures 3.8a, 3.9a, and 3.10a). Cd/PO_4 shows a broadly similar distribution to NO_3/PO_4, driven by similarities in their vertical profiles (Figures 3.4a and 3.4c).

3.4.3.2 Si/PO_4 and Zn/PO_4

Si/PO_4 and Zn/PO_4 are broadly comparable to the nutrient-type distribution of NO_3/PO_4, as the Southern Ocean is replete in both Si and Zn and both elements are scarce at low latitudes (Figures 3.10c and 3.10d). Like NO_3/PO_4, elevated Si/PO_4 and Zn/PO_4 conditions found in the Southern Ocean are induced by high Si standing stocks in upper waters which are supplied by the upwelling of nutrient-rich deep waters (Figures 3.4d, 3.4e, 3.9c, and 3.9d). Severe depletion of PO_4 in the subtropical North Atlantic means that both Si/PO_4 and Zn/PO_4 are greatest here, despite low Si and Zn standing stocks compared to the Southern Ocean. The distribution of Zn/PO_4 is similar to that of Si/PO_4 (Figures 3.10d and 3.10e).

3.4.3.3 Co/PO_4, Fe/PO_4, and Mn/PO_4

The large-scale distributions of Co/PO_4, Fe/PO_4, and Mn/PO_4 are different to those resources that have a nutrient-type distribution (Figures 3.10e, 3.10g). High latitudes are depleted in Co, Fe, and Mn relative to PO_4, while low latitudes are at least five-fold more replete in Co, Fe, and Mn. Dust input and low standing stocks of nutrient-like elements drive elevated availability of Co, Fe, and Mn at low latitudes. Co stocks may be enhanced where mixed layers overlay oxygen depleted zones due to the greater residence time of dissolved Co in low oxygen conditions (Hawco et al., 2016)

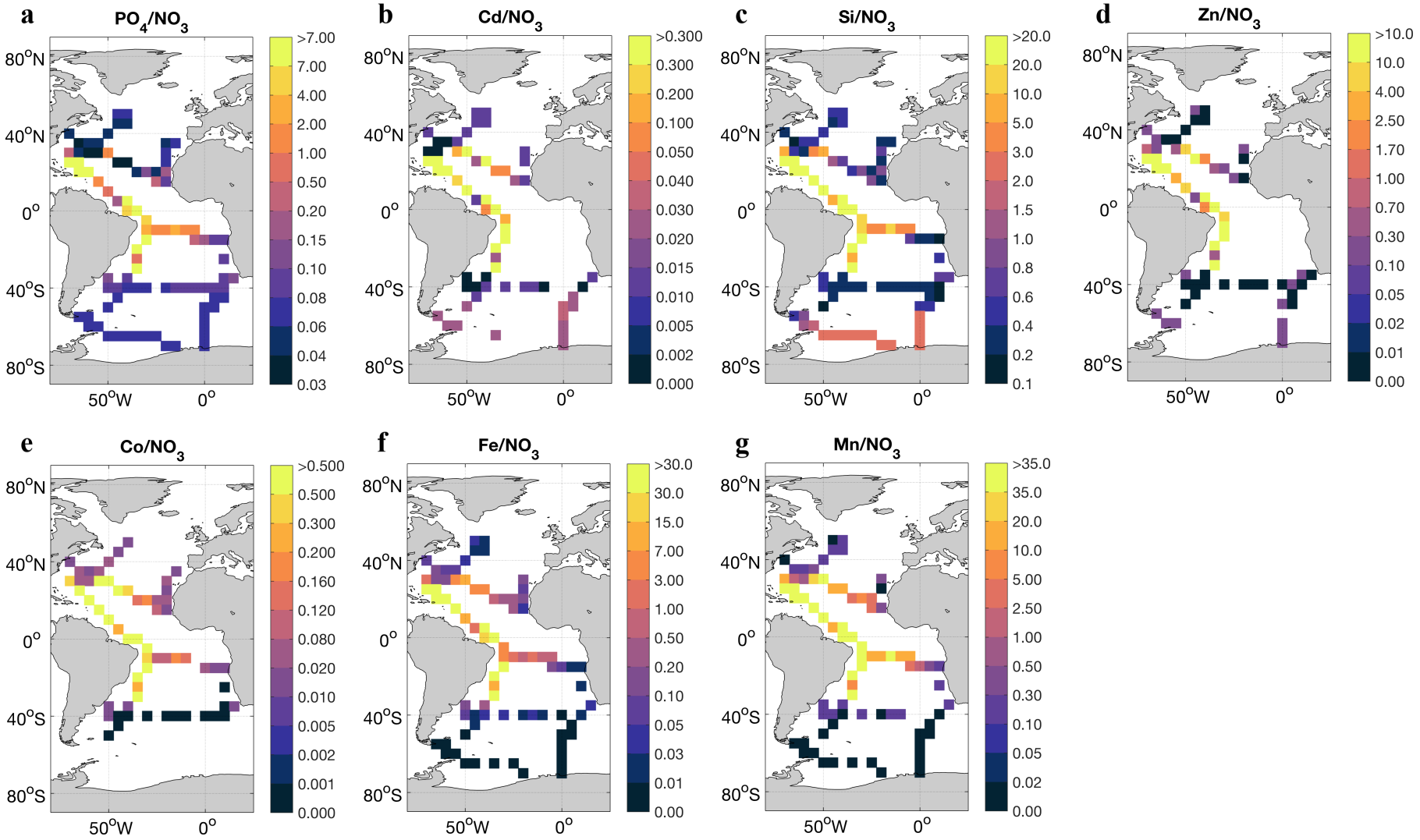
a
PO4/NO3
>7.00
7.00
4.00
2.00
1.00
0.50
0.20
0.15
0.10
0.08
0.06
0.04
0.03
b
Cd/NO3
>0.300
0.300
0.200
0.100
0.050
0.040
0.030
0.020
0.015
0.010
0.005
0.002
0.000
c
Si/NO3
>20.0
20.0
10.0
5.0
3.0
2.0
1.5
1.0
0.8
0.6
0.4
0.2
0.1
d
Zn/NO3
>10.0
10.0
4.00
2.50
1.70
1.00
0.70
0.30
0.10
0.05
0.02
0.01
0.00
e
Co/NO3
>0.500
0.500
0.300
0.200
0.160
0.120
0.080
0.020
0.010
0.005
0.002
0.001
0.000
f
Fe/NO3
>30.0
30.0
15.0
7.00
3.00
1.00
0.50
0.20
0.10
0.05
0.03
0.01
0.00
g
Mn/NO3
>35.0
35.0
20.0
10.0
5.00
2.50
1.00
0.50
0.30
0.10
0.05
0.02
0.00
80°N
40°N
0°
40°S
80°S
50°W
0°

Figure 3.11. Elemental stoichiometry of depth integrated resource profiles obtained from the *GEOTRACES* 2017 IDP (Schlitzer et al., 2018). Profiles integrated to the maximum depth reached by the mixed layer over one year, as defined by ECCOv4b (Forget et al., 2015, Fukumori et al., 2017). (a, c) mol mol^{-1}, (b, d-g) mmol mol^{-1}. Calculations were completed on a profile by profile basis, placed in 5 x 5 degree bins and median reported above.

(Tagliabue et al., 2018). In the Southern Ocean, subsurface Fe stocks are deeper than winter mixing levels (Tagliabue et al., 2014), which results in low mixed-layer Fe/PO_4 (Figures 3.6b and 3.10f). In contrast, upper mixed layers are richer in Fe in the North Atlantic subtropical gyre (Sedwick et al., 2005), which increases mixed-layer Fe/PO_4 throughout this region (Figure 3.10f). There is an increase in Fe/PO_4 in the western Atlantic around 35°S which is attributed to the offshore export of Fe-rich Brazilian shelf water (Rijkenberg et al., 2014).

Finally, mixed-layer Mn/PO_4 is relatively high throughout the tropics due to both the drawdown of PO_4 and enhanced mixed-layer Mn levels arising from dust input and maintenance of surface dissolved Mn by photoreduction (Figure 3.10g) (Sunda et al., 1983, Jickells et al., 2005, Mahowald et al., 2005). The Mn/PO_4 ratio also decreases towards polar regions, and as this element is also elevated in low oxygen waters, it tends to exhibit an increasing availability in mixed layers overlying the western oxygen depleted zones (Figure 3.10g).

3.4.3.4 Ranking the Availability of Nutrient-Type and Scavenged-Type Resources

The variability in vertical profiles discussed in sections 3.1 and 3.2 generates a progressive transition from nutrient-type to scavenged-type profiles, which varies between resources. We use a correlation approach to rank each resource between two end-member resources: nutrient-type nitrate and scavenged-type manganese. The ranking is performed on the Atlantic integrated resource stocks in the winter mixed layer of each resource relative to phosphate, as phosphate is a well sampled macronutrient that avoids interactions with the nitrogen cycle (Figure 3.10). We then rank resource on a continuum between NO_3/PO_4 and Mn/PO_4, (Series [1], Table S3.1).

	NO_3/PO_4	Mn/PO_4	Difference
NO_3/PO_4	1	-0.45	1.45
Cd/PO_4	0.58	-0.36	0.94
Si/PO_4	0.22	0.12	0.10
Zn/PO_4	-0.03	0.44	-0.47
Co/PO_4	-0.11	0.90	-1.01
Fe/PO_4	-0.34	0.92	-1.26
Mn/PO_4	-0.45	1	-1.45

Table 3.1. Correlation of mixed layer integrated resource balances with end-member balances NO_3/PO_4 and Mn/PO_4. Computed as Spearman's rho using each profile where data is available. The difference between both correlations was used to rank resources from nutrient type to scavenged type.

$$(Nutrient\ type) \quad \frac{NO_3}{PO_4} : \frac{Cd}{PO_4} : \frac{Si}{PO_4} : \frac{Zn}{PO_4} : \frac{Co}{PO_4} : \frac{Fe}{PO_4} : \frac{Mn}{PO_4} \quad (Scavenged\ type) \text{ [1]}$$

The ranking in Series [1] reveals Cd/PO_4 is most comparable to NO_3/PO_4 for the full Atlantic data set, likely due to the noted similarities in the biogeochemical cycling of Cd and NO_3 (Bruland, 1980). Next in the series is Si/PO_4 and Zn/PO_4. The input of Si and Zn to the upper ocean from atmospheric deposition and rivers is analogous; further, both undergo remineralization deep in the water column and hence dis- play comparable profiles (Bruland, 1980). Si and Zn are likely decoupled in Series [1] as reversible scavenging influences Zn only (Weber et al., 2018). Finally, Co/PO_4 and Fe/PO_4 are most similar to Mn/PO_4. Dust is a major input of Co, Fe, and Mn (Jickells et al., 2016) causing elevated surface concentrations akin to scavenged-type profiles; however, the trace elements are differentially sensitive to oxygen causing variations in the associated vertical profiles (Rijkenberg et al., 2012, van Hulten et al., 2017, Tagliabue et al., 2018).

The combination of (i) marked variability in the vertical profiles of different resources, (ii) resource-specific nutricline depths, and (iii) regional variations in the depth of winter mixing drives substantial variability in resource availability for marine microbes created across the Atlantic Ocean. This variability arises from the transition of different resources from exhibiting nutrient-like to scavenged-type variability and leads to the high latitudes being relatively replete in the nutrient-like elements NO_3, PO_4, Cd, Si, and Zn, and the low latitudes being relatively replete in Co, Fe, and Mn.

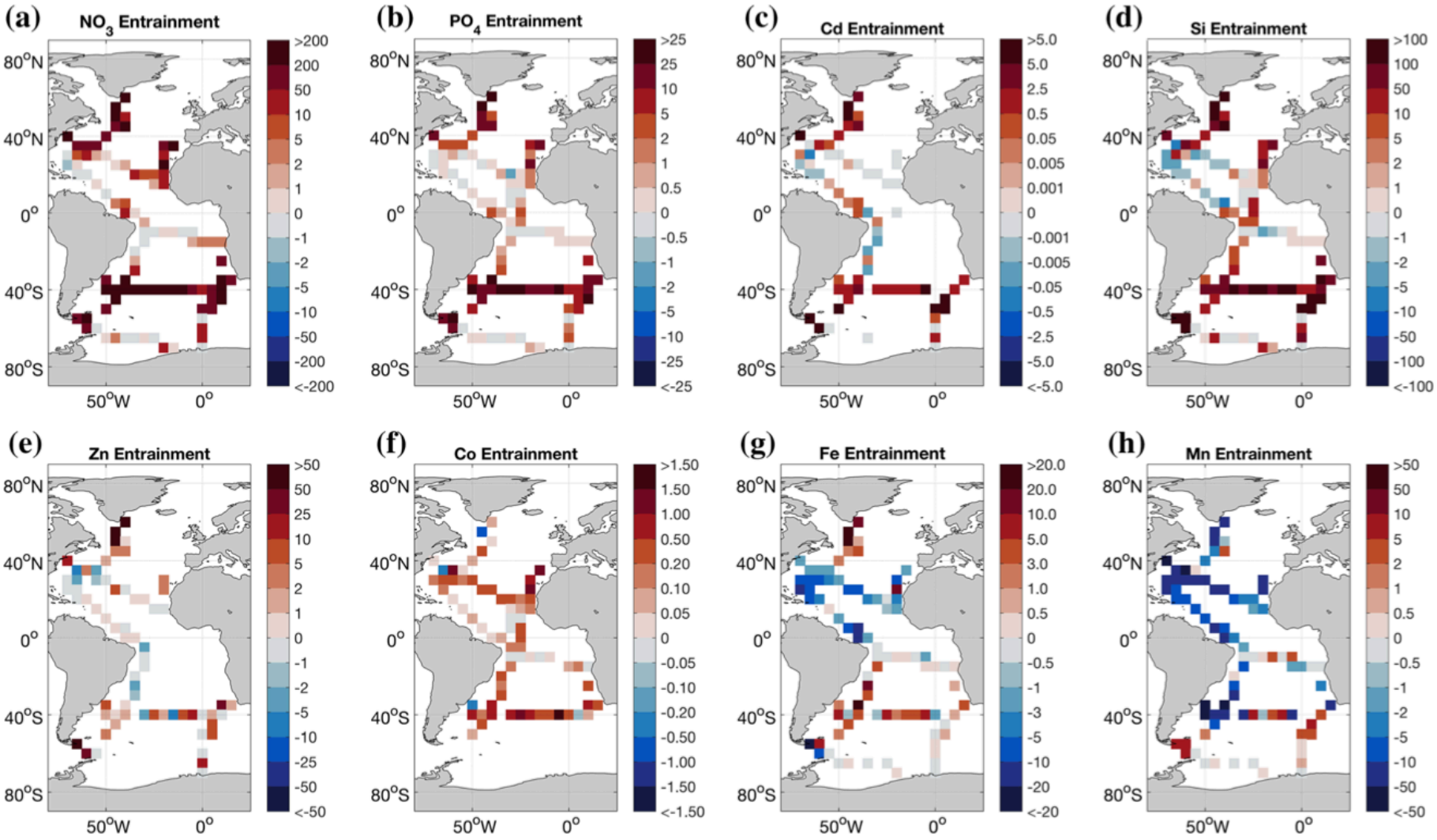
(a)
NO3 Entrainment
>200
200
50
10
5
2
1
0
-1
-2
-5
-10
-50
-200
<-200
(b)
PO4 Entrainment
>25
25
10
5
2
1
0.5
0
-0.5
-1
-2
-5
-10
-25
<-25
(c)
Cd Entrainment
>5.0
5.0
2.5
0.5
0.05
0.005
0.001
0
-0.001
-0.005
-0.05
-0.5
-2.5
-5.0
<-5.0
(d)
Si Entrainment
>100
100
50
10
5
2
1
0
-1
-2
-5
-10
-50
-100
<-100
(e)
Zn Entrainment
>50
50
25
10
5
2
1
0
-1
-2
-5
-10
-25
-50
<-50
(f)
Co Entrainment
>1.50
1.50
1.00
0.50
0.20
0.10
0.05
0
-0.05
-0.10
-0.20
-0.50
-1.00
-1.50
<-1.50
(g)
Fe Entrainment
>20.0
20.0
10.0
5.0
3.0
1.0
0.5
0
-0.5
-1
-3
-5
-10
-20
<-20
(h)
Mn Entrainment
>50
50
10
5
2
1
0.5
0
-0.5
-1
-2
-5
-10
-50
<-50
80°N
40°N
0°
40°S
80°S
50°W
0°

Figure 3.12. Entrainment flux of NO_3, PO_4, Si (all mmol m^{-2} $year^{-1}$), Cd, Zn, Fe, Co, and Mn (all μmol m^{-2} $year^{-1}$) to the Atlantic Ocean and Southern Ocean. Physical model data from ECCOv4r3 (Forget et al., 2015; Fukumori et al., 2017). Biogeochemical data from the 2017 *GEOTRACES* intermediate data product (Schlitzer et al., 2018).

3.4.4 Vertical Entrainment of Resources

The vertical profiles of different resources and the covariance of the nutricline and winter mixing depth creates a range of different resource regimes. The vertical profiles of different resources and depth of seasonal mixing are used to calculate the flux of resources into the mixed layer in response to the entrainment of underlying waters. We acknowledge that there are physical supply mechanisms that operate in addition, but contend that the entrainment flux is likely to be predominant in many cases (Williams et al., 2000, Williams and Follows, 2003a, Tagliabue et al., 2014, Achterberg et al., 2018). In this analysis, a positive entrainment flux reflects an increase in mixed-layer resource concentration, while a negative entrainment flux reflects dilution of mixed-layer resource concentration.

3.4.4.1 NO_3, PO_4, and Cd Entrainment

The entrainment of NO_3 and PO_4 into the seasonal mixed layer varies over several orders of magnitude throughout the Atlantic Ocean. The largest NO_3 and PO_4 entrainment flux estimates are located in the North Atlantic subpolar gyre and along 40°S, >200 mmol NO_3 m^{-2} $year^{-1}$ and >100 mmol PO_4 m^{-2} $year^{-1}$ (Figures 3.12a and 3.12b). The diagnosed NO_3 and PO_4 fluxes here result from large property gradients in the vertical and the depth attained by winter mixing which exceeds the nutricline depth (Figures 3.6a, 3.6b, and 3.8a). In subtropical regions, the entrainment fluxes of NO_3 and PO_4 are greatly reduced (Figures 3.12a and 3.12b) as the winter mixing does not access the nitracline (Figures 3.6a and 3.8a). In regions of the high latitude Southern Ocean, the vertical entrainment of macronutrients is low (Figures 3.12a and 3.12b) despite high standing stocks (Figures 3.4a and 3.4b), which is because the vertical gradients of NO_3 and PO_4 are insufficient to drive a large macronutrient flux (Figures 3.4a, 3.4b, 3.12a, and 3.12b). The large-scale pattern in the entrainment flux

of Cd is similar to that of NO_3 and PO_4, with maximum fluxes of >5 μmol m^{-2} $year^{-1}$ in high latitude regions. However, a small negative entrainment flux for Cd of ~ −0.001 to −0.005 μmol m^{-2} $year^{-1}$ occurs in some subtropical regions (Figure 3.12c) where there are slight increases in upper ocean Cd and the Cd nutricline is far deeper than the winter mixed-layer depth (Figure 3.6a).

3.4.4.2 Si and Zn Entrainment

The entrainment of Si is similar to that of other macronutrients NO_3 and PO_4, excluding the subtropical North Atlantic, with maximal values of >100 mmol m^{-2} $year^{-1}$ being widespread (Figure 3.12d). However, in the subtropical North Atlantic, the small subsurface minima in Si drives a small negative entrainment flux of -1 and -2 mmol m^{-2} $year^{-1}$. Here, mixed-layer Si becomes slightly diluted by the entrainment of relatively low Si waters from below. The entrainment of Zn into the mixed layer is largest in the North Atlantic subpolar gyre and around Drake Passage, where deep mixed layers access subsurface Zn stocks and cause entrainment fluxes of >50 μmol m^{-2} $year^{-1}$ (Figure 3.12e). Like Cd, the Zn entrainment flux in the South Atlantic is negative, and both resources display a large offset between their respective nutricline depth and the winter mixed-layer depth (Figure 3.9b and 3.9c). Generally, the entrainment of Zn exhibits the greatest small-scale variability.

3.4.4.3 Co, Fe, and Mn Entrainment

Co exhibits a nutrient-type profile over the depths of seasonal mixing (Figure 3.4f) which drives a positive entrainment flux that reaches >1.5 μmol m^{-2} $year^{-1}$ the subtropical North Atlantic and along 40°S (Figure 3.12f). In the subtropical Atlantic, Co concentrations increase with depth to ~300 m due to underlying low oxygen waters, which elevates subsurface Co stocks and drives entrainment of around 0.5 μmol m^{-2} $year^{-1}$ (Figures 3.4f and 3.12f). Although the seasonal cycle of the mixed layer is large in the North Atlantic subpolar gyre, the vertical profile of Co is relatively uniform causing a very low entrainment flux of Co compared to that of other resources.

The entrainment flux of Fe reaches >10 μmol m^{-2} $year^{-1}$ in the North Atlantic subpolar gyre and along 40°S as winter mixing accesses subsurface Fe stocks (Figures 3.8b and

3.12g). In the Fe-limited Southern Ocean, the entrainment of Fe into the mixed layer is notably lower (~1–5 μmol m^{-2} $year^{-1}$) as the winter mixed-layer depth does reach subsurface iron stocks (Figures 3.8b and 3.12g). Seasonal entrainment acts to erode the mixed-layer Fe stock significantly in the subtropical North Atlantic, with dilution rates of >10 μmol m^{-2} $year^{-1}$ common for this region (Figure 3.12g). Similarly, the scavenged distribution of Mn causes seasonal entrainment to dilute mixed-layer Mn stocks by as much as 10–50 μmol m^{-2} $year^{-1}$ throughout much of the Atlantic (Figure 3.12h). There is a positive Mn entrainment flux of up to 10 nmol m^{-2} $year^{-1}$ in the Southern Ocean due to the combination of muted surface maxima and winter mixing crossing vertical Mn gradients (Figures 3.4h, 3.9f and 3.12h).

3.5 Discussion

3.5.1 Biological Impacts of Variability in Resource Availability

The broad resource availability regimes identified in this study cause the deficiency of multiple resources throughout the Atlantic Ocean mixed layer. Deficiency may eventually lead to limitation as mixed-layer resource stocks become exhausted during phytoplankton growth. For instance, in some regions, the winter mixed-layer NO_3/PO_4 ratio is 8 mol mol^{-1} (e.g., eastern subtropical South Atlantic, Figure 3.10a), which indicates a deficiency in NO_3 relative to PO_4 compared to Redfield 16N:1P (Redfield, 1934). The mixed layer shoals and biological uptake occurs at Redfield N:P, and the NO_3/PO_4 is reduced further as more NO_3 is removed than PO_4 compared to the original conditions. In this case, initial deficiency of NO_3 would lead to growth limitation by NO_3 assuming all other requirements are met. Growth limitation by NO_3 or Fe can be derived by a relationship between relative surface concentrations of NO_3 and Fe (Browning et al., 2017a). If we apply this relationship to our winter mixed-layer resource stocks (rather than simply surface data), we find that 42% of individual locations are singularly limited by Fe, 25% exhibit Fe-N serial limitation, 14% display colimitation, 9% show N-Fe serial limitation, and 11% are singularly limited by N. The high latitude North Atlantic, Southern Ocean, and the Benguela upwelling region display signals of singular Fe limitation, highlighting the potential of Fe to exert a remote influence over low latitude biogeochemistry. There is a small region of singular N-limitation in the North Atlantic subtropical gyre. Fe-N and N-Fe serial

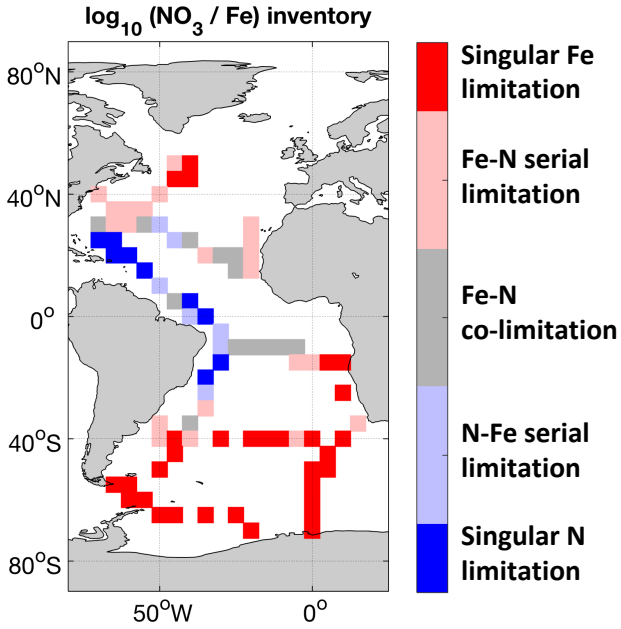

Figure 3.13. $Log_{10}(NO_3/Fe)$ in the maximum annual mixed layer. Following Browning et al. (2017), $log_{10}(NO_3/Fe)$ is used to define limitation categories. Mixed layers are defined by ECCOv4b (Forget et al., 2015, Fukumori et al., 2017), biogeochemical observations from the *GEOTRACES* 2017 IDP (Schlitzer et al., 2018).

limitation, as well as Fe-N colimitation emerge as common features of the low latitude oceans (Figure 3.13). This indicates that variability in mixed-layer resource stocks (driven by vertical profiles and the depth of mixing) has the potential to drive large-scale patterns in nutrient (co) limitation.

Resource availability restricts productivity in the upper mixed layer, and microbial community structure may also be affected (Ward et al., 2013, Saito et al., 2014). For instance, when waters are deplete in NO_3, but replete in PO_4 and Fe, diazotrophs are able to exploit the N limitation of non-N fixing plankton and flourish (LaRoche and Breitbarth, 2005, Sohm et al., 2011, Ward et al., 2013). We find that such conditions arise in the east of the subtropical North Atlantic near the African coast, where NO_3/PO_4 decreases, indicating enhanced PO_4 supply and Fe stocks remain high (Figures 3.10a and 3.10f). This pattern agrees well with the distribution of diazotroph communities in the subtropical North Atlantic gyre (Ratten et al., 2015). Similarly, a database of diazotroph biomass (Luo et al., 2012) indicates high surface levels in the subtropical North Atlantic and between in 22.5°S and 37.5°S the western South

Atlantic, which coincides with regions of low NO_3 and high Fe mixed-layer conditions we identified in this study (Figures 3.10a and 3.10f). The observed west to east transition from nanophytoplankton to picophytoplankton along 40°S (Browning et al., 2014) is coincident with a decline in Fe/PO_4, Zn/PO_4, Mn/PO_4, Cd/PO_4, and Co/PO_4 from west to east (Figure 3.10). New findings of diatoms in the subtropical North Atlantic (Lampe et al., 2019) are in agreement with elevated Si/PO_4 stocks we find in this region (Figure 3.10c). Overall, our results suggest that the broad resource regimes established in the Atlantic Ocean influence marine ecosystems.

While it is possible to link resource availability to the estimates of phytoplankton demand for various resources (e.g., Ho et al., 2003) to derive a "Redfield balance" (Redfield, 1934), doing so would ignore important interactions between trace elements, which dictates the interior physiology of marine phytoplankton (Sunda, 1989). For instance, new evidence suggests Zn and Mn can outcompete Co for a common uptake mechanism when Co is deficient, altering the link between resource availability and cellular accumulation (Hawco and Saito, 2018). In addition, the uptake of P from dissolved organic P at low PO_4 concentrations via alkaline phosphatase can be colimited by Zn and Fe (Shaked et al., 2006, Mahaffey et al., 2014, Browning et al., 2017b). Finally, many organisms adjust their biochemical apparatus under Fe stress, with for example, flavodoxin being produced instead of the Fe-containing ferredoxin (LaRoche et al., 1996) or the Cu-containing plastocyanin replacing the Fe-containing cytochrome b6 (Peers and Price, 2006). Moreover, Co and Zn are interchangeable in the carbon acquisition enzyme carbonic anhydrase (Sunda and Huntsman, 1995). In order to accurately diagnose the dominant limiting resource in a given region, we must develop our conceptual and theoretical understanding of trace metal interactions and account for the plasticity of phytoplankton interior stoichiometry instead of using fixed thresholds. In this context, expanding data sets of phytoplankton cell quotas (Ho et al., 2003, Finkel et al., 2006, Twining and Baines, 2013) and nutrient stress (Saito et al., 2014, Wu et al., 2019) would be invaluable in linking resource availability and demand.

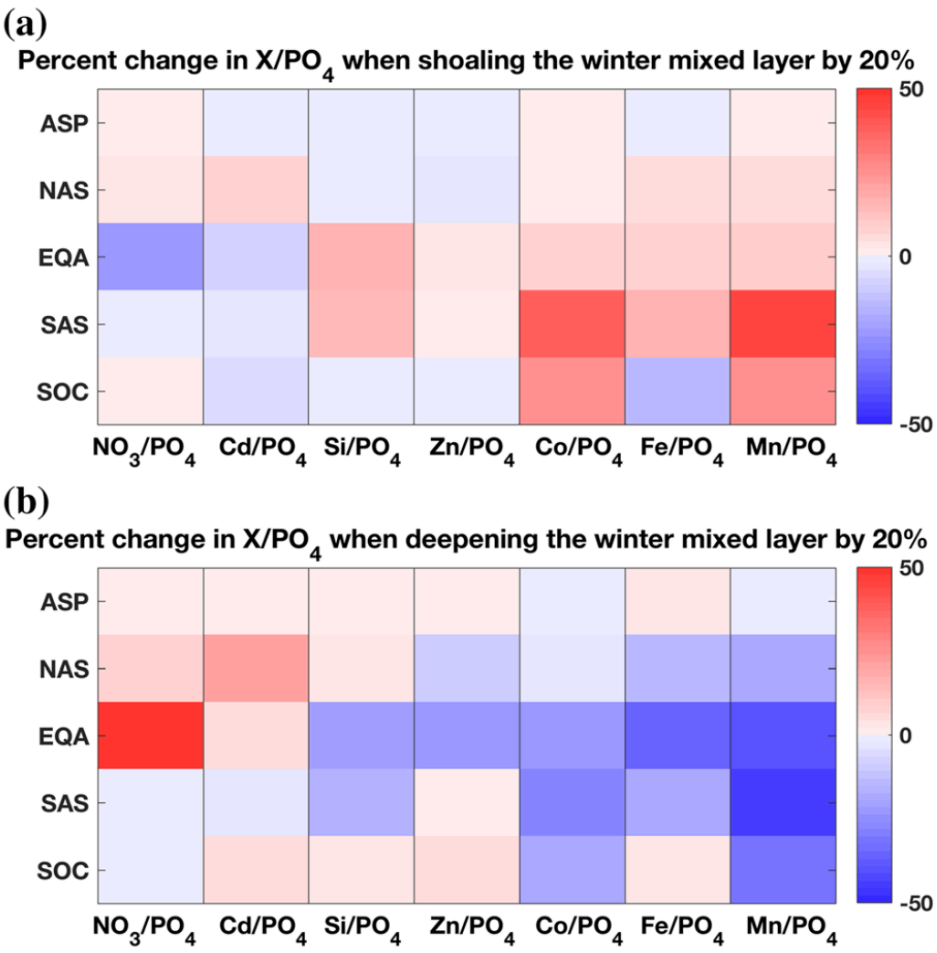

Figure 3.14. Biogeochemical province median percentage change in the elemental stoichiometry of resources in the winter mixed layer when the maximum annual mixed-layer depth is (a) shoaled and (b) deepened by 20%. Mixed-layer depth from ECCOv4r3 (Forget et al., 2015; Fukumori et al., 2017). Biogeochemical provinces are the Atlantic sub-polar gyre (ASP), North Atlantic sub-tropical (NAS), equatorial Atlantic (EQA), South Atlantic subtropical (SAS), and the Southern Ocean (SOC). An increase in X/PO4 corresponds to an increase in the availability of X relative to PO4 in the mixed layer compared to initial conditions. Ordered by nutrient type to scavenged-type resource (see text). Biogeochemical data from the 2017 *GEOTRACES* Intermediate Data Product (Schlitzer et al., 2018).

3.5.2 Variability in the Winter Mixed-Layer

The seasonal cycle of the mixed layer exhibits interannual variability (Holte et al., 2017) due to changes in physical controls (de Boyer Montegut et al., 2004) or climate

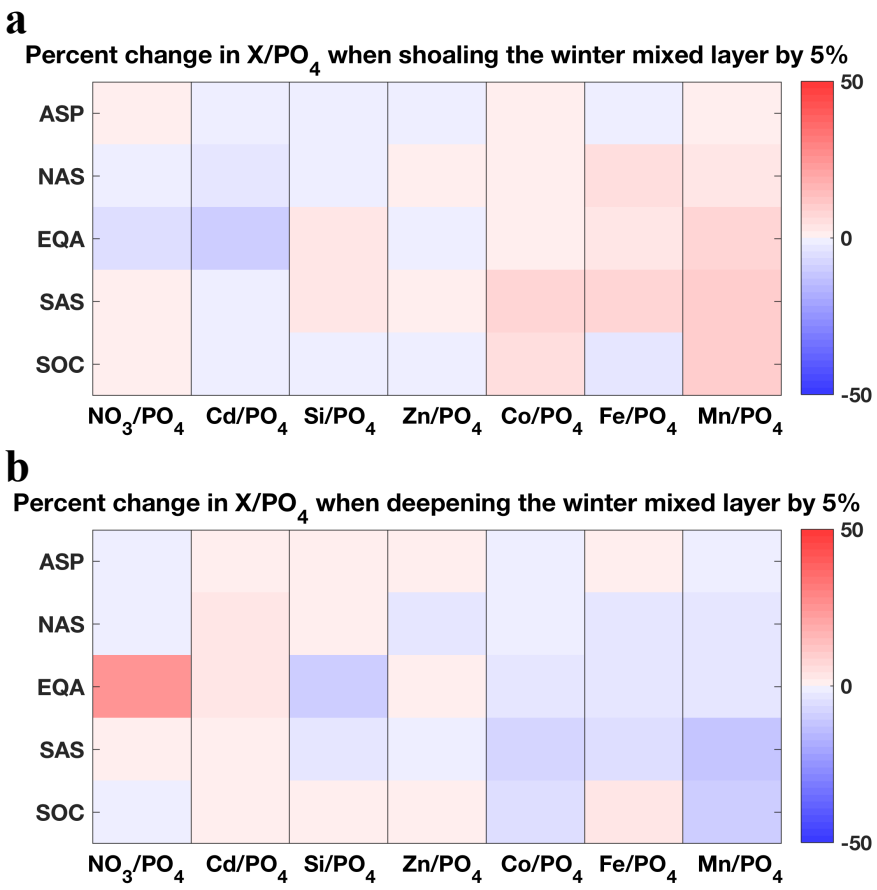

Figure 3.15. Biogeochemical province median percentage change in the elemental stoichiometry of resources in the winter mixed layer when the maximum annual mixed-layer depth is (a) shoaled and (b) deepened by 5%. Mixed layer depth from ECCOv4r3 (Forget et al., 2015, Fukumori et al., 2017). Biogeochemical provinces are the Atlantic sub-polar gyre (ASP), North Atlantic sub-tropical (NAS), equatorial Atlantic (EQA), South Atlantic subtropical (SAS) and the Southern Ocean (SOC). An increase in X/PO_4 corresponds to an increase in the supply of X relative to PO_4 in entrainment compared to initial conditions. Likewise, a decrease in X/PO_4 corresponds to the entrainment flux supplying more PO_4 relative to X. Ordered by nutrient type to scavenged-type resource (see text). Biogeochemical data from the 2017 *GEOTRACES* Intermediate Data Product (Schlitzer et al., 2018).

modes (Sallee et al., 2010). It is possible that mixed-layer anomalies may markedly alter the growth environment due to the changes in the mixed-layer resource availability (Barber and Chavez, 1983). To test this, we explored two different scenarios where the depth of the maximum annual mixed-layer depth was increased

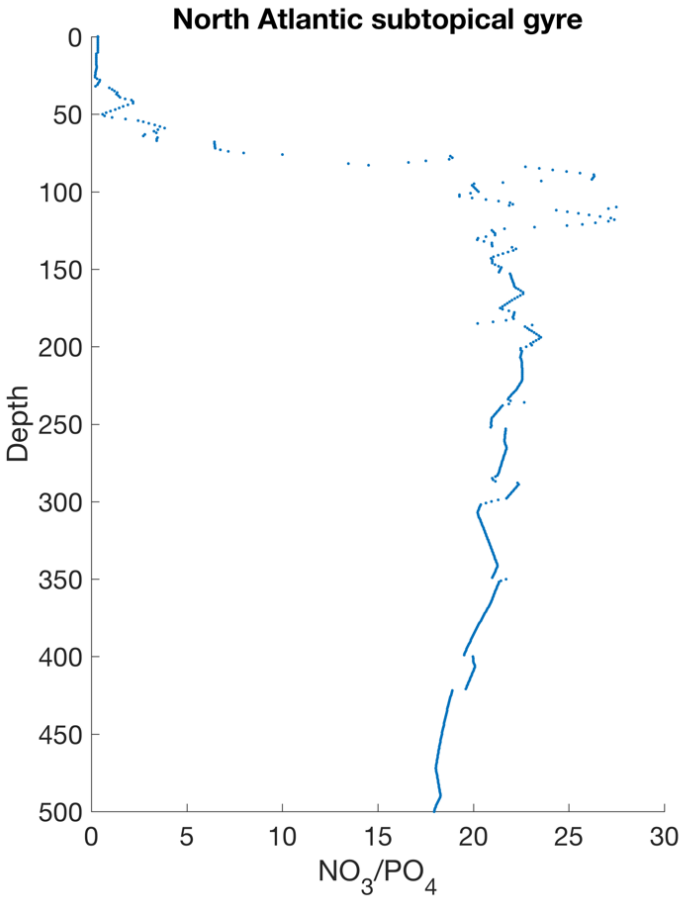

Figure 3.16. Mean ratio of NO_3 and PO_4 (mol:mol) in the upper 500m of the North Atlantic subtropical gyre. Data taken from the 2017 *GEOTRACES* IDP (Schlitzer et al., 2018).

and decreased by a modest (5%) and large (20%) degree by altering the mixed-layer thickness (H) in equation (1) accordingly.

The integrated resource stocks decrease when the depth of winter mixing was reduced; however, there were notable fluctuations in relative stock of different resources (i.e., the ratio of a given resource to PO_4; Figures 3.14 and 3.15). Under both shoaling scenarios presented, decreasing the winter mixed-layer depth decreases NO_3/PO_4 in the equatorial Atlantic (Figures 3.14a and 3.15a). In the North and South Atlantic subtropical gyres, under the 5% shoaling case and the 20% shoaling case, opposing responses in mixed-layer NO_3/PO_4 occur as the NO_3 and PO_4 stoichiometry varies with depth (Figure 3.16). In the equatorial Atlantic and South Atlantic gyre, Si/PO_4, Zn/PO_4, Co/PO_4, Fe/PO_4, and Mn/PO_4 all increase alongside the decrease in NO_3/PO_4 and Cd/PO_4, implying Si and non-nutrient type trace elements become more abundant relative to NO_3, PO_4 and Cd under reduced winter mixing (Figure 3.14). In general, Si, Zn, and Fe all show greater availability relative to PO_4 at low latitudes and less availability relative to PO_4 in the most polar provinces. Fe, Co and Mn become more

available everywhere relative to PO_4, excluding Fe in the Atlantic subpolar gyre and Southern Ocean. The changes under the 20% deepening scenario are generally opposite to those under the 20% shoaling scenario, deeper winter mixed layers lead to decreases in resource availability of Si, Zn, Co, Fe, and Mn relative to PO_4 in low latitude provinces. In some cases, shoaling and deepening drives the same response, which is attributed to gradients in the vertical profile of resource stoichiometries (Figure 3.16).

The effect of reducing the winter mixed-layer depth is likely to benefit nitrogen fixing diazotrophs in the equatorial Atlantic and South Atlantic gyre as NO_3/PO_4 is reduced while Fe/PO_4 increases, expanding the diazotroph niche (Ward et al., 2013). Additionally, increased Zn/PO_4 may promote alkaline phosphatase activity in these regions and alleviate PO_4 stress (Mahaffey et al., 2014). Overall, our results suggest that NO_3/PO_4 will increase in high latitudes while mid to low latitudes become richer in Si and non-nutrient type trace elements, allowing diazotrophs to thrive under reduced winter mixing, while the success of non-diazotrophs will be hampered.

3.5.3 Wider Considerations

3.5.3.1 Additional Resource Pathways to the Mixed-Layer

The entrainment of resources into the mixed layer is augmented by additional supply pathways. Dust is a source of resources to the ocean surface (Jickells et al., 2005), and by combining typical modelled deposition rates (Mahowald et al., 2005, Duce et al., 2008), subtropical North Atlantic solubility measurements (Shelley et al., 2018), and crustal ratios (Rudnick and Gao, 2003), we estimate average annual dust fluxes of 9.9 ± 11.5 N, 0.02 ± 0.03 P, and 2.0 ± 4.1 Si (all mmol m^{-2} $year^{-1}$), 0.4 ± 0.8 × 10^{-1} Cd , 0.5 ± 1.0 Zn, 0.05 ± 0.11 Co, 50.0 ± 100.0 Fe, and 8.2 ± 16.3 Mn (all μmol m^{-2} $year^{-1}$) across all stations included in this study. The strongest dust influence is likely to be in the subtropical North Atlantic, where it may compensate for the loss of Fe and Mn from entrainment. However, as dust inputs of Fe and Mn are greater than the entrainment losses we estimate, it is likely that additional removal processes, such as scavenging and biological uptake, are operating on aerosol derived Fe and Mn. The minimal abundance of N and P in Earth's crust causes dust to be relatively depleted in N and P compared to Si, Fe, and Mn (Rudnick & Gao, 2003). N-fixation rates of up

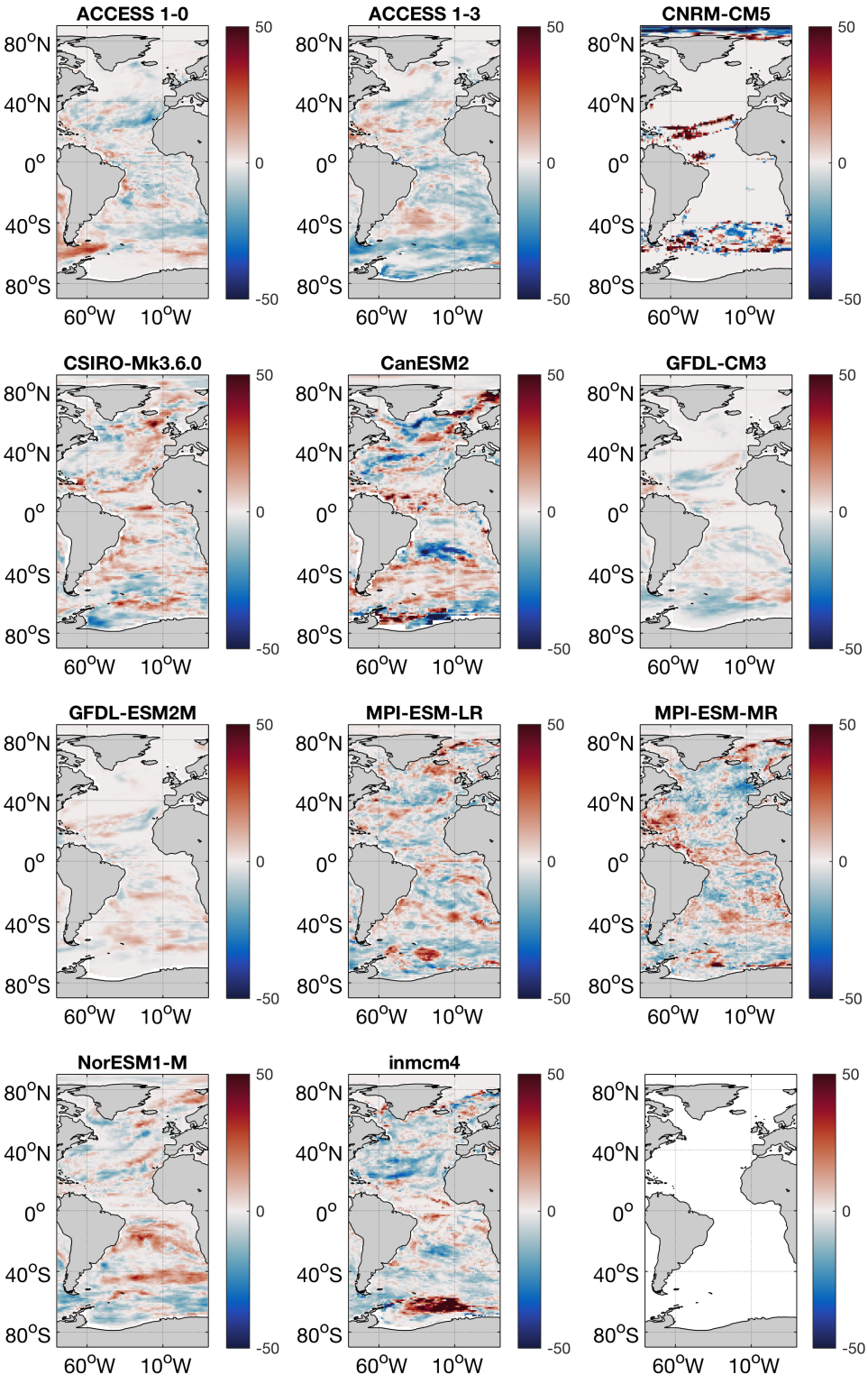

Figure 3.17. Percentage difference in the decadal mean maximum annual mixed layer depth between historical data (2005-2014) and future scenario (2091- 2100) under the RCP8.5 warming scenario. All models included are part of the Coupled Model Intercomparison Project – Phase 5 (CMIP5) (Taylor et al., 2012).

to 65 mmol N m^{-2} $year^{-1}$ have been observed in the subtropical North Atlantic (Moore et al., 2009), outweighing the entrainment input of N in this region (Figure 3.12a).

Wind-driven Ekman transport in the North Atlantic may also provide up to 60 mmol N m^{-2} $year^{-1}$ on the northern flank of the subtropical gyre (Williams and Follows, 1998), comparable to our estimates of NO_3 entrainment in the same region. In the north-western Atlantic, Gulf Stream rings have been suggested to deliver Fe to the subtropical gyre at a rate of 3.4 ± 1.9 μmol Fe m^{-2} $year^{-1}$ when averaged across the subtropical gyre area (Conway et al., 2018). This extra Fe would counter-act the estimated losses from entrainment of around −1 to −10 μmol Fe m^{-2} $year^{-1}$ in the region (Figure 3.12g). The comparison of entrainment with other physical supply pathways will vary across broad dynamical regimes. For example, in coastal or tropical regions upwelling is important; conversely, in downwelling regions such as subtropical gyres, entrainment will form a key pathway of resources to the euphotic zone (McGillicuddy, 2016). Additional physical process, such as horizontal advection (Palter et al., 2005)or mixing due to wind-driven internal waves (Whalen et al., 2018), operate alongside entrainment; however, we are unable to estimate their influence with the data sets used in this study. The external supply of resources to the winter mixed layer may alter the mixed-layer resource stoichiometry. Properly assessing the influence of the total external supply necessitates a complete understanding of each pathway.

3.5.3.2 Better Constraining Entrainment Estimates

Increased stratification may reduce winter mixed-layer depth, however; ocean warming may cause stronger thermal gradients to form (Rhein et al., 2013). This will increase the barrier presented by the main thermo- cline located between the surface mixed layer and deeper water, reducing the ventilation of the upper ocean(Frolicher et al., 2009). In such a scenario, the supply of resources to the mixed layer from diapycnal diffusion and upwelling is diminished, increasing the role of entrainment where nutriclines are located above the winter mixed-layer depth.

In order to better constrain the role of entrainment and future changes we require improved observational data coverage. In many high latitude systems (e.g., Southern Ocean), winter-time observations are scarce, affecting our estimates of the winter nutriclines and mixed-layer depths and subsequently entrainment at these locations.

Monthly observations of resources, particularly when the mixed layer is deepening, are key to better constraining entrainment fluxes. In this study, we reconstruct winter profiles based on density structure rather than applying direct monthly observations. We require better understanding on how ocean warming will impact upper ocean physics, both spatially and temporally, as well as subsequent response in biogeochemical processes (e.g., remineralization depth). At present, there is little coherency in the projected changes to winter mixed-layer depths in models included in the Coupled Model Intercomparison Project— Phase 5 (CMIP5; Figure 3.17) (Taylor et al., 2012, Sallee et al., 2013). To fully understand the future role of entrainment compared to other major sources, other factors such as atmospheric resource supplies should be considered (Mahowald and Luo, 2003).

3.6 Conclusions

This study synthesizes biogeochemical observational data with output from a physical ocean state estimation to determine basin-scale patterns in mixed-layer resource availability throughout the Atlantic Ocean. We find NO_3/PO_4 and Mn/PO_4 are endmembers displaying maxima in the high and low latitudes, respectively, due to their nutrient-like and scavenged-like characteristics. Cd/PO_4, Si/PO_4, Zn/PO_4, and Co/PO_4 tend to fall in between these two endmembers, while Fe/PO_4 shows different behaviour in different regions of the Atlantic Ocean. These variations arise primarily due to the regional differences in the offset between the winter mixed-layer depth and the associated nutricline. When nutrient-type profiles prevail, the entrainment of thermocline waters into the mixed layer acts to alleviate deficiency of these resources. However, in regions where resources display scavenged-type profiles, then entrainment can cause a dilution of upper ocean stocks. This dilution occurs most prominently for Mn and Fe in the North Atlantic subtropical gyre and equatorial Atlantic and implies that the elevated upper ocean stocks must be sustained by other pro- cesses (e.g., dust deposition, lateral advection). Entrainment replenishes nutrient-type resources in the mixed layer and dilutes scavenged-type elements in the mixed layer. Future changes in the depth of winter-mixing will have a subsequent impact on mixed-layer resource availability. We apply a N-Fe relationship to mixed-layer resource availability to infer singular N-limitation in the low latitude Atlantic and singular Fe-limitation in the high latitude Atlantic in close proximity to the Labrador

Sea. Singular Fe-limitation in high latitude regions, particularly at deep water formation sites, suggests the remote influence of Fe over low latitude biogeochemistry as deep waters are transferred vertically. However, to fully link any change in the relative availability of various resources to phytoplankton growth requires a complete understanding of the stoichiometric plasticity and the colimitation of cellular processes, which is currently unavailable.

Chapter 4

The Vertical Supply of Resources to the Low Latitude Surface Ocean Estimated by *In-Situ* Techniques

Shaun. J. Rigby[1], Richard. G. Williams[1], Eric P. Achterberg[2] and Alessandro Tagliabue[1]

[1] Department of Earth, Ocean and Ecological Sciences, School of Environmental Science, University of Liverpool, UK.

[2] GEOMAR Helmholtz Centre for Ocean Research Kiel, Kiel, Germany.

4.0 Preamble

Study motivation

The *GEOTRACES* programme provides a wealth of information on the distribution of trace elements and their isotopes, and major nutrients in the ocean. However, the single 'snapshot' view inherent to shipboard transect studies hinders the study of physical processes which vary temporally. In this chapter, helium, which is a biologically and chemically inert tracer, is used to estimate rates of physical exchanges in the upper ocean directly from *GEOTRACES* cruises. We are subsequently able to combine mixing estimates with resource profiles to infer resource fluxes from in situ observations alone. Our findings demonstrated that the vertical resource flux was sensitive to both mixing rates and resource gradients. Oxygen has established links to the distributions of key resources, we therefore used GA03 and GP16 as the ideal testbed to investigate this link further due to the wide range of oxygen environments observed along both transects.

Key Points

- Vertical mixing is larger by a factor of ~7 during periods of active entrainment in the subtropical North Atlantic.
- Generally, resource gradients are correlated with oxygen gradients, however there are regional contrasts and differences between resources.
- Along tropical and subtropical ocean transects, variability in resource fluxes is driven by spatial changes in vertical mixing rather than variability in vertical gradients.
- In the subtropical North Atlantic, the cellular elemental composition of dinoflagellates is similar to that of the upwards flux. In contrast, the trace-element demand of diatoms is not met by vertical exchanges, suggesting diatoms rely on additional trace-element sources such as aeolian deposition.

Publication and Author Contribution

The work completed within this chapter has been prepared for submission to *Frontiers: Marine Science* with authors Shaun J. Rigby, Richard G. Williams, Eric P. Achterberg and Alessandro Tagliabue. Shaun J. Rigby designed the research, completed analysis and wrote the manuscript. Richard G. Williams and Eric P. Achterberg provided editorial critiques. Alessandro Tagliabue was crucial in the research design, analysis process and manuscript production.

Citation

Rigby, S. J., Williams, R. G., Achterberg, E. P., & Tagliabue, A., (2020). The Vertical Supply of Resources to the Low Latitude Surface Ocean Estimated by *In Situ* Techniques. PhD Dissertation, University of Liverpool.

4.1 Abstract

The delivery of resources to the upper ocean is important in sustaining primary production. Physical processes, such as the winter-time entrainment of underlying waters into the mixed-layer and diapycnal mixing, are key in the vertical transfer of resources to biota in the euphotic zone. While the distribution of bio-essential resources is routinely observed during oceanographic field campaigns, in situ measurements of vertical transport are often lacking, especially for trace micronutrients. In this study, we exploit helium observations alongside profiles of nitrate (NO_3), phosphate (PO_4), silicic acid (Si), zinc (Zn), cobalt (Co), iron (Fe) and manganese (Mn) from *GEOTRACES* cruises to quantify vertical resource exchanges in the subtropical North Atlantic and equatorial Pacific. The helium flux gauge approach is used to integrate physical signals from single in situ measurements to demonstrate that vertical mixing is larger by a factor ~7 during entrainment periods compared to detrainment periods. Enhanced vertical mixing increases the transfer of key resources, however, overall vertical fluxes are also controlled by each unique resource distributions. There are strong relationships between the vertical gradients of oxygen and NO_3, PO_4, Si, Co and Mn, but not Fe and Zn in the subtropical North Atlantic. While in the equatorial Pacific, NO_3, PO_4, Si, Fe and Mn vertical gradients exhibited strong relationships with oxygen gradients, but Co and Zn did not. A linear model demonstrates that resource flux variability is primarily driven by variability in physical mixing in the subtropical North Atlantic and by both variability in resource gradients and physical mixing in the equatorial Pacific. Resource flux estimates are compared to concurrent in situ measurements of marine phytoplankton composition to show that the cellular demands of dinoflagellates are met, while diatoms must rely on other resource supplies to meet cellular requirements. Our results demonstrate the importance of considering temporally varying physical processes when assessing transect data and have implications for understanding the response of resource fluxes to future shifts in global oxygen distributions.

4.2 Introduction

Basin-scale field campaigns deliver high resolution snapshots of trace elements and their isotopes. Understanding the role of physical processes in setting upper ocean resource distributions identified by transect studies requires quantification of temporally and spatially varying processes (Rijkenberg et al., 2012, Tuerena et al., 2019). In the upper ocean, the seasonal entrainment of underlying waters into the mixed layer causes the vertical exchange of multiple tracers, including bio-essential resources which are fundamental to sustaining primary production (Jenkins, 1988, Williams and Follows, 2003a, Tagliabue et al., 2014, Stanley et al., 2015, Achterberg et al., 2018, Rigby et al., 2020). The *in-situ* quantification of entrainment demands regular observation of the mixed-layer depths and trace metal resources throughout the year, which is logistically challenging. Consequently, *in-situ* estimates of physical exchanges between the mixed layer and underlying thermocline during periods of active and inactive entrainment alongside contemporaneous resource observations are lacking. Tracer techniques integrate physical signals over long time periods to offer temporal insights from single point observations (Jenkins, 1988, Jenkins and Doney, 2003, Stanley et al., 2015). The *GEOTRACES* programme offers tracer observations alongside a suite of key resources in two different hydrographic settings, the sub-tropical North Atlantic (GA03) and equatorial Pacific (GP16), where the amplitude of the annual mixed-layer cycle is large and small, respectively (Jenkins et al., 2015, Peters et al., 2018a). This provides an opportunity to quantify tracer exchanges in the two regions and to infer the role of seasonal entrainment in increasing mixing rates to the upper ocean.

The transfer of resources across the base of the mixed layer is governed by diffusivity and vertical gradients in resource profiles. Directly beneath the surface mixed layer, diapycnal diffusivity (K_z) ranges from ~10^{-3} to ~10^{-4} m s^{-2} (Blain et al., 2008, Rijkenberg et al., 2012, Cronin et al., 2015), while in the quiescent mid-depth open ocean, lower K_z estimates of ~10^{-6} m s^{-2} are typical (Martin et al., 2010). There is a seasonal cycle in K_z, which is associated with seasonal changes in wind-stress and is stronger in the upper ocean (Wu et al., 2011). Vertical gradients in resource profiles are established by multiple processes (Tagliabue, 2019, Rigby et al., 2020). Low

oxygen environments influence the biogeochemical cycles of nitrate (NO_3), cobalt (Co), iron (Fe) and manganese (Mn) due to changes in redox chemistry, scavenging and release from sediments (Moffett and Ho, 1996, Hawco et al., 2016, Heller et al., 2017). In the absence of oxygen, NO_3 is the favorable acceptor of electrons during respiration, resulting in the reduction and denitrification of bioavailable nitrogen forms (NO_3, nitrite and ammonium) to biologically unavailable gaseous forms (nitric oxide, nitrous oxide and di-nitrogen). Nitrite (NO_2), an indicator of denitrification, accumulates under oxygen levels less than 0.05 mmol m^{-3} (Thamdrup et al., 2012). In the modern ocean, the solubility of Co, Fe and Mn is limited by the presence of oxygen (Sunda, 2012). In the South Atlantic at the Benguela-Angola front, Co and oxygen demonstrate a strong relationship in the oxygen minimum zone (OMZ) due to subsurface coastal inputs, lateral advection and slow scavenging rates in the OMZ (Noble et al., 2012). In oxic waters, dissolved Fe(II) is rapidly oxidized into the less soluble Fe(III), resulting in lower dissolved Fe concentrations (Millero et al., 1987, Millero and Sotolongo, 1989). Oxygen minimum zones are proposed as major sources of Fe to the ocean interior due to the depleted levels of oxygen and hydrogen peroxide, the main oxidizing agents of Fe (Scholz et al., 2014). The relationship between Mn and oxygen is well established and linked to the recycling of organic material and dissolution on Mn oxyhydroxides which drives increases in Mn concentrations concurrent with oxygen minimum zones (Landing and Bruland, 1987, Lewis and Luther Iii, 2000). Systematic links between oxygen gradients and resource gradients may highlight the importance of preformed resources and low oxygen subsurface waters in setting the magnitude of resource fluxes during seasonal entrainment. There are contrasts in the distribution of oxygen between the subtropical North Atlantic and equatorial Pacific, thus providing a suitable testbed to explore the linkages between oxygen gradients and diapycnal resource fluxes (Jenkins et al., 2015, Peters et al., 2018a).

The availability of NO_3, phosphate (PO_4), silicic acid (Si), zinc (Zn), Co, Fe and Mn in the upper ocean supports biological productivity (Sunda, 1989, Twining and Baines, 2013). The regeneration of export at depth has established macro-nutrient resource ratios of $C_{org} : N : P : -O_2 = 117 \pm 14 : 16 \pm 1 : 1 : 170 \pm 10$ (Anderson and Sarmiento, 1994). Resources are required by marine phytoplankton to maintain their cellular

functions, ranging from nitrogen for use in DNA and proteins, to Fe in fundamental cellular enzymes (Raven, 1988b), to Zn in carbon-acquisition enzyme carbonic anhydrase (Sunda, 1989), and Co as part of vitamin B12 (Rodionov et al., 2003). While differences in cellular compositions between phytoplankton taxa group have been observed (Sunda, 1989, Ho et al., 2003, Twining and Baines, 2013), there is plasticity in the demand of trace metal resources within taxa groups due to substitution (Prince and Morel, 1990, Morel et al., 2020), storage strategies (Cohen et al., 2018, Lampe et al., 2019) and the competitive inhibition of uptake mechanisms (Hawco and Saito, 2018). Differences in the stoichiometry of resource availability, which is partially maintained by the vertical resource flux, and *in-situ* cellular compositions of phytoplankton drives resource deficiency (Moore, 2016). Productivity is limited by resource availability where cellular demands are not met (Moore et al., 2013). There are numerous studies into the role of NO_3 and Fe as the major limiting nutrients, restricting the growth of marine phytoplankton (Boyd et al., 2001, Hopkinson and Barbeau, 2008, Browning et al., 2017a, Hogle et al., 2018). Browning et al., (2017) performed bioassay experiments to study linkages between N, Fe and Co limitation between the Benguela Upwelling Region and South Atlantic gyre, developing a metric to infer N-Fe singular-, secondary- and co-limitation from N:Fe ratios. In the eastern equatorial Pacific, projections of the response of productivity to climate change demonstrate the importance of cellular quotas in the context of changes to nutrient limitation regimes, but are restricted by the availability of current *in-situ* estimates of processes in the Fe cycle and nutrient regimes (Tagliabue et al., 2020).

Using *GEOTRACES* (www.geotraces.org) data in the equatorial Pacific and subtropical North Atlantic, we apply the helium flux gauge approach to estimate physical exchange rates and infer vertical resource fluxes into productive regions where entrainment is inactive and active. By comparing these low-latitude regions, we provide seasonally varying *in-situ* estimates of physical mixing and estimate the vertical flux of NO_3, PO_4, Si, Zn, Co, Fe and Mn. Linkages between vertical oxygen gradients, vertical resource gradients and K_z are explored to identify the principle mechanism controlling variability in vertical resource fluxes. The resource flux stoichiometry is compared to the cellular composition of marine phytoplankton in the subtropical North Atlantic Ocean to demonstrate the reliance of two phytoplankton taxa on upwards resource flux. Finally, we employ an iron-nitrogen limitation

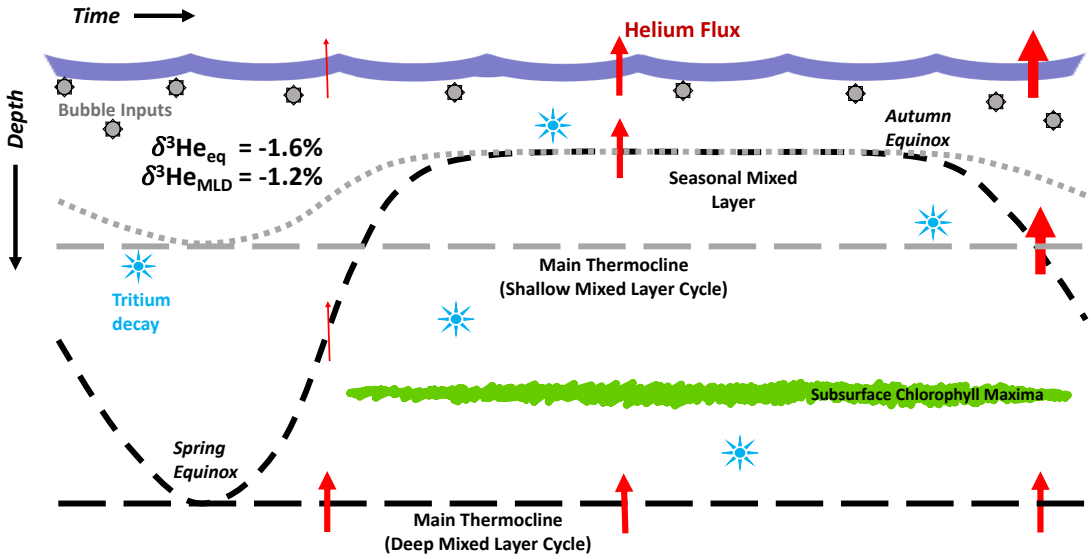

Figure 4.1. Schematic view of the mixed layer helium budget and evolution with time (horizontal axis). Sources of helium are bubble inputs (grey circles), tritium decay (blue stars) and the deepening of the mixed layer (dotted grey line for equatorial regions, dashed black line for subtropical regions). The loss of helium is through the air-sea interface. Helium transfers across boundaries are given relative magnitudes (thickness of red arrows).

relationship to demonstrate an east-west transition in resource limitation of waters supplied to the upper water column in the equatorial Pacific.

4.3 Methods

4.3.1 Datasets

Observational data were collected on *GEOTRACES* (www.geotraces.org) section cruises GA03 in the subtropical North Atlantic, 6th November 2011 to 11th December 2011, and GP16 in the equatorial Pacific, 25th October 2013 to 20th December 2013 and extracted from the IDP2017v2 (Schlitzer et al., 2018). Helium analyses were completed at the Woods Hole Oceanographic Institute (Jenkins et al., 2019). Local mixed-layer depths (MLDs) were estimated by the de Boyer Montegut et al. (2004) density criterion, where density is calculated using the Gibbs Seawater Toolbox with

shipboard measurements of temperature and salinity (IOC et al., 2010). The monthly climatology of mixed-layer depth was extracted from the ECCO (Estimating the Climate and Circulation of the Ocean, version 4 release 3) global circulation model along the GA03 and GP16 cruise transects (Forget et al., 2015, Fukumori et al., 2017). Estimates of the euphotic depth during both field campaigns were retrieved from the Globcolor project (Fanton d'Andon et al., 2009, Maritorena et al., 2010)

4.3.2 Air-Sea Helium Flux

The air-sea flux of He is sustained by three sources of helium into the mixed-layer: (1) air injection, (2) *in-situ* tritium decay and (3) upwards flux from below, equation [4.1], referred to hereafter as the helium budget (Figure 4.1).

$$He_{Gas\ Exchange} = He_{Air\ Injection} + He_{Tritium} + He_{Upward} \qquad [4.1]$$

Where

$$He_{Gas\ Exchange} = k_s\left([He_{Eq}] - [He_{MLD}]\right) \qquad [4.2]$$

Where He_{eq} is the concentration of helium at equilibrium with the atmosphere, calculated using helium solubility which includes an isotopic fractionation effect (Benson and Krause, 1980) and molecular diffusivity which is a function of both temperature and salinity (Bourg and Sposito, 2008). He_{MLD} is the mean mixed layer He concentration. We apply the air-sea exchange parameterization (K_s) of Liang et al. (2013), hereafter L13. Briefly, air-sea flux of a gas is given by equation [4.3] (L13).

$$k_s = 1.352 \times 10^{-4}\, u^a \left(\frac{Sc}{660}\right)^{-0.5} \qquad [4.3]$$

Where u^a is the air-side frictional velocity given by

$$u^a = \sqrt{Cd}\, u_{10} \qquad [4.4]$$

Where u_{10} is the wind speed at 10 m above sea-level and Cd is related to wind speed by the following relationship, equation [4.5]:

$$Cd = \begin{cases} 0.0012 & (u_{10} < 11\ m\ s^{-1}) \\ (0.49 + 0.065\ u_{10}) \times 10^{-3} & (11 \leq u_{10} \leq 20\ m\ s^{-1}) \\ 0.0018 & (u_{10} > 20\ m\ s^{-1}) \end{cases} \quad [4.5]$$

The Schmidt number (Sc) of helium is temperature dependent (Jähne et al., 1987), resulting in a seasonal cycle associated to the air-sea flux. At a temperature of 20°C and salinity 35‰, the Schmidt number of He is 165 and that of ^{3}He is 145 (Jähne et al., 1987, Wanninkhof, 2014).

Air injection included in the helium budget is calculated from L13. Air injection occurs through bubbles which completely dissolved and bubbles which partially then return to the surface, equation [4.6].

$$He_{Air\ Injection} = He_{Completely\ Trapped} + He_{Partially\ Trapped} \quad [4.6]$$

Bubbles are generated by breaking waves at the air-sea interface and entrained into the mixed layer by turbulence (see L13). Completely trapped bubbles are those which undergo complete dissolution following entrainment, injecting atmospheric helium into the surface mixed layer. The completely trapped bubble coefficient, k_c is calculated by equation [4.7].

$$k_c = 5.56\ (u^w)^{3.86} \quad [4.7]$$

where u^w is the water-side frictional velocity

$$u^w = 0.034\ u^a \quad [4.8]$$

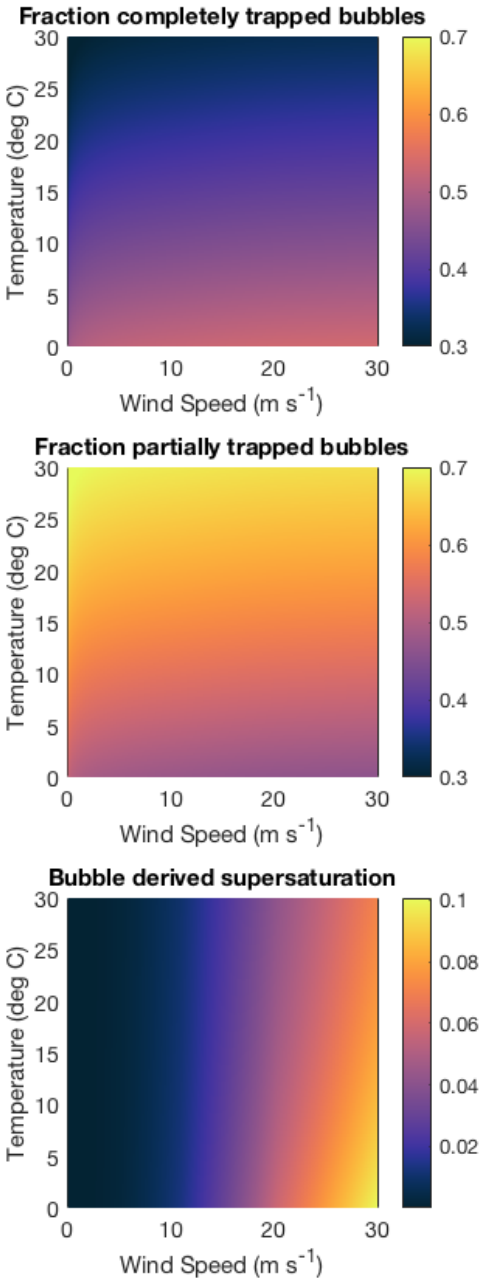

Figure 4.2. Dependence of bubble components and supersaturation on temperature and wind speed following the Liang et al. (2013) parameterization.

Partially trapped bubbles are entrained into the mixed layer, however, do not completely dissolve and return to the surface. The partially trapped bubble coefficient, k_p, is calculated by equation [4.9].

$$k_p = 5.5\ (u^w)^{2.76}\ \left(\frac{Sc}{660}\right)^{-0.67} \quad [4.9]$$

The contribution to the total bubble flux from completely and partially trapped bubbles approximately 70% and 30% respectively (Figure 4.2), however is dependent upon wind speed and temperature. Air injected by bubbles is assumed to be in equilibrium with the overlying atmosphere.

The hydrostatic pressure acting on entrained bubbles is given by ΔP, equation [4.10],

$$\Delta P = 1.52\ (u^w)^{1.06} \quad [4.10]$$

Bubble-derived supersaturation of helium is given by Δe, equation [4.11],

$$\Delta e = \frac{\left(\frac{k_c}{K_H} + k_p\,\Delta P\right)}{k_s + k_p} \quad [4.11]$$

Where K_H is the Henry constant and equal to 3.9 x 10^{-4} for He (Krause and Benson, 1989). The isotopic fractionation associated with the dissolution of helium in seawater is included in our calculations following Benson and Krause (1980).

There are numerous models available to parameterize air-sea exchange and incorporate bubble fluxes (Wanninkhof, 1992, Woolf, 1997, Wanninkhof and McGillis, 1999, Stanley et al., 2009, Liang et al., 2013, Wanninkhof, 2014) which are dependent upon wind speed (Figure 4.3). Choice of the cubic parameterizations tends to lead to higher air-sea exchange estimates at high wind speeds and lower air-sea exchange estimates at low wind speeds (Figure 4.3). Here, our choice of L13 is based on the performance of each model compared to nitrogen supersaturation in the upper ocean (Emerson and Bushinsky, 2016). At low wind speeds (< 10 m s^{-1}) as observed in our dataset, the choice of air-sea flux model affects the calculated flux by up to a factor of 2 compared to other examined parameterizations in Figure 4.3 (Emerson and Bushinsky, 2016). There is an error of 20% associated with air-sea flux

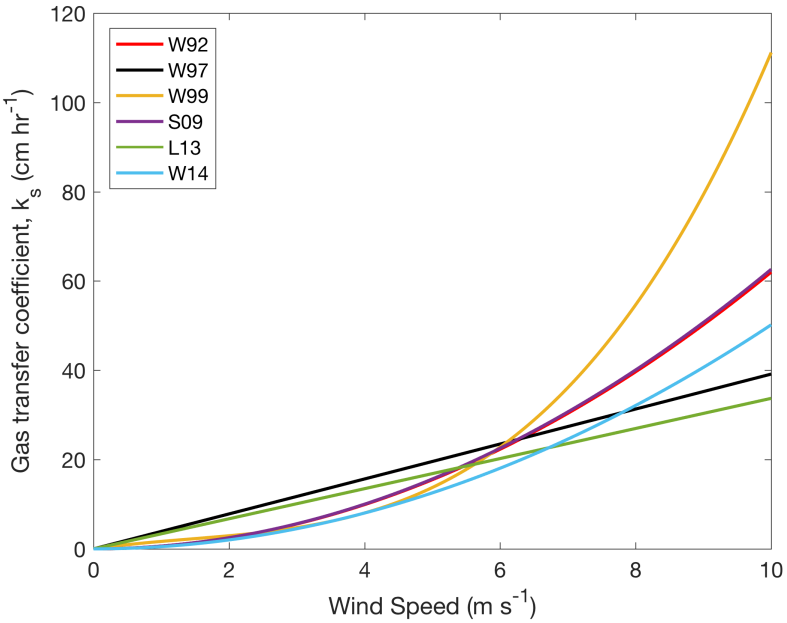

Figure 4.3. Gas transfer co-efficient relation with wind speed for various parameterizations. Included are Wanninkhof (1992), red, Woolf (1997), black, Wanninkhof (1999), yellow, Stanley et al. (2009), purple, Liang et al. (2013), green and Wanninkhof (2014), blue.

parametrizations due to the propagation of errors in calculations of model coefficients, the Schmidt number and associated wind speeds (Wanninkhof, 2014).

The final parameter in the helium is that sourced from the *in-situ* decay of tritium. Tritium is measured in tritium units (TU), where 1 TU = 0.1181 Bq, equating to 118.1 atoms of ^3He m^{-3} s^{-1} or 6.18 x 10^{-3} pmol He^3 yr^{-1}. This quantity is then removed from the helium budget described by equation [4.1]

4.3.3 Inferred Effective Vertical Diffusivity and Resource Fluxes

The effective K_z (m^2 s^{-1}) is inferred by dividing the residual air-sea helium flux by the gradient in He between the two depth bounds, z_1 and z_2 of choice, equation [4.12]

$$Inferred\ K_z = \frac{He_{flux}}{\left(\frac{\delta He}{\delta z}\right)_{z_2}^{z_1}} \qquad [4.12]$$

Helium is biologically and chemically inert and is therefore an ideal tracer of physical processes. Here, a helium mass balance is used to infer the effective K_z. Importantly, the inferred effective K_z does not solely represent diapycnal diffusivity within the seasonal thermocline, but also encompasses turbulent fluxes within the mixed layer. The inferred effective K_z captures the roles of additional physical processes, such as entrainment and eddy stirring, which augment diffusivity in driving vertical exchange in the upper ocean, see Box 1 (Kraus and Turner, 1967). Hence, the inferred effective K_z is larger than typical open-ocean estimates diapycnal diffusivity due to the inclusion of additional physical processes which increase the rate of vertical transfers.

Resource fluxes between depth boundaries are calculated from the effective K_z in combination with the appropriate resource gradient, equation [4.13],

$$R_{flux} = K_z \times \frac{\delta R}{\delta z} \qquad [4.13]$$

where R is a given resource and δz is the vertical spacing between depth boundaries.

The depth and seasonal cycle of the mixed layer controls resource availability and the magnitude of winter-time entrainment. The mean local mixed-layer depth from shipboard observations is 61 ± 19m in the subtropical North Atlantic and 38 ± 20m in equatorial Pacific (Figure 4.4a). However, the underlying processes in driving the MLD at the time of sampling in each basin are in contrast. In the subtropical Atlantic, data was taken during late-autumn and early-winter months, meaning the mixed layer is deepening as the mechanical forcing of wind combined with the cooling of the upper water column breaks down summer-time stratification (Figure 4.4b). In the equatorial Pacific dataset, observations were made during late-spring and early-summer. Here, thermal inputs and reduced winds drive the stratification and a shoaling of the MLD during summer months (Figure 4.4c). Using ECCO mixed layer climatology at the time of sampling, the mixed layer in the subtropical North Atlantic was deepening at a rate of 1.40 m d^{-1}, whereas the mixed layer in the equatorial Pacific was shoaling at a rate of 0.15 m d^{-1}. The seasonal differences between available data in the equatorial Pacific and subtropical North Atlantic therefore allow direct comparison between the effect of entrainment and diapycnal mixing on the total nutrient supply (Box 1).

Box 1

$\frac{\partial N}{\partial t} + \frac{\partial}{\partial z}\overline{w'N'} + \frac{\partial}{\partial z}\left(\kappa\frac{\partial N}{\partial z}\right) = 0$	The mixed layer balance equation, where a change in nutrient concentration, N (left-hand side term), is balanced with eddy turbulent fluxes (middle term, where z is depth and w is vertical velocity) and diffusion (right-hand side term, where k is diapycnal diffusivity).
$h\frac{\partial N}{\partial t} + [(\overline{w'N'})]_{-h}^{0} + \left[\kappa\frac{\partial N}{\partial z}\right]_{-h}^{0} = 0$	Integration of the mixed layer balance from the surface (z = 0) to the base of the mixed layer (z = -h).
$\Longrightarrow [(\overline{w'N'})]_{-h}^{0} = \Lambda\,\Delta N\frac{dh}{dt}$	Integrating eddy turbulent fluxes over the mixed layer is equal to changes in the nutrient concertation as the mixed layer deepens
$h\frac{\partial N}{\partial t} + \Lambda\,\Delta N\frac{dh}{dt} + \left[\kappa\frac{\partial N}{\partial z}\right]_{-h}^{0} = 0$	Re-arranging to include the Heaviside function
$\Lambda \equiv \Lambda\left(\frac{dh}{dt}\right) = \begin{matrix}1\\0\end{matrix}\ for\ \frac{dh}{dt} \gtrless 0$	Where Λ is the Heaviside function and non-zero when the mixed layer is deepening (Kraus and Turner, 1967).
$\kappa_{Inferred}\left(\frac{\delta N}{dz}\right) = \kappa\frac{\partial N}{\partial z} + \Lambda\,\Delta N\frac{dh}{dt}$	The total flux is equal to the diffusive flux and turbulent flux
$\kappa_{Inferred} = \kappa + \frac{\Lambda\,\Delta N}{\frac{\partial N}{\partial z}}\frac{dh}{dt}$	$K_{inferred}$ is the sum of the diffusive and turbulent components

Alongside seasonal differences in the two datasets studied here, there are contrasts in the interaction between the MLD and euphotic depth. In the subtropical North Atlantic, the summer-time mixed layer is shallower than the euphotic depth, meaning irradiance levels are sufficient to support mixed-layer productivity in summer while adequate resources are available. In winter months, the MLD from the ECCO climatology deepens to below the depth of the euphotic zone from the Globcolor climatology, meaning resources are delivered to the euphotic zone by the seasonal entrainment of thermocline waters (Figures 4.4b). In the equatorial Pacific, the amplitude of the seasonal MLD cycle is muted compared to the subtropical North Atlantic (Figure 4.4c) and remains shallower than the euphotic depth throughout the

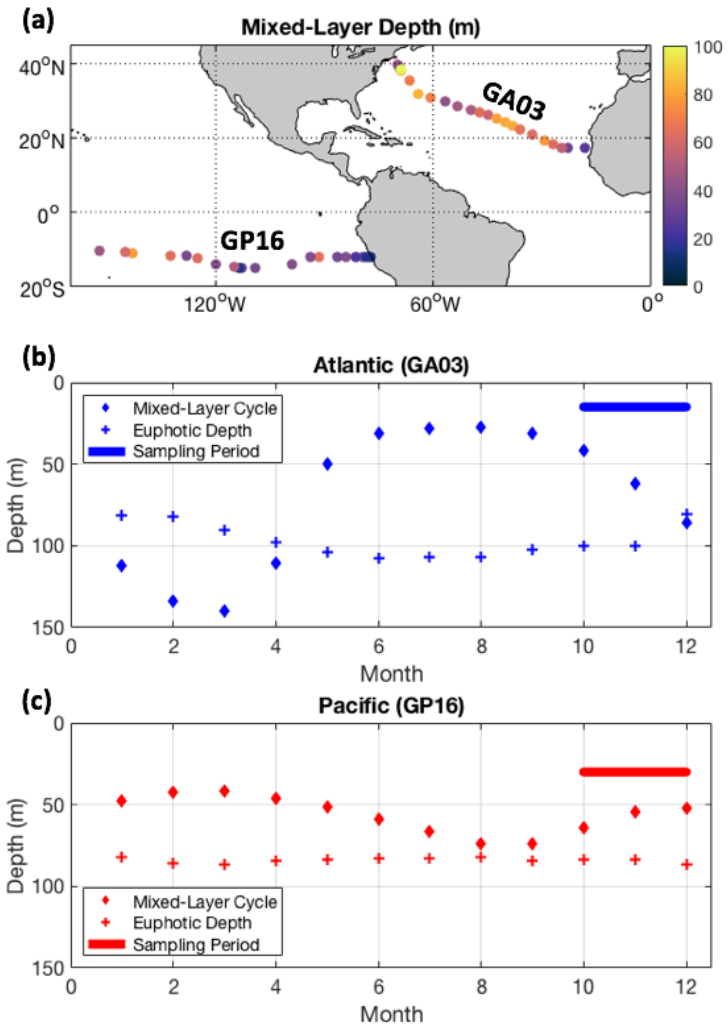

Figure 4.4. (a) In situ mixed-layer depth at stations where helium data is available in the subtropical North Atlantic (GA03) and the equatorial Pacific (GP16). Climatology of the annual mixed-layer depth cycle (diamonds) and euphotic depth (crosses) in the (b) subtropical North Atlantic and (c) the equatorial Pacific. Horizontal bars denote the sampling periods of GA03 and GP16. GA03 and GP16 data from the 2018 *GEOTRACES* (Schlitzer et al., 2018), mixed-layer depth climatology from the ECCO global circulation model (Forget et al., 2015, Fukumori et al., 2017) and euphotic depth from the Globcolor project (Fanton d'Andon et al., 2009, Maritorena et al., 2010).

year. This permits primary production in and below the mixed layer (where nutrient demands are met). Therefore, examining the resource flux into the mixed layer is not representative of resource supply to biota as winter-time entrainment does not extend to below the euphotic depth.

In the subtropical North Atlantic, we consider resource fluxes between the local MLD and winter MLD to provide estimates of K_z and resource fluxes to biota during periods of entrainment. In the equatorial Pacific, the isopycnal at which chlorophyll concentrations fall below 20% of the chlorophyll maxima is identified and resource fluxes are estimated between the 20% chlorophyll isopycnal and that plus 1 kg $m^{-3,}$ hereafter referred to as the low chlorophyll layer. This criterion is selected to identify the productive region of the water column where resource supply is sustaining growth over long periods. The choice of depth ranges applied here permits the calculation of K_z where entrainment is active and inactive in delivering resources to biota.

4.4 Results

4.4.1 Mixed-Layer Helium Fluxes and Inferred Vertical Mixing

Variation in δ^3He equilibrium value (δ^3He_{eq}) can arise from changes in temperature, salinity and air-injection processes. In the subtropical North Atlantic section, measurements towards the west are at higher latitudes than those in the east, thus cooler waters cause a slight decrease in δ^3He_{eq}. Likewise, the upwelling of cooler waters in the eastern Pacific drives an east-west gradient in the mixed layer δ^3He_{eq}. The mixed layer δ^3He_{eq} is consistent in both the subtropical North Atlantic and the equatorial Pacific at around -1.6% (Figure 4.5a). Mixed layer δ^3He is generally greater than δ^3He_{eq} in both the Atlantic and Pacific datasets leading to outgassing fluxes. The median outgassing flux of δ^3He is 2.42 % m d^{-1} in the subtropical North Atlantic and 1.18 % m d^{-1} in the equatorial Pacific (Figure 4.5b). Both are comparable to previous estimates of 2.83 % m d^{-1} in the Sargasso Sea (Jenkins and Doney, 2003). In the subtropical North Atlantic dataset, the δ^3He outgassing flux is largest in the Gulf Stream and also increases from the center of the gyre towards the Mauritian Upwelling Zone. In the equatorial Pacific, the δ^3He outgassing flux is generally consistent

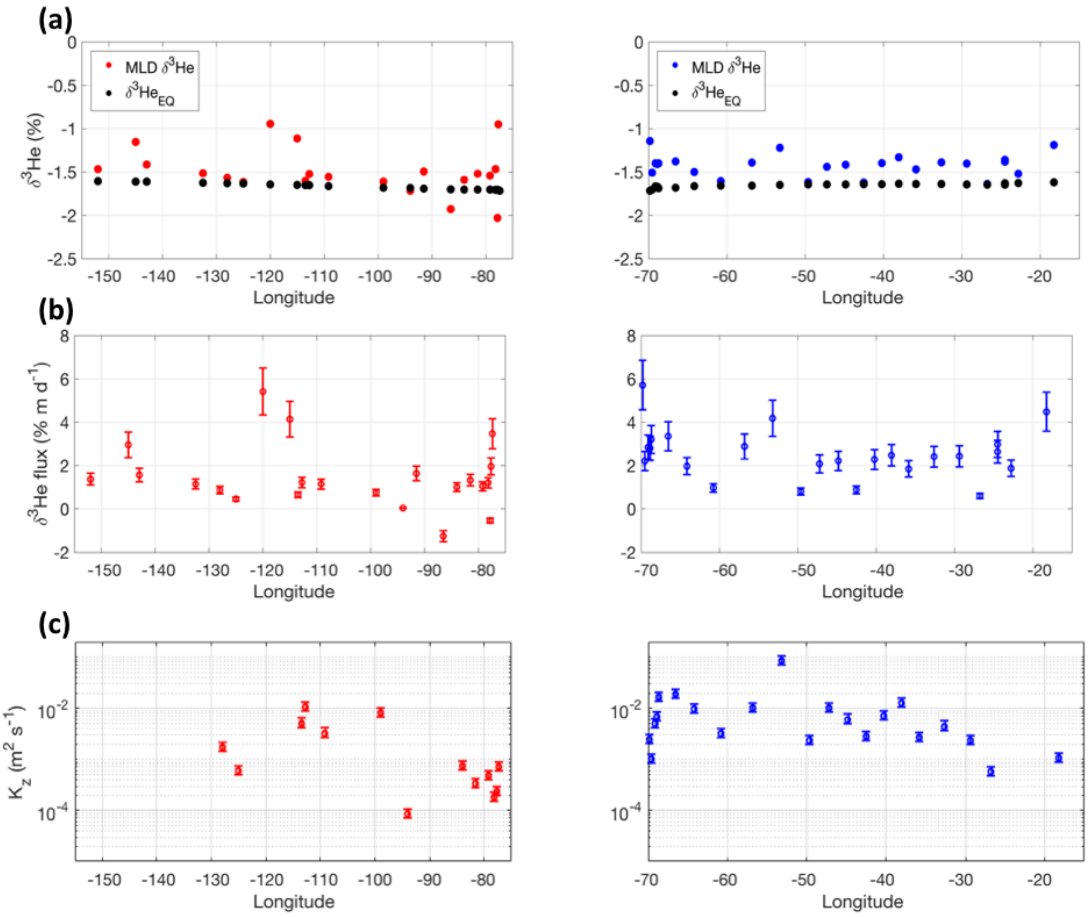

Figure 4.5. Equatorial Pacific (left panels, red) and subtropical Atlantic (right panels, blue). (a) Mixed layer observed δ^3He (coloured) and δ^3He equilibrium value based on temperature and salinity (black), both in %. (b) Outgassing of δ^3He at the air-sea interface (% m d^{-1}) using parameterizations of Liang et al. (2013) and error analysis of Wanninkhof (2014). (c) Inferred vertical diffusivity (K_z) from the air-sea flux and δ^3He gradient between the local mixed layer and winter mixed-layer (m^2 s^{-1}). Helium data from the *GEOTRACES* 2017 Intermediate Data Product (Schlitzer et al., 2017).

throughout, with large outgassing fluxes located between -120°E and -115°E, as well as towards the Peruvian upwelling zone.

The rate of vertical exchange is inferred from the outgassing flux by accounting for the vertical gradient in δ^3He between the local mixed-layer and the winter mixed-layer, equation [4.12]. The inferred effective K_z is larger in the subtropical North Atlantic (median = 5.0×10^{-3} m^2 s^{-1}, interquartile range = $2.4 - 10.1 \times 10^{-3}$ m^2 s^{-1}) compared to

the equatorial Pacific (median = 7.1×10^{-4} m^2 s^{-1}, interquartile range = $3.1 – 37.3 \times 10^{-4}$ m^2 s^{-1}) by a factor of 7 (Figure 4.5c). In the equatorial Pacific, inferred K_z is larger towards the center of the transect, decreasing towards the Peruvian upwelling zone. Similarly, in the subtropical North Atlantic, inferred effective K_z decreases towards the Mauritanian upwelling zone. There is a rapid increase in inferred effective K_z from the coastal stations into the turbulent gulf stream in the subtropical North Atlantic.

As winter-time entrainment is only active in the subtropical North Atlantic dataset, the increase in the inferred effective K_z between the two regions allows us to highlight the key role of this process in enhancing the transport of any tracer into the mixed layer. Other mixing processes, such as diapycnal diffusion, eddy turbulence and the breaking of internal waves also contribute to the effective K_z in both regions studied. The calculation of the inferred effective K_z requires at least one measurement of δ^3He between the local MLD and winter MLD. This reduces the number of K_z estimates in the equatorial Pacific ($n_{He\ profiles} = 23$, $n_{Kz} = 13$) as the seasonal mixed layer cycle is narrow, reducing the number of δ^3He measurements available. Overall, our inferred K_z demonstrates the importance of winter-time entrainment in increasing the rate at which properties are transferred into the mixed layer.

4.4.2 Resource Gradients and Oxygen Gradient Correlations

The magnitude of vertical resource fluxes is modulated by the rate of vertical mixing and strength of vertical gradients in resource profiles. Regions of low oxygen concentrations are linked bacterial respiration during the regeneration of sinking organic matter, which increases subsurface resource stocks and strengthens vertical resource gradients. Similarly, the cycling of trace element resources is differentially sensitive to low oxygen levels, meaning greater quantities of some trace elements are retained in deoxygenated waters.

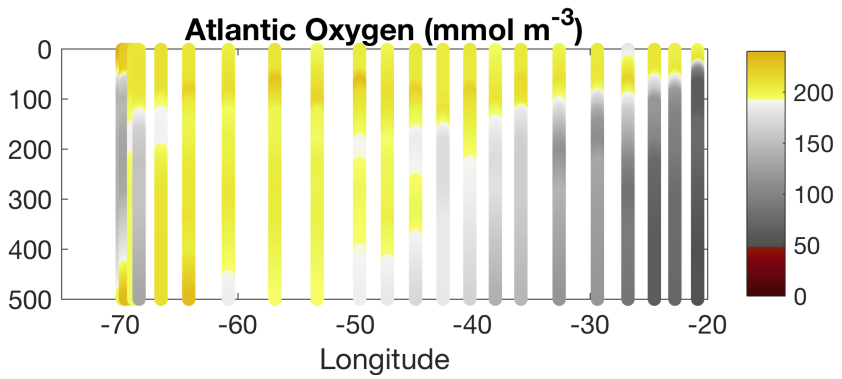

Figure 4.6. Atlantic Oxygen concentration (mmol m^{-3}) along the *GEOTRACES* GA03 subtropical North Atlantic transect (Schlitzer et al., 2017).

4.4.2.1 Subtropical North Atlantic

In the subtropical North Atlantic, oxygen is near saturation throughout the upper 500 m in the west and in the upper ~100 m to the east relative to the minimum of 50.3 mmol m^{-3} in the most eastern profile at 410 m depth (Figure 4.6). Vertical gradients in oxygen between the winter MLD and local MLD are strongest at gyre boundaries and in the east of the transect (Figure 4.7a). The relationship between resource gradients and oxygen gradients, hereafter referred to as $\nabla_{R:O2}$ (d[d(R)/dz] / d[d(O_2)/dz], where R is a given resource), is used to infer strength of resource accumulation or depletion when transitioning into a low oxygen environment. Between the local MLD and annual maximum MLD, d(O_2)/dz is negative while d(NO_3)/dz is positive, meaning that concentrations of NO_3 increase with depth as oxygen levels decrease in all cases (Figure 4.7b), indicating oxygen consumption during the regeneration of sinking material. The relationship between oxygen gradients and NO_3 gradients ($\nabla_{NO3:O2}$ = -0.14 mol m^{-4} / mol m^{-4}, R^2 = 0.95) reveals that strong negative gradients oxygen are mirrored by strong positive gradients in NO_3. Both PO_4 and Si show a similar relationship with oxygen as NO_3, however the magnitude of vertical gradients in PO_4 ($\nabla_{PO4:O2}$ = -0.0097 mol m^{-4} / mol m^{-4}, R^2 = 0.96) and Si ($\nabla_{Si:O2}$ = -0.033 mol m^{-4} / mol m^{-4}, R^2 = 0.75) are weaker compared to NO_3, meaning the subsequent vertical fluxes of PO_4 and Si are weaker than that of NO_3 between the local mixed-layer depth and winter mixed-layer depth.

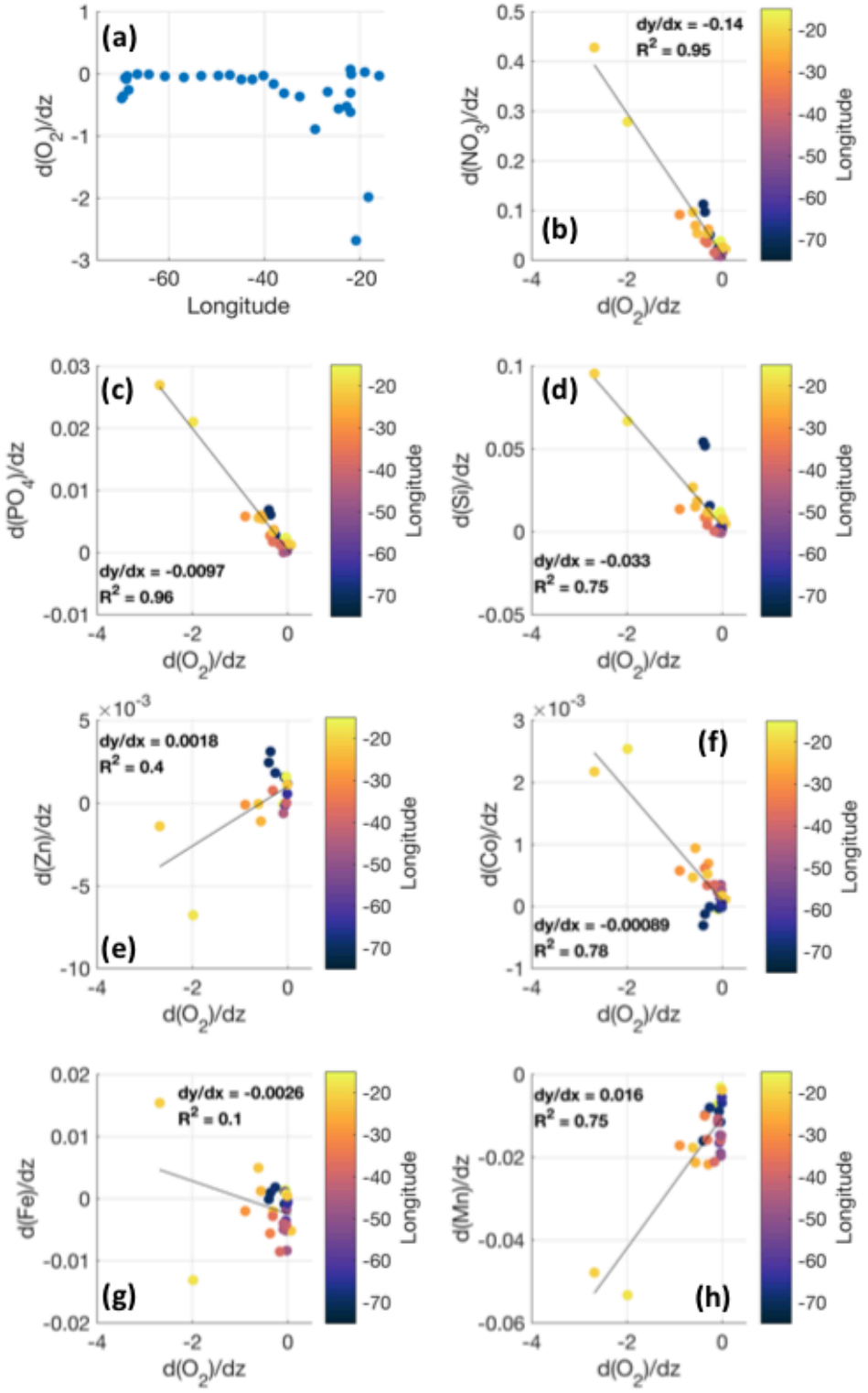

Figure 4.7. Between the local mixed-layer depth to the winter mixed-layer depth, (a) vertical oxygen gradients (mmol m^{-4}), (b – h) relationships between multiple resource gradients (b – d, mmol m^{-4}, e – h, µmol $m^{-4)}$ and oxygen gradients in (mmol m^{-4}) along the *GEOTRACES* GA03 subtropical North Atlantic transect (Schlitzer et al., 2017).

The relationships of Zn, Co, Fe and Mn with oxygen differ from those of NO_3, PO_4 and Si. Gradients in the vertical profiles of Co and Mn correlate well with oxygen gradients ($\nabla_{Co:O2}$ = -0.00089 mmol m^{-4} / mol m^{-4}, R^2 = 0.78, $\nabla_{Mn:O2}$= 0.016 mmol m^{-4} / mol m^{-4}, R^2 = 0.75) compared to that of Zn and Fe ($\nabla_{Zn:O2}$= -0.0018 mmol m^{-4} / mol m^{-4}, R^2 = 0.40, $\nabla_{Fe:O2}$= -0.0026 mmol m^{-4} / mol m^{-4}, R^2 = 0.10). Co exhibits differing relationships with oxygen in the east and west. In the east, Labrador Sea water controls the Co distribution, masking any signals due to oxygen (Noble et al., 2017). In the west, negative Co gradients occur alongside negative oxygen gradients, suggesting both Co and oxygen are consumed at depth. In the east, negative oxygen gradients are concurrent with positive Co gradients, highlighting the established linkage between oxygen and Co availability (Noble et al., 2017). Both Mn and oxygen show negative gradients between the local MLD and winter MLD, however, Mn gradients are formed by the photoreduction of Mn-oxides, increasing Mn stocks in upper layers, while oxygen gradients are formed by consumption at depth (Sunda and Huntsman, 1994). There are regional differences in the relationship of Zn with oxygen. In the west, vertical Zn are positive and strengthen as oxygen gradients are negative and strengthen, while in the east, Zn gradients become increasingly negative as negative oxygen gradients increase in magnitude, consistent with the scavenging of Zn onto sinking biogenic particles in the region (Conway and John, 2014). Contrasts between the eastern and western boundaries are also driven by differences in the sedimentary inputs of Zn, which are inconsistent throughout the water column and affected by a range of processes (Conway and John, 2014). However, differences in water mass mixing is the dominant process controlling Zn gradients along the GA03 (Roshan and Wu, 2015). Like Zn, Fe gradients alongside oxygen gradients show poor correlations, suggests additional processes, such as aeolian deposition and marginal inputs, are important in regulating the vertical Fe profiles.

4.4.2.2 Equatorial Pacific

In contrast to the subtropical North Atlantic, oxygen concentrations in the equatorial Pacific fall below detection limits in the OMZ (Figure 4.8). The OMZ is most prevalent in the east, associated with the Peruvian Coastal Upwelling site, where enhanced productivity in surface waters results in enhanced export and microbial

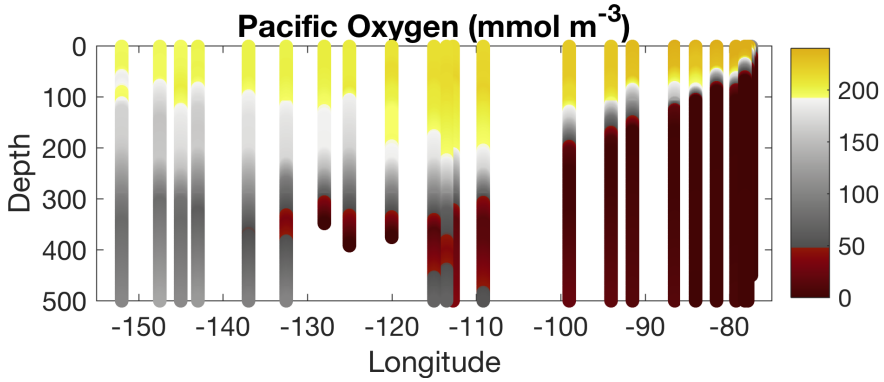

Figure 4.8. Pacific oxygen concentration (mmol m^{-3}) along the *GEOTRACES* GP16 equatorial Pacific transect (Schlitzer et al., 2017).

activity at depth consumes oxygen. Low oxygen concentrations persist in the subsurface throughout the GP16 transect. Oxygen contours deepen from the coastal upwelling site to the center of the transect at -115°E due to the circulation in the region, where upwelled cool low-oxygen waters are transferred below warm surface waters in the open ocean and form Equatorial Subsurface Water (Peters et al., 2018a).

In the equatorial Pacific, oxygen gradients in the low chlorophyll layer are strongest around the OMZ at -100°E (Figure 4.9a). NO_3, PO_4 and Si exhibit the expected inverse relationships with oxygen (Figure 4.9b - d) and are comparable to those in the subtropical North Atlantic. However, the magnitude of the NO_3 gradients compared to oxygen gradients ($\nabla_{NO3:O2}$ = -0.062, R^2 = 0.70) is a factor ~4 larger in the subtropical North Atlantic than in the equatorial Pacific as NO_3 is reduced to NO_2 and subsequently NO, N_2O and N_2 through denitrification in oxygen deplete conditions as found in the equatorial Pacific (Peters et al., 2018b). Unlike NO_3, the gradients in PO_4 and oxygen ($\nabla_{PO4:O2}$ = -0.0089, R^2 = 0.90) are of similar magnitudes between the subtropical North Atlantic and equatorial Pacific. Gradients in Si compared to gradients in oxygen ($\nabla Si_{:O2}$ = -0.12, R^2 = 0.79) are stronger in the equatorial Pacific than the subtropical North Atlantic, suggesting increased dissolution of biogenic silica in the equatorial Pacific.

In the equatorial Pacific, Fe and Mn exhibit strong relationships with oxygen ($\nabla_{Fe:O2}$ = -0.0023, R^2 = 0.86, $\nabla_{Mn:O2}$ = = -0.0046, R^2 = 0.71) compared to that for Zn and Co ($\nabla_{Zn:O2}$ = -0.0008, R^2 = 0.09, $\nabla_{Co:O2}$ =-0.0002, R^2 = 0.41). Both Fe and Mn gradients

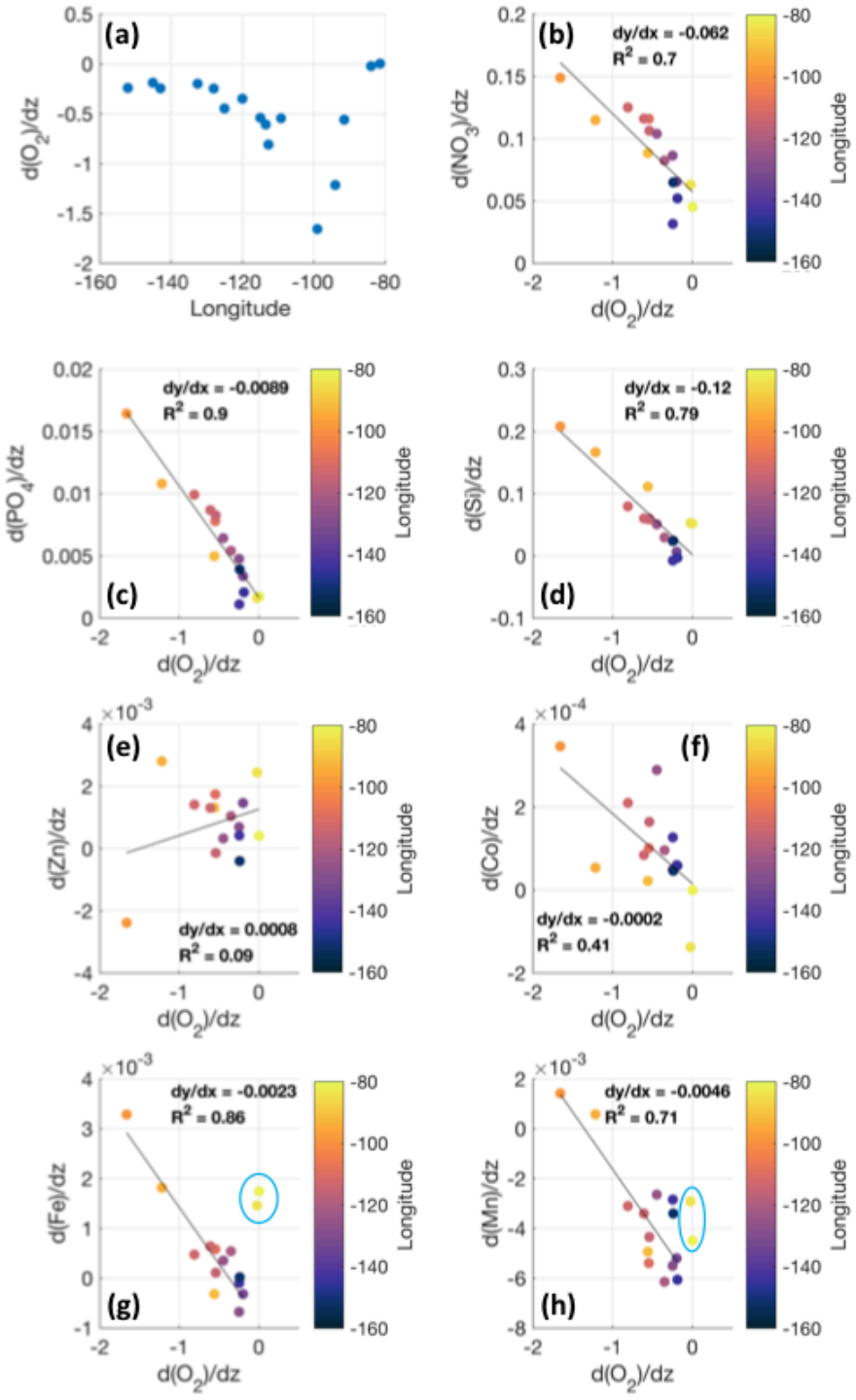

Figure 4.9. Between the density layer at which chlorophyll falls to 20% of the maximum and that plus 1 kg m^{-3}, (a) strength of vertical oxygen gradients, (b – h) relationships between multiple resource gradients (b – d, mmol m^{-4}, e – h, µmol $m^{-4)}$ and oxygen gradients in (mmol m^{-4}) along the *GEOTRACES* GP16 equatorial Pacific (Schlitzer et al., 2017). Datapoints in blue circles are removed from the calculation of the slope and R^2 due to the influence of marginal inputs.

exhibit strong negative relations with oxygen gradients, meaning sharp positive Fe and Mn gradients form where oxygen becomes depleted, leading to a subsequent resource flux. In the Fe and Mn analysis, the two most eastern vertical profiles are omitted as throughout the depth range of interest, oxygen is depleted, meaning no oxygen gradients form. Instead, Fe and Mn are strongly influenced by marginal inputs which are not the focus of this study. Gradients in Zn and oxygen exhibit low R^2 values in both transects, meaning processes influencing the Zn distribution are independent of oxygen. The relationship between Co and oxygen gradients is a ~4.5 less in the equatorial Pacific, low R^2 values omit this observation from further analysis, suggesting different, oxygen independent, processes affect Co in the equatorial Pacific which is not the case in the subtropical North Atlantic. Overall, our results demonstrate the strong dependence of Fe and Mn gradients with gradients in oxygen, while gradients in Zn and Co are affected by other processes.

4.4.3 Atlantic Nutrient Fluxes and Flux Stoichiometry within the Winter Mixed-Layer

The inferred effective K_z is combined with the vertical gradient in resource profiles between the mixed-layer depths at the time of observation and in winter to calculate resource fluxes into the mixed layer. The resource flux is large where either the inferred K_z or resource gradients (dR/dz, where R is given resource and z is depth) are large. Generally, nutrient type resources NO_3, PO_4 and Si exhibit greater fluxes at the gyre boundaries and minimal fluxes in the center of the subtropical North Atlantic gyre (Figures 4.10a, b, c). This emerges as the water column is depleted in NO_3, PO_4 and Si, forming weak nutriclines (dR/dz_{max}) in the center of the gyre. Elevated fluxes in the east arise due to strong gradients in the vertical profiles of each resource formed by the Mauritanian Upwelling Zone. In the west, the turbulent Gulf Stream causes deep winter-mixed layers which facilitate access deep subsurface stocks.

The vertical distribution, and hence vertical flux, of trace-elements Zn, Co, Fe and Mn differs from those of macronutrients NO_3, PO_4 and Si. The Zn flux generally decreases from west to east, becoming negative in the east, meaning mixed-layer Zn availability decreases due to entrainment as surface maxima are eroded (Figure 4.10d). The Co

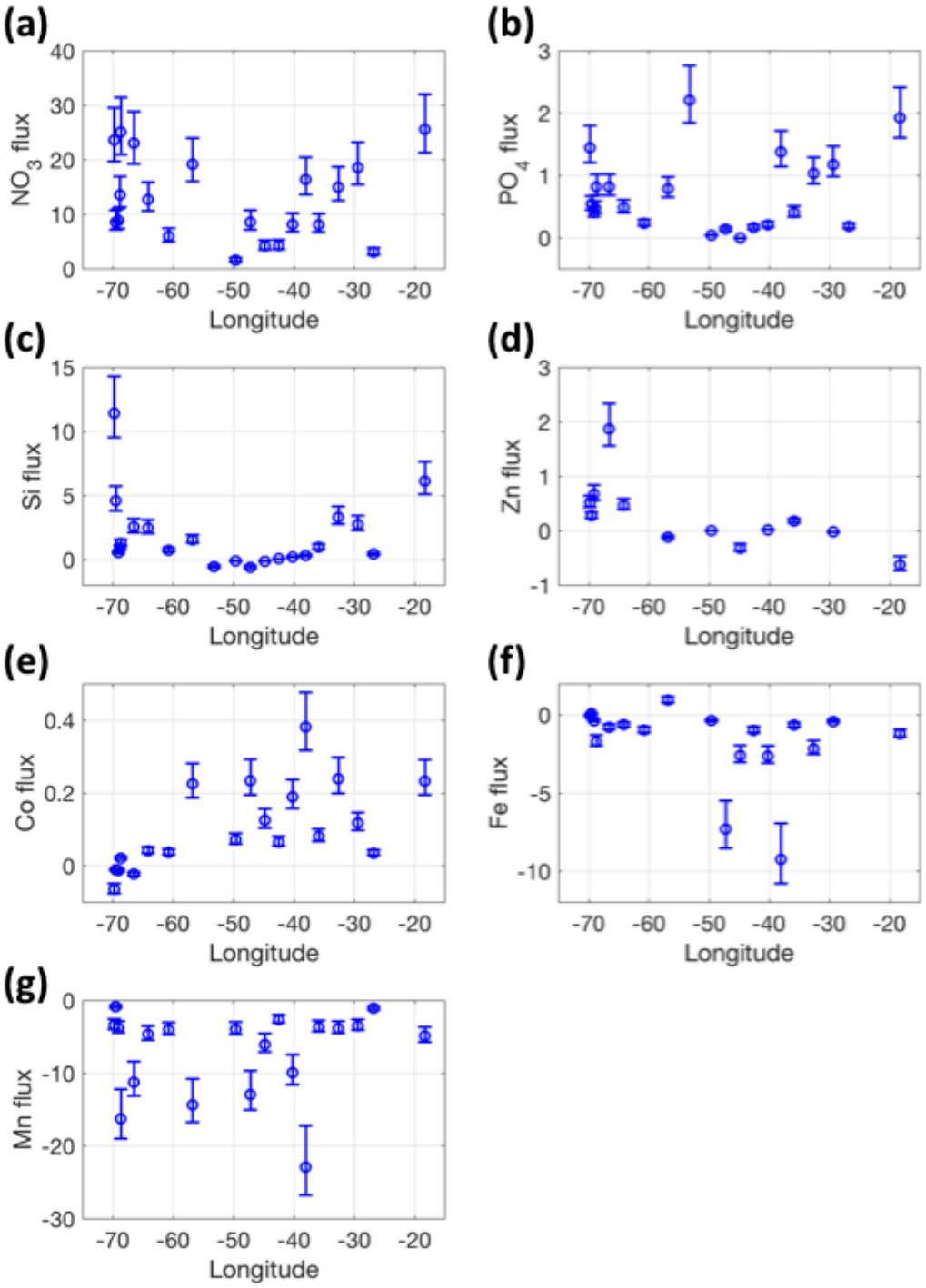

Figure 4.10. Upwards (a – c) macronutrient flux (mmol m^{-2} d^{-1}), and (d – g) micronutrient flux (µmol m^{-2} d^{-1}) into the local mixed layer during winter-time entrainment. Data in the subtropical North Atlantic Ocean along *GEOTRACES* transect GA03 (Schlitzer et al., 2017). Errorbars reported result from uncertainty in the air-sea exchange parameterization (Wanninkhof, 2014) used to infer vertical diffusivity.

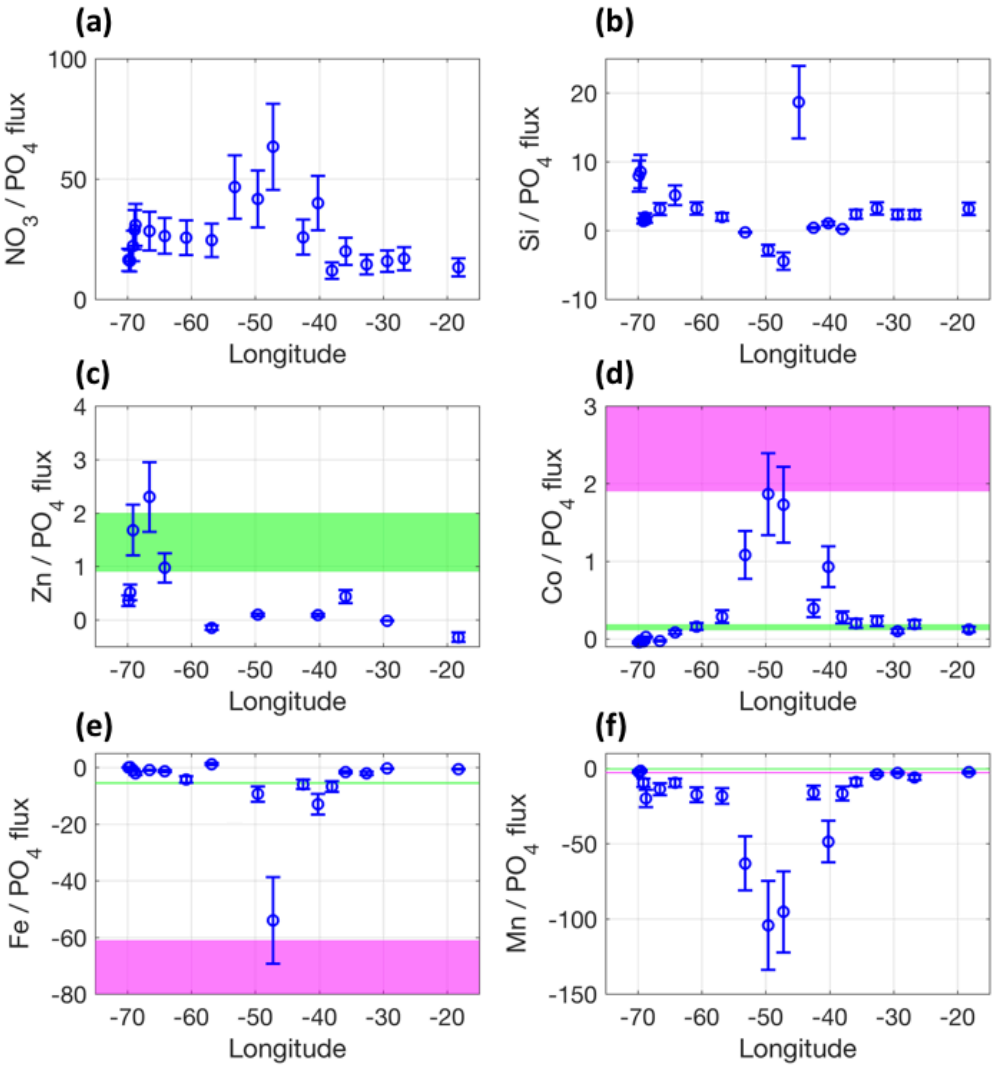

the

Figure 4.11. Stoichiometry of the upward nutrient fluxes (Figure 4) relative to PO_4. (a, b) macronutrient flux stoichiometry (mol mol^{-1}) and (c – f) micronutrient flux stoichiometry, (mmol mol^{-1}) into the local mixed layer during winter-time entrainment. Data in the subtropical North Atlantic Ocean along *GEOTRACES* transect GA03 (Schlitzer et al., 2017). Errorbars reported result from uncertainty in the air-sea exchange parameterization (Wanninkhof, 2014) used to infer vertical diffusivity. Shaded regions highlight the cellular trace metal stoichimonetry of diatoms (magenta) and that of picoplankton and flagellates (green), data from Twining et al. (2015). Note the cellular Zn/PO4 of diatoms is greater than 4 mmol mol^{-1} and does not appear in (c).

flux shows the reverse trend to Zn, increasing from west to east (Figure 4.10e). The structure in the Co flux distribution results from elevated subsurface Co concentrations in the low oxygen conditions in the east (Figure 4.10e), generating larger vertical

gradients in Co and hence increasing the vertical flux. Additionally, surface maxima in Co profiles to the west are eroded by winter-mixing, inducing a negative flux (Figure 10e). The inferred vertical flux of Fe and Mn is generally negative throughout subtropical North Atlantic (Figures 4.10f, 4.10g). Negative fluxes estimated here are indicative of these elements exhibiting scavenged type vertical profiles. Both Fe and Mn are deposited at the surface via dust in the region (Jickells et al., 2016), establishing seasonal surface maxima that are diluted during winter entrainment (Rigby et al., 2020). In the case of Mn, surface concentrations can be buffered against removal by the photoreduction of manganese oxides (Sunda and Huntsman, 1994).

The resource stoichiometry in the vertical nutrient flux enables insight into the relative differences in vertical fluxes and exhibits considerable variation, both spatially and between resources. The NO_3/PO_4 flux is maximal in the center of the North Atlantic subtropical gyre (Figure 4.11a), driven by a deepening of the phosphocline (dPO_4/dz_{max}) relative to the nitracline (dNO_3/dz_{max}), meaning subsurface nitrate stocks are more easily accessed by mixing. The lowest NO_3/PO_4 flux, 18 mol/mol, is located towards the Mauritania upwelling zone in the east. Si/PO_4 shows the opposite structure to NO_3/PO_4, decreasing from the western boundary to the center of the gyre, where Si/PO_4 becomes negative, highlighting a surface maximum in Si (Figure 4.11b). Zn/PO_4 is greatest in the Gulf Stream where deep winter mixed layers are able to access Zn stocks (Figure 4.11c), however in the central and eastern gyre Zn/PO_4 is reduced due to the reversible scavenging of Zn which does not affect PO_4 (Weber et al., 2018) or lack of Zn in waters originating in the Southern Ocean which influence the eastern region of the transect (Wyatt et al., 2014, Jenkins et al., 2015). Co/PO_4 shows a similar distribution to NO_3/PO_4, where the maxima are found in the center of the gyre (Figure 4.11d). At the western boundary, Co/PO_4 is negative due to an enrichment of Co in the upper water column inducing small negative Co flux. Towards the eastern boundary, expected increases in Co/PO_4, as Co is sensitive to low oxygen conditions, are masked by contemporaneous increases in PO_4 due to the upwelling of major nutrient rich deep waters. Both Fe/PO_4 and Mn/PO_4 show negative stoichiometric fluxes due to the scavenged type nature of Fe and Mn resource profiles (Figures 4.11e, f). The spatial pattern in the Fe/PO_4 and Mn/PO_4 fluxes cause the availability of Fe and Mn to decrease non-uniformly across the subtropical North Atlantic gyre relative to PO_4 during entrainment events.

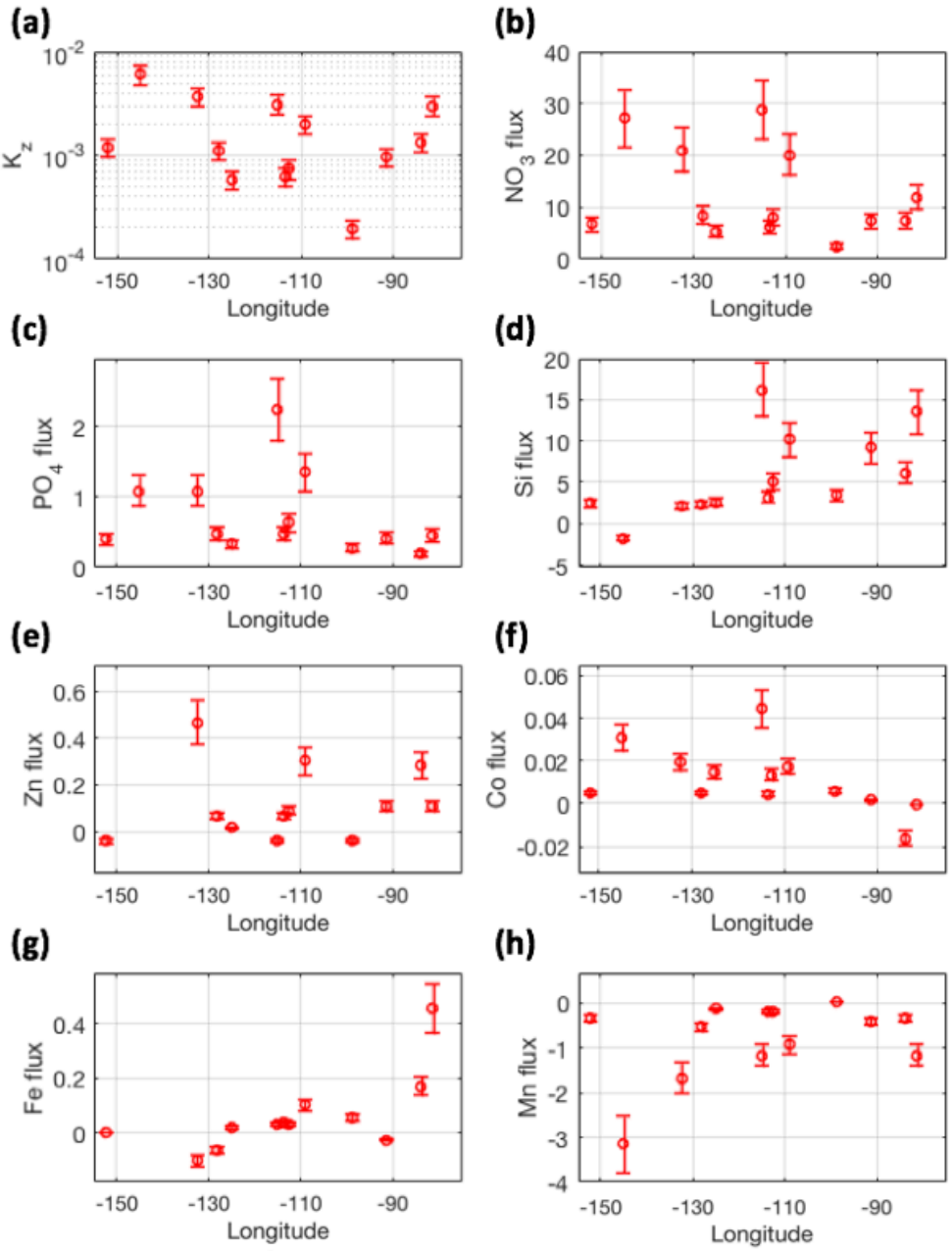

Figure 4.12. (a) Inferred vertical diffusivity (m^2 s^{-1}) used to calculate the upwards (b – d) macronutrient flux (mmol m^{-2} d^{-1}) and (e – h) micronutrient flux (µmol m^{-2} d^{-1}) into the productive region of the water column. Data in the equatorial Pacific Ocean along *GEOTRACES* transect GP16 (Schlitzer et al., 2017). Errorbars reported result from uncertainty in the air-sea exchange parameterization (Wanninkhof, 2014) used to infer vertical diffusivity.

4.4.4 Pacific Productive Zone

4.4.4.1 Inferred Diapycnal Mixing

In previous sections (Section 4.1.1) we have discussed the inferred K_z between the local mixed-layer depth and winter mixed-layer depth. To estimate resource fluxes into the Pacific productive zone, K_z is recalculated using the upwards helium flux and vertical gradients in the low chlorophyll layer. The median inferred K_z into the productive region of the water column is 1.1×10^{-3} m^2 s^{-1} (interquartile range = 0.7 – 3.0×10^{-3} m^2 s^{-1}). The inferred K_z into the productive region is larger (Figure 4.12a) and less variable than K_z between the local and winter MLD in the same region (Figure 4.4c) due to seasonal detrainment (shoaling) in the winter MLD at the time of sampling. However, comparison between the median estimates of inferred K_z is difficult due to the availability of observations in the vertical dimension. For instance, at the most western station, helium measurements are available between the isopycnal at the base of productive region and that plus 1 kg m^{-3}; however, there is insufficient data to estimate K_z between the local and winter mixed-layer depth. Nevertheless, we are able to estimate the resource flux into the productive region where sufficient helium measurements are available to calculate K_z.

4.4.4.2 Resource Flux and Flux Stoichiometry to Biota

In the equatorial Pacific, the vertical flux of resources varies spatially and between resource. The upward flux of NO_3 through the low chlorophyll layer follows a similar structure to the inferred K_z, where large NO_3 fluxes occur alongside high K_z estimates west of -100^{o}E (Figure 4.12b). Both inferred K_z and the NO_3 flux increase eastward of -100^{o}E. There is a mismatch between the magnitude of the NO_3 flux to similar K_z values due to spatial changes in gradient of the NO_3 vertical profile. The PO_4 flux distribution is akin to NO_3, reflecting high K_z estimates in the west and weaker vertical gradients in the east (Figure 4.12c). The Si flux increases eastward along the equatorial pacific transect. The increase is driven by depleted upper waters to the west, meaning vertical gradients within the defined density stratum are insufficient to cause a vertical flux, however, towards the east of the transect, vertical Si gradients exist in upper

waters and drive an upwards flux (Figure 4.12d). Overall, NO_3 and PO_4 fluxes show similar distributions, while the Si flux increases eastward.

The vertical fluxes of trace-elements demonstrate a range of spatial structures in the equatorial Pacific. The Zn flux shows little spatial structure or concurrence to high K_z estimates (Figure 4.12e). The Co flux decreases from west to east, indicating the Co vertical profile transitions from nutrient like in the west to scavenged like in the east (Figure 4.12f). The scavenged-like profile of Co in the east is linked to the sensitivity of Co to the low oxygen environment located beneath the main thermocline (Figure 4.8). Fe is depleted in the upper waters of the equatorial Pacific resulting in low Fe flux estimates, however; the upwards Fe flux increases at the continental margin due to sedimentary inputs of Fe at depth forming gradients in the Fe vertical profile (Figure 4.12g). The Mn flux is downwards throughout the section, indicative of the expected scavenged type nature of Mn, while the magnitude of the Mn flux is set by the K_z estimate (Figure 4.12h). Overall, resource fluxes exhibit differing spatial structures, linked to the inferred K_z and underlying processes, such as redox chemistry in oxygen minimum zones and marginal inputs, which drive the individual resource distributions.

The stoichiometry of a given resource flux relative to the PO_4 flux emulates the relationship between the resource and PO_4 within the selected density bounds. The NO_3/PO_4 flux into the productive layer decreases from the west to the center of the transect, then increases towards the Peruvian upwelling zone (Figure 4.13a). This spatial structure indicates the nitracline is shallower at the edges of the transect, relative to the phosphocline. Si/PO_4 shows a clear increase from west to east as the upper water column is deplete in Si to the west and Si nutricline shoals eastward relative to the phosphocline (Figure 4.13b). The Zn/PO_4 flux stoichiometry is inconsistent as the low absolute fluxes in both Zn and PO_4 are highly sensitive to small gradients in the vertical resource profile (Figure 4.13c). Co/PO_4 decreases from east to west as Co transitions from a nutrient-type to a scavenged-type vertical profile while PO_4 remains nutrients type (Figure 4.13d). Fe/PO_4 shows a distribution similar in structure to that of Si/PO_4, where the flux stoichiometry is relatively low in the open ocean and increases towards the ocean margin (Figure 4.13e). Si and Fe exhibit similar patterns in absolute flux, however, the resource fluxes are driven by different

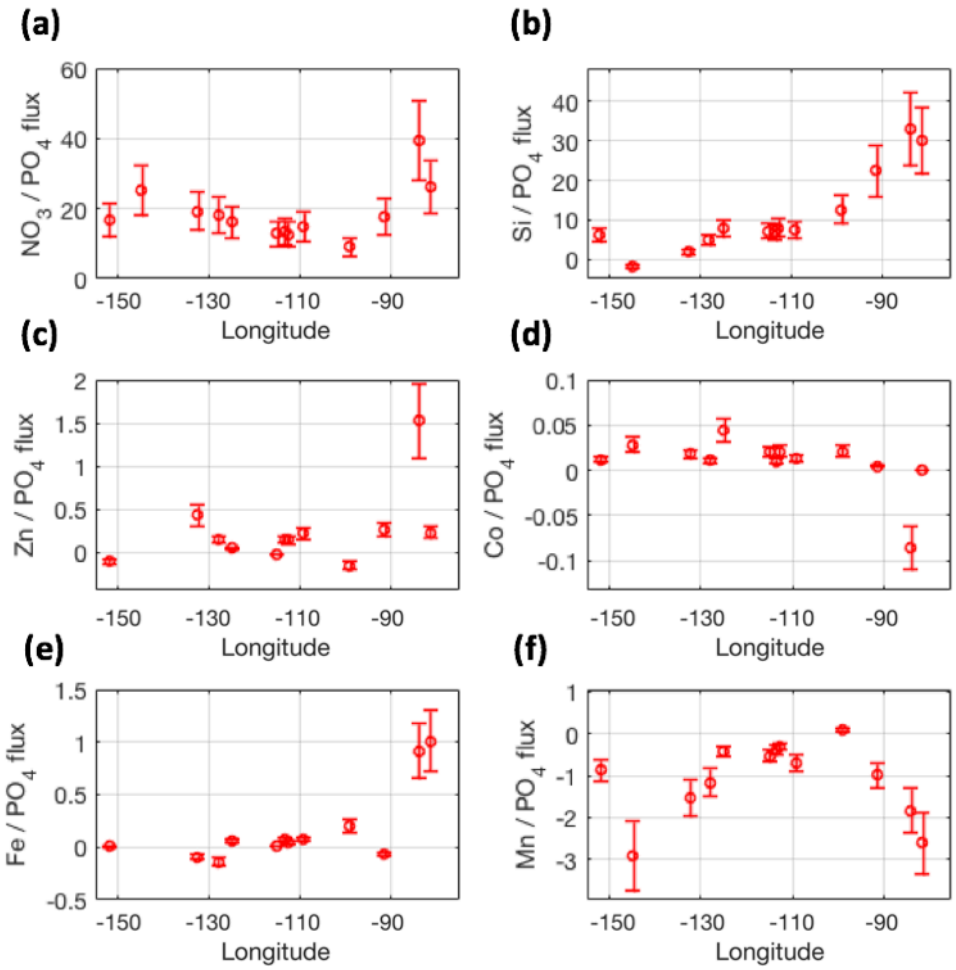

Figure 4.13. Stoichiometry of the upward nutrient fluxes relative to PO_4. (a, b) macronutrient flux stoichiometry (mol mol^{-1}) and (c – f) micronutrient flux stoichiometry (mmol mol^{-1}) into the productive region of the water column. Data in the equatorial Pacific Ocean along *GEOTRACES* transect GP16 (Schlitzer et al., 2017). Errorbars reported result from uncertainty in the air-sea exchange parameterization (Wanninkhof, 2014) used to infer vertical diffusivity.

mechanisms as discussed above. Mn/PO_4 is negative throughout, meaning that while Mn concentrations are diluted, PO_4 concentrations increase (Figure 4.13f).

The data used in this study represent two different oceanographic regimes, leading to stark differences in the resource fluxes (Figure 4.10, 4.12). The vertical fluxes of NO_3 and PO_4 are a factor ~2 smaller in the equatorial Pacific than in the subtropical North Atlantic, while the vertical Si flux is similar between regions. In contrast, Zn and Mn fluxes are a factor ~5 smaller in the equatorial Pacific than the subtropical North

Atlantic and Co and Fe fluxes are a factor ~10 smaller in the equatorial Pacific than the subtropical North Atlantic. Therefore, the stoichiometry of the vertical fluxes is varied between the regions studied. Generally, the vertical resource flux is depleted in Zn, Co, Fe and Mn relative to PO_4 in the equatorial Pacific compared to subtropical North Atlantic.

4.5 Discussion

4.5.1 Inferred Effective K_z from Transect Studies

Our results demonstrate that the winter-time entrainment of thermocline waters into the mixed layer increases the physical transfer of properties by a factor of ~7. Previous studies have also investigated the seasonal cycle in K_z (Wu et al., 2011, Whalen et al., 2015). From 300 m to 1800 m depth, a seasonal cycle in K_z has been observed in the Southern Ocean (Wu et al., 2011). The seasonal cycle in K_z is attributed to concurrent changes in wind stress and is more pronounced in the upper ocean, the largest change in K_z is found from 300 m to 600 m, where K_z increases by a factor ~2 from autumn to winter (Wu et al., 2011). Similarly, Whalen et al. (2015) demonstrated that the seasonal cycle in K_z increases mixing by a factor 2 – 5 from 300 m to 900 m in mid-latitudes due to the prevalence of storms. In this study, we focus on depths shallower than 300m and hence the seasonal cycle of the mixed layer is included in our calculation of K_z, and therefore increases seasonality in K_z. The seasonal cycle apparent in K_z is important when considering the temporal extrapolation of single point data provided by ocean transect studies, particularly in regions where deep mixed layers occur.

In this study, physical processes acting during the two oceanographic transects included are in contrast and directly comparing their upper ocean resource distributions is complex. In the subtropical North Atlantic transect, the mixed layer is deepening, and winter-time entrainment therefore plays an important role in setting mixed-layer resource stocks. However, in the equatorial Pacific entrainment is inactive and the transfer of resources from the thermocline to the mixed layer is diminished. While we are able to demonstrate the importance of entrainment when

interpreting upper ocean distributions in the subtropical North Atlantic, applying our finding to the global ocean is challenged by regional differences in the amplitudes of annual mixed-layer cycles. For example, in the sub-tropical North Atlantic, the mixed-layer depth varies from 31 m in August to 142 m in March, in contrast, the annual maximum mixed-layer depth extends to ~500 m in the high latitude North Atlantic (Holte et al., 2017). Therefore, as the amplitude of the mixed layer may be greater or smaller than our study site, the increase in the physical transfer of properties during periods of entrainment is greater or less than ~7, respectively. This has important implications in driving seasonality in the delivery of resources to the mixed layer and subsequent phytoplankton growth. Further, our results demonstrate the need to consider the dominant physical processes at the time of observation when interpreting and comparing snapshots of the upper ocean.

4.5.2 Linkages Between the Oxycline and Nutriclines

Vertical resource fluxes are established by K_z and gradients in the vertical profiles of resources. Results in the subtropical North Atlantic and equatorial Pacific provide insights into the relationships between the strength of oxygen gradients and vertical resource gradients. Generally, the magnitude of resource gradients is linked to the strength of oxygen gradients in both transects. NO_3, PO_4 and Si show inverse relationships with oxygen, suggesting preformed resources or local regeneration at depth are important in both regions (Figure 4.7). There are regional differences in the relationships of each trace-metal with oxygen. Zn gradients demonstrate a weak correlation with oxygen gradients ($R^2 = 0.4$, GA03, and $R^2 = 0.09$, GP16), however; in the subtropical North Atlantic there are systematic contrasts in the east and west (Figure 4.7). In the west, Zn gradients and oxygen gradients are negatively correlated, while the reverse is true in the east. Zonal differences in the distribution of Zn have been attributed to the relative influence of water masses in the region (Roshan and Wu, 2015). In the west, both Atlantic Equatorial Water and North Atlantic Central Water influence the water column equally, while in the east, Atlantic Equatorial Water is not present (Roshan and Wu, 2015). Poor correlations of Zn with oxygen in the subtropical North Atlantic are observed in this study and Roshan and Wu (2015) and are mirrored in the equatorial Pacific (Figure 4.9). Stronger Co gradients coincide with

stronger oxygen gradients in the equatorial Pacific compared to the subtropical North Atlantic. In the subtropical North Atlantic, the influence of oxygen on Fe is unclear due to the role of other processes, such as aeolian deposition and marginal inputs, in regulating Fe availability. However, in the equatorial Pacific, Fe gradients and oxygen gradients demonstrate a clear linkage, excluding data near the continental margin where sedimentary inputs mask the role of oxygen gradients. The relationship between Mn gradients and oxygen gradients is opposite in the subtropical North Atlantic and equatorial Pacific, where Mn gradients strengthen and weaken respectively as oxygen gradients increase. Overall, our results demonstrate that there are links between Zn, Co, Fe and Mn gradients with oxygen gradients, however those links are not causal.

4.5.3 Contextualising Vertical Resource Fluxes

The supply of resources to the mixed layer in the subtropical North Atlantic by winter-time entrainment is augmented by aeolian deposition (dust). We calculate soluble resource supply based on an aeolian deposition model (Mahowald et al., 2005), crustal ratios (Rudnick and Gao, 2003) and mineral solubility measured during the GA03 expedition (Shelley et al., 2018). In the subtropical North Atlantic, the rate at which NO_3, PO_4 and Si are deposited at the surface is less than 1% of the rate at which they are transferred across the base of the mixed layer by physical mixing processes, highlighting the role of entrainment in replenishing depleted macronutrient stocks (Table 4.1). The daily supply of micronutrients Zn and Co the mixed layer via dust is outweighed by the supply via physical mixing as dust is depleted in both Zn and Co. While dust is consider as a major source of Fe to the subtropical North Atlantic (Jickells et al., 2005, Baker and Jickells, 2017), the soluble Fe supply from lithogenic sources is 0.28 ± 0.39 μmol m^{-2} d^{-1}, while the Fe loss through physical processes is 1.7 ± 2.58 μmol m^{-2} d^{-1} (Figure 4.10, Table 4.1). The mismatch is partially explained by considering that winter-time entrainment is active for up to 6 months per year, whereas dust is deposited at the surface ocean throughout the year. Dust derived surface Fe stocks accumulate in the shallow summer-mixed layer before winter-time entrainment effectively washes out the surface maxima. Like Fe, the loss of Mn during the physical exchange (14 ± 30 μmol m^{-2} d^{-1}) between the surface mixed-layer and thermocline does not equate to the input from dust (0.048 ± 0.063 μmol m^{-2} d^{-1}).

		Supply Pathway	
		Dust	Vertical Transport
Resource	NO_3	0.080 ± 0.078	17 ± 21
	PO_4	0.000099 ± 0.000130	0.71 ± 0.62
	Si	0.015 ± 0.020	1.9 ± 2.8
	Zn	0.0030 ± 0.0045	0.24 ± 0.63
	Co	0.00031 ± 0.00040	0.22 ± 0.52
	Fe	0.28 ± 0.39	-1.7 ± 2.6
	Mn	0.048 ± 0.063	-14 ± 30

Table 4.1. Flux of NO_3, PO_4 and Si (all mmol m^{-2} d^{-1}), Zn, Co, Fe and Mn (all μmol m^{-2} d^{-1}) into the surface mixed layer via soluble dust deposition and vertical transport during the GA03 cruise.

Additional processes are required to maintain mixed-layer Mn stocks, such as lateral transport from margins and the photoreduction of manganese-oxides (van Hulten et al., 2017). Generally, the magnitude of resource supply via vertical transport estimates outweighs estimates of dust inputs to the mixed layer.

The subtropical North Atlantic experiences episodic dust storm events throughout the year, culminating in some of the largest short-term (hours to days) dust fluxes over the global open ocean (Duce and Tindale, 1991, Aumont et al., 2008). During the collection of data in the subtropical North Atlantic, equipment was blanketed by a layer of North African dust (Boyle et al., 2015a). The loss of Fe during entrainment calculated in this study therefore reflects downward transport following an extreme dust event. However, dust deposition rates are sourced from an annual deposition model which distributes dust evenly throughout the year and therefore does not account for the episodic nature of deposition events. Hence, caution must be taken when comparing estimates of resource supply from single point observations with output from annual deposition fields.

In contrast to the subtropical North Atlantic, the supply of resources to biota in the equatorial Pacific via dust is minimal due to a lack of proximal arid regions (Jickells et al., 2005). Instead, internal recycling and the offshore transport of sedimentary-derived resources plays an important role in fueling primary production in the upper

water column (Vedamati et al., 2014, Rafter et al., 2017). However, export must be replenished by external supply pathways over long time periods, meaning physical transfers into the productive zone, such as those estimated in this study, are important to sustain growth.

4.5.4 Are Resource Fluxes Governed by K_z or Nutriclines?

In the previous section, we argue that the physical transfer of resources from the thermocline to the mixed layer is crucial in maintaining nutrient stocks. The physical flux is derived from K_z, which varies spatially (Figure 4.5), and vertical resource gradients, which varies spatially and between resources (Rigby et al., 2020). We apply a linear model to calculate the resource flux as a function of normalized vertical resource gradients and K_z (Table 4.2). The linear model performs well ($p < 0.05$, 95% confidence interval) in 22 of the 32 measured variables (K_z and resource gradients, repeated for each resource) in Table 4.2. However, NO_3 and Co are the only resources where the linear model successfully operates in both regions ($p < 0.05$, 95% confidence interval, NO_3 $R^2_{ATLANTIC} = 0.97$, NO_3 $R^2_{PACIFIC} = 0.83$, Co $R^2_{ATLATIC} = 0.93$, Co $R^2_{PACIFIC} = 0.70$). In the subtropical North Atlantic, K_z causes most variability in the resource flux of NO_3, Zn, Co and Mn, while vertical gradients and

		GA03			GP16		
		K_z	d[N]/dz	R^2	K_z	d[N]/dz	R^2
Resource Flux	**NO_3**	0.70	0.26	0.97	0.89	0.77	0.83
	PO_4	0.35	0.34	0.75	0.74	*0.55*	0.48
	Si	*-0.05*	0.65	0.72	*0.16*	*0.30*	0.06
	Cd	*-1.03*	*1.02*	0.77	1.01	0.35	0.88
	Zn	1.75	0.08	0.69	*0.68*	0.45	0.61
	Co	1.28	0.27	0.93	1.17	0.69	0.70
	Fe	0.80	0.92	0.58	*-1.29*	*1.56*	0.35
	Mn	1.21	0.36	0.98	1.20	*0.05*	0.98

Table 4.2. Coefficients from the linear model applied to the resource flux, modelled as a function of normalized vertical diffusivity (K_z) and normalized resource gradients (d[N]/dz). Red values highlight linear models where a confidence interval of 95% is not met. Data from the GEOTRACES 2017 Intermediate Data Product (Schlitzer et al., 2017), located in the subtropical North Atlantic (GA03) and equatorial Pacific (GP16).

K_z play near equal roles in modulating the fluxes of PO_4 and Fe. In the equatorial Pacific, K_z causes most variation in the vertical flux of Cd and Co, while the NO_3 physical flux is influenced by K_z and the vertical NO_3 gradient equally. In the subtropical North Atlantic, the linear model produces coefficients for vertical gradients that is 37% and 21% of the coefficient for mixing in the case of NO_3 and Co, respectively. In contrast, the linear model coefficient for vertical gradients causing resource flux variability in the equatorial Pacific is 87% and 59% of the physical mixing coefficient in the case of NO_3 and Co, respectively. This result demonstrates the greater role of mixing in establishing vertical resource fluxes in the subtropical North Atlantic compared to the equatorial Pacific, where the relative role of vertical resource gradients is increased.

4.5.5 Impact of Resource Fluxes on Biota

In the subtropical North Atlantic, direct measurements of the resource composition of specific phytoplankton were taken using synchrotron x-ray fluorescence methods allowing a direct comparison between the trace element resource fluxes and biological accumulation to highlight regions of resource deficiency (Twining et al., 2015). In general, there are taxon specific and element specific differences in the mismatch between the resource supply stoichiometry and cellular accumulation. The upwards Zn/PO_4 flux throughout the Atlantic dataset is well below the cellular stoichiometry of diatoms (12 ± 3 mmol/mol) throughout the Atlantic section, meaning supply is deficient in Zn relative to PO_4 (Figure 4.11). The cellular Zn/PO_4 accumulation of picoplankton (1.8 ± 0.2 mmol/mol) and flagellates (1.2 ± 0.3 mmol/mol) matches the Zn/PO_4 supply stoichiometry in the western boundary, however upwards supply to the central and eastern gyre is Zn deficient. The upwards Co/PO_4 flux is deficient in Co for diatoms (3.1 ± 1.2 mmol/mol) throughout the subtropical North Atlantic gyre, but Co/PO_4 fluxes are similar to picoplankton (0.15 ± 0.04 mmol/mol) and flagellate (0.04 ± 0.01 mmol/mol) accumulation for much of the transect (Figure 4.11). Negative Fe/PO_4 and Mn/PO_4 fluxes signify a loss of Fe and Mn relative to PO_4. The physical Fe/PO_4 downward flux is generally smaller than Fe/PO_4 accumulation in diatoms (75 ± 15 mmol/mol), picoplankton (5.0 ± 0.4 mmol/mol) and flagellates (5.0 ± 0.9 mmol/mol), meaning uptake by biota is a greater sink of Fe than downward mixing,

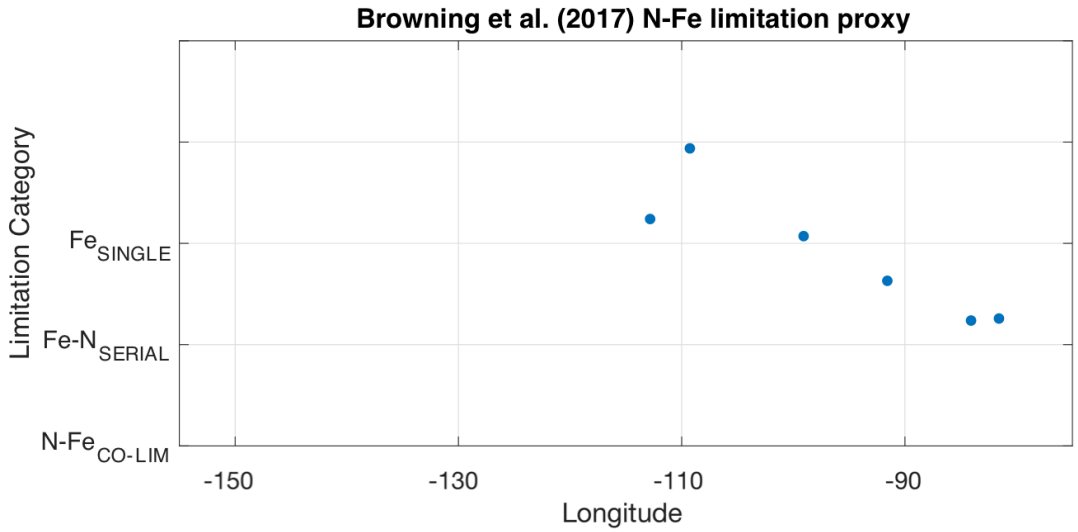

Figure 4.14. Transition in nutrient limitation category in the upwards supply to the productive zone in the equatorial Pacific (GP16), defined as the region with elevated fluorescence. Limitation is defined following the formulation in Browning et al. (2017). Data from the *GEOTRACES* 2017 Intermediate Data product (Schlitzer et al., 2017).

relative to changes in PO_4 due to biological uptake and downward mixing (Figure 4.11). The reverse of Fe/PO_4 is true for Mn/PO_4, where the downward flux of Mn/PO_4 far exceeds the typical accumulation in biomass (diatoms = 75 ± 15 mmol/mol, picoplankton = 5.0 ± 0.4 mmol/mol, flagellates = 5.0 ± 0.9 mmol/mol). Overall, our results suggest that diatom accumulation rates exceed the upward resource of Co and Zn relative to PO_4, while the accumulation by flagellates and picoplankton is deficient in Zn, relative to PO_4, in the central and eastern gyre. Previous studies have demonstrated that biota in the subtropical North Atlantic are primarily NO_3 deficient and secondarily PO_4 deficient (Moore, 2016). In this study, we find Co or Zn deficiency in the upwards flux by comparisons to cellular accumulation, meaning biota are reliant upon additional resource supply pathways to augment the supply of Co and Zn by vertical mixing.

In the equatorial Pacific, measurements of phytoplankton cellular composition concurrent with resource observations are unavailable. However, we apply the N-Fe proxy identified by Browning et al. (2017a) to our estimates of vertical resource supply through the low chlorophyll layer to gauge the prevalence of singular-, serial-, or co-

limitation by N and Fe (Figure 4.14). In the center of the equatorial Pacific section, resource supply into the productive zone is singularly Fe limited. Fe-limitation is reduced with proximity to the continental margin, where resource supply becomes Fe-N serial limited. The transition in the N-Fe limitation proxy demonstrates that the upward resource flux is generally richer in Fe compared to NO_3 towards the continental margin. Changes in the NO_3/Fe flux stoichiometry are induced by differences in the gradients of Fe and NO_3. Moving eastward, gradients in Fe strengthen relative to gradients in NO_3, meaning the vertical flux is richer is Fe towards the east, thus reducing the potential for Fe limitation. The vertical flux of Fe is important as intense chlorophyll maxima are located at depth in the region and the adaptation of phytoplankton to low light at depth requires additional Fe (Sunda and Huntsman, 1997). Therefore, the upwards flux in the eastern equatorial Pacific is better able to support high Fe demands of phytoplankton located in the subsurface chlorophyll maxima.

4.5.6 Wider Considerations

Climate projections over the next century project an overall increase in ocean stratification (Lefebvre and Goosse, 2008, Sen Gupta et al., 2009, Capotondi et al., 2012). Enhanced stratification causes a decrease in vertical exchange. The linear model applied in this study (Table 4.2) demonstrates that resource fluxes differ in sensitivity to changes in mixing between resource, while regional contrasts are also important. In a system where both mixing and vertical gradients vary, some resources are more sensitive to changes in mixing. For example, in the subtropical North Atlantic, NO_3, Zn, Co and Mn are highly sensitive to changes in mixing rather than changes in their vertical gradients (Table 4.2), meaning future changes in mixing may induce a stronger response in the fluxes of NO_3, Zn, Co and Mn compared to PO_4 and Fe. This result has important implications in the Fe replete subtropical North Atlantic, where a reduction in NO_3 supply from below accompanied by relatively smaller changes in PO_4 and Fe supply enhances the niche for nitrogen fixing phytoplankton by elevating the Fe/N and P/N supply ratio (Ward et al., 2013). In the equatorial Pacific, resource fluxes are less sensitive to changes in mixing, meaning that the

implications of reduced mixing in warming ocean will be largely controlled by changes in vertical resource profiles and their vertical gradients.

In this study, oxygen gradients are linked to gradients in vertical resource profiles (Figure 4.7, 4.9). Historical reconstructions of upper ocean oxygen content over the past 50 years have demonstrated a decrease in the oxygen content in most regions of the global ocean (Stramma et al., 2008, Schmidtko et al., 2017, Bindoff et al., 2019). The decrease in oxygen content is primarily due to two processes: (1) warming and the associated reduction in oxygen solubility, and (2) an increase in stratification which reduces ventilation, promoting interior respiration and the consumption of oxygen at depth (Bindoff et al., 2019). Changes to the distribution of oxygen has important consequences for the cycling of resources which are affected by oxygen. For example, in the equatorial Pacific, the 0.05 mmol m^{-3} oxygen contour, which is an important threshold for denitrification and the accumulation of nitrite (Thamdrup et al., 2012), extends from the coastal upwelling site to -100^{o}E at present (Figure 4.8). However, as OMZ expand by volume, the 0.05 mmol m^{-3} oxygen contour may extend westward, affecting the distribution of nitrogen-species and denitrification.

As OMZs expand, vertical gradients in oxygen will alter, shifting vertical gradients of trace-element resources and thereby altering the associated resource flux. In the case of water where subsurface oxygen levels are below detection limits (for example, eastern equatorial Pacific), the future warming and reduction in solubility will decrease oxygen content at the surface, causing a reduction in the vertical gradient of oxygen. The decrease in oxygen gradients causes a similar decrease in the vertical gradients of Co, Fe and Mn (Figure 4.9), reducing their vertical flux. In contrast, numerous studies have demonstrated that the subsurface ocean (100m – 600m depth) is losing oxygen at a greater rate than the surface layer (0m – 100m), causing an increase in vertical oxygen gradients (Helm et al., 2011, Ito et al., 2017, Schmidtko et al., 2017). In this case, the increase in vertical oxygen gradients would cause an increase in vertical Co, Fe and Mn gradients and increase the resource flux. However, global models tend to project overall decreases in net primary production (Bopp et al., 2013, Laufkötter et al., 2015, Bindoff et al., 2019), demonstrating that sharper resource gradients do not mitigate against projected increases in stratification in reducing the resource flux. This hypothesis is future supported by the linear model results presented

in Table 4.2 which show K_z plays the dominant role in setting resource fluxes. In summary, the response of vertical resource gradients to future changes in oxygen distributions varies between resource and scenario, with important consequences that affect the vertical flux of key bio-essential resources.

4.6 Conclusions

In this study, we quantify the physical transfer of resources into the upper ocean from *in-situ* observations in the subtropical North Atlantic and equatorial Pacific. The underlying physical processes acting in each region are in contrast. Winter-time entrainment is active in the subtropical North Atlantic only, which leads to a factor 7 enhancement in the transfer of properties through the base of the mixed layer. We show that broad patterns in the supply of resources to the upper ocean are dependent upon physical mixing and vertical gradients in key resources, which are shaped by underlying physical and biogeochemical processes, such as the vertical oxygen gradient. NO_3, PO_4, Si and Co exhibited a clear relationship with oxygen in the subtropical North Atlantic. Relationships between NO_3, PO_4, Si, Co, Fe and Mn and oxygen differ in the equatorial Pacific, due to regional differences in their biogeochemical cycling. In the subtropical North Atlantic, NO_3, PO_4 and Si physical fluxes are greater towards gyre boundaries, Zn fluxes decrease eastward, while Co fluxes increase eastward. Physical mixing decreases the availability of scavenged resources Fe and Mn in the mixed layer. Resource flux structures are less clear in the equatorial Pacific. Our results show that vertical gradients play a greater role in causing resource flux variability in the equatorial Pacific compared to the subtropical North Atlantic where the effective K_z dominates. This has important implications when considering how future changes to stratification and oxygen minimum zones affect resource fluxes and subsequent productivity.

Chapter 5

Resource Fluxes Inferred by Application of Vertical Microstructure Profilers Along the Mid-Atlantic Ridge in the Subtropical Atlantic Ocean

Shaun. J. Rigby[1], Carl P. Spingys[2], Alessandro Tagliabue[1], Eric P. Achterberg[3], J. A. Mattias Green[4], Maeve C. Lohan[2], Alistair Lough[5], Joseph A. Resing[6], E. Malcolm S. Woodward[7] and Richard. G. Williams[1]

[1] Department of Earth, Ocean and Ecological Sciences, School of Environmental Science, University of Liverpool, UK.

[2] School of Ocean and Earth Sciences, University of Southampton, National Oceanography Centre, Southampton, UK.

[3] GEOMAR Helmholtz Centre for Ocean Research Kiel, Kiel, Germany.

[4] School of Ocean Sciences, Bangor University, Menai Bridge, UK.

[5] Faculty of Environment, University of Leeds, Leeds, UK.

[6] Joint Institute for the Study of the Atmosphere and the Ocean, University of Washington and NOAA-PMEL, 7600 Sand Point Way NE, Seattle, Washington 98115, USA.

[7] Plymouth Marine Laboratory, Plymouth, UK.

5.0 Preamble

Study Motivation

The importance of rough topographic features, such as mid-ocean ridges and sea mounts, in elevating diapycnal diffusivity is widely accepted (Whalen et al., 2012, Tuerena et al., 2019). However, the importance of topographical depth in governing upper ocean mixing and driving changes in the vertical flux of key macro- and micro-nutrients had yet to be quantified. In this work, vertical microstructure profiler observations from the Ridgemix programme and resource observations from the FRidge programme were combined to quantify differences in resource fluxes between two topographic sites. While an increase in mixing at the shallow site was observed, a similar increase in resource flux estimates was not. We therefore focused on determining the biological and physical drivers for the vertical resource profiles, which proved to be key in modulating the resource fluxes. This finding prompted a wider hypothesis on the importance of changes to vertical gradients in resource profiles during periodic processes and over long-term change.

Key Points

- In the upper 1000 m, diapycnal diffusivity is a factor ~2 greater at a shallow topographic site (z = 2673 m) compared to a deep topographic site (z = 3553 m) along the Mid-Atlantic Ridge.
- The pairing of vertical microstructure profiler measurements with vertical resource profiles from seasonally differing field campaigns should be based on the geographic positions and external forcing from the wind and tides.
- Changes in vertical fluxes due to increases in diapycnal diffusivity are mitigated by weaker gradients in vertical resource profiles, which are influenced by regeneration and supply by remote water masses.

Publication and Author Contribution

The work completed within this chapter has been prepared for submission to *EGU: Biogeosciences* with authors Shaun. J. Rigby, Carl P. Spingys, Alessandro Tagliabue, Eric P. Achterberg, J. A. Mattias Green, Maeve C. Lohan, Alistair Lough, Joseph A. Resing, E. Malcolm S. Woodward and Richard. G. Williams. Shaun J. Rigby designed the research, completed analysis and wrote the manuscript. Carl P. Spingys provided VMP datasets, initial water mass contribution scripts, and shared feedback throughout the analysis and writing up phases. Alessandro Tagliabue aided with initial research question design, ran initial water mass contribution scripts, and provided editorial critiques. Eric P. Achterberg provided editorial critiques. J. A. Mattias Green shared output from the tidal model. Maeve C. Lohan, Alistair Lough, Joseph A. Resing and E. Malcolm S. Woodward collected and analyzed samples during the FRidge field campaign. Richard G. Williams was crucial in the research design, analysis process and manuscript production. Thanks go to the scientists and crew of the Ridgemix and GA13 research cruise for the collection of physical and biogeochemical data used throughout this chapter.

Citation

Rigby, S. J., Spingys, C. P., Tagliabue, A., Achterberg, E. P., & Williams, R. G. (2020b). Resource fluxes inferred by vertical microstructure profilers along the mid-atlantic ridge in the subtropics. PhD Dissertation, University of Liverpool.

5.1 Abstract

The physical supply of resources to the upper ocean is key in sustaining primary productivity and carbon export over long time periods. Interactions between the internal tide and rough topography of the ocean floor are known to elevate diapycnal mixing over mid-ocean ridges, increasing the vertical upward transport of nitrate to the subsurface chlorophyll maximum. However, the role of topographic depth in regulating vertical trace element fluxes remains unexplored. Here we show diapycnal mixing in the thermocline is greater where the vertical spacing between the thermocline and mid-Atlantic ridge is narrower, but the vertical resource flux is modulated by gradients in their associated vertical profiles. We use *in-situ* vertical microstructure profilers to quantify diffusivity (K_z) as 0.50 x 10^{-5} (0.39 x 10^{-5} – 0.67 x 10^{-5}) m^2 s^{-1} and 0.92 x 10^{-5} (0.71 x 10^{-5} – 1.3 x 10^{-5}) m^2 s^{-1} in the upper 1000 m at deep and shallow sites along the mid-Atlantic ridge, respectively. By combining these K_z profiles with *in-situ* observations of nitrate, phosphate, silicic acid, dissolved iron, dissolved manganese and dissolved aluminium, we demonstrate that the enhancement in K_z does not necessarily result in larger vertical resource fluxes. This is because the response of resource fluxes to an increased K_z over shallow topography is mitigated by weaker vertical resource gradients, due to a range of biological and physical processes associated with regeneration and the contribution of different water-masses. We find diapycnal exchanges supply the nutrient-type resources nitrate, phosphate and silicic acid to the upper ocean, while the surface maxima in scavenged-type resources manganese and aluminium are eroded. Diapycnal exchanges deliver iron to the upper ocean at the northern shallow topographic site and remove iron at the southern deep topographic site, highlighting the importance of horizontal gradients. Overall, while the spacing between topographic features and the thermocline influences diapycnal exchanges, however local vertical gradients in resources must also be considered in quantifying overall vertical resource fluxes.

5.2 Introduction

Resources, including nitrate (NO_3), phosphate (PO_4), silicic acid (Si), iron (Fe) and manganese (Mn) are required by marine phytoplankton to maintain growth and cellular functions (Falkowski et al., 1998, Sunda, 1989, Twining and Baines, 2013). However, key resources are exported from the upper ocean as unrecycled material sinks to below the euphotic zone (Martin et al., 1987, Boyd et al., 2019). For instance, in the oligotrophic subtropical North Atlantic, the carbon export flux from the primary production zone has been estimated as 0.8 ± 0.7 mmol C m^{-2} d^{-1} (Owens et al., 2015).

Resources are replenished in the upper ocean by external supply pathways, including winter-time entrainment (Rigby et al., 2020, Tagliabue et al., 2014), aeolian deposition (Jickells et al., 2016, Baker and Jickells, 2017), lateral advection (Williams et al., 2006) and diapycnal diffusion (Rijkenberg et al., 2012, Painter et al., 2014).

Vertical gradients in the resource vertical profiles combined with the diapycnal diffusivity (K_z) induces resource transport down concentration gradients. The magnitude of the overall vertical diapycnal diffusion flux is the product of K_z and the depth derivative of the resource concentration (dR/dz). In the ocean interior, K_z is primarily maintained by power inputs from internal tides and surface wind stress (Egbert and Ray, 2000, Alford, 2003). Estimates of K_z vary from 10^{-6} to 10^{-5} m^2 s^{-1} in the quiescent deep ocean to 10^{-4} to 10^{-2} m^2 s^{-1} in the upper ocean and around topographical features such as ocean ridges and sea mounts (Ledwell et al., 1998, Martin et al., 2010, Whalen et al., 2015, Tuerena et al., 2019). The magnitude of K_z is affected by surface wind forcing (Whalen et al., 2018) and tidal forcing (Munk and Wunsch, 1998, Waterhouse et al., 2014, Kunze, 2017, Vic et al., 2019), where K_z is larger at high wind speeds (Whalen et al., 2012) and spring tides when close to topography (Tuerena et al., 2019). Wind stress generates near-inertial internal waves at the base of the surface mixed-layer, which radiate downward into the ocean interior and result in turbulent mixing (Alford et al., 2016). The internal tide interacts with the Mid-Atlantic Ridge to release tidal energy which is available for diapycnal mixing (Vic et al., 2018). For instance, in the upper 500 m, K_z is larger over the Mid-Atlantic Ridge by a factor of 4 to 10 compared to K_z estimates in adjacent deeper waters,

subsequently increasing the on-ridge supply of NO_3 to the deep chlorophyll maxima (Tuerena et al., 2019).

NO_3, PO_4 and Si are examples of nutrient-type resources, Mn and Al are scavenged-type resources, while Fe is a hybrid-type resource (Tagliabue, 2019). Generally, nutrient-type resources are depleted in surface waters due to biological uptake and are regenerated at depth. Regeneration rates are measured by Apparent Oxygen Utilisation (AOU), which estimates the undersaturation of oxygen at depth due to bacterial consumption during organic matter remineralisation (Redfield, 1934, Anderson and Sarmiento, 1994). Nutrient-type resources are influenced by remote water masses at depth. Antarctic Intermediate Water, rich in Si, is subducted in the Southern Ocean and propagates to low latitudes where diapycnal processes cause the vertical transfer of end-member properties (Sarmiento et al., 2004). Scavenged-type resources exhibit surface maxima and concentrations decrease with depth. In the subtropical North Atlantic, surface maxima in Al are used to identify regions of high dust deposition rates (Han et al., 2008, Measures et al., 2008). Hybrid-type resource profiles typically decrease in concentration from the surface to sub-surface minima and are regenerated at depth, driven by scavenged-type behaviour in the upper water column and nutrient-type behaviour at depth. In the upper 150 m, Fe shows nutrient-type behaviour in the mid-latitude and eastern North Atlantic, while Fe exhibits scavenged-type behaviour elsewhere in the North Atlantic (Kunde et al., 2019). The distinct vertical profiles of each resource type govern the effect of K_z on diapycnal transport.

The role of topographic features in increasing K_z is widely accepted (Ledwell et al., 1998, Waterhouse et al., 2014, Whalen et al., 2015, Tuerena et al., 2019), however differences in K_z along mid-ocean ridges are not well understood. Variations in K_z linked to topographic depth could play an important role in establishing multiple resource supply regimes over a single large topographic feature (such as a mid ocean ridge), with important implications for the upper ocean biome. Further, diapycnal resource flux calculations along the Mid-Atlantic Ridge are yet to include scavenged-type and hybrid-type resources and hence study the role of vertical gradients in setting fluxes for different resource types (Rigby et al., 2020).

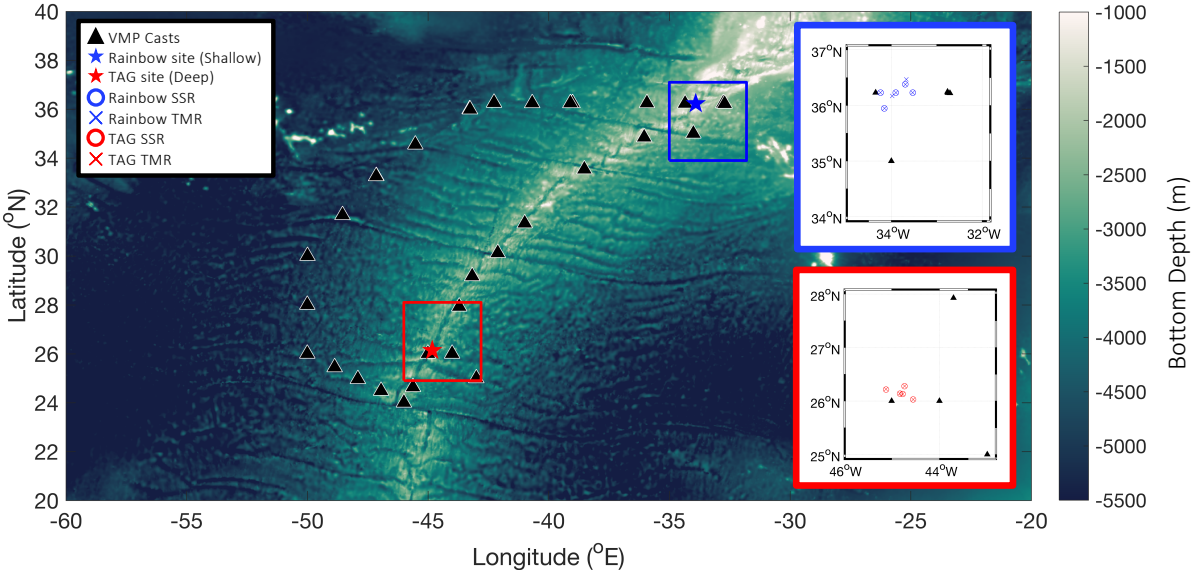

Figure 5.1. Geographical positions of VMP casts (black triangles), Rainbow (blue star) and TAG (red star) hydrothermal sites. Inserts show the positions of VMP casts (black triangle) stainless steel rosette casts (SSR, circles) and trace metal clean rosette casts (TMR, crosses) near to the Rainbow (blue box) and TAG (red box) hydrothermal sites. Data sourced from both the Ridgemix project and the UK *GEOTRACES* GA13 section.

In this study, data from two field campaigns in the subtropical North Atlantic are combined to estimate K_z and infer resource fluxes at two sites along the Mid-Atlantic Ridge. The Rainbow and Trans-Atlantic Geotraverse (TAG) hydrothermal sites are highly sampled topographical features and sit within the axial valley at ~2400m depth and ~3600m depth respectively, ideally suited to test the importance of topographical depth on setting upper ocean K_z. We consider the implications of changes to mixing and vertical resource gradients during two scenarios: the spring-neap tidal cycle and in a future warming ocean. We hypothesise (1) during spring tides, stronger mixing is augmented by stronger resource gradients to greatly increase resources fluxes and (2) long-term reductions in mixing are accompanied by the formation of stronger resource gradients which mitigate reductions in vertical resource supply due to a decrease in K_z.

5.3 Methods

5.3.1 Observational Data

Data used in this study were sourced from two field campaigns in the subtropical North Atlantic (Figure 5.1). The RidgeMix project, May 2015 to June 2015, provides 29 VMP casts with data available throughout the upper 1000m (see Tuerena et al., 2019, for a full description of RidgeMix). The *GEOTRACES* section GA13, December 2017 to February 2018, deployed an additional 5 VMP casts in the study region. Biogeochemical observations from GA13 at the Rainbow (36.23°N, 33.90°W) and TAG (26.14°N, 44.83°W) hydrothermal vent sites are used here. In total, 7 stainless-steel rosette casts and 8 trace metal rosette casts were performed in the near vicinity of Rainbow (within 33.55°W to 34.24°W, 35.95°N to 36.47°N). At TAG, 5 stainless-steel rosette casts and 7 trace metal rosette casts were conducted close to the hydrothermal vent site (within 45.12°W to 44.55°W, 26.03°N to 26.28°N). Vertical profiles of NO_3, PO_4 and Si from both rosette systems are used to calculate diapycnal fluxes, while Fe, Mn and Al are available from the trace metal clean rosette system only. The bottom depth at each GA13 rosette cast is extracted from the ETOPO1 global relief model (Amante and Eakins, 2009). ARGO estimates of K_z were provided by Whalen et al. (2018).

5.3.2 Vertical Microstructure Profiler Processing

Vertical microstructure profilers (VMPs) are freefalling apparatus which provide meter-resolution measurements of pressure, temperature, salinity and turbulent dissipation (ε (m^2 s^{-3})). Diapycnal diffusivity (K_z) is calculated from

$$K_z(m^2\ s^{-1}) = \Gamma \frac{\varepsilon}{N^2} \quad [1]$$

where Γ is the mixing efficiency set as 0.2 which is typical for shear driven turbulence in regions of strong stratification (Gregg et al., 2018) and N is the buoyancy frequency, where

$$N\ (s^{-1}) = \sqrt{-\frac{g}{\rho}\frac{d\rho}{dz}} \qquad [2]$$

where g is acceleration due to gravity (9.81 m s^{-2}), ρ is density (kg m^{-3}) and z is depth (m). Vertical profiles of K_z were binned into 100m bins to reduce noise associated with VMP profiles and emulate the availability of ARGO K_z observations and biogeochemical data in the vertical. Here, bootstrap averages with 95% confidence intervals are reported in VMP profiles.

5.3.3 Resource Profile and VMP Pairing

VMP data and resource profiles exist from seasonally differing field campaigns in the subtropical North Atlantic. Therefore, resource profiles and VMPs are paired upon on the following criteria: (1) spatial separation, (2) analogous external forcing or (3) within the Rossby Radius of deformation.

5.3.3.1 Spatial Separation

The distance (in meters) from each vertical resource profile to all VMP casts was calculated. The spatially closest 5 VMP profiles were averaged and upper and lower bounds found from bootstrap fit confidence intervals.

5.3.3.2 External Forcing

Surface wind forcing and tidal forcing are assumed as the main driving processes which set the magnitude and shape of the vertical K_z profile. The turbulent dissipation rate of surface forcing and tidal forcing are calculated and are directly compared. Surface forcing by wind is estimated following Burchard (2009),

$$\varepsilon\ (W\ kg^{-1}\ or\ m^2\ s^{-3}) = \frac{(u^s)^3}{\kappa\ z_0^s} \qquad [3]$$

where κ is the von Kármán parameter (= 0.4), u^s is the surface friction velocity,

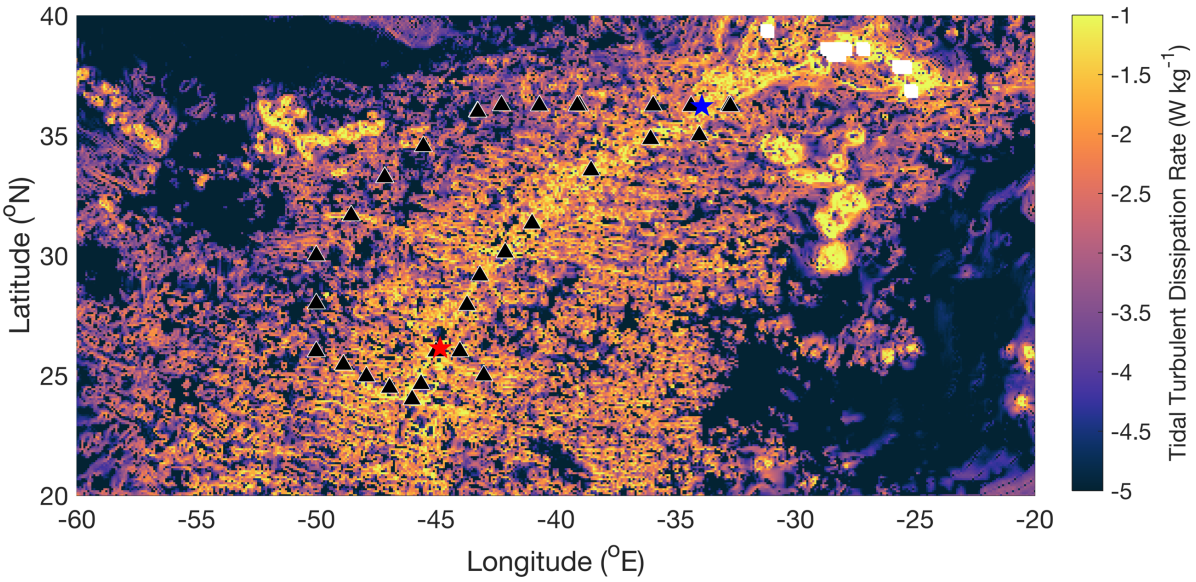

Figure 5.2. Tidal dissipation rate (W kg^{-1}) in the subtropical North Atlantic around the Mid-Atlantic Ridge. Data from the TPXO8 tidal model (Egbert and Erofeeva, 2002). VMP casts (black triangles), Rainbow (blue star) and TAG (red star) hydrothermal sites. Geographic positions of interest from the RidgeMix project and GA13.

$$u^s\ (m\ s^{-1}) = \sqrt{c_d^w \frac{\rho_a}{\rho_0} W^2} \qquad [4]$$

where ρ_a and ρ_0 are the density of air and seawater at the surface respectively, W is wind speed (m s^{-1}) extracted from the ERA5 reanalysis and shipboard measurements, c^w_d is the surface drag co-efficient,

$$c_d^w = \begin{cases} 0.001 \times (0.49 + 0.065W), & for\ W > 10\ m\ s^{-1} \\ 0.00114, & else \end{cases} \qquad [5]$$

In equation [3], z_o^s is the surface roughness length, where

$$z_0^s\ (m) = a_c \frac{(u^s)^2}{g} \qquad [6]$$

where a_c = 1400 which links surface roughness and wave state (Charnock, 1955, Craig and Banner, 1994).

The tidal dissipation rate from 100 m – 500 m (Figure 5.2) at each VMP and resource profile site is extracted from global fields produced in Tuerena et al. (2019) using the TPXO8 tidal model (Egbert and Erofeeva, 2002).

The 5 VMP sites with most comparable external forcing to that at each resource profile were averaged and upper and lower bounds found from bootstrap fit confidence intervals.

5.3.3.3 Rossby Deformation Radius

The Rossby Deformation Radius (L_d) is the horizontal scale at which a physical process is arrested by rotation (Chelton et al., 1998, Williams and Follows, 2013), equation [7],

$$L_d\ (m) = \frac{N\ H}{f} \qquad [7]$$

where H is the thermocline thickness (m), f is the Coriolis parameter (s^{-1}) and N is the buoyancy frequency (s^{-1}), given by equation [2].

5.3.3.4 Spring-Neap Tidal Cycle Contrasts During Equipment Deployment

The Rainbow and TAG sites were occupied from 3rd January 2018 to 10th January 2018 and 20th January 2018 to 27th January 2018, respectively. During the Rainbow occupation, the lunar phase advanced from *waning gibbous* to *third quarter* to *waning crescent*, meaning samples were captured during neap tides. At TAG, the lunar phase advanced from *waxing crescent* to *first quarter* to *waxing gibbous*, also meaning that samples were collected neap tides. Therefore, we assert that differences in resource profiles between the TAG and Rainbow sites are not caused by tidal phase differences in this study. A range of VMP profiles are paired with resource profiles to estimate

vertical resource fluxes. The most commonly paired VMPs to resource profiles at Rainbow were deployed on 9th June 2016, 10th June 2016, 12th June 2016, 15th June 2016 and 22nd Jan 2018. These VMP deployments were approximately 2 days from the occurrence of neap tides. Similarly, at TAG, the most commonly used VMPs to calculate resource fluxes were deployed on 12th June 2016, 16th June 2016, 28th June 2016 and 20th January 2018, which were approximately 2.75 days from the occurrence of neap tides. Overall, consideration of the time at which equipment was deployed and the concurrent phase of the spring-neap tidal cycle suggests that tides will have a minimal effect on the differences between derived resource fluxes at the TAG and Rainbow sites in this study. However, we acknowledge that the spring-neap tidal cycle does influence the magnitude of vertical mixing, particularly around regions of rough topography (e.g. Tuerena et al. (2019)).

5.3.4 Diapycnal Resource Flux

K_z is combined with vertical gradients in resource profiles to calculate the diapycnal resource flux, R_u, equation [8],

$$R_u\ (mol\ m^{-2}s^{-1}) = \kappa_z \times \frac{d[R]}{dz} \qquad [8]$$

where [R] denotes a resource concentration (mol m^{-3}).

5.3.5 Water Mass Analysis

Water mass contributions at the TAG and Rainbow sites were identified using Modified Optimum Multiparameter Analysis (MOMPA) following Jenkins et al., (2015). The approach uses five conservative tracers: potential temperature, salinity, silicic acid, N-star and P-star in combination with end-member water mass properties to deconstruct the water column into contributing water masses. Each conservative tracer is weighted to reduce dependency on tracers with larger uncertainty in sampling or end-member composition (See Section 2.5.1.2 for additional details).

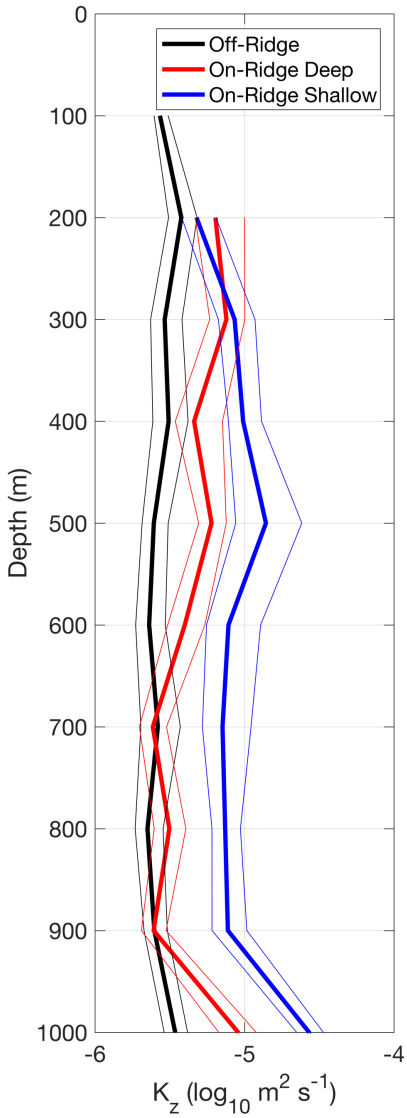

Figure 5.3. Comparison of K_z ($\log_{10}$ m^2 s^{-1}) profiles using off-ridge (black) VMPs and VMPs around the deep TAG hydrothermal site (red) and shallow Rainbow hydrothermal site (blue). Upper and lower bounds (thin lines) are a 95% confidence interval calculated using the bootstrap approach.

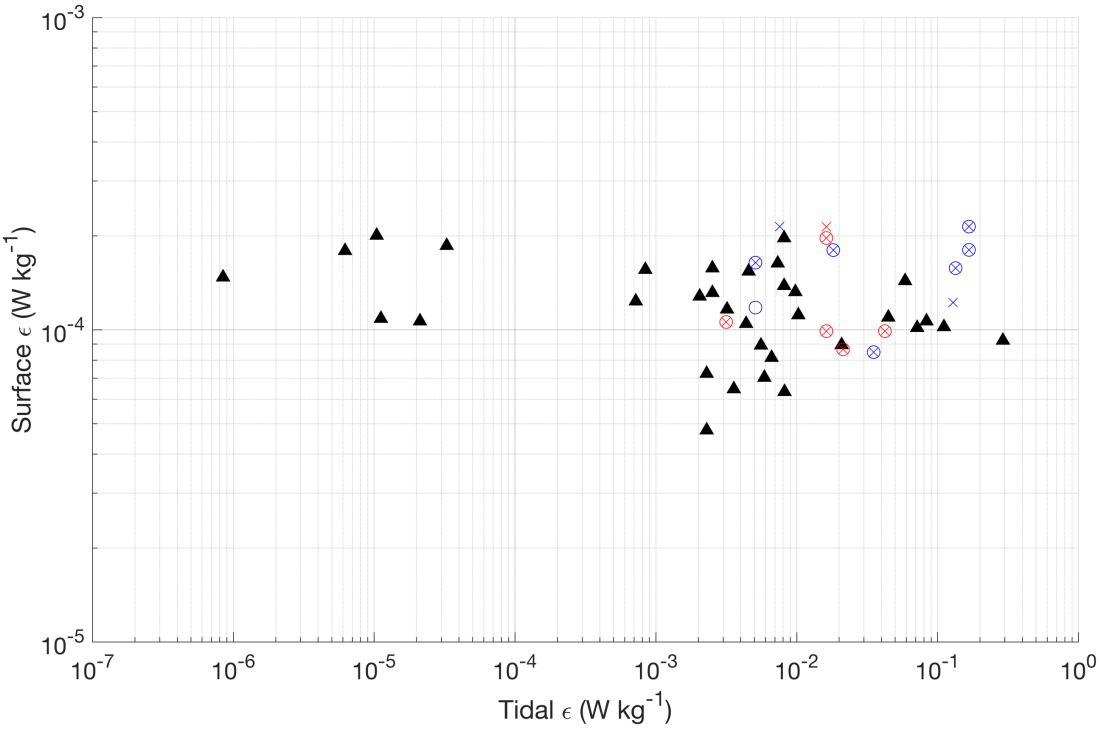

Figure 5.4. Comparison of tidal and surface turbulent dissipation rates (W kg^{-1}) at VMP (black triangles), stainless steel rosette (SSR, circles) and trace metal rosette (TMR, crosses) casts. Data from SSR and TMR are from casts performed at the Rainbow (blue) and TAG (red) hydrothermal systems along the Mid-Atlantic Ridge. 29 VMP casts from RidgeMix augmented by 5 VMP casts from (GEOTRACES GA13), SSR and TMR data is from FRidge.

5.4 Results

5.4.1 Diapycnal Diffusivity

In order to examine the role of shallow topography on upper ocean mixing, an analysis of off-ridge and on-ridge VMPs at Rainbow and TAG was performed, showing that as bottom depth decreased, K_z in the upper 1000 m increased (Figure 5.3). The mean bottom depth of off-ridge, deep topographic (TAG) and shallow topographic (Rainbow) VMP sites were 4468 m, 3289 m and 2086 m, respectively. K_z in the upper 1000m increased from 0.29×10^{-5} ($0.24 \times 10^{-5} – 0.37 \times 10^{-5}$) $m^2\ s^{-1}$ at the off-ridge site, to 0.50×10^{-5} ($0.39 \times 10^{-5} – 0.67 \times 10^{-5}$) $m^2\ s^{-1}$ at the deep topographic site, to 0.92×10^{-5} ($0.71 \times 10^{-5} – 1.3 \times 10^{-5}$) $m^2\ s^{-1}$ at the shallow topographic site. K_z is

indistinguishable between both on-ridge sites at 300 m, however off-ridge K_z is notably reduced (Figure 5.3). At 500 m, there is a clear separation in the K_z profile at each site, showing distinct variations in upper ocean vertical mixing between deep, intermediate and shallow topographic sites (Figure 5.3). Between 700 m and 900 m, there is no clear difference in K_z between off-ridge VMPs and those at the deep topographic site (bootstrapped average and 95% confidence intervals), while K_z is elevated at the shallow topographic site. Differences in K_z between the study sites is caused by their external forcing mechanisms, the wind and tides.

5.4.2 External Forcing of K_z

At each VMP and resource profile, the tidal and surface turbulent dissipation rates were calculated to assess the variability in seasonally differing field campaigns (Figure 5.4). The range of tidal turbulent dissipation rate during VMP deployments encompasses that during resource observations, meaning suitable estimates of mixing from VMPs can be applied to resource profiles based on tidal forcing alone. At Rainbow sites with large tidal turbulent dissipation rates ($> 1 \times 10^{-1}$ W kg^{-1}), VMPs with comparable surface forcing are unavailable. However, across the full dataset, surface turbulent dissipation rates do not exceed 3×10^{-4} W kg^{-1}, meaning surface forcing is negligible at high rates of tidal dissipation. At the sites of interest, TAG and Rainbow, tidal turbulent dissipation rate is greater than 3.1×10^{-3} W kg^{-1} in all cases, whereas the surface turbulent dissipation rate is consistently less than 2.2×10^{-4} W kg^{-1}, meaning K_z is most sensitive to tidal turbulent dissipation rate at the on-ridge study sites. Both tidal forcing and surface forcing are used to assign K_z profiles to resource profiles on the basis on environmental conditions at the time of sampling, however that process is dominated by tidal forcing at our study sites. Tidal forcing remains the dominant mechanical forcing when in the vicinity of the Mid-Atlantic Ridge, irrespective of choice between wind speeds extracted from ERA5 reanalysis or wind speed measure directly from shipboard apparatus.

5.4.3 Choice of Spatial VMP and Resource Profile Pairing Criteria

VMP profiles must be paired with resource profiles in order to calculate vertical resources fluxes. There are three approaches to pair VMP and resource profiles: (1) spatial separation, (2) external forcing and (3) within the Rossby Radius of deformation (Section 5.3.3). To understand the importance of the VMP and resource profile pairing criteria, ARGO measurements of vertical diffusivity (Whalen et al., 2018) were explored to demonstrate how vertical profiles of K_z varied using multiple pairing approaches (Figure 5.5). Choice of the nearest ARGO profile to Rainbow and TAG is a suitable first-order K_z estimate, however provides no information on spatial variability in the system (Figure 5.5a). Averaging all ARGO data within one Rossby Radius allows for spatial variations around TAG and Rainbow to be considered (Figure 5.5b). Setting the criteria to all profiles within a 4^o longitude by 4^o latitude box centred at the site causes no significant differences between TAG and Rainbow as physical processes operate on smaller length-scales than the criteria (Figure 5.5c). We now consider ARGO profiles where VMP data are available for comparison (Figures 5.5d – f). By using the ARGO profile co-located with a VMP cast, no significant difference between off-ridge and on-ridge K_z profiles is apparent from 200 m to 300 m (Figure 5.5d). However, by expanding the criteria to all ARGO profiles within one Rossby radius of each VMP, a significant difference between on-ridge and off-ridge K_z profiles emerges (Figure 5.5e), as reported by Tuerena et al. (2019). Further expansion of the spatial criteria to a 4^o longitude by 4^o latitude box centred at each VMP site results in no significant differences between on-ridge and off-ridge sites (Figure 5.5f). Therefore, pairing resource profiles to VMPs within one Rossby radius is advantageous compared to larger spatial choices or the geographically nearest profile.

5.4.4 Diapycnal Resource Fluxes

Resource fluxes from 250m to 550m were determined by combining vertical resource profiles with K_z profiles, showing distinct supply regimes at each study site (Table 5.1). At both sites, K_z is lowest in VMPs assigned based on external forcing alone. K_z is a factor ~2 larger when using VMPs within one Rossby Radius of the resource

profiles at TAG and Rainbow compared to VMPs selected by forcing alone. Between sites, the bootstrapped average K_z is elevated at the shallower Rainbow site (z_{bottom} = 2367 m) compared to the TAG site (z_{bottom} = 3553 m). However, this increase is not reflected in the vertical flux of nutrient-type resources NO_3, PO_4 and Si. For instance, applying VMPs within one Rossby Radius to resource profiles causes K_z estimates at Rainbow to be 42% greater than those at TAG, yet the overall NO_3 flux is larger at TAG, meaning stronger vertical gradients in NO_3 at TAG compensate for the increase in K_z. Diapycnal exchanges increase the flux of NO_3, PO_4 and Si above 250 m as concentrations increase with depth in their vertical profile. In contrast, scavenged-type resources Mn and Al are lost from the upper ocean by diapycnal exchange, suggesting Mn and Al surface maxima are eroded by physical processes at both sites. Hybrid-type resource Fe is transported upwards at Rainbow and downwards at TAG in the 250-550 m depth range, implying the scavenged-type part of the Fe profile persists to a greater depth at TAG, meaning the Fe minima are also deeper at TAG. The direction of each resource flux is consistent when using ARGO estimates of K_z in place of VMP estimates of K_z (Table 5.2). However, the flux magnitude increases as ARGO K_z is greater than VMP estimates. This elevation in K_z is likely due to seasonal bias within the datasets, which causes variation in ARGO data by a factor of 2 in the subtropical North Atlantic and by a factor of 2 to 5 in the 30°N to 40°N latitude band due to storms (Whalen et al., 2012). Overall, our results suggest the response in resources fluxes to changes in K_z between topographic sites is mitigated by a strengthening or weakening of vertical gradients in resource profiles.

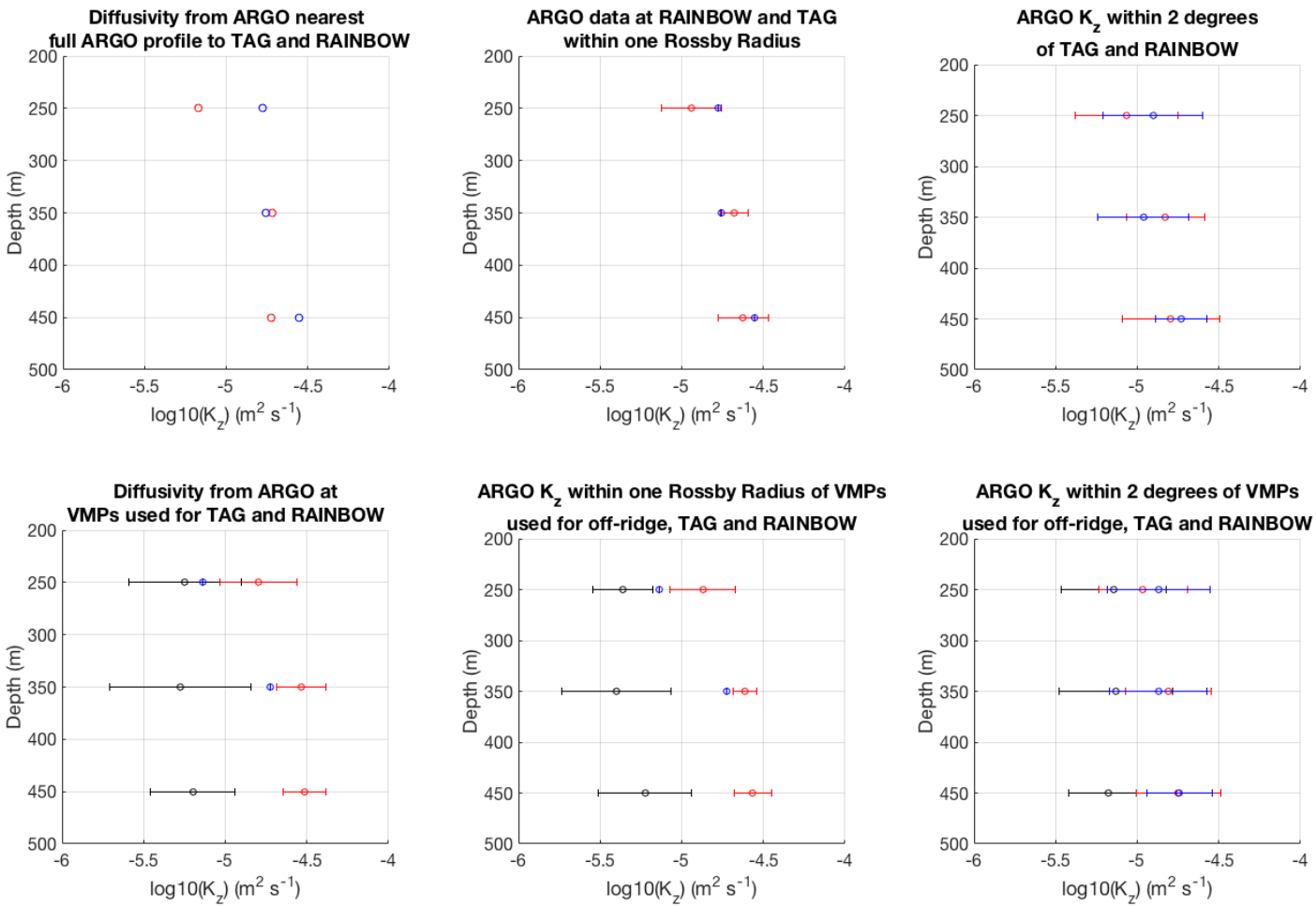

Figure 5.5. Diapycnal diffusivity (log10, m^2 s^{-1}) at (a-c) Rainbow (blue) and TAG (red) hydrothermal sites along the Mid-Atlantic Ridge and (d-f) at VMP casts at off-ridge (black), Rainbow (blue) and TAG (red) along the Mid-Atlantic Ridge. ARGO profiles included in analysis are (a, d) adjacent profiles to sites of interest, (b, e) all profiles available within one Rossby Radius and (c, f) all available profiles within 2 longitude-latitude degrees.

			Resource Flux 250m to 550m		
		K_z	NO_3	PO_4	Si
Rainbow z_{bottom}=2367m	Nearest VMP	9.72 (6.85 - 14.9) x 10^{-6}	6.31 (4.48 - 9.57)	0.41 (0.29 - 0.63)	3.57 (2.49 - 5.52)
	Forcing VMP	6.57 (4.89 - 9.35) x 10^{-6}	4.22 (3.16 - 5.98)	0.27 (0.20 - 0.39)	2.33 (1.74 - 3.30)
	Rossby VMP	14.6 (10.8 - 19.7) x 10^{-6}	9.53 (7.07 - 12.80)	0.62 (0.46 - 0.83)	5.49 (4.05 - 7.42)
TAG z_{bottom}=3553m	Nearest VMP	6.21 (4.70 - 8.80) x 10^{-6}	6.18 (4.65 - 8.84)	0.39 (0.29 - 0.55)	2.62 (1.98 - 3.71)
	Forcing VMP	5.79 (4.18 - 8.72) x 10^{-6}	5.82 (4.24 - 8.67)	0.38 (0.27 - 0.57)	2.70 (1.94 - 4.07)
	Rossby VMP	10.3 (8.36 - 13.3) x 10^{-6}	10.5 (8.50 - 13.5)	0.68 (0.55 - 0.88)	4.91 (3.98 - 6.28)

		Resource Flux 250m to 550m		
		Fe	Mn	Al
Rainbow z_{bottom}=2367m	Nearest VMP	0.35 (0.23 - 0.56)	-0.06 (-0.05 to -0.08)	-0.88 (-0.64 to -1.28)
	Forcing VMP	0.23 (0.16 - 0.37)	-0.04 (-0.03 to -0.06)	-0.54 (-0.42 to -0.74)
	Rossby VMP	0.35 (0.25 - 0.47)	-0.14 (-0.11 to -0.19)	-1.45 (-1.07 to -1.96)
TAG z_{bottom}=3553m	Nearest VMP	-0.14 (-0.11 to -0.20)	-0.09 (-0.07 to -0.13)	-3.72 (-2.78 to -5.37)
	Forcing VMP	-0.12 (-0.08 to -0.19)	-0.07 (-0.05 to -0.10)	-3.18 (-2.35 to -4.65)
	Rossby VMP	-0.15 (-0.12 to -0.20)	-0.11 (-0.08 to -0.14)	-5.76 (-4.64 to -7.48)

Table 5.1. Diapycnal diffusivity (K_z, m^2 s^{-1}) and vertical resource flux estimates from 250 m to 550 m depth at the Rainbow and TAG hydrothermal sites along the Mid-Atlantic Ridge. NO_3, PO_4 and Si flux estimates given in mmol m^{-2} yr^{-1}, Fe, Mn and Al flux estimates in µmol m^{-2} yr^{-1}. Reported K_z and resource flux estimates are bootstrapped averages with 95% confidence intervals. K_z estimated from 29 VMP casts during RidgeMix field campaign and augmented by 5 VMP casts from the GA13) field campaign. Resource concentration data are from GA13 in all cases.

			Nutrient Flux 250m to 550m					
		K_z	NO_3	PO_4	Si	Fe	Mn	Al
Rainbow z_{bottom}=2367m	Station ARGO	-	-	-	-	-	-	-
	Rossby ARGO	-	-	-	-	-	-	-
	2 degrees ARGO	15.4×10^{-6}	11.21	0.71	5.52	0.42	-0.20	-1.86
TAG z_{bottom}=3553m	Station ARGO	15.0×10^{-6}	18.28	1.13	6.94	-0.78	-0.37	-13.48
	Rossby ARGO	16.0×10^{-6}	20.16	1.26	7.74	-0.70	-0.35	-12.17
	2 degrees ARGO	16.1×10^{-6}	18.51	1.16	7.17	-0.70	-0.33	-12.24

Table 5.2. Diapycnal diffusivity (K_z, $m^2\ s^{-1}$) and vertical resource flux estimates from 250 m to 550 m depth at the Rainbow and TAG hydrothermal sites along the Mid-Atlantic Ridge. NO_3, PO_4 and Si flux estimates given in mmol $m^{-2}\ yr^{-1}$, Fe, Mn and Al flux estimates in μmol $m^{-2}\ yr^{-1}$. K_z estimated from ARGO float data (Whalen et al. 2012). Resource concentration data from GA13.

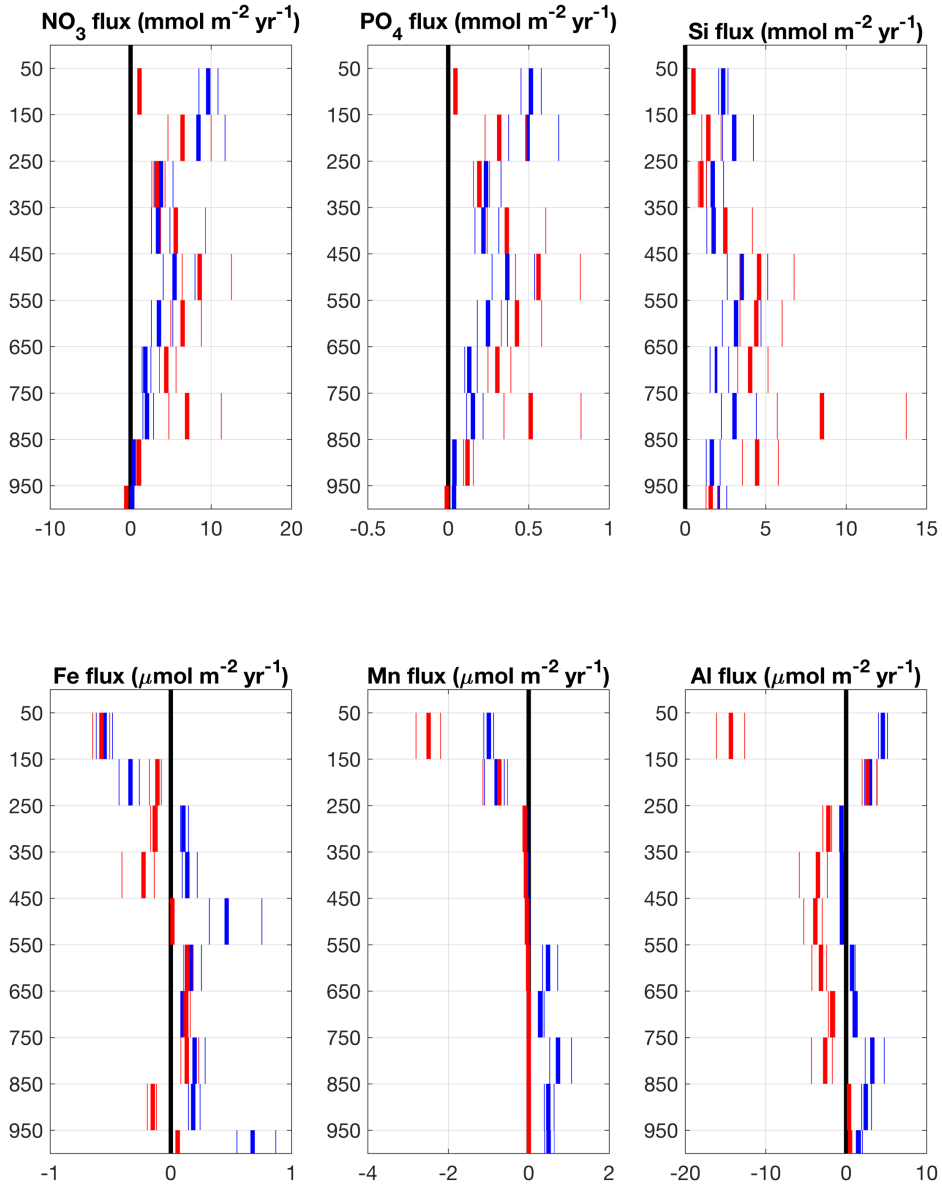

Figure 5.6. Vertical resource flux estimates in the upper 1000m at the Rainbow (blue) and TAG (red) hydrothermal sites along the Mid-Atlantic Ridge. NO_3, PO_4 and Si flux estimates given in mmol m^{-2} yr^{-1}, Fe, Mn and Al flux estimates in µmol m^{-2} yr^{-1}. Estimates of vertical diffusivity from RidgeMix and resource data from FRidge (GEOTRACES GA13) field campaigns.

5.4.5 Vertical Resource Flux Structure

To examine vertical structure and variations in the resource flux estimates, vertical flux profiles were grouped by site and averaged in 100 m depth intervals, showing

similarities in NO_3, PO_4 and Si fluxes and contrasts in Fe, Mn and Al fluxes between the Rainbow and TAG sites (Figure 5.6). At Rainbow, the upwards flux of NO_3 and PO_4 is greatest from 50 m to 150 m depth and generally decreases with depth, excluding a flux convergence at 450 m depth. The persistent NO_3 and PO_4 flux divergence at Rainbow suggests additional sources augment the upwards flux of both resources to sustain the divergent flux, such as lateral transport or regeneration at depth. The vertical structure in NO_3 and PO_4 fluxes is less clear at TAG. The Si flux at both sites follows a similar structure to NO_3 and PO_4 fluxes, however the Si flux maxima at TAG is located between 750 m to 850 m depth. Due to the hybrid-type behaviour of Fe, surface maxima in Fe are eroded at both sites by diapycnal mixing. The downwards flux of Fe extends to 250 m depth at Rainbow and 450 m depth at TAG, indicating contrasts in the length scale of the scavenged-type region of the Fe profile. Below 250 m and 450 m depths at Rainbow and TAG respectively, Fe is transport is upwards due to the nutrient-type behaviour of Fe at depth. At TAG, the structure observed in the Mn flux is caused by the attenuation of Mn concentrations from the surface to a near-consistent concentration (~0.2 nM) below 250 m depth, meaning a reduction in vertical Mn gradients and induced diapycnal Mn fluxes with depth. In contrast, below 550 m depth at Rainbow, there is an upwards flux in Mn which is induced as Mn concentrations increase with depth due to a source at depth. The vertical Al flux at TAG is dominated by downwards transport, likely due to the influence of aeolian deposition at the surface. However, between 150 m depth and 250 m depth at both sites, Al is transported upwards, suggesting subsurface peak in Al. At Rainbow, below 550 m there is an upwards flux in both Al and Mn as their concentrations increase with depth. In summary, the structure of vertical fluxes is dependent upon vertical gradients in the given resource profile, which are driven by a combination of physical processes and biogeochemical cycling.

5.4.6 Water Mass Contributions

A water mass analysis was performed to identify contributing water masses in the upper 1500 m at the Rainbow and TAG hydrothermal sites (Figure 5.7). At both sites, there are large (>20%) influences of Mediterranean Overflow Water (MOW), Antarctic Intermediate Water (AAIW), Upper Labrador Sea Water (ULSW) and

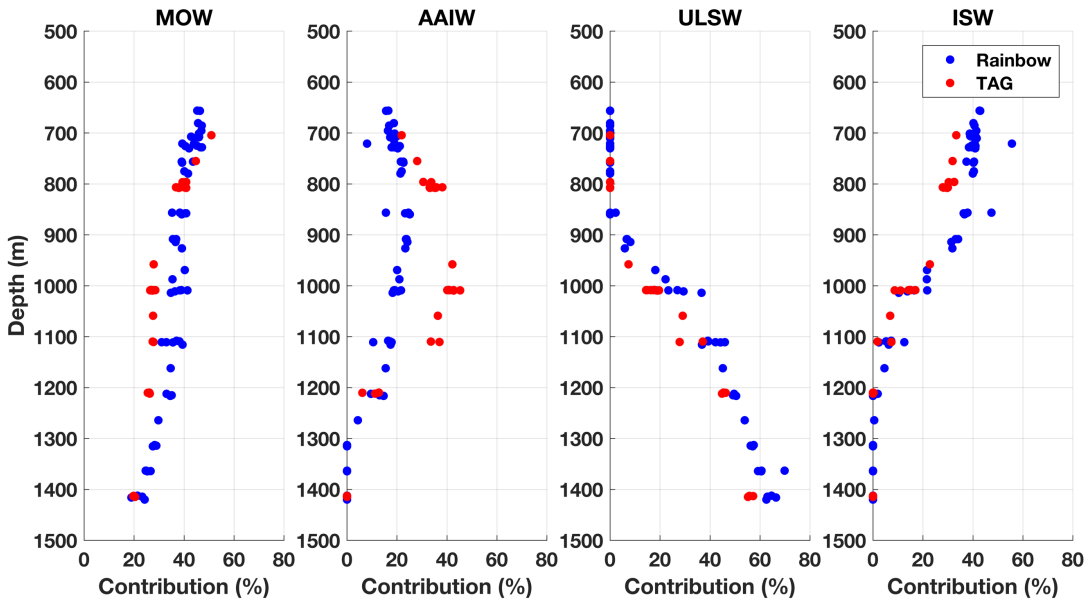

Figure 5.7. Water mass contributions (%) at the TAG (red) and Rainbow (blue) study sites, following the methodology of Jenkins et al., (2015) to identify contributions of Mediterranean Overflow Water (MOW), Antarctic Intermediate Water (AAIW), Upper Labrador Sea Water (ULSW) and Irminger Sea Water (ISW).

Irminger Sea Water (ISW). At both sites, the contribution of MOW to the water column is ~45% to 50% at ~700 m depth and decreases to ~20% to 25% at ~1425 m depth. However, there are differences in the vertical gradient of MOW between the two sites. The reduction in MOW from 700 m to 1000 m depth is stronger at TAG than at Rainbow, meaning that over this depth bound gradients in conservative tracers associated with MOW are also greater at TAG. The maximum contribution of AAIW is 25% (860 m depth) and 45% (1010 m depth) at Rainbow and TAG, respectively. Differences in the AAIW contribution are expected as TAG is located 10-degreees south of Rainbow and are important due to the high silicate end-member composition of AAIW (Table 2.1). ULSW is absent above 800 m depth at both sites, increasing to a contribution of ~60% at 1400 m depth at both sites. As the vertical structure of ULSW contributions are similar between sites, ULSW is not expected to cause differences in the vertical fluxes of conservative tracers between TAG and Rainbow. Finally, the influence of ISW is largest at ~700 m at both sites, however the contribution of ISW is larger at Rainbow (~40%) than at TAG (34%). Overall, our results demonstrate there are differences in the influence of major water masses

between the Rainbow and TAG site, most notably in AAIW from ~800 m depth to ~1100 m depth.

5.5 Discussion

In this work, we combined *in-situ* VMP observations of K_z and resource profiles to calculate resource fluxes along the Mid-Atlantic Ridge and assess the role of topography in elevating upper ocean mixing and the response in resource fluxes. In doing so, we quantified the replenishment of upper ocean resources following loss to biological export and scavenging. VMP profiles demonstrated an increased K_z at the shallow Rainbow site when compared to the TAG site. However, the magnitude of NO_3, PO_4 and Si fluxes at both sites was comparable, meaning reduced diapycnal diffusivity at the TAG site was mitigated by stronger gradients in resource profiles. The diapycnal flux of trace elements Fe, Mn and Al differs strongly between the two sites. Specifically, between 250 m and 550 m depth, we found that Fe is supplied and removed by diapycnal exchanges at the Rainbow and TAG sites respectively.

5.5.1 Comparison of Diapycnal fluxes to Other Supply Estimates

The NO_3 fluxes identified here are generally smaller than those estimated during spring and neap tides in Tuerena et al. (2019). However, NO_3 fluxes estimated in Tuerena et al. (2019) are representative of fluxes at the base of the deep chlorophyll maxima (DCM), which is a highly productive region of the water column. Hence, NO_3 gradients are sharp at the base of the DCM due to consumption, subsequently elevating the NO_3 flux. In this study, sharp features in resource profiles are lost due to the vertical resolution of available measurements necessitating the use of 100 m bins in the vertical dimension. Tuerena et al. (2019) demonstrate the sensitivity of the vertical NO_3 flux to the spring-neap tidal cycle. The diapycnal fluxes of other resources, including PO_4, Si, Co, Fe and Mn, are therefore sensitive to the spring-neap tidal cycle and may vary by a factor of 8 due to temporal changes in K_z. In the thermocline, eddy stirring along sloping isopycnals has been linked to vertical NO_3 fluxes from 1 to 10 mmol N m^{-2} yr^{-1}, comparable to NO_3 estimates in this study, suggesting this process plays an important role in the transfer of NO_3 and other resources in the subtropical

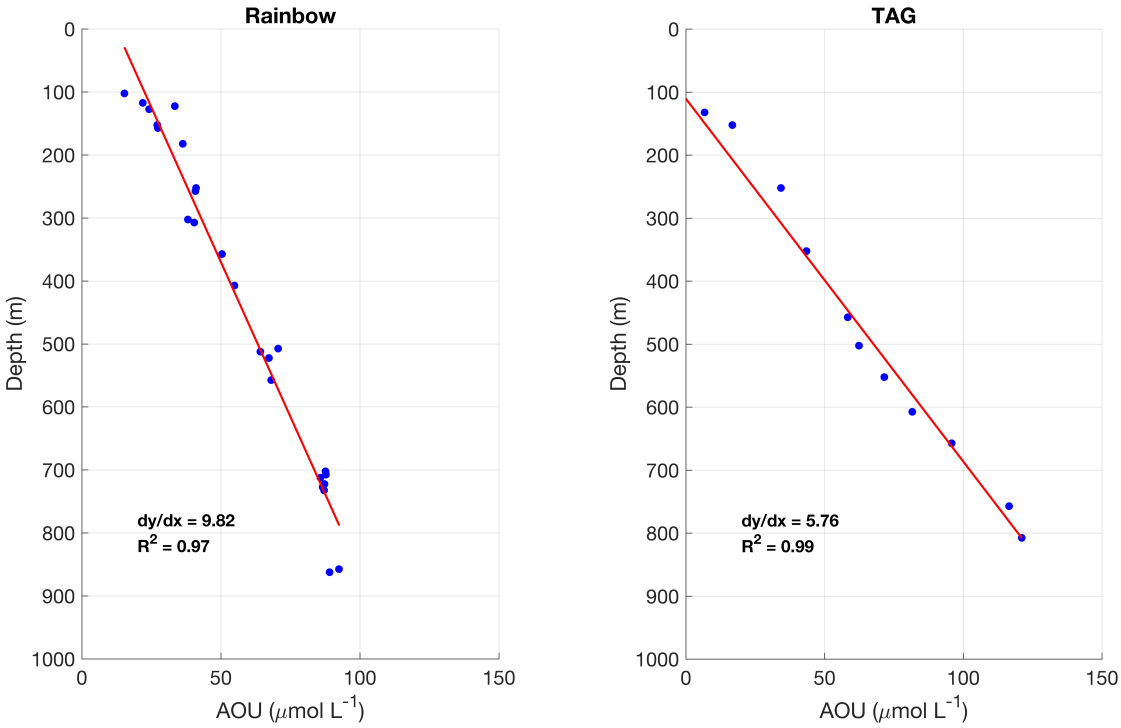

Figure 5.8. Apparent Oxygen Utilisation (AOU, µmol L^{-1}) in the upper 1000m at the Rainbow (blue) and TAG (red) hydrothermal sites along the Mid-Atlantic Ridge. Data from the stainless-steel rosette on the FRidge (*GEOTRACES* GA13) field campaign.

North Atlantic (Spingys et al., *in prep*). In the upper 160 m of the subtropical North Atlantic, salt-fingering and turbulence due to internal waves deliver 85 ± 44 mmol N m^{-2} yr^{-1} and 15 ± 7 mmol N m^{-2} yr^{-1} (Dietze et al., 2004). Finally, the winter-time entrainment of NO_3 and PO_4 into the mixed layer in the region is low compared to the diapycnal transfers in the upper ocean as the mixed-layer does not access deep NO_3 and PO_4 stock (Rigby et al., 2020). Both entrainment and diapycnal processes act to erode surface maxima in Fe and Mn, however, the magnitude of surface losses due to entrainment outweigh losses due to diapycnal exchanges. Through the thermocline, upwards Fe fluxes at Rainbow and TAG are comparable to low Fe fluxes estimated in the North Atlantic subtropical gyre and North Atlantic tropical gyre respectively (Ussher et al., 2013). Diffusive Fe fluxes into the mixed layer are greater in high latitudes compared to the low latitude North Atlantic (Painter et al., 2014).

5.5.2 Importance and drivers of the vertical resource profile

In the upper 1000 m, K_z is larger at the Rainbow site than at the TAG site by 57%, 13% and 41% following the nearest, forcing and Rossby Radius VMP assignment criteria respectively (Table 5.1); however, vertical resource fluxes remain comparable. Differences in the vertical resource flux caused by a reduction in K_z at the TAG site must be compensated by stronger vertical gradients at the TAG site compared to the Rainbow site. The vertical profiles of each resource are shaped by biological and physical processes.

5.5.2.1 Processes influencing the NO_3, PO_4 and Si vertical profiles

Nutrient-type resources NO_3, PO_4 and Si become exhausted in the upper water column due to consumption during primary production. As organic material is exported from the surface mixed layer to underlying waters, NO_3, PO_4 and Si are supplied at depth by the regeneration of organic material, a process which consumes oxygen. The vertical gradient in AOU (d[AOU]/dz) from 100 m to 1000 m depth decreases from 0.17 µmol L^{-1} m^{-1} at the TAG site (R^2 = 0.99, Figure 5.8) to 0.10 µmol L^{-1} m^{-1} (R^2 = 0.97, Figure 5.8), resulting in stronger vertical gradients of regenerated material at the Rainbow site. The reduction in the vertical gradient of AOU and regenerated NO_3, PO_4 and Si mitigates changes in the diapycnal flux due to increases in physical mixing. Therefore, stronger vertical gradients in tracer profiles are inherent to regions of reduced vertical mixing, meaning that decreases in vertical mixing do not always result in concurrent reductions to vertical resource transport.

Water masses originating from high latitudes are recognised to regulate productivity in the tropical ocean (Sarmiento et al., 2004). In this study, we identify an elevation in the vertical flux of NO_3, PO_4 and Si from 750 m to 850 m depth at the TAG site (Figure 5.6). Water mass analysis shows the contribution of Antarctic Intermediate Waters (AAIW) to the water column peaks at 45% around ~1000 m depth at TAG. The end-member composition of AAIW is rich in NO_3, PO_4 and Si compared to other major contributing water masses (Mediterranean Overflow Water, Upper Labrador Sea Water and Irminger Sea Water, Figure 5.7) in the region (Jenkins et al., 2015). The

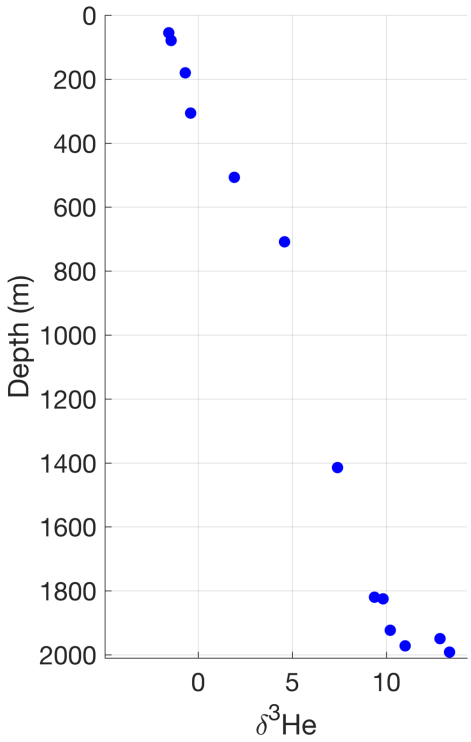

Figure 5.9. Vertical profile of δ^3He (%) at the Rainbow hydrothermal site on the Mid-Atlantic Ridge. Data from the stainless-steel rosette on the FRidge (*GEOTRACES* GA13) field campaign.

increase in the AAIW water contribution from 21% to 35% between ~700 m and ~800 m depth forms gradients in the vertical profiles of NO_3, PO_4 and Si, which increases the vertical flux (Figure 5.7). From ~800 m to 1000 m, the contribution of AAIW increases from 35% to 42%, a notably weaker AAIW contribution than in overlying waters, resulting in weaker resource gradients and weaker vertical fluxes (Figure 5.7). Overall, our results demonstrate the importance of physical processes in shaping nutrient-type profiles at low latitude systems and subsequent resources fluxes.

5.5.2.2 Processes Influencing the Fe Vertical Profile

In contrast to nutrient-type resources, diapycnal mixing may increase and reduce Fe availability in the upper water column. There is a downward flux of Fe in the upper 250 m and 450 m at the Rainbow and TAG sites respectively. At both sites, surface maxima exist due to dust derived surface maxima. The depth at which the downwards Fe flux meets the upwards Fe flux signifies a subsurface minimum in the vertical Fe profile and flux convergence, resulting in a build-up of Fe acting to erode the minima. As Fe is a hybrid-type resource, the shift from a downward flux to an upward flux identifies a transition from the scavenged-type to nutrient-type region of the Fe profile.

The contrasting depth at which Fe transitions from scavenged-type to nutrient-type is likely due to greater dust deposition rates at TAG (Jickells et al., 2005, Baker et al., 2013) or enhanced scavenging rates at the Rainbow site. There is an influence of MOW at both TAG and Rainbow sites (Figure 5.7). Although the Mediterranean receives large quantities of Saharan dust (and therefore Fe), biological uptake and scavenging of Fe prior to MOW entering the North Atlantic basin result in no subsurface Fe signal associated with MOW (Hatta et al., 2015). Overall, we demonstrate that the vertical Fe fluxes at TAG and Rainbow are controlled by local processes rather than remote influences.

5.5.2.3 Processes Influencing the Mn and Al Vertical Profiles

Mn and Al are generally associated with scavenged-type vertical profiles due to atmospheric deposition and the photoreduction of Mn oxides in the upper ocean and the high Al content of dust in the subtropical North Atlantic, resulting in large surface stocks and downward Mn and Al fluxes due to diapycnal mixing. The Mn flux profile at TAG is typical of Mn in the deep ocean as surface maxima are eroded by mixing, while at depth the vertical Mn concentration is ~ 0.2 nmol kg^{-1}, resulting in negligible diapycnal fluxes due to the absence of vertical gradients. There is an upward flux of both Mn and Al from below 550 m depth at the Rainbow site, indicative of a subsurface Mn and Al source which is transported vertically by diapycnal mixing. Water mass analysis from ~700 m to ~1100 m has demonstrated a strong influence of Mediterranean Outflow Water in the subtropical North Atlantic. MOW is recognised as a major source of Al at mid-depths in the North Atlantic (Jenkins et al., 2015, Menzel Barraqueta et al., 2018). However, the contribution of MOW to the water column decreases with depth at both sites, conceptually this would result in a contemporaneous decrease in Al concentrations with depth and downwards Al flux. There are two candidate processes which may act as a subsurface source of Mn and Al at the Rainbow site: (1) lateral transport and (2) hydrothermal inputs. The Azores current is the southern extension of the Gulf Stream and forms the north-eastern limb of the North Atlantic subtropical Gyre. The Azores current influences hydrography at the Rainbow site (Thurnherr and Richards, 2001), meaning an upstream source of Mn or Al maybe transported along isopycnals, then accessed by diapycnal mixing. Alternatively, the elevation in Mn and Al may be augmented by hydrothermal inputs

at depth (Hatta et al., 2015, Measures et al., 2015, Resing et al., 2015). This hypothesis is supported a strong vertical gradient in excess 3-helium, a conservative tracer of hydrothermal inputs (Figure 5.9). In summary, the vertical flux of Mn and Al is dependent upon K_z and gradients in their vertical profiles, which are affected by a myriad of local and remote processes.

5.5.3 Wider Considerations

Results from this study have demonstrated the need to consider changes in both the vertical resources profile and vertical mixing when determining resource fluxes. Here, we discuss the relevance of this finding in relation to a short-term process, the spring-neap tidal cycle, and a long-term process, enhanced stratification associated with future warming oceans from the present to 2100.

5.5.3.1 Spring-Neap Resource Pulses

Evidence presented in section 5.5.2.1 demonstrates that in a reduced mixing environment, regeneration permits the accumulation of NO_3, PO_4 and Si at depth, strengthening vertical gradients in their associated vertical profiles. We are able to use this assertion to speculate on the role of the spring-neap tidal cycle in enhancing the resource flux, which has been demonstrated to increase the NO_3 flux by a factor of 9 over the mid-Atlantic Ridge (Tuerena et al. 2019). During neap tides (reduced mixing), subsurface resource stocks are increased by the regeneration and remineralization of detrital organic matter sinking from above. As K_z is low during neap tides, strong vertical gradients form between the productive upper ocean and underlying waters. During subsequent spring tides, an increase in K_z is observed over rough topography. The elevation in K_z and stronger vertical gradients which formed in previous weeks during neap tides couple to greatly increase resource fluxes. This process erodes vertical gradients and the system returns to neap tidal conditions, where a reduced K_z and weaker vertical gradients cause a decrease in the vertical resource flux. The coupled effect of changes to K_z and vertical gradients during the spring-neap tidal cycle results in greater variance in the resource flux compared to that in K_z alone. In this theoretical case, a factor three increase in resource gradients and a factor three increase in K_z amplify the resource flux by a factor nine, highlighting that observed

changes to K_z alone do not directly correspond to changes in the vertical resource flux. While the dataset used for this study is unsuitable to quantify this process due to temporal limitations of observations, we hypothesise that the spring-neap tidal cycle delivers regular pulses of key resources to the upper ocean biome in productive regions.

In this study, we demonstrate the importance of topographical depth relative to the thermocline in regulating diapycnal exchanges in the upper ocean. Previous work has shown that interactions between the spring-neap tidal cycle and topography drives pulses in the delivery of NO_3 to the subsurface chlorophyll maxima (Tuerena et al., 2019). We are therefore able to infer similar pulses in the delivery of other resources, such as PO_4, Si, Fe and Mn, to the sub-tropical North Atlantic over rough topography; however, we are unable to directly quantify these exchanges in this study. This inference may be expanded to other regions of the global ocean. Vertical pulses of key resources due to the tidal cycle are important in regions where resource availability restricts productivity, such as Fe-limitation in the Southern Ocean (Moore et al., 2013, Wu et al., 2019), where periodic pulses in mixing over seamounts or ridges drive sporadic increases in productivity if Fe delivery is enhanced during spring tides. This inference is currently challenged by a lack of in-situ data, where both K_z and Fe are regularly sampled over the spring-neap tidal cycle near to rough topography, allowing quantification of changes to K_z, resource profiles and subsequently the vertical flux.

5.5.3.2 Mitigation to Decreased Mixing

Future projections of the global ocean biogeochemistry report a reduction in mixing due to enhanced warming and stratification, inducing a reduction in resource supply to the upper ocean and subsequent reduction in productivity (Bopp et al., 2001, Lefebvre and Goosse, 2008, Sen Gupta et al., 2009, Capotondi et al., 2012, Bindoff et al., 2019). However, over long periods where mixing rates are gradually reduced, subsurface resource stocks accumulate due to regeneration and a lack of mixing to erode the concentration maxima. This causes a strengthening of vertical resource gradients at depth as resource profiles adjust to weakened K_z and therefore mitigates against reduced mixing acting to decrease the vertical resource flux. In addition, changes to biogeochemical process may further enhance subsurface resource stocks

and vertical gradients in resource limited waters. For example, in a warming ocean, remineralization rates are expected to increase (Boscolo-Galazzo et al., 2018), leading to an enhanced supply of resources at depth and further strengthening vertical gradients in resource profiles where export is maintained. While recent work has demonstrated that increases in respiration rates are more sensitive to temperature than rates of primary production (Barton et al., 2020) resulting in enhanced recycling in the euphotic zone and less export to underlying waters, we contend that over long periods resources are ultimately exported from the euphotic zone and must be resupplied by external sources. We suggest that in a reduced mixing scenario, vertical resource profiles adjust to K_z and resource gradients are strengthened, meaning assumptions that productivity decreases proportionally to reductions in K_z alone are incorrect.

The long-term view is further challenged by changes to circulation pathways which form vertical gradients in resource profiles and sustain primary production (Jenkins and Doney, 2003, Sarmiento et al., 2004). Nutrient streams are characterized by strong subsurface boundary currents associated with enhanced subsurface nutrient concentrations, inducing regions of significant resource transport at depth (Williams et al., 2006, Palter and Lozier, 2008). Nutrient streams transport resources from depth in mid-latitudes to the upper ocean in high latitudes as isopycnals outcrop; vertical mixing processes then transfer these resources into the mixed-layer (Pelegrí et al., 1996). Recent works have demonstrated that in a future ocean, a slowing of nutrient streams and decrease in winter mixed-layer depths causes a decrease in productivity as resource supply is diminished (Tagklis et al., 2020, Whitt and Jansen, 2020). Productivity is further diminished by considering that as nutrient streams slow vertical gradients in resource profiles weaken, particularly at high latitudes, meaning the vertical flux is reduced. Alongside changes in nutrient streams, water mass contributions will alter in the future ocean (Meijers, 2014). As demonstrated in this study, water mass contributions influence vertical resource gradients and subsequent vertical fluxes, hence warranting further study. Overall, we speculate that long-term changes to both K_z and circulation pathways alter the distribution of resources causing a complex response in vertical resource fluxes which sustain primary production.

5.6 Conclusions

VMP derived estimates of diapycnal diffusion are combined with resource profiles to calculate the vertical flux of NO_3, PO_4, Si, Fe, Mn and Al at two topographical sites along the Mid-Atlantic Ridge. We show an elevation in upper ocean K_z at the shallow Rainbow site (z_{bottom} = 2367 m) compared to the deeper TAG site (z_{bottom} = 3553 m). VMPs were paired to resource profiles based on multiple criteria. Using an ARGO float data climatology of K_z, we demonstrate that the use of VMPs within one Rossby radius of a resource profile is most representative of K_z at the resource profile site. In addition, we find that K_z in the upper ocean is driven primarily by tidal forcing while wind inputs play a background role. From 250 m – 550 m, diapycnal exchanges supply nutrient-type resources to the upper ocean, while eroding surface maxima in scavenged-type resources. Fe is transported downwards at the TAG site and upwards at the Rainbow site as the sub-surface minima of Fe is deeper at TAG. Although K_z is larger at Rainbow compared to TAG, vertical fluxes remain comparable due to contrasts in the vertical resource gradients between Rainbow and TAG. The shape of vertical resource profiles differs between the two sites due to physical and biological processes. We demonstrate that at the TAG site, stronger vertical gradients result from the presence of aged water that have undergone more remineralisation, while the influence of AAIW was also greater than at the Rainbow site, mitigating changes in vertical mixing between the two sites.

Our results demonstrate the need to consider changes in vertical resource profiles alongside changes in mixing to diagnose subsequent effects on resource supply. During short-term periods of reduced mixing followed by periods of enhanced mixing, such as the spring-neap tidal cycle, resources accumulate at depth during neap tides and subsequent enhancements in mixing during spring tide then increase resource vertical supply. The combination of periodic enhanced mixing and stronger vertical gradients generates pulses in resource supply to upper ocean biota. In contrast, the prevailing view is that in a future warming ocean the vertical supply of resources to the upper ocean is diminished due to enhanced stratification. Future reductions in mixing, and subsequently resource supply, are mitigated by the formation of stronger vertical gradients in resource profiles under a reduced mixing regime, enhanced

regeneration at depth due to the temperature dependence of metabolic processes and changes to water mass circulation pathways.

6. Conclusions

The overarching aim of this thesis was to provide new insights into the distribution of bio-essential resources and the processes governing their supply to the upper ocean to support primary production. Specifically, initial research questions concerned the availability of trace-elements in the winter mixed-layer depth, the role of winter-time entrainment, regional and temporal variations in diapycnal mixing and the influence of topographic features on resources fluxes. The new knowledge produced in this thesis allows us to understand observed patterns in marine phytoplankton, key processes sustaining their growth and anticipate how those patterns may change in the future. This has achieved by synthesizing modelling and *in-situ* observations in the fields of both physical oceanography and marine biogeochemistry. As well as developing our understanding of upper ocean resource cycling, this thesis paves the way for avenues of future research.

6.1 Thesis Findings

In Chapter 3, output from the Estimating the Circulation and Climate of the Ocean (ECCO) global circulation model was combined with observational data from *GEOTRACES* to investigate the availability of resources throughout the winter mixed layer in the Atlantic Ocean. Results demonstrated that there are clear basin-scale regimes in the relative availability and winter-time entrainment of resources, which are dependent on the vertical profile of each resource. Resource availability is high where the mixed-layer depth extends to below the nutricline in winter, while mixed-layer resources remain depleted if subsurface stocks are not accessed by winter mixing. Offsets in the depth and shape of vertical gradients between resources establishes large-scale regimes in resource availability and stoichiometry. For example, in the subtropical North Atlantic, NO_3 and PO_4 exhibit nutrient-type profiles and are depleted in surface waters, while the reverse is the case for scavenged-type resource Mn, leading to low estimates of NO_3/PO_4 and high estimates of Mn/PO_4 in the region. Further, comparison of N and Fe stocks show singular N-limitation in the subtropical North Atlantic and singular Fe-limitation in high latitudes. Fe limitation in deep water formations sites, such as the Labrador Sea, eludes to a key role of high latitude Fe stocks in regulating low latitude biogeochemistry. The relative availability

of resources sits on a continuum between nutrient-type resource NO_3/PO_4 and scavenged-type resource Mn/PO_4, where resources are correlated to end-members as follows: NO_3/PO_4, Cd/PO_4, Si/PO_4, Zn/PO_4, Co/PO_4, Fe/PO_4, Mn/PO_4. The shape of vertical resource profiles also alters the role of entrainment in governing mixed-layer resource availability. In winter, the seasonal deepening of the mixed layer entrains underlying waters into the mixed layer, replenishing nutrient-type resources lost to export. However, seasonal entrainment reduces the availability of scavenged-type resources, as surface maxima are eroded and resource stocks diluted. Finally, as the depth attained by winter mixing is highly variable, Chapter 3 investigated changes in resource availability under multiple mixing scenarios. While the response was complex and highly varied between resource and region, results demonstrated that the mixed layer in the low latitude Atlantic Ocean becomes richer in Si, Zn, Co, Fe and Mn relative to PO_4 under a reduced mixing scenario. Changes to the stoichiometry of the mixed layer has important ecological consequences such as resource deficiency or changes in phytoplankton community structure.

Data captured by ocean transect field campaigns, such as those in *GEOTRACES*, offer single snapshots of the ocean environment. To further investigate the temporal role of mixing and winter-time entrainment from *GEOTRACES* observations, Chapter 4 used helium, a chemically and biologically inert noble gas, as a tracer of mixing which integrates physical signals. By estimating rates of air-sea gas exchange, air injection by bubble processes and the *in-situ* decay of tritium, a residual flux of helium due to diapycnal transfers from below was calculated. The residual flux was then used alongside the vertical gradient of helium to infer total physical transprt. Data from two seasonally differing field campaigns were used to demonstrate that vertical mixing in the seasonal thermocline is greater by a factor of 7 when winter-time entrainment is active. This demonstrates that temporal changes in physical processes must be considered when interpreting single point observations. As Chapter 3 highlighted the key role of resource gradients in setting the vertical resource flux, in Chapter 4 we the explored linkages between oxygen gradients and resource gradients in the equatorial Pacific and subtropical North Atlantic. In both regions, NO_3, PO_4, Si, and Mn displayed strong relationships with oxygen. However, Co displayed a strong relationship with oxygen in the subtropical North Atlantic only, while Fe displayed a strong relationship with oxygen in the equatorial Pacific only. Zn did not show strong

linkages to oxygen in either region. A simple linear model was applied to estimate the relative role of resource gradients and diapycnal mixing in explaining the resource fluxes at each station. This approach showed that variation in diapycnal mixing was the main driver of variability in resource fluxes in the subtropical North Atlantic, while both resource gradients and diapycnal mixing were important in the equatorial Pacific. In the subtropical North Atlantic, resource fluxes were compared to the accumulation of resources within multiple groups of phytoplankton taxa to show that the cellular composition of nanophytoplankton and dinoflagellates was similar to the stoichiometry of the upwards flux. However, the stoichiometry of the upwards flux differed to the cellular stoichiometry of diatoms, suggesting diatoms may accumulate resources from other external sources, such as aeolian deposition. Finally, the Fe-N limitation algorithm developed by Browning et al. (2017a) was applied to resource fluxes in the equatorial Pacific to demonstrate the transition from Fe-N serial limitation in the Peruvian Upwelling Zone to Fe-singular limitation in the open ocean.

Chapter 5 builds on the temporal variations in diapycnal mixing identified in Chapter 4 by exploring spatial changes in diapycnal mixing in the upper ocean around regions of rough topography. Vertical microstructure profiler data from the RidgeMix project enabled direct comparisons of mixing between a shallow topographic site and a deep topographic site from *in-situ* data. Data is available from two key sites along the Mid-Atlantic Ridge, Rainbow hydrothermal vent site (z = 2673m) and TAG hydrothermal vent site (z = 3553m). Snapshots of mixing were used to demonstrate an increase in mixing by a factor two in the upper 1000m at the shallow site compared to the deep site. The Rainbow and TAG sites were also highly sampled areas during the GA13 field campaign, meaning vertical profiles of resources are available at both sites. However, the physical and biogeochemical datasets were from differing cruises. Vertical resource profiles from GA13 and vertical microstructure profilers from RidgeMix were paired dependent upon geographical position and by similar external forcing by the wind and tides. ARGO floats were used to identify that the pairing of profiles by external forcing and within one Rossby Radius is most representative of mixing. Vertical fluxes of NO_3, PO_4, Si, Fe, Mn and Al were computed at both hydrothermal vent sites, however, the increase in diapycnal mixing did not always result in increases to the resource flux. The increase in diapycnal mixing at the shallow topographic site was mitigated by a reduction in the strength of vertical resource

gradients. NO_3, PO_4 and Si are nutrient-type resources and hence supplied to the upper ocean by diapycnal mixing at both sites. The behaviour of Fe is different between the two sites, as diapycnal mixing removes Fe at the TAG site, while Fe is removed from the upper ocean at the Rainbow site. Surface maxima in Mn and Al are eroded by diapycnal mixing at both sites. Differences in the vertical gradients of resources between the two hydrothermal sites are partially attributed to differences in the contribution of water masses. At the TAG site, the influence of Antarctic Intermediate Water is greater than at the Rainbow site, resulting in stronger gradients of resources associated with Antarctic Intermediate Water, such as Si. The analysis completed in Chapter 5 drew linkages to temporally varying processes. For example, during the short-term periodic processes such as the spring-neap tidal cycle, a reduction in mixing during neap tides permits the accumulation of resources at depth, increasing vertical gradients. Subsequent increases in mixing during spring tides are coupled with stronger resource gradients formed during neap tides to induce strong, periodic pulses of resources to biota in the upper ocean. During long-term changes such as ocean warming, reduced mixing permits the strengthening of vertical resource gradients and mitigates changes to the vertical resource flux. This hypothesis challenges the current first-order view that a reduction in mixing causes a proportional decrease in the vertical resource flux and subsequent decrease in upper ocean productivity.

6.2 Future Directions

This thesis presented the stoichiometry of NO_3, PO_4, Si, Cd, Co, Zn, Fe and Mn in the winter mixed-layer of the Atlantic Ocean. Due to practical constraints, vertical resource profiles are not currently available at monthly resolution and at global coverage, particularly for trace elements. Hence, in Chapter 3, monthly resource profiles are reconstructed by conserving resource concentrations on isopycnals and using physical hydrography from the ECCO model. There is currently a trend towards marine autonomy, ranging from moorings, drifting deep ARGO floats and biogeochemical ARGO floats, to pilotable sea gliders and slocum gliders. Advances in marine autonomy will enable significantly greater coverage of the global ocean, both temporally and spatially, as well as targeted studies in remote regions. Moorings are typically deployed to collect a time-series of hydrographic conditions at a fixed location, such as the RAPID array (McCarthy et al., 2015), and will be exploited to

provide a time-series of trace elements in future studies. The ARGO programme monitors the global ocean by use of 3906 operational drifters (as of November 2020, https://www.ocean-ops.org/board?t=argo) and recently received additional funding for the biogeochemical ARGO platforms, which includes the measurement of oxygen, nitrate and chlorophyll. Ocean gliders are able to continuously record observations for thousands of kilometers while the pilot resides in an onshore command center, negating the need for expensive ship time and the deployment of personnel to remote environments such as the Southern Ocean in winter. However, sensors able to measure trace element availability at oceanic concentrations are not yet operational, hence limiting the capabilities of marine autonomy in biogeochemical studies. Trace element sensors are currently restricted by their sensitivity, size, power requirements and supporting infrastructure (Grand et al., 2019). The operational use of trace element sensors is anticipated by 2030 (Grand et al., 2019). The development of trace element sensors and continued improvements to autonomous vehicles will enable more accurate depictions of biogeochemical processes which are currently hindered by the availability of in situ observations, such as the calculation of winter mixed-layer resource availability and monthly entrainment in Chapter 3 of this thesis. However, until such equipment is available, traditional transect studies focused on regions of biogeochemical importance will remain crucial to advancing our understanding. For example, this thesis has identified the potential for Fe limitation in North Atlantic deep-water formation sites, suggesting that high latitude Fe exerts a remote influence over low latitude biogeochemistry. However, sufficient observations to further investigate this hypothesis are unavailable at present.

Linking relative resource availability to the composition of marine phytoplankton to predict regions of resource limitation was an early ambition of this thesis, however, this was considered unfeasible with current datasets. We require studies on the composition of marine phytoplankton, both at taxon and community level, under numerous resource replete conditions as well as under singular-, serial-, and co-limited conditions. The importance of considering resource conditions was evidenced by Hawco et al. (2018), where increasing the availability of Zn and Mn caused a decrease in productivity as the Co uptake mechanism was inhibited by Zn and Mn. Proteomic and metabolomic studies are further advancing our understanding of resource limited phytoplankton by investigating protein signatures under resource stress (Saito et al.,

2014, Wu et al., 2019). In biogeochemical models, resource limitation by nitrogen, phosphorus, silicic acid or iron is considered by following a simple law of the minimum approach (Galbraith et al., 2010, Dunne et al., 2013, Aumont et al., 2015). Further, the Biogeochemical Southern Ocean State Estimate uses the BLING model which does not include Mn (Galbraith et al., 2010, Verdy and Mazloff, 2017), however, *in-situ* studies have recognised Mn deficiency in the region (Moore, 2016, Wu et al., 2019). Future efforts should be made to expand the number of resources included in biogeochemical models, particularly Co, Zn and Mn. Such advances may then be used to investigate the importance of high latitude trace element cycling in setting deep water compositions and subsequent controls on low latitude biogeochemistry. Overall, to directly link resource stoichiometry to resource limitation requires a complete comprehension of phytoplankton growth under a range of resource replete and deplete conditions, which is currently unavailable.

In Chapters 3, 4 and 5, the vertical distribution and supply of bio-essential resources is linked to gradients in vertical resources which are influenced by oxygen minimum zones, changes to vertical mixing and the contribution of remote water masses. Each influencing process is projected to change over the 21st century. The logical progression from this thesis is therefore to further investigate forward-looking speculations based on major findings presented here. The shape of vertical resource profiles governs the availability of resources in the mixed layer, however, how will resource profiles change throughout the 21st century? A warmer ocean is likely to affect the rate of numerous metabolic processes, this will alter the vertical profile of each resource differently and therefore alter mixed layer resource stoichiometry. Future changes to ocean oxygen content remain uncertain (Stramma et al., 2008, Deutsch et al., 2014, Bindoff et al., 2019). In Chapter 4, regional differences in linkages between oxygen and multiple resources were identified. Hence, the role of oxygen in modulating resource gradients in other regions of the global ocean is important and requires further study. Finally, physical changes to the global ocean during the 21st century will have significant implications on the vertical supply of resources to the upper ocean. How do future changes to ocean circulation affect the vertical gradients of bio-essential resources? Biogeochemical implications of a slowdown to nutrient streams in the Atlantic have been noted by recent works (Tagklis et al., 2020, Whitt and Jansen, 2020). Marine heatwaves exist in the ocean for days to

months and are projected to increase in frequency over the 21st century (Frölicher et al., 2018, Oliver et al., 2019). How does the regional warming of the upper ocean affect resource profiles, diapycnal mixing and subsequent resource supply? Is there an accumulation of resources in the subsurface during marine heatwave events which is transferred to biota and stimulates additional primary production when the ocean returns to regular conditions? Overall, understanding future changes to processes which influence the vertical distribution and transfers of resources is important and demands further research.

References

ACHTERBERG, E. P., STEIGENBERGER, S., MARSAY, C. M., LEMOIGNE, F. A. C., PAINTER, S. C., BAKER, A. R., CONNELLY, D. P., MOORE, C. M., TAGLIABUE, A. & TANHUA, T. 2018. Iron Biogeochemistry in the High Latitude North Atlantic Ocean. *Scientific Reports,* 8.

ALFORD, M. H. 2003. Redistribution of energy available for ocean mixing by long-range propagation of internal waves. *Nature,* 423**,** 159-162.

ALFORD, M. H., MACKINNON, J. A., SIMMONS, H. L. & NASH, J. D. 2016. Near-Inertial Internal Gravity Waves in the Ocean. *Annual Review of Marine Science,* 8**,** 95-123.

AMANTE, C. & EAKINS, B. W. 2009. *ETOPO1 1 Arc-Minute Global Relief Model: Procedures, Data Sources and Analysis.* [Online]. NOAA Technical Memorandum NESDIS NGDC-24. National Geophysical Data Center, NOAA. doi: 10.7289/V5C8276M. [Accessed 17/07/2020].

ANDERSON, L. A. & SARMIENTO, J. L. 1994. Redfield ratios of remineralization determined by nutrient data analysis. *Global Biogeochemical Cycles,* 8**,** 65-80.

ANDERSON, R. F. 2020. GEOTRACES: Accelerating Research on the Marine Biogeochemical Cycles of Trace Elements and Their Isotopes. *Annual Review of Marine Science,* 12**,** 49-85.

AUMONT, O., BOPP, L. & SCHULZ, M. 2008. What does temporal variability in aeolian dust deposition contribute to sea-surface iron and chlorophyll distributions? *Geophysical Research Letters,* 35.

AUMONT, O., ETHÉ, C., TAGLIABUE, A., BOPP, L. & GEHLEN, M. 2015. PISCES-v2: an ocean biogeochemical model for carbon and ecosystem studies. *Geosci. Model Dev.,* 8**,** 2465-2513.

BAKER, A. R., ADAMS, C., BELL, T. G., JICKELLS, T. D. & GANZEVELD, L. 2013. Estimation of atmospheric nutrient inputs to the Atlantic Ocean from 50°N to 50°S based on large-scale field sampling: Iron and other dust-associated elements. *Global Biogeochemical Cycles,* 27**,** 755-767.

BAKER, A. R. & CROOT, P. L. 2010. Atmospheric and marine controls on aerosol iron solubility in seawater. *Marine Chemistry,* 120**,** 4-13.

BAKER, A. R., FRENCH, M. & LINGE, K. L. 2006. Trends in aerosol nutrient solubility along a west–east transect of the Saharan dust plume. *Geophysical Research Letters,* 33.

BAKER, A. R. & JICKELLS, T. D. 2017. Atmospheric deposition of soluble trace elements along the Atlantic Meridional Transect (AMT). *Progress in Oceanography,* 158**,** 41-51.

BARBER, R. T. & CHAVEZ, F. P. 1983. Biological Consequences of El-Nino. *Science,* 222**,** 1203-1210.

BARTON, S., JENKINS, J., BUCKLING, A., SCHAUM, C. E., SMIRNOFF, N., RAVEN, J. A. & YVON-DUROCHER, G. 2020. Evolutionary temperature compensation of carbon fixation in marine phytoplankton. *Ecology Letters,* 23**,** 722-733.

BENSON, B. B. & KRAUSE, D. 1980. Isotopic fractionation of helium during solution: A probe for the liquid state. *Journal of Solution Chemistry,* 9**,** 895-909.

BINDOFF, N. L., CHEUNG, W. W. L., KAIRO, J. G., ARÍSTEGUI, J., GUINDER, V. A., HALLBERG, R., HILMI, N., JIAO, N., KARIM, M. S., LEVIN, L., O'DONOGHUE, S., PURCA CUICAPUSA, S. R., RINKEVICH, B., SUGA, T., TAGLIABUE, A. & WILLIAMSON, P. 2019. *Changing Ocean, Marine Ecosystems, and Dependent Communities. In: IPCC Special Report on the Ocean and Cryosphere in a Changing Climate [H.-O. Pörtner, D.C. Roberts, V. Masson-Delmotte, P. Zhai, M. Tignor, E. Poloczanska, K. Mintenbeck, A. Alegría, M. Nicolai, A. Okem, J. Petzold, B. Rama, N.M. Weyer (eds.)]. In press.*

BLAIN, S., SARTHOU, G. & LAAN, P. 2008. Distribution of dissolved iron during the natural iron-fertilization experiment KEOPS (Kerguelen Plateau, Southern Ocean). *Deep Sea Research Part II: Topical Studies in Oceanography,* 55**,** 594-605.

BOPP, L., MONFRAY, P., AUMONT, O., DUFRESNE, J. L., LE TREUT, H., MADEC, G., TERRAY, L. & ORR, J. C. 2001. Potential impact of climate change on marine export production. *Global Biogeochemical Cycles,* 15**,** 81-99.

BOPP, L., RESPLANDY, L., ORR, J. C., DONEY, S. C., DUNNE, J. P., GEHLEN, M., HALLORAN, P., HEINZE, C., ILYINA, T., SÉFÉRIAN, R., TJIPUTRA, J. & VICHI, M. 2013. Multiple stressors of ocean ecosystems in the 21st century: projections with CMIP5 models. *Biogeosciences,* 10**,** 6225-6245.

BOSCOLO-GALAZZO, F., CRICHTON, K. A., BARKER, S. & PEARSON, P. N. 2018. Temperature dependency of metabolic rates in the upper ocean: A positive feedback to global climate change? *Global and Planetary Change,* 170**,** 201-212.

BOURG, I. C. & SPOSITO, G. 2008. Isotopic fractionation of noble gases by diffusion in liquid water: Molecular dynamics simulations and hydrologic applications. *Geochimica et Cosmochimica Acta,* 72**,** 2237-2247.

BOYD, P. W., CLAUSTRE, H., LEVY, M., SIEGEL, D. A. & WEBER, T. 2019. Multi-faceted particle pumps drive carbon sequestration in the ocean. *Nature,* 568**,** 327-335.

BOYD, P. W., CROSSLEY, A. C., DITULLIO, G. R., GRIFFITHS, F. B., HUTCHINS, D. A., QUEGUINER, B., SEDWICK, P. N. & TRULL, T. W. 2001. Control of phytoplankton growth by iron supply and irradiance in the subantarctic Southern Ocean: Experimental results from the SAZ Project. *Journal of Geophysical Research: Oceans,* 106**,** 31573-31583.

BOYD, P. W. & ELLWOOD, M. J. 2010. The biogeochemical cycle of iron in the ocean. *Nature Geoscience,* 3**,** 675-682.

BOYD, P. W., ELLWOOD, M. J., TAGLIABUE, A. & TWINING, B. S. 2017. Biotic and abiotic retention, recycling and remineralization of metals in the ocean. *Nature Geoscience,* 10**,** 167-173.

BOYE, M., WAKE, B. D., GARCIA, P. L., BOWN, J., BAKER, A. R. & ACHTERBERG, E. P. 2012. Distributions of dissolved trace metals (Cd, Cu, Mn, Pb, Ag) in the southeastern Atlantic and the Southern Ocean. *Biogeosciences,* 9**,** 3231-3246.

BOYLE, E. A., ANDERSON, R. F., CUTTER, G. A., FINE, R., JENKINS, W. J. & SAITO, M. 2015a. Introduction to the U.S. GEOTRACES North Atlantic Transect (GA-03): USGT10 and USGT11 cruises. *Deep Sea Research Part II: Topical Studies in Oceanography,* 116**,** 1-5.

BOYLE, E. A., ANDERSON, R. F., CUTTER, G. A., FINE, R., JENKINS, W. J. & SAITO, M. 2015b. Introduction to the US GEOTRACES North Atlantic Transect (GA-03): USGT10 and USGT11 cruises. *Deep-Sea Research Part Ii-Topical Studies in Oceanography,* 116**,** 1-5.

BREWER, P. G., SPENCER, D. W. & ROBERTSO.DE 1972. Trace-Element Profiles from Geosecs-Ii Test Station in Sargasso Sea. *Earth and Planetary Science Letters,* 16**,** 111-&.

BROECKER, W. S., BLANTON, S., SMETHIE JR, W. M. & OSTLUND, G. 1991. Radiocarbon decay and oxygen utilization in the Deep Atlantic Ocean. *Global Biogeochemical Cycles,* 5**,** 87-117.

BROWNING, T. J., ACHTERBERG, E. P., RAPP, I., ENGEL, A., BERTRAND, E. M., TAGLIABUE, A. & MOORE, C. M. 2017a. Nutrient co-limitation at the boundary of an oceanic gyre. *Nature,* 551**,** 242-+.

BROWNING, T. J., ACHTERBERG, E. P., YONG, J. C., RAPP, I., UTERMANN, C., ENGEL, A. & MOORE, C. M. 2017b. Iron limitation of microbial phosphorus acquisition in the tropical North Atlantic. *Nature Communications,* 8.

BRULAND, K. W. 1980. Oceanographic Distributions of Cadmium, Zinc, Nickel, and Copper in the North Pacific. *Earth and Planetary Science Letters,* 47**,** 176-198.

BRULAND, K. W., KNAUER, G. A. & MARTIN, J. H. 1978. Cadmium in Northeast Pacific Waters. *Limnology and Oceanography,* 23**,** 618-625.

BRULAND, K. W. & LOHAN, M. C. 2003. Controls of Trace Metals in Seawater. *Treatise on Geochemistry,* 6**,** 625.

BURCHARD, H. 2009. Combined Effects of Wind, Tide, and Horizontal Density Gradients on Stratification in Estuaries and Coastal Seas. *Journal of Physical Oceanography,* 39**,** 2117-2136.

CAPONE, D. G., BURNS, J. A., MONTOYA, J. P., SUBRAMANIAM, A., MAHAFFEY, C., GUNDERSON, T., MICHAELS, A. F. & CARPENTER, E. J. 2005. Nitrogen fixation by Trichodesmium spp.: An important source of new nitrogen to the tropical and subtropical North Atlantic Ocean. *Global Biogeochemical Cycles,* 19.

CAPOTONDI, A., ALEXANDER, M. A., BOND, N. A., CURCHITSER, E. N. & SCOTT, J. D. 2012. Enhanced upper ocean stratification with climate change in the CMIP3 models. *Journal of Geophysical Research-Oceans,* 117.

CHARNOCK, H. 1955. Wind stress on a water surface. *Quarterly Journal of the Royal Meteorological Society,* 81**,** 639-640.

CHELTON, D. B., DESZOEKE, R. A., SCHLAX, M. G., EL NAGGAR, K. & SIWERTZ, N. 1998. Geographical Variability of the First Baroclinic Rossby Radius of Deformation. *Journal of Physical Oceanography,* 28**,** 433-460.

CHEN, D., BUSALACCHI, A. J. & ROTHSTEIN, L. M. 1994. The roles of vertical mixing, solar radiation, and wind stress in a model simulation of the sea surface temperature seasonal cycle in the tropical Pacific Ocean. *Journal of Geophysical Research: Oceans,* 99**,** 20345-20359.

COHEN, N. R., MANN, E., STEMPLE, B., MORENO, C. M., RAUSCHENBERG, S., JACQUOT, J. E., SUNDA, W. G., TWINING, B. S. & MARCHETTI, A. 2018. Iron storage capacities and associated ferritin gene expression among marine diatoms. *Limnology and Oceanography,* 63**,** 1677-1691.

COLEMAN, J. E. 1992. Structure and Mechanism of Alkaline Phosphatase. *Annual Review of Biophysics and Biomolecular Structure,* 21**,** 441-483.

CONWAY, T. M., HAMILTON, D. S., SHELLEY, R. U., AGUILAR-ISLAS, A. M., LANDING, W. M., MAHOWALD, N. M. & JOHN, S. G. 2019. Tracing and constraining anthropogenic aerosol iron fluxes to the North Atlantic Ocean using iron isotopes. *Nature Communications,* 10.

CONWAY, T. M. & JOHN, S. G. 2014. The biogeochemical cycling of zinc and zinc isotopes in the North Atlantic Ocean. *Global Biogeochemical Cycles,* 28**,** 1111-1128.

CONWAY, T. M. & JOHN, S. G. 2015. Biogeochemical cycling of cadmium isotopes along a high-resolution section through the North Atlantic Ocean. *Geochimica Et Cosmochimica Acta,* 148**,** 269-283.

CONWAY, T. M., PALTER, J. B. & DE SOUZA, G. F. 2018. Gulf Stream rings as a source of iron to the North Atlantic subtropical gyre. *Nature Geoscience,* 11**,** 594-+.

CRAIG, H. & TUREKIAN, K. K. 1980. The GEOSECS program: 1976–1979. *Earth and Planetary Science Letters,* 49**,** 263-265.

CRAIG, P. D. & BANNER, M. L. 1994. Modeling Wave-Enhanced Turbulence in the Ocean Surface Layer. *Journal of Physical Oceanography,* 24**,** 2546-2559.

CRONIN, M. F., PELLAND, N. A., EMERSON, S. R. & CRAWFORD, W. R. 2015. Estimating diffusivity from the mixed layer heat and salt balances in the North Pacific. *Journal of Geophysical Research: Oceans,* 120**,** 7346-7362.

CROOT, P. L., BAARS, O. & STREU, P. 2011. The distribution of dissolved zinc in the Atlantic sector of the Southern Ocean. *Deep-Sea Research Part Ii-Topical Studies in Oceanography,* 58**,** 2707-2719.

CUTTER, G. A. & BRULAND, K. W. 2012. Rapid and noncontaminating sampling system for trace elements in global ocean surveys. *Limnology and Oceanography: Methods,* 10**,** 425-436.

DARWIN, C. 1846. An account of the Fine Dust which often falls on Vessels in the Atlantic Ocean. *Quarterly Journal of the Geological Society,* 2**,** 26.

DE BAAR, H. J. W. 1994. von Liebig's law of the minimum and plankton ecology (1899–1991). *Progress in Oceanography,* 33**,** 347-386.

DE BOYER MONTEGUT, C., MADEC, G., FISCHER, A. S., LAZAR, A. & IUDICONE, D. 2004. Mixed layer depth over the global ocean: An

examination of profile data and a profile-based climatology. *Journal of Geophysical Research-Oceans,* 109.

DE BOYER MONTEGUT, C., VIALARD, J., SHENOI, S. S. C., SHANKAR, D., DURAND, F., ETHE, C. & MADEC, G. 2007. Simulated seasonal and interannual variability of the mixed layer heat budget in the northern Indian Ocean. *Journal of Climate,* 20**,** 3249-3268.

DEUTSCH, C., BERELSON, W., THUNELL, R., WEBER, T., TEMS, C., MCMANUS, J., CRUSIUS, J., ITO, T., BAUMGARTNER, T., FERREIRA, V., MEY, J. & VAN GEEN, A. 2014. Centennial changes in North Pacific anoxia linked to tropical trade winds. *Science,* 345**,** 665-668.

DIETZE, H., OSCHLIES, A. & KÄHLER, P. 2004. Internal-wave-induced and double-diffusive nutrient fluxes to the nutrient-consuming surface layer in the oligotrophic subtropical North Atlantic. *Ocean Dynamics,* 54**,** 1-7.

DUCE, R. A., LAROCHE, J., ALTIERI, K., ARRIGO, K. R., BAKER, A. R., CAPONE, D. G., CORNELL, S., DENTENER, F., GALLOWAY, J., GANESHRAM, R. S., GEIDER, R. J., JICKELLS, T., KUYPERS, M. M., LANGLOIS, R., LISS, P. S., LIU, S. M., MIDDELBURG, J. J., MOORE, C. M., NICKOVIC, S., OSCHLIES, A., PEDERSEN, T., PROSPERO, J., SCHLITZER, R., SEITZINGER, S., SORENSEN, L. L., UEMATSU, M., ULLOA, O., VOSS, M., WARD, B. & ZAMORA, L. 2008. Impacts of atmospheric anthropogenic nitrogen on the open ocean. *Science,* 320**,** 893-897.

DUCE, R. A., LISS, P. S., MERRILL, J. T., ATLAS, E. L., BUAT-MENARD, P., HICKS, B. B., MILLER, J. M., PROSPERO, J. M., ARIMOTO, R., CHURCH, T. M., ELLIS, W., GALLOWAY, J. N., HANSEN, L., JICKELLS, T. D., KNAP, A. H., REINHARDT, K. H., SCHNEIDER, B., SOUDINE, A., TOKOS, J. J., TSUNOGAI, S., WOLLAST, R. & ZHOU, M. 1991. The atmospheric input of trace species to the world ocean. *Global Biogeochemical Cycles,* 5**,** 193-259.

DUCE, R. A. & TINDALE, N. W. 1991. Atmospheric transport of iron and its deposition in the ocean. *Limnology and Oceanography,* 36**,** 1715-1726.

DULAQUAIS, G., BOYE, M., RIJKENBERG, M. J. A. & CARTON, X. 2014. Physical and remineralization processes govern the cobalt distribution in the deep western Atlantic Ocean. *Biogeosciences,* 11**,** 1561-1580.

DUNNE, J. P., JOHN, J. G., SHEVLIAKOVA, E., STOUFFER, R. J., KRASTING, J. P., MALYSHEV, S. L., MILLY, P. C. D., SENTMAN, L. T., ADCROFT, A. J., COOKE, W., DUNNE, K. A., GRIFFIES, S. M., HALLBERG, R. W., HARRISON, M. J., LEVY, H., WITTENBERG, A. T., PHILLIPS, P. J. & ZADEH, N. 2013. GFDL's ESM2 Global Coupled Climate–Carbon Earth System Models. Part II: Carbon System Formulation and Baseline Simulation Characteristics. *Journal of Climate,* 26**,** 2247-2267.

EGBERT, G. D. & EROFEEVA, S. Y. 2002. Efficient Inverse Modeling of Barotropic Ocean Tides. *Journal of Atmospheric and Oceanic Technology,* 19**,** 183-204.

EGBERT, G. D. & RAY, R. D. 2000. Significant dissipation of tidal energy in the deep ocean inferred from satellite altimeter data. *Nature,* 405**,** 775-778.

EMERSON, S. & BUSHINSKY, S. 2016. The role of bubbles during air-sea gas exchange. *Journal of Geophysical Research: Oceans,* 121**,** 4360-4376.

EPPLEY, R. W. & PETERSON, B. J. 1979. Particulate organic matter flux and planktonic new production in the deep ocean. *Nature,* 282**,** 677-680.

FALKOWSKI, P. G., BARBER, R. T. & SMETACEK, V. 1998. Biogeochemical controls and feedbacks on ocean primary production. *Science,* 281**,** 200-206.

FALKOWSKI, P. G., ZIEMANN, D., KOLBER, Z. & BIENFANG, P. K. 1991. Role of eddy pumping in enhancing primary production in the ocean. *Nature,* 352**,** 55-58.

FANTON D'ANDON, O., MANGIN, A., LAVENDER, S., ANTOINE, D., MARITORENA, S., MOREL, A. & BARROT, G. GlobColour - the European Service for Ocean Colour. Proceedings of the 2009 IEEE International Geoscience & Remote Sensing Symposium, July 12-17 2009 2009 South Africa.

FIELD, C. B., BEHRENFELD, M. J., RANDERSON, J. T. & FALKOWSKI, P. 1998. Primary production of the biosphere: Integrating terrestrial and oceanic components. *Science,* 281**,** 237-240.

FINKEL, Z. V., QUIGG, A., RAVEN, J. A., REINFELDER, J. R., SCHOFIELD, O. E. & FALKOWSKI, P. G. 2006. Irradiance and the elemental stoichiometry of marine phytoplankton. *Limnology and Oceanography,* 51**,** 2690-2701.

FORGET, G., CAMPIN, J. M., HEIMBACH, P., HILL, C. N., PONTE, R. M. & WUNSCH, C. 2015. ECCO version 4: an integrated framework for non-linear inverse modeling and global ocean state estimation. *Geoscientific Model Development,* 8**,** 3071-3104.

FORRYAN, A., MARTIN, A. P., SROKOSZ, M. A., POPOVA, E. E., PAINTER, S. C. & STINCHCOMBE, M. C. 2012. Turbulent nutrient fluxes in the Iceland Basin. *Deep-Sea Research Part I-Oceanographic Research Papers,* 63**,** 20-35.

FRÖLICHER, T. L., FISCHER, E. M. & GRUBER, N. 2018. Marine heatwaves under global warming. *Nature,* 560**,** 360-364.

FROLICHER, T. L., JOOS, F., PLATTNER, G. K., STEINACHER, M. & DONEY, S. C. 2009. Natural variability and anthropogenic trends in oceanic oxygen in a coupled carbon cycle-climate model ensemble. *Global Biogeochemical Cycles,* 23.

FUKUMORI, I., WANG, O., FENTY, I., FORGET, G., HEIMBACH, P. & PONTE, R. M. 2017. ECCO Version 4 Release 3, http://hdl.handle.net/1721.1/110380, doi:1721.1/110380. Available at ftp://ecco.jpl.nasa.gov/Version4/Release3/doc/v4r3_estimation_synopsis.pdf.

GALBRAITH, E. D., GNANADESIKAN, A., DUNNE, J. P. & HISCOCK, M. R. 2010. Regional impacts of iron-light colimitation in a global biogeochemical model. *Biogeosciences,* 7**,** 1043-1064.

GARCIA, H. E., WEATHERS, K., PAVER, C. R., SMOLYAR, I., BOYER, T. P., LOCARNINI, R. A., ZWENG, M. M., MISHONOV, A. V., BARANOVA, O. K., SEIDOV, D. & REAGAN, J. R. 2018. World Ocean Atlas 2018, Volume 4: Dissolved Inorganic Nutrients (phosphate, nitrate and nitrate+nitrite, silicate). A. Mishonov Technical Ed.; NOAA Atlas NESDIS 84, 35 pp.

GORDON, R. M., MARTIN, J. H. & KNAUER, G. A. 1982. Iron in north-east Pacific waters. *Nature,* 299**,** 611-612.

GRAND, M. M., LAES-HUON, A., FIETZ, S., RESING, J. A., OBATA, H., LUTHER, G. W., TAGLIABUE, A., ACHTERBERG, E. P., MIDDAG, R., TOVAR-SÁNCHEZ, A. & BOWIE, A. R. 2019. Developing Autonomous Observing Systems for Micronutrient Trace Metals. *Frontiers in Marine Science,* 6**,** 35.

GREGG, M. C., D'ASARO, E. A., RILEY, J. J. & KUNZE, E. 2018. Mixing Efficiency in the Ocean. *Annual Review of Marine Science,* 10**,** 443-473.

GRUBER, N., KEELING, C. D. & BATES, N. R. 2002. Interannual variability in the North Atlantic Ocean carbon sink. *Science,* 298**,** 2374-2378.

GRUBER, N. & SARMIENTO, J. L. 1997. Global patterns of marine nitrogen fixation and denitrification. *Global Biogeochemical Cycles,* 11**,** 235-266.

HAN, Q., MOORE, J. K., ZENDER, C., MEASURES, C. & HYDES, D. 2008. Constraining oceanic dust deposition using surface ocean dissolved Al. *Global Biogeochemical Cycles,* 22.

HART, T. J. 1942. Discovery Reports XXI. 343-344.

HATTA, M., MEASURES, C. I., WU, J. F., ROSHAN, S., FITZSIMMONS, J. N., SEDWICK, P. & MORTON, P. 2015. An overview of dissolved Fe and Mn distributions during the 2010-2011 US GEOTRACES north Atlantic cruises:

GEOTRACES GA03. *Deep-Sea Research Part Ii-Topical Studies in Oceanography,* 116**,** 117-129.

HAWCO, N. J., OHNEMUS, D. C., RESING, J. A., TWINING, B. S. & SAITO, M. A. 2016. A dissolved cobalt plume in the oxygen minimum zone of the eastern tropical South Pacific. *Biogeosciences,* 13**,** 5697-5717.

HAWCO, N. J. & SAITO, M. A. 2018. Competitive inhibition of cobalt uptake by zinc and manganese in a pacific Prochlorococcus strain: Insights into metal homeostasis in a streamlined oligotrophic cyanobacterium. *Limnology and Oceanography,* 0.

HELLER, M. I., LAM, P. J., MOFFETT, J. W., TILL, C. P., LEE, J.-M., TONER, B. M. & MARCUS, M. A. 2017. Accumulation of Fe oxyhydroxides in the Peruvian oxygen deficient zone implies non-oxygen dependent Fe oxidation. *Geochimica et Cosmochimica Acta,* 211**,** 174-193.

HELM, K. P., BINDOFF, N. L. & CHURCH, J. A. 2011. Observed decreases in oxygen content of the global ocean. *Geophysical Research Letters,* 38.

HEM, J. D. 1985. *Study and interpretation of the chemical characteristics of natural water*, Department of the Interior, US Geological Survey.

HO, T. Y., QUIGG, A., FINKEL, Z. V., MILLIGAN, A. J., WYMAN, K., FALKOWSKI, P. G. & MOREL, F. M. M. 2003. The elemental composition of some marine phytoplankton. *Journal of Phycology,* 39**,** 1145-1159.

HOGLE, S. L., DUPONT, C. L., HOPKINSON, B. M., KING, A. L., BUCK, K. N., ROE, K. L., STUART, R. K., ALLEN, A. E., MANN, E. L., JOHNSON, Z. I. & BARBEAU, K. A. 2018. Pervasive iron limitation at subsurface chlorophyll maxima of the California Current. *Proceedings of the National Academy of Sciences,* 115**,** 13300.

HOLTE, J., TALLEY, L. D., GILSON, J. & ROEMMICH, D. 2017. An Argo mixed layer climatology and database. *Geophysical Research Letters,* 44**,** 5618-5626.

HOLZER, M., PRIMEAU, F. W., DEVRIES, T. & MATEAR, R. 2014. The Southern Ocean silicon trap: Data-constrained estimates of regenerated silicic acid, trapping efficiencies, and global transport paths. *Journal of Geophysical Research-Oceans,* 119**,** 313-331.

HOPKINSON, B. M. & BARBEAU, K. A. 2008. Interactive influences of iron and light limitation on phytoplankton at subsurface chlorophyll maxima in the eastern North Pacific. *Limnology and Oceanography,* 53**,** 1303-1318.

IOC, SCOR & IAPSO 2010. The international thermodynamic equation of seawater – 2010: Calculation and use of thermodynamic properties. Intergovernmental

Oceanographic Commission, Manuals and Guides No. 56, UNESCO (English), 196 pp. Available from www.TEOS-10.org

ITO, T., MINOBE, S., LONG, M. C. & DEUTSCH, C. 2017. Upper ocean O2 trends: 1958–2015. *Geophysical Research Letters,* 44**,** 4214-4223.

JÄHNE, B., HEINZ, G. & DIETRICH, W. 1987. Measurement of the diffusion coefficients of sparingly soluble gases in water. *Journal of Geophysical Research: Oceans,* 92**,** 10767-10776.

JENKINS, W. J. 1988. Nitrate flux into the euphotic zone near Bermuda. *Nature,* 331**,** 521-523.

JENKINS, W. J. & DONEY, S. C. 2003. The subtropical nutrient spiral. *Global Biogeochemical Cycles,* 17.

JENKINS, W. J., DONEY, S. C., FENDROCK, M., FINE, R., GAMO, T., JEAN-BAPTISTE, P., KEY, R., KLEIN, B., LUPTON, J. E., NEWTON, R., RHEIN, M., ROETHER, W., SANO, Y., SCHLITZER, R., SCHLOSSER, P. & SWIFT, J. 2019. A comprehensive global oceanic dataset of helium isotope and tritium measurements. *Earth Syst. Sci. Data,* 11**,** 441-454.

JENKINS, W. J., SMETHIE, W. M., BOYLE, E. A. & CUTTER, G. A. 2015. Water mass analysis for the U.S. GEOTRACES (GA03) North Atlantic sections. *Deep Sea Research Part II: Topical Studies in Oceanography,* 116**,** 6-20.

JICKELLS, T. D., AN, Z. S., ANDERSEN, K. K., BAKER, A. R., BERGAMETTI, G., BROOKS, N., CAO, J. J., BOYD, P. W., DUCE, R. A., HUNTER, K. A., KAWAHATA, H., KUBILAY, N., LAROCHE, J., LISS, P. S., MAHOWALD, N., PROSPERO, J. M., RIDGWELL, A. J., TEGEN, I. & TORRES, R. 2005. Global iron connections between desert dust, ocean biogeochemistry, and climate. *Science,* 308**,** 67-71.

JICKELLS, T. D., BAKER, A. R. & CHANCE, R. 2016. Atmospheric transport of trace elements and nutrients to the oceans. *Philosophical Transactions of the Royal Society a-Mathematical Physical and Engineering Sciences,* 374.

KLUNDER, M. B., LAAN, P., MIDDAG, R., DE BAAR, H. J. W. & VAN OOIJEN, J. C. 2011. Dissolved iron in the Southern Ocean (Atlantic sector). *Deep-Sea Research Part Ii-Topical Studies in Oceanography,* 58**,** 2678-2694.

KRAUS, E. B. & TURNER, J. S. 1967. A One-Dimensional Model of Seasonal Thermocline .2. General Theory and Its Consequences. *Tellus,* 19**,** 98-&.

KRAUSE, D. & BENSON, B. B. 1989. The solubility and isotopic fractionation of gases in dilute aqueous solution. IIa. solubilities of the noble gases. *Journal of Solution Chemistry,* 18**,** 823-873.

KUNDE, K., WYATT, N. J., GONZÁLEZ-SANTANA, D., TAGLIABUE, A., MAHAFFEY, C. & LOHAN, M. C. 2019. Iron Distribution in the Subtropical North Atlantic: The Pivotal Role of Colloidal Iron. *Global Biogeochemical Cycles,* 33**,** 1532-1547.

KUNZE, E. 2017. Internal-Wave-Driven Mixing: Global Geography and Budgets. *Journal of Physical Oceanography,* 47**,** 1325-1345.

KUSTKA, A. B., SAÑUDO-WILHELMY, S. A., CARPENTER, E. J., CAPONE, D., BURNS, J. & SUNDA, W. G. 2003. Iron requirements for dinitrogen- and ammonium-supported growth in cultures of Trichodesmium (IMS 101): Comparison with nitrogen fixation rates and iron: carbon ratios of field populations. *Limnology and Oceanography,* 48**,** 1869-1884.

LAMPE, R. H., WANG, S., CASSAR, N. & MARCHETTI, A. 2019. Strategies among phytoplankton in response to alleviation of nutrient stress in a subtropical gyre. *The ISME Journal*.

LANDING, W. M. & BRULAND, K. W. 1987. The contrasting biogeochemistry of iron and manganese in the Pacific Ocean. *Geochimica et Cosmochimica Acta,* 51**,** 29-43.

LANDRY, M. R., BARBER, R. T., BIDIGARE, R. R., CHAI, F., COALE, K. H., DAM, H. G., LEWIS, M. R., LINDLEY, S. T., MCCARTHY, J. J., ROMAN, M. R., STOECKER, D. K., VERITY, P. G. & WHITE, J. R. 1997. Iron and grazing constraints on primary production in the central equatorial Pacific: An EqPac synthesis. *Limnology and Oceanography,* 42**,** 405-418.

LANDSCHÜTZER, P., GRUBER, N., HAUMANN, F. A., RÖDENBECK, C., BAKKER, D. C. E., VAN HEUVEN, S., HOPPEMA, M., METZL, N., SWEENEY, C., TAKAHASHI, T., TILBROOK, B. & WANNINKHOF, R. 2015. The reinvigoration of the Southern Ocean carbon sink. *Science,* 349**,** 1221.

LAROCHE, J., BOYD, P. W., MCKAY, R. M. L. & GEIDER, R. J. 1996. Flavodoxin as an in situ marker for iron stress in phytoplankton. *Nature,* 382**,** 802-805.

LAROCHE, J. & BREITBARTH, E. 2005. Importance of the diazotrophs as a source of new nitrogen in the ocean. *Journal of Sea Research,* 53**,** 67-91.

LAUFKÖTTER, C., VOGT, M., GRUBER, N., AITA-NOGUCHI, M., AUMONT, O., BOPP, L., BUITENHUIS, E., DONEY, S. C., DUNNE, J., HASHIOKA, T., HAUCK, J., HIRATA, T., JOHN, J., LE QUÉRÉ, C., LIMA, I. D., NAKANO, H., SEFERIAN, R., TOTTERDELL, I., VICHI, M. & VÖLKER, C. 2015. Drivers and uncertainties of future global marine primary production in marine ecosystem models. *Biogeosciences,* 12**,** 6955-6984.

LEDWELL, J. R., WATSON, A. J. & LAW, C. S. 1998. Mixing of a tracer in the pycnocline. *Journal of Geophysical Research-Oceans,* 103**,** 21499-21529.

LEE, M. M. & WILLIAMS, R. G. 2000. The role of eddies in the isopycnic transfer of nutrients and their impact on biological production. Journal of Marine Research, 58, 895-917.

LEFEBVRE, W. & GOOSSE, H. 2008. Analysis of the projected regional sea-ice changes in the Southern Ocean during the twenty-first century. *Climate Dynamics,* 30**,** 59-76.

LEWIS, B. L. & LUTHER III, G. W. 2000. Processes controlling the distribution and cycling of manganese in the oxygen minimum zone of the Arabian Sea. *Deep Sea Research Part II: Topical Studies in Oceanography,* 47**,** 1541-1561.

LIANG, J.-H., DEUTSCH, C., MCWILLIAMS, J. C., BASCHEK, B., SULLIVAN, P. P. & CHIBA, D. 2013. Parameterizing bubble-mediated air-sea gas exchange and its effect on ocean ventilation. *Global Biogeochemical Cycles,* 27**,** 894-905.

LOCARNINI, R. A., V., M. A., BARANOVA, O. K., BOYER, T. P., ZWENG, M. M., GARCIA, H. E., REAGAN, J. R., SEIDOV, D., WEATHERS, K., PAVER, C. R. & SMOLYAR, I. 2018. World Ocean Atlas 2018, Volume 1: Temperature. A. Mishonov Technical Ed.; NOAA Atlas NESDIS 81, 52 pp.

LONGHURST, A. R. 2007. *Ecological geography of the sea,* Amsterdam ; Boston, MA, Academic Press.

LUDWIG, M. L. & MATTHEWS, R. G. 1997. Structure-based perspectives on B-12-dependent enzymes. *Annual Review of Biochemistry,* 66**,** 269-313.

LUO, Y. W., DONEY, S. C., ANDERSON, L. A., BENAVIDES, M., BERMAN-FRANK, I., BODE, A., BONNET, S., BOSTROM, K. H., BOTTJER, D., CAPONE, D. G., CARPENTER, E. J., CHEN, Y. L., CHURCH, M. J., DORE, J. E., FALCON, L. I., FERNANDEZ, A., FOSTER, R. A., FURUYA, K., GOMEZ, F., GUNDERSEN, K., HYNES, A. M., KARL, D. M., KITAJIMA, S., LANGLOIS, R. J., LAROCHE, J., LETELIER, R. M., MARANON, E., MCGILLICUDDY, D. J., MOISANDER, P. H., MOORE, C. M., MOURINO-CARBALLIDO, B., MULHOLLAND, M. R., NEEDOBA, J. A., ORCUTT, K. M., POULTON, A. J., RAHAV, E., RAIMBAULT, P., REES, A. P., RIEMANN, L., SHIOZAKI, T., SUBRAMANIAM, A., TYRRELL, T., TURK-KUBO, K. A., VARELA, M., VILLAREAL, T. A., WEBB, E. A., WHITE, A. E., WU, J. & ZEHR, J. P. 2012. Database of diazotrophs in global ocean: abundance, biomass and nitrogen fixation rates. *Earth System Science Data,* 4**,** 47-73.

MAHAFFEY, C., REYNOLDS, S., DAVIS, C. E. & LOHAN, M. C. 2014. Alkaline phosphatase activity in the subtropical ocean: insights from nutrient, dust and trace metal addition experiments. *Frontiers in Marine Science,* 1.

MAHOWALD, N. M., BAKER, A. R., BERGAMETTI, G., BROOKS, N., DUCE, R. A., JICKELLS, T. D., KUBILAY, N., PROSPERO, J. M. & TEGEN, I. 2005. Atmospheric global dust cycle and iron inputs to the ocean. *Global Biogeochemical Cycles,* 19.

MAHOWALD, N. M. & LUO, C. 2003. A less dusty future? *Geophysical Research Letters,* 30.

MARITORENA, S., HEMBISE FANTON D'ANDON, O., MANGIN, A. & SIEGEL, D. A. 2010. Merged satellite ocean color data products using a bio-optical model: Characteristics, benefits and issues. *Remote Sensing of Environment,* 114**,** 1791-1804.

MARRA, J., BIDIGARE, R. R. & DICKEY, T. D. 1990. Nutrients and Mixing, Chlorophyll and Phytoplankton Growth. *Deep-Sea Research Part a-Oceanographic Research Papers,* 37**,** 127-143.

MARTIN, A. P., LUCAS, M. I., PAINTER, S. C., PIDCOCK, R., PRANDKE, H., PRANDKE, H. & STINCHCOMBE, M. C. 2010. The supply of nutrients due to vertical turbulent mixing: A study at the Porcupine Abyssal Plain study site in the northeast Atlantic. *Deep-Sea Research Part Ii-Topical Studies in Oceanography,* 57**,** 1293-1302.

MARTIN, J. H. 1990. Glacial-Interglacial Co2 Change: The Iron Hypothesis. *Paleoceanography,* 5**,** 1-13.

MARTIN, J. H. & FITZWATER, S. E. 1988. Iron-Deficiency Limits Phytoplankton Growth in the Northeast Pacific Subarctic. *Nature,* 331**,** 341-343.

MARTIN, J. H., FITZWATER, S. E. & GORDON, R. M. 1991. We Still Say Iron-Deficiency Limits Phytoplankton Growth in the Sub-Arctic Pacific. *Journal of Geophysical Research-Oceans,* 96**,** 20699-20700.

MARTIN, J. H., KNAUER, G. A., KARL, D. M. & BROENKOW, W. W. 1987. VERTEX: carbon cycling in the northeast Pacific. *Deep Sea Research Part A. Oceanographic Research Papers,* 34**,** 267-285.

MCCARTHY, G. D., SMEED, D. A., JOHNS, W. E., FRAJKA-WILLIAMS, E., MOAT, B. I., RAYNER, D., BARINGER, M. O., MEINEN, C. S., COLLINS, J. & BRYDEN, H. L. 2015. Measuring the Atlantic Meridional Overturning Circulation at 26°N. *Progress in Oceanography,* 130**,** 91-111.

MCGILLICUDDY, D. J. 2016. Mechanisms of Physical-Biological-Biogeochemical Interaction at the Oceanic Mesoscale. *Annual Review of Marine Science, Vol 8,* 8**,** 125-+.

MEASURES, C., HATTA, M., FITZSIMMONS, J. & MORTON, P. 2015. Dissolved Al in the zonal N Atlantic section of the US GEOTRACES 2010/2011 cruises and the importance of hydrothermal inputs. *Deep Sea Research Part II: Topical Studies in Oceanography,* 116**,** 176-186.

MEASURES, C. I., LANDING, W. M., BROWN, M. T. & BUCK, C. S. 2008. High-resolution Al and Fe data from the Atlantic Ocean CLIVAR-CO2 Repeat Hydrography A16N transect: Extensive linkages between atmospheric dust and upper ocean geochemistry. *Global Biogeochemical Cycles,* 22.

MEIJERS, A. J. S. 2014. The Southern Ocean in the Coupled Model Intercomparison Project phase 5. *Philosophical Transactions of the Royal Society A: Mathematical, Physical and Engineering Sciences,* 372**,** 20130296.

MENZEL BARRAQUETA, J. L., SCHLOSSER, C., PLANQUETTE, H., GOURAIN, A., CHEIZE, M., BOUTORH, J., SHELLEY, R., CONTREIRA PEREIRA, L., GLEDHILL, M., HOPWOOD, M. J., LACAN, F., LHERMINIER, P., SARTHOU, G. & ACHTERBERG, E. P. 2018. Aluminium in the North Atlantic Ocean and the Labrador Sea (GEOTRACES GA01 section): roles of continental inputs and biogenic particle removal. *Biogeosciences,* 15**,** 5271-5286.

MIDDAG, R., DE BAAR, H. J. W. & BRULAND, K. W. 2019. The Relationships Between Dissolved Zinc and Major Nutrients Phosphate and Silicate Along the GEOTRACES GA02 Transect in the West Atlantic Ocean. *Global Biogeochemical Cycles,* 33**,** 63-84.

MIDDAG, R., DE BAAR, H. J. W., LAAN, P., CAI, P. H. & VAN OOIJEN, J. C. 2011. Dissolved manganese in the Atlantic sector of the Southern Ocean. *Deep-Sea Research Part Ii-Topical Studies in Oceanography,* 58**,** 2661-2677.

MIDDAG, R., VAN HEUVEN, S. M. A. C., BRULAND, K. W. & DE BAAR, H. J. W. 2018. The relationship between cadmium and phosphate in the Atlantic Ocean unravelled. *Earth and Planetary Science Letters,* 492**,** 79-88.

MILLERO, F. J. & SOTOLONGO, S. 1989. The oxidation of Fe(II) with H2O2 in seawater. *Geochimica et Cosmochimica Acta,* 53**,** 1867-1873.

MILLERO, F. J., SOTOLONGO, S. & IZAGUIRRE, M. 1987. The oxidation kinetics of Fe(II) in seawater. *Geochimica et Cosmochimica Acta,* 51**,** 793-801.

MILLS, M. M., RIDAME, C., DAVEY, M., LA ROCHE, J. & GEIDER, R. J. 2004. Iron and phosphorus co-limit nitrogen fixation in the eastern tropical North Atlantic. *Nature,* 429**,** 292-294.

MOFFETT, J. W. & HO, J. 1996. Oxidation of cobalt and manganese in seawater via a common microbially catalyzed pathway. *Geochimica et Cosmochimica Acta,* 60**,** 3415-3424.

MOORE, C. M. 2016. Diagnosing oceanic nutrient deficiency. *Philosophical Transactions of the Royal Society a-Mathematical Physical and Engineering Sciences,* 374.

MOORE, C. M., MILLS, M. M., ACHTERBERG, E. P., GEIDER, R. J., LAROCHE, J., LUCAS, M. I., MCDONAGH, E. L., PAN, X., POULTON, A. J., RIJKENBERG, M. J. A., SUGGETT, D. J., USSHER, S. J. & WOODWARD, E. M. S. 2009. Large-scale distribution of Atlantic nitrogen fixation controlled by iron availability. *Nature Geoscience,* 2**,** 867-871.

MOORE, C. M., MILLS, M. M., ARRIGO, K. R., BERMAN-FRANK, I., BOPP, L., BOYD, P. W., GALBRAITH, E. D., GEIDER, R. J., GUIEU, C., JACCARD, S. L., JICKELLS, T. D., LA ROCHE, J., LENTON, T. M., MAHOWALD, N. M., MARANON, E., MARINOV, I., MOORE, J. K., NAKATSUKA, T., OSCHLIES, A., SAITO, M. A., THINGSTAD, T. F., TSUDA, A. & ULLOA, O. 2013. Processes and patterns of oceanic nutrient limitation. *Nature Geoscience,* 6**,** 701-710.

MOREL, F. M. M., LAM, P. J. & SAITO, M. A. 2020. Trace Metal Substitution in Marine Phytoplankton. *Annual Review of Earth and Planetary Sciences,* 48**,** 491-517.

MOREL, F. M. M. & PRICE, N. M. 2003. The biogeochemical cycles of trace metals in the oceans. *Science,* 300**,** 944-947.

MUNK, W. & WUNSCH, C. 1998. Abyssal recipes II: energetics of tidal and wind mixing. *Deep Sea Research Part I: Oceanographic Research Papers,* 45**,** 1977-2010.

NIELSDOTTIR, M. C., MOORE, C. M., SANDERS, R., HINZ, D. J. & ACHTERBERG, E. P. 2009. Iron limitation of the postbloom phytoplankton communities in the Iceland Basin. *Global Biogeochemical Cycles,* 23.

NOBLE, A. E., LAMBORG, C. H., OHNEMUS, D. C., LAM, P. J., GOEPFERT, T. J., MEASURES, C. I., FRAME, C. H., CASCIOTTI, K. L., DITULLIO, G. R., JENNINGS, J. & SAITO, M. A. 2012. Basin-scale inputs of cobalt, iron, and manganese from the Benguela-Angola front to the South Atlantic Ocean. *Limnology and Oceanography,* 57**,** 989-1010.

NOBLE, A. E., OHNEMUS, D. C., HAWCO, N. J., LAM, P. J. & SAITO, M. A. 2017. Coastal sources, sinks and strong organic complexation of dissolved cobalt within the US North Atlantic GEOTRACES transect GA03. *Biogeosciences,* 14**,** 2715-2739.

OKIN, G. S., BAKER, A. R., TEGEN, I., MAHOWALD, N. M., DENTENER, F. J., DUCE, R. A., GALLOWAY, J. N., HUNTER, K., KANAKIDOU, M., KUBILAY, N., PROSPERO, J. M., SARIN, M., SURAPIPITH, V., UEMATSU, M. & ZHU, T. 2011. Impacts of atmospheric nutrient deposition on marine productivity: Roles of nitrogen, phosphorus, and iron. *Global Biogeochemical Cycles,* 25.

OLIVER, E. C. J., BURROWS, M. T., DONAT, M. G., SEN GUPTA, A., ALEXANDER, L. V., PERKINS-KIRKPATRICK, S. E., BENTHUYSEN, J. A., HOBDAY, A. J., HOLBROOK, N. J., MOORE, P. J., THOMSEN, M. S., WERNBERG, T. & SMALE, D. A. 2019. Projected Marine Heatwaves in the 21st Century and the Potential for Ecological Impact. *Frontiers in Marine Science,* 6**,** 734.

OMAND, M. M. & MAHADEVAN, A. 2015. The shape of the oceanic nitracline. *Biogeosciences,* 12**,** 3273-3287.

OSBORN, T. R. 1980. Estimates of the Local Rate of Vertical Diffusion from Dissipation Measurements. *Journal of Physical Oceanography,* 10**,** 83-89.

OSCHLIES, A. 2002. Nutrient supply to the surface waters of the North Atlantic: A model study. *Journal of Geophysical Research-Oceans,* 107.

OWENS, S. A., PIKE, S. & BUESSELER, K. O. 2015. Thorium-234 as a tracer of particle dynamics and upper ocean export in the Atlantic Ocean. *Deep Sea Research Part II: Topical Studies in Oceanography,* 116**,** 42-59.

PAINTER, S. C., HENSON, S. A., FORRYAN, A., STEIGENBERGER, S., KLAR, J., STINCHCOMBE, M. C., ROGAN, N., BAKER, A. R., ACHTERBERG, E. P. & MOORE, C. M. 2014. An assessment of the vertical diffusive flux of iron and other nutrients to the surface waters of the subpolar North Atlantic Ocean. *Biogeosciences,* 11**,** 2113-2130.

PALTER, J. B. & LOZIER, M. S. 2008. On the source of Gulf Stream nutrients. *Journal of Geophysical Research: Oceans,* 113.

PALTER, J. B., LOZIER, M. S. & BARBER, R. T. 2005. The effect of advection on the nutrient reservoir in the North Atlantic subtropical gyre. *Nature,* 437**,** 687-692.

PEERS, G. & PRICE, N. M. 2006. Copper-containing plastocyanin used for electron transport by an oceanic diatom. *Nature,* 441**,** 341-344.

PELEGRÍ, J. L., CSANADY, G. T. & MARTINS, A. 1996. The North Atlantic nutrient stream. *Journal of Oceanography,* 52**,** 275-299.

PETERS, B. D., JENKINS, W. J., SWIFT, J. H., GERMAN, C. R., MOFFETT, J. W., CUTTER, G. A., BRZEZINSKI, M. A. & CASCIOTTI, K. L. 2018a. Water mass analysis of the 2013 US GEOTRACES eastern Pacific zonal transect (GP16). *Marine Chemistry,* 201**,** 6-19.

PETERS, B. D., LAM, P. J. & CASCIOTTI, K. L. 2018b. Nitrogen and oxygen isotope measurements of nitrate along the US GEOTRACES Eastern Pacific Zonal Transect (GP16) yield insights into nitrate supply, remineralization, and water mass transport. *Marine Chemistry,* 201**,** 137-150.

PRINCE, N. M. & MOREL, F. M. M. 1990. Cadmium and cobalt substitution for zinc in a marine diatom. *Nature,* 344**,** 658–660.

RAFTER, P. A., SIGMAN, D. M. & MACKEY, K. R. M. 2017. Recycled iron fuels new production in the eastern equatorial Pacific Ocean. *Nature Communications,* 8**,** 1100.

RATTEN, J. M., LAROCHE, J., DESAI, D. K., SHELLEY, R. U., LANDING, W. M., BOYLE, E., CUTTER, G. A. & LANGLOIS, R. J. 2015. Sources of iron and phosphate affect the distribution of diazotrophs in the North Atlantic. *Deep-Sea Research Part Ii-Topical Studies in Oceanography,* 116**,** 332-341.

RAVEN, J. A. 1988a. The Iron and Molybdenum use Efficiencies of Plant Growth with Different Energy, Carbon and Nitrogen Sources. *The New Phytologist,* 109**,** 279-287.

RAVEN, J. A. 1988b. The Iron and Molybdenum Use Efficiencies of Plant-Growth with Different Energy, Carbon and Nitrogen-Sources. *New Phytologist,* 109**,** 279-287.

RAVEN, J. A., EVANS, M. C. W. & KORB, R. E. 1999. The role of trace metals in photosynthetic electron transport in O2-evolving organisms. *Photosynthesis Research,* 60**,** 111-150.

REDFIELD, A. 1934. On the properties of organic derivatives in sea water and their relation to the composition of phytoplankton. *R. J. Daniel [ed.], James Johnstone memorial volume, University Press of Liverpool***,** 177-192.

REDFIELD, A. C. 1958. THE BIOLOGICAL CONTROL OF CHEMICAL FACTORS IN THE ENVIRONMENT. *American Scientist,* 46**,** 230A-221.

RESING, J. A., SEDWICK, P. N., GERMAN, C. R., JENKINS, W. J., MOFFETT, J. W., SOHST, B. M. & TAGLIABUE, A. 2015. Basin-scale transport of

hydrothermal dissolved metals across the South Pacific Ocean. *Nature,* 523**,** 200-U140.

RHEIN, M., RINTOUL, S. R., AOKI, S., CAMPOS, E., CHAMBERS, D., FEELY, R. A., GULEV, S., JOHNSON, G. C., JOSEY, S. A., KOSTIANOY, A., MAURITZEN, C., ROEMMICH, D., TALLEY, L. D. & WANG, F. 2013. Observations: Ocean. *In:* STOCKER, T. F., QIN, D., PLATTNER, G.-K., TIGNOR, M., ALLEN, S. K., BOSCHUNG, J., NAUELS, A., XIA, Y., BEX, V. & MIDGLEY, P. M. (eds.) *Climate Change 2013: The Physical Science Basis. Contribution of Working Group I to the Fifth Assessment Report of the Intergovernmental Panel on Climate Change.* Cambridge, United Kingdom and New York, NY, USA: Cambridge University Press.

RIGBY, S. J., WILLIAMS, R. G., ACHTERBERG, E. P. & TAGLIABUE, A. 2020. Resource Availability and Entrainment are driven by offsets between Nutriclines and Winter Mixed-Layer Depth. *Global Biogeochemical Cycles,* n/a**,** e2019GB006497.

RIJKENBERG, M. J. A., MIDDAG, R., LAAN, P., GERRINGA, L. J. A., VAN AKEN, H. M., SCHOEMANN, V., DE JONG, J. T. M. & DE BAAR, H. J. W. 2014. The Distribution of Dissolved Iron in the West Atlantic Ocean. *Plos One,* 9.

RIJKENBERG, M. J. A., STEIGENBERGER, S., POWELL, C. F., VAN HAREN, H., PATEY, M. D., BAKER, A. R. & ACHTERBERG, E. P. 2012. Fluxes and distribution of dissolved iron in the eastern (sub-) tropical North Atlantic Ocean. *Global Biogeochemical Cycles,* 26.

RODIONOV, D. A., VITRESCHAK, A. G., MIRONOV, A. A. & GELFAND, M. S. 2003. Comparative Genomics of the vitamin B-12 metabolism and regulation in prokaryotes. *Journal of Biological Chemistry,* 278**,** 41148-41159.

ROSHAN, S. & WU, J. 2015. Water mass mixing: The dominant control on the zinc distribution in the North Atlantic Ocean. *Global Biogeochemical Cycles,* 29**,** 1060-1074.

RUDNICK, R. L. & GAO, S. 2003. Composition of the continental crust. *In:* HOLLAND, H. D. & TUREKIAN, K. K. (eds.) *Treatise on Geochemistry.* Elsevier, Oxford, UK.

SAITO, M. A., GOEPFERT, T. J. & RITT, J. T. 2008. Some thoughts on the concept of colimitation: Three definitions and the importance of bioavailability. *Limnology and Oceanography,* 53**,** 276-290.

SAITO, M. A., MCILVIN, M. R., MORAN, D. M., GOEPFERT, T. J., DITULLIO, G. R., POST, A. F. & LAMBORG, C. H. 2014. Multiple nutrient stresses at

intersecting Pacific Ocean biomes detected by protein biomarkers. *Science,* 345**,** 1173-1177.

SALLEE, J. B., SHUCKBURGH, E., BRUNEAU, N., MEIJERS, A. J. S., BRACEGIRDLE, T. J., WANG, Z. & ROY, T. 2013. Assessment of Southern Ocean water mass circulation and characteristics in CMIP5 models: Historical bias and forcing response. *Journal of Geophysical Research-Oceans,* 118**,** 1830-1844.

SALLEE, J. B., SPEER, K. G. & RINTOUL, S. R. 2010. Zonally asymmetric response of the Southern Ocean mixed-layer depth to the Southern Annular Mode. *Nature Geoscience,* 3**,** 273-279.

SARMIENTO, J. L., GRUBER, N., BRZEZINSKI, M. A. & DUNNE, J. P. 2004. High-latitude controls of thermocline nutrients and low latitude biological productivity. *Nature,* 427**,** 56-60.

SCHLITZER, R., ANDERSON, R. F., DODAS, E. M., LOHAN, M., GEIBERE, W., TAGLIABUE, A., BOWIE, A., JEANDEL, C., MALDONADO, M. T., LANDING, W. M., COCKWELL, D., ABADIE, C., ABOUCHAMI, W., ACHTERBERG, E. P., AGATHER, A., AGULIAR-ISLAS, A., VAN AKEN, H. M., ANDERSEN, M., ARCHER, C., AURO, M., DE BAAR, H. J., BAARS, O., BAKER, A. R., BAKKER, K., BASAK, C., BASKARAN, M., BATES, N. R., BAUCH, D., VAN BEEK, P., BEHRENS, M. K., BLACK, E., BLUHM, K., BOPP, L., BOUMAN, H., BOWMAN, K., BOWN, J., BOYD, P., BOYE, M., BOYLE, E. A., BRANELLEC, P., BRIDGESTOCK, L., BRISSEBRAT, G., BROWNING, T., BRULAND, K. W., BRUMSACK, H. J., BRZEZINSKI, M., BUCK, C. S., BUCK, K. N., BUESSELER, K., BULL, A., BUTLER, E., CAI, P., MOR, P. C., CARDINAL, D., CARLSON, C., CARRASCO, G., CASACUBERTA, N., CASCIOTTI, K. L., CASTRILLEJO, M., CHAMIZO, E., CHANCE, R., CHARETTE, M. A., CHAVES, J. E., CHENG, H., CHEVER, F., CHRISTL, M., CHURCH, T. M., CLOSSET, I., COLMAN, A., CONWAY, T. M., COSSA, D., CROOT, P., CULLEN, J. T., CUTTER, G. A., DANIELS, C., DEHAIRS, F., DENG, F. F., DIEU, H. T., DUGGAN, B., DULAQUAIS, G., DUMOUSSEAUD, C., ECHEGOYEN-SANZ, Y., EDWARDS, R. L., ELLWOOD, M., FAHRBACH, E., FITZSIMMONS, J. N., FLEGAL, A. R., FLEISHER, M. Q., VAN DE FLIERDT, T., FRANK, M., FRIEDRICH, J., FRIPIAT, F., FROLLJE, H., GALER, S. J. G., GAMO, T., GANESHRAM, R. S., GARCIA-ORELLANA, J., GARCIA-SOLSONA, E., GAULT-RINGOLD, M., GEORGE, E., et al. 2018. The GEOTRACES Intermediate Data Product 2017. *Chemical Geology,* 493**,** 210-223.

SCHMIDTKO, S., STRAMMA, L. & VISBECK, M. 2017. Decline in global oceanic oxygen content during the past five decades. *Nature,* 542**,** 335-339.

SCHOLZ, F., SEVERMANN, S., MCMANUS, J. & HENSEN, C. 2014. Beyond the Black Sea paradigm: The sedimentary fingerprint of an open-marine iron shuttle. *Geochimica et Cosmochimica Acta,* 127**,** 368-380.

SEDWICK, P. N., CHURCH, T. M., BOWIE, A. R., MARSAY, C. M., USSHER, S. J., ACHILLES, K. M., LETHABY, P. J., JOHNSON, R. J., SARIN, M. M. & MCGILLICUDDY, D. J. 2005. Iron in the Sargasso Sea (Bermuda Atlantic Time-series Study region) during summer: Eolian imprint, spatiotemporal variability, and ecological implications. *Global Biogeochemical Cycles,* 19.

SEN GUPTA, A., SANTOSO, A., TASCHETTO, A. S., UMMENHOFER, C. C., TREVENA, J. & ENGLAND, M. H. 2009. Projected Changes to the Southern Hemisphere Ocean and Sea Ice in the IPCC AR4 Climate Models. *Journal of Climate,* 22**,** 3047-3078.

SHAKED, Y., XU, Y., LEBLANC, K. & MOREL, F. M. M. 2006. Zinc availability and alkaline phosphatase activity in Emiliania huxleyi: Implications for Zn-P co-limitation in the ocean. *Limnology and Oceanography,* 51**,** 299-309.

SHARPLES, J., MIDDELBURG, J. J., FENNEL, K. & JICKELLS, T. D. 2017. What proportion of riverine nutrients reaches the open ocean? *Global Biogeochemical Cycles,* 31**,** 39-58.

SHELLEY, R. U., LANDING, W. M., USSHER, S. J., PLANQUETTE, H. & SARTHOU, G. 2018. Regional trends in the fractional solubility of Fe and other metals from North Atlantic aerosols (GEOTRACES cruises GA01 and GA03) following a two-stage leach. *Biogeosciences,* 15**,** 2271-2288.

SHELLEY, R. U., ROCA-MARTÍ, M., CASTRILLEJO, M., SANIAL, V., MASQUÉ, P., LANDING, W. M., VAN BEEK, P., PLANQUETTE, H. & SARTHOU, G. 2017. Quantification of trace element atmospheric deposition fluxes to the Atlantic Ocean (>40°N; GEOVIDE, GEOTRACES GA01) during spring 2014. *Deep Sea Research Part I: Oceanographic Research Papers,* 119**,** 34-49.

SIEGEL, D. A., MCGILLICUDDY JR, D. J. & FIELDS, E. A. 1999. Mesoscale eddies, satellite altimetry, and new production in the Sargasso Sea. *Journal of Geophysical Research: Oceans,* 104**,** 13359-13379.

SIMPSON, J. H. & SHARPLES, J. 2012. *Introduction to the Physical and Biological Oceanography of Shelf Seas,* Cambridge, Cambridge University Press.

SOHM, J. A., WEBB, E. A. & CAPONE, D. G. 2011. Emerging patterns of marine nitrogen fixation. *Nature Reviews Microbiology,* 9**,** 499-508.

SPINGYS, C. P., WILLIAMS, R. G., TUERENA, R., NAVEIRA GARABATO, A. C., VIC, C., FORRYAN, A. & SHARPLES, J. *in prep*. The nutrient supply

from diapycnal mixing and eddy stirring for the oligotrophic North Atlantic. *Manuscript submitted for publication*

STANLEY, R. H. R., JENKINS, W. J., DONEY, S. C. & LOTT III, D. E. 2015. The 3He flux gauge in the Sargasso Sea: a determination of physical nutrient fluxes to the euphotic zone at the Bermuda Atlantic Time-series Site. *Biogeosciences,* 12**,** 5199-5210.

STANLEY, R. H. R., JENKINS, W. J., LOTT III, D. E. & DONEY, S. C. 2009. Noble gas constraints on air-sea gas exchange and bubble fluxes. *Journal of Geophysical Research: Oceans,* 114.

STRAMMA, L., JOHNSON, G. C., SPRINTALL, J. & MOHRHOLZ, V. 2008. Expanding Oxygen-Minimum Zones in the Tropical Oceans. *Science,* 320**,** 655.

SUNDA, W. 2012. Feedback Interactions between Trace Metal Nutrients and Phytoplankton in the Ocean. *Frontiers in Microbiology,* 3**,** 204.

SUNDA, W. G. 1989. Trace Metal Interactions with Marine Phytoplankton. *Biological Oceanography,* 6**,** 411-442.

SUNDA, W. G. & HUNTSMAN, S. A. 1994. Photoreduction of manganese oxides in seawater. *Marine Chemistry,* 46**,** 133-152.

SUNDA, W. G. & HUNTSMAN, S. A. 1995. Cobalt and zinc interreplacement in marine phytoplankton: Biological and geochemical implications. *Limnology and Oceanography,* 40**,** 1404-1417.

SUNDA, W. G. & HUNTSMAN, S. A. 1997. Interrelated influence of iron, light and cell size on marine phytoplankton growth. *Nature,* 390**,** 389-392.

SUNDA, W. G., HUNTSMAN, S. A. & HARVEY, G. R. 1983. Photo-Reduction of Manganese Oxides in Seawater and Its Geochemical and Biological Implications. *Nature,* 301**,** 234-236.

TAGKLIS, F., ITO, T. & BRACCO, A. 2020. Modulation of the North Atlantic deoxygenation by the slowdown of the nutrient stream. *Biogeosciences,* 17**,** 231-244.

TAGLIABUE, A. 2019. Elemental Distribution: Overview *In:* COCHRAN, J. K., BOKUNIEWICZ, H. J. & YAGER, P. L. (eds.) *Encyclopedia of Ocean Sciences.* 3 ed. London: Elsevier.

TAGLIABUE, A., BARRIER, N., DU PONTAVICE, H., KWIATKOWSKI, L., AUMONT, O., BOPP, L., CHEUNG, W. W. L., GASCUEL, D. & MAURY,

O. 2020. An iron cycle cascade governs the response of equatorial Pacific ecosystems to climate change. *Global Change Biology,* n/a.

TAGLIABUE, A., BOPP, L., DUTAY, J. C., BOWIE, A. R., CHEVER, F., JEAN-BAPTISTE, P., BUCCIARELLI, E., LANNUZEL, D., REMENYI, T., SARTHOU, G., AUMONT, O., GEHLEN, M. & JEANDEL, C. 2010. Hydrothermal contribution to the oceanic dissolved iron inventory. *Nature Geoscience,* 3**,** 252-256.

TAGLIABUE, A., HAWCO, N. J., BUNDY, R. M., LANDING, W. M., MILNE, A., MORTON, P. L. & SAITO, M. A. 2018. The Role of External Inputs and Internal Cycling in Shaping the Global Ocean Cobalt Distribution: Insights From the First Cobalt Biogeochemical Model. *Global Biogeochemical Cycles,* 32**,** 594-616.

TAGLIABUE, A., SALLEE, J. B., BOWIE, A. R., LEVY, M., SWART, S. & BOYD, P. W. 2014. Surface-water iron supplies in the Southern Ocean sustained by deep winter mixing. *Nature Geoscience,* 7**,** 314-320.

TANHUA, T., OLSSON, K. A. & JEANSSON, E. 2005. Formation of Denmark Strait overflow water and its hydro-chemical composition. *Journal of Marine Systems,* 57**,** 264-288.

TAYLOR, K. E., STOUFFER, R. J. & MEEHL, G. A. 2012. An Overview of Cmip5 and the Experiment Design. *Bulletin of the American Meteorological Society,* 93**,** 485-498.

THAMDRUP, B., DALSGAARD, T. & REVSBECH, N. P. 2012. Widespread functional anoxia in the oxygen minimum zone of the Eastern South Pacific. *Deep Sea Research Part I: Oceanographic Research Papers,* 65**,** 36-45.

THURNHERR, A. M. & RICHARDS, K. J. 2001. Hydrography and high-temperature heat flux of the Rainbow hydrothermal site (36°14′N, Mid-Atlantic Ridge). *Journal of Geophysical Research: Oceans,* 106**,** 9411-9426.

TRÉGUER, P., NELSON, D. M., VAN BENNEKOM, A. J., DEMASTER, D. J., LEYNAERT, A. & QUÉGUINER, B. 1995. The Silica Balance in the World Ocean: A Reestimate. *Science,* 268**,** 375.

TUERENA, R. E., GANESHRAM, R. S., GEIBERT, W., FALLICK, A. E., DOUGANS, J., TAIT, A., HENLEY, S. F. & WOODWARD, E. M. S. 2015. Nutrient cycling in the Atlantic basin: The evolution of nitrate isotope signatures in water masses. *Global Biogeochemical Cycles,* 29**,** 1830-1844.

TUERENA, R. E., WILLIAMS, R. G., MAHAFFEY, C., VIC, C., GREEN, J. A. M., NAVEIRA-GARABATO, A., FORRYAN, A. & SHARPLES, J. 2019.

Internal Tides Drive Nutrient Fluxes Into the Deep Chlorophyll Maximum Over Mid-ocean Ridges. *Global Biogeochemical Cycles,* 33**,** 995-1009.

TWINING, B. S. & BAINES, S. B. 2013. The Trace Metal Composition of Marine Phytoplankton. *Annual Review of Marine Science, Vol 5,* 5**,** 191-215.

TWINING, B. S., NODDER, S. D., KING, A. L., HUTCHINS, D. A., LECLEIR, G. R., DEBRUYN, J. M., MAAS, E. W., VOGT, S., WILHELM, S. W. & BOYD, P. W. 2014. Differential remineralization of major and trace elements in sinking diatoms. *Limnology and Oceanography,* 59**,** 689-704.

TWINING, B. S., RAUSCHENBERG, S., MORTON, P. L. & VOGT, S. 2015. Metal contents of phytoplankton and labile particulate material in the North Atlantic Ocean. *Progress in Oceanography,* 137**,** 261-283.

USSHER, S. J., ACHTERBERG, E. P., POWELL, C., BAKER, A. R., JICKELLS, T. D., TORRES, R. & WORSFOLD, P. J. 2013. Impact of atmospheric deposition on the contrasting iron biogeochemistry of the North and South Atlantic Ocean. *Global Biogeochemical Cycles,* 27**,** 1096-1107.

VAN HULTEN, M., MIDDAG, R., DUTAY, J. C., DE BAAR, H., ROY-BARMAN, M., GEHLEN, M., TAGLIABUE, A. & STERL, A. 2017. Manganese in the west Atlantic Ocean in the context of the first global ocean circulation model of manganese. *Biogeosciences,* 14**,** 1123-1152.

VEDAMATI, J., GOEPFERT, T. & MOFFETT, J. W. 2014. Iron speciation in the eastern tropical South Pacific oxygen minimum zone off Peru. *Limnology and Oceanography,* 59**,** 1945-1957.

VERDY, A. & MAZLOFF, M. R. 2017. A data assimilating model for estimating Southern Ocean biogeochemistry. *Journal of Geophysical Research: Oceans,* 122**,** 6968-6988.

VIC, C., NAVEIRA GARABATO, A. C., GREEN, J. A. M., SPINGYS, C., FORRYAN, A., ZHAO, Z. & SHARPLES, J. 2018. The Lifecycle of Semidiurnal Internal Tides over the Northern Mid-Atlantic Ridge. *Journal of Physical Oceanography,* 48**,** 61-80.

VIC, C., NAVEIRA GARABATO, A. C., GREEN, J. A. M., WATERHOUSE, A. F., ZHAO, Z., MELET, A., DE LAVERGNE, C., BUIJSMAN, M. C. & STEPHENSON, G. R. 2019. Deep-ocean mixing driven by small-scale internal tides. *Nature Communications,* 10**,** 2099.

WANNINKHOF, R. 1992. Relationship between wind speed and gas exchange over the ocean. *Journal of Geophysical Research: Oceans,* 97**,** 7373-7382.

WANNINKHOF, R. 2014. Relationship between wind speed and gas exchange over the ocean revisited. *Limnology and Oceanography: Methods,* 12**,** 351-362.

WANNINKHOF, R. & MCGILLIS, W. R. 1999. A cubic relationship between air-sea CO2 exchange and wind speed. *Geophysical Research Letters,* 26**,** 1889-1892.

WARD, B. A., DUTKIEWICZ, S., MOORE, C. M. & FOLLOWS, M. J. 2013. Iron, phosphorus, and nitrogen supply ratios define the biogeography of nitrogen fixation. *Limnology and Oceanography,* 58**,** 2059-2075.

WATERHOUSE, A. F., MACKINNON, J. A., NASH, J. D., ALFORD, M. H., KUNZE, E., SIMMONS, H. L., POLZIN, K. L., ST. LAURENT, L. C., SUN, O. M., PINKEL, R., TALLEY, L. D., WHALEN, C. B., HUUSSEN, T. N., CARTER, G. S., FER, I., WATERMAN, S., NAVEIRA GARABATO, A. C., SANFORD, T. B. & LEE, C. M. 2014. Global Patterns of Diapycnal Mixing from Measurements of the Turbulent Dissipation Rate. *Journal of Physical Oceanography,* 44**,** 1854-1872.

WEBER, T., JOHN, S., TAGLIABUE, A. & DEVRIES, T. 2018. Biological uptake and reversible scavenging of zinc in the global ocean. *Science,* 361**,** 73-+.

WHALEN, C. B., MACKINNON, J. A. & TALLEY, L. D. 2018. Large-scale impacts of the mesoscale environment on mixing from wind-driven internal waves. *Nature Geoscience,* 11**,** 842-+.

WHALEN, C. B., MACKINNON, J. A., TALLEY, L. D. & WATERHOUSE, A. F. 2015. Estimating the Mean Diapycnal Mixing Using a Finescale Strain Parameterization. *Journal of Physical Oceanography,* 45**,** 1174-1188.

WHALEN, C. B., TALLEY, L. D. & MACKINNON, J. A. 2012. Spatial and temporal variability of global ocean mixing inferred from Argo profiles. *Geophysical Research Letters,* 39.

WHITT, D. B. & JANSEN, M. F. 2020. Slower nutrient stream suppresses Subarctic Atlantic Ocean biological productivity in global warming. *Proceedings of the National Academy of Sciences***,** 202000851.

WILLIAMS, R. G. 1988. Modification of ocean eddies by air-sea interaction. *Journal of Geophysical Research: Oceans,* 93**,** 15523-15533.

WILLIAMS, R. G. & FOLLOWS, M. J. 1998. The Ekman transfer of nutrients and maintenance of new production over the North Atlantic. *Deep-Sea Research Part I-Oceanographic Research Papers,* 45**,** 461-489.

WILLIAMS, R. G. & FOLLOWS, M. J. 2003a. *Physical transport of nutrients and the maintenance of biological production,* New York, Springer-Verlag.

WILLIAMS, R. G. & FOLLOWS, M. J. 2003b. Physical transport of nutrients and the maintenance of biological production, 19-51, In `Ocean Biogeochemistry: The role of the ocean carbon cycle in global change'. Edited by M. Fasham. Springer. ISBN: 3-540-42398-2

WILLIAMS, R. G. & FOLLOWS, M. J. 2013. *Ocean Dynamics and the Carbon Cycle: Principles and Mechanisms,* Cambridge, UK, Cambridge Univ. Press.

WILLIAMS, R. G., MCLAREN, A. J. & FOLLOWS, M. J. 2000. Estimating the convective supply of nitrate and implied variability in export production over the North Atlantic. *Global Biogeochemical Cycles,* 14**,** 1299-1313.

WILLIAMS, R. G., ROUSSENOV, V. & FOLLOWS, M. J. 2006. Nutrient streams and their induction into the mixed layer. *Global Biogeochemical Cycles,* 20.

WOOLF, D. K. 1997. Bubbles and their role in gas exchange. *In:* LISS, P. S. & DUCE, R. A. (eds.) *The Sea Surface and Global Change.* Cambridge: Cambridge University Press.

WU, L., JING, Z., RISER, S. & VISBECK, M. 2011. Seasonal and spatial variations of Southern Ocean diapycnal mixing from Argo profiling floats. *Nature Geoscience,* 4**,** 363-366.

WU, M., MCCAIN, J. S. P., ROWLAND, E., MIDDAG, R., SANDGREN, M., ALLEN, A. E. & BERTRAND, E. M. 2019. Manganese and iron deficiency in Southern Ocean Phaeocystis antarctica populations revealed through taxon-specific protein indicators. *Nature Communications,* 10.

WYATT, N. J., MILNE, A., WOODWARD, E. M. S., REES, A. P., BROWNING, T. J., BOUMAN, H. A., WORSFOLD, P. J. & LOHAN, M. C. 2014. Biogeochemical cycling of dissolved zinc along the GEOTRACES South Atlantic transect GA10 at 40 S. *Global Biogeochemical Cycles,* 28**,** 44-56.

ZWENG, M. M., REAGAN, J. R., SEIDOV, D., BOYER, T. P., LOCARNINI, R. A., GARCIA, H. E., MISHONOV, A. V., BARANOVA, O. K., WEATHERS, K., PAVER, C. R. & SMOLYAR, I. 2018. World Ocean Atlas 2018, Volume 2: Salinity. A. Mishonov Technical Ed.; NOAA Atlas NESDIS 82, 50 pp.